

# **Ultrafast acoustic response of semiconductor heterostructures analyzed by time-resolved hard X-ray diffraction**

Der Fakultät für Physik  
der Universität Duisburg-Essen vorgelegte

## **Dissertation**

zum Erwerb des akademischen Grades eines Doktors der  
Naturwissenschaften  
(Dr. rer. nat.)

von  
**Mohammadmahdi Afshari**  
aus Teheran (Iran)

Referent: Prof. Dr. Klaus Sokolowski-Tinten  
Korreferent: Prof. Dr. Sascha Schäfer

Prüfer: Prof. Dr. Dmitry Turchinovich  
Vorsitzender des Prüfungsausschusses: Prof. Dr. Jürgen König  
Tag der mündlichen Prüfung: 30. Juli 2018



---

Hiermit erkläre ich,

- dass ich die eingereichte Dissertation selbstständig verfasst habe.
- dass ich die Erlangung des akademischen Grades eines Doktors der Naturwissenschaften (Dr. rer. nat.) anstrebe.
- dass ich nur die angegebenen Hilfsmittel verwendet habe und alle wörtlich oder inhaltlich übernommenen Stellen als solche kenntlich gemacht habe.
- dass die vorliegende Arbeit weder im Aus- noch im Inland in gleicher oder ähnlicher Form einer anderen Prüfungsbehörde vorgelegt wurde.

Duisburg, Juni 2018

## Kurzfassung

Die Dynamik des Gitters hat einen weitreichenden Einfluss auf die fundamentalen Eigenschaften von Materie durch die Kopplung von strukturellen, elektronischen und magnetischen Freiheitsgraden. Insbesondere gerichteter Druck und Deformationen können die physikalischen Eigenschaften von Halbleitern, wie die elektronische Bandstruktur und den Ladungstransport beeinflussen. Diese Effekte haben insbesondere in modernen nano-skalierten Bauelementen an Bedeutung gewonnen und werden, sowohl statisch als auch dynamisch, auch zum gezielten Materialdesign verwendet. Ultraschnelle Röntgenbeugung in Kombination mit Ultrakurzimpulsanregung ist ein vielversprechender Ansatz, transiente Verspannungszustände in Materie mit atomarer räumlicher und der notwendigen zeitlichen Auflösung zu untersuchen.

Ultrakurze Laserimpulse liefern die Möglichkeit, Energie in begrenzte Bereiche eines Materials auf sehr kurzen Zeitskalen einzubringen. Diese Energie ist zunächst im elektronischen Subsystem deponiert. Anschließend transferieren die erzeugten „heißen Ladungsträger“ ihre Überschussenergie auf der Zeitskala von typischerweise Pikosekunden an das Gitter. Beides, die elektronische Anregung sowie die quasi-isochore Heizung des Materials führen zu einer nahezu instantanen Erhöhung des Druckes. Die Relaxation dieses Druckes erzeugt Verspannungswellen, welche als kohärente Superposition von akustischen Phononen verstanden werden können.

In dieser Arbeit wurde ein neues Anregungs-Abfrage-Experiment, basierend auf ultrakurzen Röntgenpulsen bei 4.5 keV (Ti- $K_{\alpha}$ ) welche durch ein laser-getriebenes Plasma erzeugt werden, entwickelt, aufgebaut und sorgfältig charakterisiert. Insbesondere der nutzbare Röntgenfluss auf der Probe wurde um beinahe eine Größenordnung gegenüber allen vorherigen Aufbauten an der Universität Duisburg-Essen gesteigert. Der erhöhte Röntgenfluss ( $10^5$  Photonen/Impuls), der kleine Röntgenfokus ( $\varnothing \sim 80 \mu\text{m}$ ), die Femtosekunden Röntgenimpulsdauer und die hohe Monochromazität machen diesen Aufbau zu einem perfekten Werkzeug um hochqualitative Röntgenmuster zur Verfolgung von selbst feinsten Änderungen in Anrege-Abfrage-Experimenten zu erzeugen.

Die ultraschnelle Röntgenbeugung wurde angewendet um die Dynamik von laser-angeregten, kohärenten akustischen Phononen (CAP) in Ge(111)-Si(111) Heterostrukturen zu untersuchen. Durch Messung der transienten Änderungen der Winkelverteilung Bragg-gestreuter Röntgenstrahlen („rocking curves“) als Funktion der Anrege-Abfrage-Zeit waren wir in der Lage, die Entwicklung der Verspannungen in beiden Materialien zu verfolgen. Eine zeitabhängige Funktion mit anfänglicher isochorem Anstieg, gefolgt von einem exponentiellen Abfall wurde eingeführt um den photo-induzierten Druck in Ge zu modellieren. Basierend hierauf wurden die experimentellen Daten reproduziert. Dies erlaubt eine Abschätzung der fluenzabhängigen elektronischen und thermo-elastischen Druckbeiträge sowie der Druckrelaxationszeiten (welche vergleichbar sind mit den akustischen Antwortzeiten in Ge, gegeben durch das Verhältnis von Filmdicke und Schallgeschwindigkeit), abzuschätzen. Es wurde geschlossen, dass Auger-Rekombination des angeregten Elektron-Loch Plasmas und die damit einhergehende langsame Aufheizung des Gitters („Auger heating“) verantwortlich sind für die beobachtete zeit- und fluenzabhängige Verspannung, welche die CAP treibt.

# Abstract

Lattice dynamics has a major effect on fundamental properties of materials due to the coupling between structural, electronic and magnetic degrees of freedom. In particular, stress and strain can alter the physical properties of semiconductors, such as electronic band structure and carrier transport properties. These effects have become particularly important in modern nano-scale electronic devices and are also used to “strain”-engineer materials with tailored properties, both statically and dynamically. Ultrafast time-resolved X-ray diffraction in combination with short pulse laser excitation is a promising approach to study transient strains in materials with atomic-scale spatial and the required high temporal resolution.

Ultrashort laser pulses provide the ability to deliver energy into confined regions of a material on very short time-scales. This energy is initially deposited in the electronic subsystem. Subsequently, the “hot” carriers transfer their excess energy to the lattice on typical time-scales of just a few ps. Both the electronic excitation as well as the quasi-isochoric heating of the material lead to a nearly instantaneous increase in pressure. Relaxation of the pressure triggers strain waves, which can be regarded as a coherent superposition of acoustic phonons.

In this work, a new optical-pump - X-ray-probe setup, based on ultrashort X-ray pulse generation at 4.5 keV (Ti- $K_{\alpha 1}$ ) with the help of a laser-driven plasma, was designed, constructed and carefully characterized. In particular, the usable X-ray flux delivered to the sample under study was increased by almost an order of magnitude compared to all previous setups used at the University of Duisburg-Essen. The enhanced X-ray flux ( $\sim 10^5$  photons/pulse), small X-ray focus on the sample ( $\varnothing \sim 80 \mu\text{m}$ ), femtosecond X-ray pulse duration and the high monochromaticity make this setup the perfect tool to measure high quality X-ray diffraction patterns to follow even subtle transient changes in a pump-probe experiment.

Based on this, ultrafast time-resolved X-ray diffraction is applied to study the dynamics of laser-generated coherent acoustic phonons (CAP) in a Ge(111)-Si(111) heterostructure following fs optical excitation. By measuring the transient changes of the angular distribution of Bragg-diffracted X-rays (rocking curves) as a function of pump-probe delay time, we are able to follow the strain evolution in both the Ge thin film (180 nm) as well as the Si substrate. A time-dependent function, with an initial isochoric rise followed by an exponential decay, is introduced to model the photo-induced pressure in Ge. Based on this, the experimental data are numerically reproduced. This allows to estimate the fluence-dependent electronic and thermo-elastic pressure contributions as well as the pressure decay time which is comparable to the acoustic response time scale defined as the Ge film thickness divided by sound velocity. It is found that Auger recombination of the excited electron-hole plasma and the associated “slow” heating of the lattice (Auger heating) are responsible for the observed time- and fluence-dependent stress driving the CAP.

# Contents

Deutsche Kurzfassung .....	IV
Abstract.....	V
Contents .....	VI
<b>Chapter 1: Introduction .....</b>	<b>1</b>
1-1 Background and motivation .....	1
1-2 Structure of the thesis.....	4
<b>Chapter 2: Brief theoretical background .....</b>	<b>5</b>
2-1 Elastic wave propagation .....	5
2-2 Photo-induced stress sources.....	9
2-2-1 Thermo-elasticity .....	10
2-2-2 Deformation potential mechanism.....	11
2-3 Theory of X-ray diffraction.....	12
2-3-1 Kinematical X-ray diffraction.....	13
2-3-2 Dynamical X-ray diffraction.....	16
2-4 Principles of laser-plasma based X-ray generation .....	19
<b>Chapter 3: Ultrashort laser-plasma based X-ray pulse source .....</b>	<b>26</b>
3-1 Femtosecond laser system.....	27
3-2 Setup configuration .....	30
3-2-1 Optical part of the setup.....	30
3-2-2 X-ray part of the setup .....	34
3-3 X-ray detection.....	38
3-4 X-ray optics.....	41
3-4-1 Toroidally bent crystal mirror.....	42

3-5 X-ray spectrum.....	46
3-6 X-ray yield optimization .....	48
3-7 Static X-ray diffraction .....	51
3-8 Normalization of measured signals.....	55
3-9 Spatial and temporal overlap between the pump and probe.....	57
3-10 Summary and outlook .....	59
<b>Chapter 4: Picosecond acoustic response of a Ge-Si heterostructure .....</b>	<b>60</b>
4-1 Relevant mechanisms for photo-induced stress generation in Ge.....	61
4-1-1 Carrier excitation and relaxation mechanisms in Ge .....	61
4-1-2 Photo-induced stress in Ge .....	68
4-2 Pump-probe experimental conditions.....	71
4-3 Detection of strain waves propagating in the Ge-Si heterostructure.....	72
4-3-1 Detection of strain waves propagating in the Ge thin film.....	73
4-3-2 Detection of strain waves propagating in the Si substrate .....	76
4-4 Modeling of the acoustic response of the Ge-Si heterostructure.....	78
4-4-1 Failure of the constant photo-induced pressure model .....	82
4-4-2 Time-dependent photo-induced pressure model.....	85
4-5 Summary and discussion.....	95
<b>Chapter 5: Summary and outlook.....</b>	<b>97</b>
5-1 Summary .....	97
5-2 Outlook.....	99
<b>Appendixes .....</b>	<b>101</b>
A. Sample material properties .....	101
A-1 Ge.....	101
A-2 Si .....	104
B. Measured and calculated rocking curves of Ge and Si .....	104
C. “Matlab” codes .....	111
<b>Bibliography .....</b>	<b>130</b>
<b>Acknowledgements .....</b>	<b>149</b>



## *Chapter 1*

### **Introduction**

Understanding lattice dynamics in solids and its coupling to the electronic and spin degrees of freedom under non-equilibrium conditions is of fundamental interest and a major theme in modern condensed matter physics. Various elementary interaction processes, like electron-electron, electron-phonon and phonon-phonon scattering govern the structural and electronic dynamics on ultrafast time-scales [1, 2]. Femtosecond laser excitation is an ideal (and often “non-destructive”) method to generate such non-equilibrium states in materials. At the same time, ultrafast pump-probe techniques allow us to directly study the response of the excited system with the required temporal resolution in the femto- to picosecond time range. With respect to the lattice dynamics, earlier all-optical pump-probe experiments provided some interesting insight into the lattice response of laser-excited metals as well as semiconductors [3-9]. These techniques, however, probe the lattice dynamics only indirectly via associated changes of the optical properties. Moreover, the probing depth of optical probes is often very small (i.e. skin depth) and, consequently, these methods can only provide information on the response of the near-surface region. In order to probe the lattice response directly and not only at the surface but deep into the bulk of materials, time-resolved diffraction techniques using ultrashort X-ray or electron pulses have been developed over the last 20 years. These approaches combine spatial **and** temporal resolution at the “atomic-scale” and allow to extend established structural sensitive techniques to the ultrafast time domain.

#### **1-1 Background and motivation**

Continuous radiation from X-ray [10], electron [11, 12] and neutron [13, 14] sources is a standard tool that has been used over the past hundred years to investigate the atomic configurations of materials at equilibrium. Although the radiation of these sources provides the required atomic-scale spatial resolution, their temporal resolution was not sufficient to reveal the ultrafast lattice dynamics of non-equilibrium states. With the advent of new types of radiation sources that provide ultrashort (femtosecond) pulses of X-rays [15-19] or electrons [20-24] during the past two decades, the required combination of temporal and spatial resolution for direct quantitative studies of ultrafast atomic motion has been realized. Based on this, both kinds of sources have made tremendous progress over the years and they are increasingly used to address many different features of the ultrafast structural dynamics.

Since the work presented in this thesis is based on time-resolved X-ray diffraction, in the following, a brief review on some aspects of the lattice dynamics revealed by optical-pump - X-ray-probe techniques are presented.

Direct monitoring of coherent acoustic phonons created by the impulsive stress in metals and semiconductors following ultrashort laser pulses excitation have been the subject of numerous studies [25-50] since Rose-Petruck *et al.* [51] used time-resolved X-ray diffraction for the first time to measure the acoustic response of a bulk GaAs crystal. Furthermore, coherent optical phonons, which are connected to the atomic displacement within the unit cell, have been detected directly as well [52-61]. Optical-pump - X-ray-probe techniques have also been widely employed to investigate phase transitions in ferroelectric [62-67] and ferromagnetic [68-74] materials following ultrafast excitation. Another interesting topic in this field is laser-induced melting, which can be of “thermal” or “non-thermal” (i.e. disordering occurs before establishing thermal equilibrium between the electronic and lattice subsystems) character [32, 50, 75-82]. More recently, ultrafast inelastic or diffuse X-ray scattering has been employed to study non-equilibrium effects/distributions in the phononic subsystem [83-87]. Covering all fundamental studies on the lattice dynamics using optical-pump - X-ray-probe approaches is beyond the scope of this thesis and the reader is referred to a number of reviews that can be found in literature [88-90].

Besides fundamental investigations on non-equilibrium lattice dynamics, continuous efforts have been made to develop and optimize ultrashort X-ray pulse sources. Until now, the currently used and potential future sources of ultrashort X-ray radiation can be sorted with respect to the X-ray generation mechanism as:

- X-ray sources based on high-order harmonic generation (HHG): In these kinds of X-ray sources, X-ray radiation (soft X-rays) is generated by the non-linear interaction of a strong laser field with atoms of noble gases [91].
- Laser-driven Betatron X-ray sources: Modern ultrashort laser systems can easily provide focused intensities above  $10^{18}$  W/cm<sup>2</sup>, where the laser-matter interaction becomes highly relativistic. At these conditions, short electron pulses at a relativistic energy range can be achieved in low-density plasmas by the so-called laser wakefield acceleration mechanism [92]. Based on this, several unique X-ray sources, spanning the radiation spectrum from soft X-rays to gamma rays, have been demonstrated/proposed [93].
- Laser-plasma based sources: These are well-established laboratory-sized ultrashort X-ray pulse sources. An ultrashort laser pulse focused on a solid target at typical intensities in the range of  $10^{16}$  to  $10^{18}$  W/cm<sup>2</sup> generates a plasma layer and accelerates electrons into the solid target. The interaction between these electrons and atoms of the target creates continuum and characteristic lines of X-ray radiation similar to an ordinary X-ray tube, but with ultrashort duration [15, 16, 59, 94-97]. With this

type of source, the first time-resolved diffraction experiment with sub-ps temporal resolution has been performed [75].

- *Accelerator-undulator based sources*: The above mentioned ultrashort X-ray pulse sources are all laser-based and laboratory-scale. However, ultrashort X-ray pulses have been generated in large-scale facilities based on relativistic electron bunches from a storage ring or a linear accelerator. When such high energy and short duration electron pulses pass through an undulator, they emit ultrashort X-ray pulses via the synchrotron radiation mechanism [98]. Typical X-ray pulse duration generated in these X-ray sources is about tens to hundreds of picoseconds, which is suitable to investigate relatively slow phenomena. Employing either bunch slicing techniques in storage rings [18] or bunch compression in linear accelerators [89] has allowed overcoming this limitation and sub-picosecond X-ray pulses have been achieved. The most dramatic advance in recent years has been the development of the so-called X-ray free-electron lasers (XFEL). In an XFEL, high brightness electron bunches of ultrashort duration from a linear accelerator propagate through a long chain of undulators, where the complex interaction of the propagating electron bunch with the generated radiation field leads to an orders of magnitude enhancement of the X-ray output, which exhibits laser-like properties (e.g. full spatial coherence) [99].

Depending on the characteristics of these sources (e.g. photon energy, pulse duration, repetition rate and coherence), they can have different applications. Sources that work in the soft X-ray regime (HHG sources and storage rings, such as ALS in the USA [18], BESSY in Germany [19]) are more appropriate for time-resolved X-ray spectroscopy [100-104]. Ultrashort hard X-ray pulses are more desired for time-resolved diffraction, since diffraction requires a wavelength shorter than the lattice constant. Therefore, XFELs (such as LCLS in the USA [105], SACLA in Japan [106] and European XFEL in Germany [107]), laser-driven Betatron and laser-plasma based sources are best suited for time-resolved diffraction experiments. While XFELs define the status in this field by providing the “best” X-ray pulses currently available with a high degree of coherence and unprecedented photon flux (about  $10^{12}$  photon/pulse), their most important drawback from a user-standpoint is the limited access. This makes laser-driven Betatron and laser-plasma based X-ray sources still an attractive alternative in not so “photon-hungry” applications, since they can be set up much easier on a laboratory scale with virtually no access limitations.

The scope of this thesis is to study the “acoustic” response of materials following femtosecond optical excitation using time-resolved X-ray diffraction. The primary aim of this work is a quantitative exploration of the contributions of different coherent acoustic phonons sources and direct measuring of generated strain waves (coherent acoustic phonons) in a Ge-Si heterostructure. The lattice strain can significantly influence fundamental properties of semiconductors, such as the electronic band structure, deformation potentials and carrier mobility [108]. These fundamental properties determine the efficiency of the semiconductor microelectronics and photonic devices [109-111]. Interestingly, strain-

induced changes to the electronic band structure of Ge have attracted considerable attention to epitaxial Ge thin films on Si substrates as a new generation of light emitting materials [112, 113].

While ultrafast electron diffraction has also been used to investigate acoustic responses [114, 115], time-resolved X-ray diffraction usually provides higher momentum resolution (i.e. higher angular resolution) compared to electron diffraction, thus, allowing sensitive measurements of the transient strain associated with laser-induced acoustic perturbations. This makes X-ray diffraction the technique of choice to study coherent acoustic phonons. In the frame of this thesis, a new ultrashort laser-plasma based X-ray pulse source has been constructed and its performance optimized that allowed the study of the above mentioned effects with high sensitivity and accuracy.

## 1-2 Structure of the thesis

The thesis is structured as follows:

Chapter 2 presents the theoretical background of coherent acoustic phonons (strain waves) generation and propagation in solids. Afterwards, the basic concepts of X-ray diffraction and the corresponding theoretical formalism to calculate X-ray diffraction patterns are discussed. This is followed by a broad review of the mechanisms relevant to the laser-plasma based generation of ultrashort X-ray pulses.

In chapter 3, the experimental setup based on a “modular” scheme for time-resolved X-ray diffraction is presented. This chapter discusses the technical features of the setup as well as its characteristics, which have been optimized for measuring the acoustic response of the sample under investigation following femtosecond optical excitation.

Chapter 4 presents the results of time-resolved diffraction experiments on a Ge-Si heterostructure after excitation by a femtosecond laser pulse. Detailed and accurate measurements of the angle- and time-resolved X-ray diffraction patterns of both the Ge overlayer and Si substrate allowed investigating the generation and propagation of strain waves (coherent acoustic phonons). The experimental data for different excitation fluences have been compared to model calculations, which combine the solution of the acoustic wave equation with dynamical diffraction theory. From this analysis, detailed information on the relevant stress contributions driving the acoustic response and their variation with excitation fluence could be obtained.

Finally, chapter 5 summarizes the contributions made in this work and provides an outlook, both technically as well as with respect to the general scientific questions.

## *Chapter 2*

### **Brief theoretical background**

Coherent lattice motions occur through several different carrier-phonon and photon-phonon coupling mechanisms in photo-excited solids. These motions usually are introduced in terms of coherent acoustic and coherent optical phonons. The coupling mechanisms resulting in coherent acoustic phonons generation are described by the thermo-elasticity, the deformation potential mechanism, the inverse piezoelectric effect and the electrostriction [90]. As mentioned earlier, time-resolved X-ray diffraction can be used to investigate the coherent lattice motion.

Although the mentioned generation processes may drive all kinds of coherent acoustic lattice motions (i.e. longitudinal and transvers coherent acoustic phonons) this chapter only attends to the longitudinal ones. In the first section, the fundamentals of elasticity and the elastic wave equation are shortly described. The second section is a brief description of the driving photo-induced stress caused by thermo-elasticity and deformation potential mechanisms. In the third section, the theory of X-ray diffraction in crystals is provided and in the last section the theoretical background of the ultrashort laser-plasma based X-ray generation is discussed.

#### **2-1 Elastic wave propagation**

The classical theory of elasticity properly describes the coherent acoustic phonons excited close to the center of the Brillouin zone. Since the wavelength of the acoustic phonons is much longer than the unit cell size, a general deformation of the solid can be described in terms of a continuous displacement vector field  $\mathbf{u}(\mathbf{r})$ . It defines the vector displacement of the point of the solid that is located at position  $\mathbf{r}$  in the reference state (i.e. in equilibrium). Another useful quantity, which describes the deformation of the solid relative to its reference state, is the strain tensor. According to the *linear elasticity theory* [116], the strain tensor  $\boldsymbol{\eta}$  is defined as

$$\eta_{mn} = \frac{1}{2} \left( \frac{\partial u_m}{\partial x_n} + \frac{\partial u_n}{\partial x_m} \right) \quad (2.1)$$

where the components  $\eta_{11}$ ,  $\eta_{22}$  and  $\eta_{33}$  are the longitudinal strains in the  $x_1$ ,  $x_2$  and  $x_3$  directions, respectively. The off-diagonal elements also present shear strains. It is not possible to discuss the deformation in a solid without introducing the relation between internal forces, or stress, and the strain tensor. The stress tensor, so to speak, is a measure of the internal mechanical forces acting within a deformable solid. In a harmonic approximation, the generalized Hook law expresses the relation between the stress and the mechanical strain in the deformed solid, so that

$$S_{ij} = C_{ijkl} \eta_{kl}^{(M)} \quad (2.2)$$

where  $\mathbf{S}$  is the stress tensor,  $\mathbf{C}$  is the elastic coefficient tensor determined by the physical properties of the solid and  $\boldsymbol{\eta}^{(M)}$  is the mechanical strain tensor caused by a mechanical load on the solid. However, other physical mechanisms can produce an effect on the behavior of the solid structure, which are not essentially mechanical; for example, the solid expands when the temperature increases. This expansion is explained by the thermal strain and as a result, the total strain of the solid is the sum of the mechanical strain and thermal strain. If thermal expansion is hindered by some means (e.g. mechanical constrains or if the heating process is too fast that a deformation of the solid is not possible in that time scale), then “thermo-elastic stress” can rise. It has to be noted that “thermo-elastic stress” might be misleading. More rigorously, one should talk about “stress due to thermal effects”, since stress is always mechanical. Heating up the solid is not the only non-mechanical event to deform the solid and as it will be discuss later, there are other non-mechanical events as well (see section 2-2). Thus, the relation between the stress tensor and the total strain tensor is

$$\mathbf{S} = \mathbf{C} \otimes \boldsymbol{\eta} + \boldsymbol{\sigma} \quad (2.3)$$

where  $\boldsymbol{\eta}$  is the total strain tensor and  $\boldsymbol{\sigma}$  is the so-called “non-mechanical stress” tensor to account for all non-mechanical phenomena. Using equation (2.3) together with the momentum conservation principle, one can derive the structure equation of motion or the elastic wave equation [116] as

$$\rho \frac{\partial^2 u_i}{\partial t^2} = \frac{1}{2} C_{ijkl} \left( \frac{\partial^2 u_k}{\partial x_j \partial x_l} + \frac{\partial^2 u_l}{\partial x_j \partial x_k} \right) + \frac{\partial \sigma_{ij}}{\partial x_j} \quad (2.4)$$

This wave equation together with initial and boundary conditions describe the temporal behavior of the deformation in the solid. In some physical problems, the deformation is approximately one-dimensional (e.g. see section 4-4). Therefore, the above equation can be simplified as a non-homogeneous 1-D wave equation

$$\frac{\partial^2 u}{\partial t^2} - V_s^2 \frac{\partial^2 u}{\partial x^2} = \frac{1}{\rho} \frac{\partial \sigma}{\partial x} \quad (2.5)$$

where  $V_s$  is the sound velocity along the x direction and  $\rho$  is the mass density.

Boundary conditions determine the interaction of an elastic wave with the interface of two different solids that gives rise to a reflected wave and a transmitted wave. They also specify the solutions of a homogeneous wave equation (i.e. the right-hand side of equation 2.5 is zero) as well. There are two boundary conditions: First, the displacement is continuous at the interface, second, the traction vector, relative to the normal direction of the interface, is continuous. The traction vector  $\mathbf{P}$  is a measure of surface forces exerted on a surface element specified with the normal vector  $\mathbf{n}$  ( $P_i = S_{ij} n_j$ ). For example, considering two half-space solids, separated by a plane at  $x = 0$ , the boundary conditions are

$$\begin{aligned} u_1^{(1)} &= u_1^{(2)}, u_2^{(1)} = u_2^{(2)}, u_3^{(1)} = u_3^{(2)} \\ S_{11}^{(1)} &= S_{11}^{(2)}, S_{21}^{(1)} = S_{21}^{(2)}, S_{31}^{(1)} = S_{31}^{(2)} \end{aligned} \quad (2.6)$$

where the upper indices indicate the solids. Applying the above conditions to a 1-D incident elastic wave on the interface of two solids, gives the following expressions for the reflection ( $r_{\text{ref}}$ ) and transmission ( $t_{1,2}$ ) coefficients

$$r_{\text{ref}} = \frac{z^{(1)} - z^{(2)}}{z^{(1)} + z^{(2)}}; \quad t_{1,2} = \frac{2z^{(1)}}{z^{(1)} + z^{(2)}} \quad (2.7)$$

where  $z^{(1)} = \rho^{(1)} \cdot V_s^{(1)}$  and  $z^{(2)} = \rho^{(2)} \cdot V_s^{(2)}$  are the acoustic impedances of the solids. In general, it is possible to find another wave equation for the strain in materials by taking a derivative with respect to  $x$  from the both sides of equation (2.5). Thus, the following equation can be obtained

$$\frac{\partial^2 \eta}{\partial t^2} - V_s^2 \frac{\partial^2 \eta}{\partial x^2} = \frac{1}{\rho} \frac{\partial^2 \sigma}{\partial x^2} \quad (2.8)$$

Applying the boundary conditions to a 1-D incident strain wave on the interface of two solids, results in the reflection and transmission coefficients for the strain wave as

$$R_{\text{ref}} = \frac{z^{(2)} - z^{(1)}}{z^{(1)} + z^{(2)}} ; T_{1,2} = \frac{V_s^{(1)}}{V_s^{(2)}} \times \frac{2z^{(1)}}{z^{(1)} + z^{(2)}} \quad (2.9)$$

An interesting case is the reflection at a free boundary (i.e.  $z^{(2)} = 0$ ). In accordance to equations (2.7) and (2.9), the reflection coefficient of the displacement wave is  $r_{\text{ref}} = 1$  and in the case of the strain wave it is  $R_{\text{ref}} = -1$ . This indicates that the strain wave only changes its sign after reflection from a free boundary.

Another important problem would be the generation of strain waves in two half-space materials. If the “non-mechanical stress” is spatial-independent, the wave equations will be homogenous and one can show that they have solutions in form of  $f(t - x/V_s)$  and  $g(t + x/V_s)$  corresponding to the waves traveling in  $+x$  and  $-x$  directions, respectively [116]. With the assumption that a negative “non-mechanical stress” is generated at times  $t > 0$  by some means (see equation (2.10)) in the material 1 at the left-hand side of the interface (located at  $x = 0$ ), one expects only two waves traveling in  $-x$  and  $+x$  directions in materials 1 and 2, respectively.

$$\sigma(t) = \begin{cases} 0 & t \leq 0 \\ -p(t) & t > 0 \end{cases} \quad (2.10)$$

By applying the boundary conditions on these two waves at the interface, it is possible to find the generated strain waves in both materials as

$$\eta^{(1)} = \begin{cases} 0 & ; |x| \geq V_s^{(1)}t \\ \frac{1}{V_s^{(1)}(z^{(1)} + z^{(2)})} p\left(t + \frac{x}{V_s^{(1)}}\right) & ; |x| < V_s^{(1)}t \end{cases} \quad (2.11)$$

$$\eta^{(2)} = \begin{cases} 0 & ; x \geq V_s^{(2)}t \\ \frac{-1}{V_s^{(2)}(z^{(1)} + z^{(2)})} p\left(t - \frac{x}{V_s^{(2)}}\right) & ; x < V_s^{(2)}t \end{cases} \quad (2.12)$$

It is evident that at positive times, two strain waves (one positive and one negative) are launched from the interface and propagate in opposite directions while they have the shape of function  $p$ .

Solving the inhomogeneous wave equation is not trivial and only in some cases there would be an analytical solution for that. For instance, Thomsen *et al.* [117] solved the inhomogeneous wave equation for a half-space solid with a thermal photo-induced stress and showed that the strain wave has a time-independent term and a bi-polar time-dependent pulse traveling into the material. Unfortunately, for the more complicated problems even in 1-D geometry (e.g. layered materials or time- and space-dependent non-mechanical sources) it is not possible to obtain an analytical solution. Therefore, numerical solution is the only method to provide the strain waves in solids.

## 2-2 Photo-induced stress sources

Although the acoustic response of a solid can be described by the mentioned classical wave equation, the source term is expressed quantum mechanically. The generation of elastic waves (coherent acoustic phonons) in solids after excitation with ultrashort light pulses is based on the conversion of the optical energy of the light pulse into the mechanical energy by the photo-induced stress (i.e. “non-mechanical stress”). The photo-induced stress is generated due to several different mechanisms, e.g. thermo-elastic effect (TE) [90, 117, 118], deformation potential mechanism (DP) [90, 117, 119], inverse piezoelectricity (PE) [90, 119, 120] and electrostriction (ES) [90, 121]. This section deals with the basic concepts of the TE and DP mechanisms, which are relevant to the work of this thesis.

### 2-2-1 Thermo-elasticity

Thermo-elasticity is a phenomenon, which discusses a volume change in solids when temperature increases (i.e. thermal expansion). The thermal expansion can be described by the thermal strain

$$3\eta^{(TE)} = \frac{\Delta V}{V} = 3\beta\Delta T \quad (2.13)$$

where  $\beta$  is the linear thermal expansion coefficient,  $V$  is the volume,  $\Delta T$  is the temperature change and  $\eta^{(TE)}$  is the thermal strain. Equation (2.13) is valid for isotropic elastic materials or single crystals with cubic symmetry. For example, crystals with triclinic symmetry are also prone to shear strains due to the temperature change. The associated stress, called thermo-elastic stress, is defined

$$\sigma_{TE} = -3B\beta\Delta T = -P_{TE} \quad (2.14)$$

where  $B$  is the bulk modulus and  $P_{TE}$  is the so-called ‘‘thermo-elastic pressure’’.

Lattice heating caused by optical excitation, in general, is a consequence of energy transfer from photo-excited electrons to the phonon subsystem. The excited electrons dissipate their excess energy interacting with the lattice and relax towards lower energy levels while phonons are emitted. These phonons have no phase relation between each other. Therefore, only the population of phonons increases and the lattice heats up.

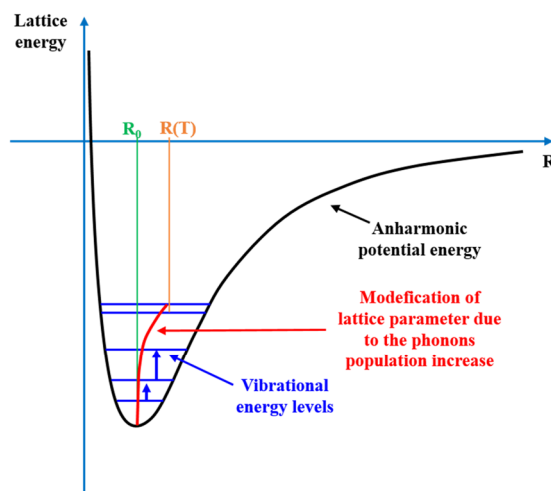


**Figure 2.1:** Modification of the lattice parameter  $R(T)$  (red solid line) when the vibrational energy increases in a lattice anharmonic potential (black curve). The increase in the vibrational energy is the direct consequence of the increase in the population of phonons.  $R_0$  is the lattice parameter at temperature  $T = 0$  K.

In typical solid-state physics books [118], it has been proved that the lattice anharmonicity is necessary to induce a volume change under temperature increase. As illustrated in figure 2.1 [90] schematically, the lattice parameter  $R$  is modified due to the anharmonic interatomic potential when the vibrational energy is elevating (i.e. increase in phonons population). The ultrafast lattice heating causes a sudden modification in the lattice parameter with a time scale much shorter than the lattice response time and as a result, the coherent acoustic phonons are generated. At a more general level in which emitted phonons are not thermalized (therefore definition of temperature is meaningless), the thermo-elastic stress for an isotropic material or a single crystal with cubic symmetry can be expressed by an isotropic tensor with diagonal components

$$\begin{aligned}\sigma_{TE} &= - \sum_{\mathbf{k}} \gamma_p(\mathbf{k}) \hbar \omega_{\mathbf{k}} \delta n_p(\mathbf{k}) \\ \gamma_p(\mathbf{k}) &= - \left( \frac{1}{\omega_{\mathbf{k}}} \right) \left( \frac{\partial \omega_{\mathbf{k}}}{\partial \eta} \right)\end{aligned}\tag{2.15}$$

where  $\gamma_p(\mathbf{k})$  is the Grüneisen factor for phonons,  $\eta$  is the longitudinal strain,  $\omega_{\mathbf{k}}$  is the phonons frequency and  $\delta n_p(\mathbf{k})$  is the change in phonons occupation at the wave vector  $\mathbf{k}$ . In this context, if phonons are in local thermal equilibrium then equation (2.15) reduces to earlier equation (2.14).

### 2-2-2 Deformation potential mechanism

The deformation potential mechanism describes the relation between the modification in energy of the electronic subsystem and the strain in solids. The electronic distribution influences the interatomic forces strongly and vice versa. Thus, any modification in one of them results in the modification in the other one. When the inter-atomic forces are modified, the equilibrium atomic positions in the lattice will be also modified, so that after some time, the solid will be deformed (i.e. the solid will be strained).

In more detail, the strain modifies the overlap of orbitals by changing the atomic distances and bond angles. These changes cause a readjustment in the electronic band structure and accordingly the electronic density at particular energy levels changes. In the other way, by exciting the electronic subsystem (e.g. photo-excitation) the local density of carriers at particular energy levels changes, which leads to a modification in the strength of atomic bonds in the excitation region. Hence, strain is generated (see figure 2.2 [90]).

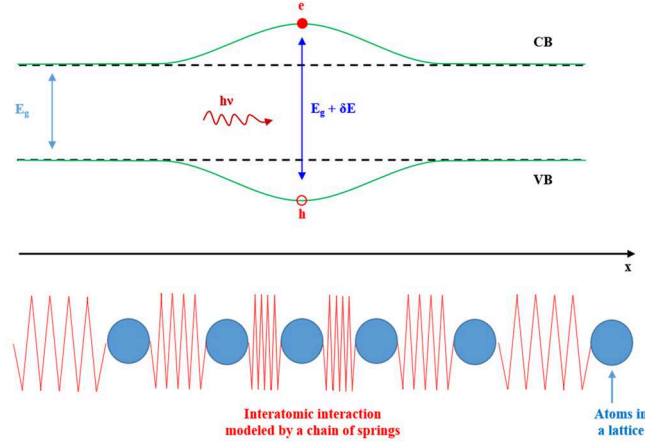


**Figure 2.2:** Schematic of the lattice deformation through the deformation potential mechanism following the photo-excited carrier generation in semiconductors. When electron-hole pairs are generated in conduction (CB) and valence (VB) band edges (indicated by black dashed lines at the equilibrium at upper panel) the local density of carriers at the edges of the bands are changed, which leads to a modification of the interatomic interaction. This modification causes a change in the interatomic distances, i.e. strain appears (lower panel). The strain in turn, results in a perturbation in the electronic band structure (green solid lines at the upper panel).

The general expression for the photo-induced stress through the deformation potential mechanism for isotropic or cubic crystals (the stress tensor is isotropic) is [90, 122-124]

$$\sigma_{DP} = - \sum_{\mathbf{k}} \delta n_e(\mathbf{k}) E_{\mathbf{k}} \gamma_e(\mathbf{k}) = \sum_{\mathbf{k}} \delta n_e(\mathbf{k}) \frac{\partial E_{\mathbf{k}}}{\partial \eta} \quad (2.16)$$

$$\gamma_e(\mathbf{k}) = - \frac{1}{E_{\mathbf{k}}} \frac{\partial E_{\mathbf{k}}}{\partial \eta}$$

where  $\gamma_e(\mathbf{k})$  is the Grüneisen factor for electrons,  $\eta$  is the longitudinal strain,  $E_{\mathbf{k}}$  is the electronic energy level,  $\partial E_{\mathbf{k}}/\partial \eta$  is the deformation potential parameter and  $\delta n_e(\mathbf{k})$  is the modification of the electronic occupation at the wave vector  $\mathbf{k}$ .

### 2-3 Theory of X-ray diffraction

Diffraction of X-rays from solids is a method to determine the equilibrium structure as well as the dynamics of a crystal lattice (e.g. coherent acoustic phonons) in solids. It is impossible to give a complete and detailed overview of the X-ray diffraction theory here. Therefore, this section discusses the basic concepts of X-ray diffraction theory for a lattice at equilibrium and under strain.

Diffraction of X-rays from materials occurs through the interaction between electrons and the X-ray beam. When the X-ray beam propagates through a piece of material, it will be attenuated. In general, there are two main types of attenuation processes. First, the absorption by exciting or ejecting electrons from the atoms (i.e. photoelectric process). Second, a part of the energy of the incident beam is transferred to the scattered radiation through scattering by electrons. There are also two distinct scattering processes known as Thomson scattering (elastic scattering) and Compton scattering (inelastic scattering). The Thomson scattering is expressed in the frame of classical physics and it is the main process to describe the diffraction of X-rays from crystals. On the other hand, the Compton scattering can be explained only in the quantum mechanics approach and furthermore, because of its incoherent nature, it gives rise to a smoothly varying background in the diffraction pattern [125]. Therefore, it is useful to assume the absorption and the Compton scattering together and introduce the so-called “*normal absorption*”. The attenuation due to the elastic scattering, which transfers a part of incident radiation energy to a coherent diffracted radiation, is called “*extinction*” [126]. There are two general theories to describe the macroscopic X-ray diffraction. The better-known and more simplified theory, the Kinematical X-ray diffraction theory that neglects the effect of extinction. In contrast, the more rigorous theory, which considers extinction, is called dynamical X-ray diffraction.

### **2-3-1 Kinematical X-ray diffraction**

In the kinematical theory, the scattering from each volume element in the crystal is assumed independent from the scattering of other volume elements (i.e. extinction is negligible), except the power loss due to the normal absorption. If the reflection from each atomic single layer is weak, one can consider that the power loss of the incident primary beam caused by the elastic scattering of one single layer is negligible. The decrease in intensity of the incident beam is thus negligibly small provided the crystal is thin enough. Under these conditions, the kinematical theory is simply the limiting form of the dynamical theory.

When a very small crystal is irradiated by the X-ray beam, which is in principle an electromagnetic wave, all electrons contribute in the scattering processes and the macroscopic field is the sum of all scattered fields. However, for materials with relative high atomic number ( $Z$ ) the majority of electrons are bound to the ion cores, which their assigned charge density follows a regular repeated pattern of the crystal lattice. Therefore, it is reasonable to consider that the macroscopic instantaneous scattered field is determined significantly by the bound electrons density at some specific directions. For an incident X-ray beam with the wavelength  $\lambda$ , the diffracted intensity  $I_p$  from a small parallelepiped crystal is given by [127]

$$I_p \propto |F|^2 \frac{\sin^2\left(\frac{\pi}{\lambda}\right) (\mathbf{s} - \mathbf{s}_0) \cdot N_1 \mathbf{a}_1}{\sin^2\left(\frac{\pi}{\lambda}\right) (\mathbf{s} - \mathbf{s}_0) \cdot \mathbf{a}_1} \times \frac{\sin^2\left(\frac{\pi}{\lambda}\right) (\mathbf{s} - \mathbf{s}_0) \cdot N_2 \mathbf{a}_2}{\sin^2\left(\frac{\pi}{\lambda}\right) (\mathbf{s} - \mathbf{s}_0) \cdot \mathbf{a}_2} \quad (2.17)$$

$$\times \frac{\sin^2\left(\frac{\pi}{\lambda}\right) (\mathbf{s} - \mathbf{s}_0) \cdot N_3 \mathbf{a}_3}{\sin^2\left(\frac{\pi}{\lambda}\right) (\mathbf{s} - \mathbf{s}_0) \cdot \mathbf{a}_3}$$

where  $F$  is the structure factor (will be discussed later),  $\mathbf{s}_0$  and  $\mathbf{s}$  are unit vectors in the direction of the incident and diffracted beams, respectively,  $\mathbf{a}_{1,2,3}$  are the unit cell's vectors and  $N_i$  ( $i = 1, 2, 3$ ) is the number of unit cell constant in the direction of  $i^{\text{th}}$  axis of the parallelepiped. The intensity depends on the multiplication of three functions of the form  $y = \sin^2 N\pi x / \sin^2 \pi x$ , where  $x_i = [(\mathbf{s} - \mathbf{s}_0) \cdot \mathbf{a}_i] / \lambda$ . Figure 2.3 illustrates the function  $y$  versus variable  $x$  for  $N = 20$  (blue solid line) and  $N = 10$  (red solid line).

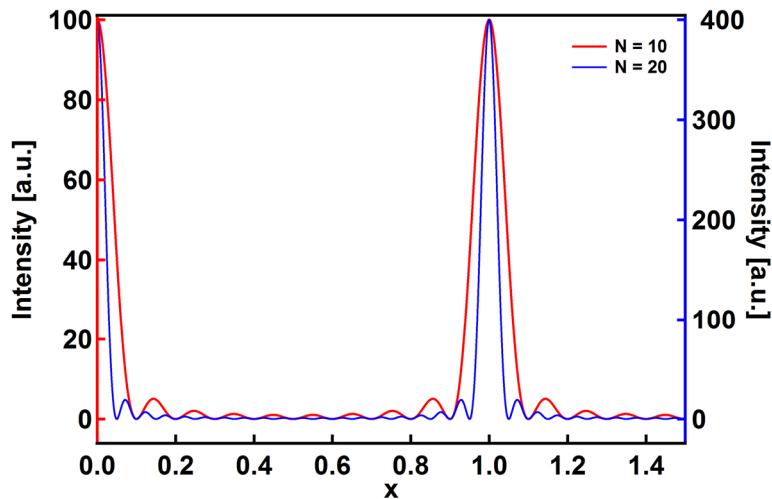


**Figure 2.3:** sketch of the function  $y = \sin^2 N\pi x / \sin^2 \pi x$  for  $N = 20$  (solid blue line) and  $N = 10$  (solid red line). The maximum occurs when  $x$  is an integer and the function is zero everywhere else except in the vicinity of  $x = k$  ( $k$  is an integer).

The function reaches its maximum value  $y_{\max} = N^2$  when  $x$  is an integer. It also depicts that by the increase in  $N$  the peak intensity increases while at the same time the width of the function decreases. For a not too thin crystal,  $N$  is much bigger than 20 and one can consider that the function  $y$  is zero everywhere except in the vicinity of  $x = k$  ( $k$  is an integer). Therefore, the intensity  $I_p$  is essentially zero unless all three functions of the form of function  $y$  are simultaneously close to their maximum values.  $I_p$  is maximum if

$$(\mathbf{s} - \mathbf{s}_0) \cdot \mathbf{a}_1 = h\lambda; (\mathbf{s} - \mathbf{s}_0) \cdot \mathbf{a}_2 = k\lambda; (\mathbf{s} - \mathbf{s}_0) \cdot \mathbf{a}_3 = l\lambda \quad (2.18)$$

This set of Equations are called Laue equations where  $h$ ,  $k$  and  $l$  are three independent integers. In accordance with the reciprocal lattice vector definition, one can say that the diffracted intensity is maximum when the wave vector transfer  $\mathbf{Q} = (2\pi/\lambda)(\mathbf{s} - \mathbf{s}_0)$  is equal to a particular reciprocal lattice vector  $\mathbf{G}_{h-k-l}$  specified by Miller indices  $h-k-l$ . It is, therefore, more convenient to express the three Laue equations (equation (2.18)) as a single vector equation and call it the Laue vector condition

$$\mathbf{Q} = \frac{2\pi}{\lambda} (\mathbf{s} - \mathbf{s}_0) = \mathbf{G}_{h-k-l} \quad (2.19)$$

It is straightforward to show that the Laue condition is equivalent to the Bragg condition. The distance between the set of planes  $h-k-l$  is  $d_{h-k-l} = 2\pi/|\mathbf{G}_{h-k-l}|$  and  $|\mathbf{Q}| = (4\pi/\lambda) \sin\theta$  where  $\theta$  is the angle between  $\mathbf{s}$  and  $\mathbf{s}_0$  with the diffracting planes. Substituting these quantities into equation (2.19), the Bragg condition for the Bragg angle  $\theta_B$  can be obtained

$$2d_{h-k-l}\sin\theta_B = \lambda \quad (2.20)$$

Under some conditions, the diffracted intensity may be zero even when the Bragg condition is fulfilled. This situation is called forbidden diffraction. According to equation (2.17), the diffracted intensity depends also upon the structure factor. The structure factor is the Fourier transform of one unit cell of the crystal and it contains all information regarding the electronic density configuration within the unit cell. From the mathematical point of view, the structure factor  $F$  related to the diffraction from a the  $h-k-l$  plane family is [127]

$$F_{h-k-l} = \sum_n f_n e^{2\pi i(hx_n + ky_n + lz_n)} \quad (2.21)$$

$$\mathbf{r}_n = x_n \mathbf{a}_1 + y_n \mathbf{a}_2 + z_n \mathbf{a}_3$$

where  $f_n$  is the atomic scattering factor and  $\mathbf{r}_n$  is the position of the  $n^{\text{th}}$  atom in the unit cell. This equation shows that for a particular  $h-k-l$  reflection the atomic arrangement in the unit cell together with the

atomic scattering factor determine the structure factor. For example, the structure factor for the (100) reflection in an fcc lattice (e.g. Cu) with one-atom basis is zero or in other words, this reflection is forbidden. In contrast, the (200) reflection is not forbidden. In the case of diamond structures (e.g. Ge), which can be considered as a convolution of the fcc lattice and a two-atom basis, the (200) reflection is forbidden and more interesting, when the lattice is zinc blend (e.g. GaAs) the (200) reflection is not forbidden because the atomic scattering factor for different types of atom is different [125]. It should be emphasized that the definition of the structure factor given by equation (2.21) and, consequently, the above discussion are valid only if the electron density in the vicinity of the ion cores is taken into account. Although this assumption, as mentioned earlier, is reasonable for high atomic number ( $Z$ ) materials, it is not always fulfilled, e.g. light elements with covalent bonding. In the latter case, the structure factor can be obtained by numerical calculations based on theoretical methods, like density functional theory [128].

### 2-3-2 Dynamical X-ray diffraction

To derive equation (2.17), both normal absorption and extinction as well as the effect of refraction (i.e. the refractive index was assumed unity) were neglected. This equation can easily be modified by including the effects of normal absorption and refraction [125, 129]. The more rigorous theory in which all these effects are taken into account is known as the dynamical X-ray theory [13, 125-127, 129-133]. This general model does not significantly change the results of the Kinematical approach regarding the direction of diffraction maxima, but the intensity profile will be drastically changed. In the following, the fundamental differential equations of the dynamical X-ray diffraction are presented.

In contrast to the kinematical theory, one has to consider the modification of the internal incident wave, which comes from the diffracted waves. In other words, inside a material the internal incident wave depends on the diffracted waves, which in turn depend on the internal incident wave. In this sense, the dynamical X-ray diffraction theory is a generalization of the electromagnetic wave refraction in which the Maxwell equations are solved with the proper boundary conditions. In the most of experimental measurements on single crystals, there is only one diffracted wave at a time. Therefore, the total electromagnetic wave inside the crystal can be assumed as a superposition of the internal incident wave and one diffracted wave, which are cross-coupled. This assumption is called two-wave approximation. B. Klar [13] showed that for a centrosymmetric crystal, the Maxwell equations lead to a compact differential equation (known also as Takagi-Taupin equation) for the normalized complex scattering amplitude  $X$ . Equation (2.22) represents this differential equation in a generalized form which includes the Debye-Waller effect [134] for both S and P polarizations [126, 130, 132, 134].

$$i \frac{dX}{dA} = X^2(1 + ik) - 2X(y + ig) + (1 + ik) \quad (2.22)$$

$$X(A) = X_1 + iX_2$$

In this expression,  $X$  is the normalized complex amplitude defined as

$$X(A) = \frac{\sqrt{|\gamma_H|} D_H^{(in)}}{\sqrt{|\gamma_0|} D_0^{(in)}} \quad (2.23)$$

where  $\gamma_0 \equiv \mathbf{n} \cdot \mathbf{s}_0$  and  $\gamma_H \equiv \mathbf{n} \cdot \mathbf{s}_H$  are the direction cosines of the external incident and diffracted waves, respectively.  $D_0^{(in)}$  is the complex amplitude of the internal incident wave (i.e. displacement vector field) and  $D_H^{(in)}$  is the complex amplitude of the internal diffracted wave corresponding to the plane family  $H \equiv (h-k-l)$  specified by the Miller indices.  $\mathbf{n}$  is the unit vector perpendicular to the surface of the crystal. The normalized complex scattering amplitude is a function of the reduced spatial coordinate  $A$  given by

$$A = \frac{R_e K_{pol} e^{-M} \lambda F'_H}{V_c \sqrt{|\gamma_0 \gamma_H|}} z \quad (2.24)$$

$$F_H = F'_H + iF''_H$$

where  $R_e$  is the classical electron radius,  $\lambda$  is the incident wavelength,  $F_H$  is the structure factor for the diffracted wave,  $V_c$  is the unit cell volume,  $K_{pol}$  is the polarization factor, which is 1 for S polarization and  $\cos(2\theta_B)$  for P polarization, the factor  $e^{-M}$  represents the Debye-Waller factor [134] and  $z$  is the depth measured from the surface of the crystal. The parameters  $g$  and  $k$  in equation (2.22) specify the X-ray absorption in the crystal, defined as

$$g = -\frac{1-b}{2\sqrt{|b|}} \frac{F_0''}{K_{pol} e^{-M} F'_H} ; \quad k = \frac{F_H''}{F'_H} \quad (2.25)$$

$$b = \frac{\gamma_0}{\gamma_H} = \frac{\mathbf{n} \cdot \mathbf{s}_0}{\mathbf{n} \cdot \mathbf{s}_H}$$

here  $F_0 = F_0' + iF_0''$  is the structure factor in the forward direction. The parameter  $y$  in equation (2.22) is the reduced angular coordinate, which contains the deviation from the Bragg condition due the refractive index of the crystal. Here  $y$  is written as

$$y = \frac{b}{\sqrt{|b|}} \frac{\pi V_c \alpha_H}{2R_e K_{pol} e^{-M} \lambda^2 F_H'} - \frac{1-b}{\sqrt{|b|}} \frac{F_0'}{2K_{pol} e^{-M} F_H'} \quad (2.26)$$

in which

$$\alpha_H = \frac{\lambda^2}{4\pi^2} (\mathbf{G}_H^2 + 2\mathbf{G}_H \cdot \boldsymbol{\beta}_0) \quad (2.27)$$

where  $\boldsymbol{\beta}_0 = (2\pi/\lambda)\mathbf{s}_0$  is the wave vector of the external incident wave. The complex scattering amplitude  $X(A)$  can be found by numerical integration of equation (2.22) with the boundary condition  $X_1(A_{max}) = X_2(A_{max}) = 0$  [134], where  $A_{max}$  corresponds to the bottom surface of crystal. By applying the boundary condition at  $A = 0$  [126, 130] the diffraction reflectivity outside the crystal can be found

$$R_{diff}(\theta - \theta_B) = |X(0)|^2 \quad (2.28)$$

Figure 2.4 shows the calculated [the “matlab” code is provided in appendix C] angle-resolved diffraction reflectivity of a 0.5 mm Si crystal corresponding to the  $(hkl) \equiv (111)$  direction. These patterns are called X-ray “*rocking curves*” as well. As it is evident, the rocking curves do not have their maxima at the Bragg angle but they are displaced towards higher angles. These displacements arise from the refraction of the incident wave when it enters the crystal. The refractive index is slightly less than unity for X-rays, so that, the maximum occurs at higher angles compared to the Bragg angle. Another feature is the difference between the rocking curves for different polarizations, particularly, the width of rocking curves. The total attenuation depth including the normal absorption depth and the characteristic length describing the extinction effect determines the width of rocking curves. Although the normal absorption depth in Si is the same for both polarizations, the extinction depth is polarization-dependent (e.g.  $\Lambda_{ext}^{(P)} \sim 2.4 \mu\text{m}$  and  $\Lambda_{ext}^{(S)} \sim 1.5 \mu\text{m}$  for the (111)-reflection of Si), so that, the rocking curve width for P polarization is narrower than the one for S polarization.

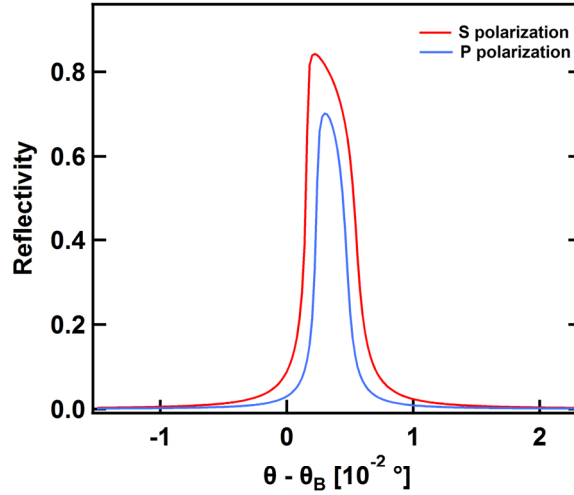


**Figure 2.4:** The calculated rocking curves for the (111)-reflection of a 0.5 mm Si substrate. The maximum of the rocking curves occur at larger angles compared to the Bragg angle due to the refraction of the incident wave as it enters the crystal. Since the extinction depth for P polarization is larger compared to S polarization, the rocking curve corresponding to P polarization is narrower than the one for S polarization.

S. Takagi [130] and B. Klar [13] showed that the above equations can be also applied for a crystal, which is under a spatial-dependent strain. The only modification appears in  $\alpha_H$ , so that for a given strain  $\eta(z)$ ,  $\alpha_H$  is

$$\alpha_H = \frac{\lambda^2}{4\pi^2} (\mathbf{G}_H^2 + 2\mathbf{G}_H \cdot \boldsymbol{\beta}_0) - \frac{\lambda |\mathbf{G}_H| \gamma_H}{\pi} \eta(z) \quad (2.29)$$

As will be discussed in chapter 4 (see subsection 4-4-1), under certain conditions the modified equations can be employed in cases that the strain has temporal and spatial dependence as well.

## 2-4 Principles of laser-plasma based X-ray generation

Focusing a femtosecond laser pulse on a solid target creates a high-density surface plasma layer [135]. Early experiments performed by Kühlke *et al.* [15] and Murnane *et al.* [16] have demonstrated that such dense plasmas represent an efficient source of hard X-rays. The emitted radiation contains continuum and characteristic line emission from the plasma and the “cold” solid behind the near surface plasma layer. As will be discussed later, due to collisionless interactions between the created plasma and the femtosecond laser pulse, a fraction of the plasma electrons are accelerated to high kinetic energy.

These electrons are usually called “*hot*” electrons, which their kinetic energy (several tens of keV) is much higher than the thermal energy of the rest of the plasma electrons (several hundreds of eV) [136]. The *hot* electrons penetrate into the cold solid underneath the plasma layer. While the major part of their energy is converted to heat, a certain fraction is converted into X-ray radiation through the processes identical to those in a Röntgen X-ray tube [10]. Some of the *hot* electrons emit X-ray photons in the vicinity of a third particle (e.g. atoms of the solid target) and get decelerated (figure 2.5-a). This emission is called “Bremsstrahlung” emission and has a continuum spectrum. At the same time, other (*hot*) electrons collide with the atoms of the target and kick out the inner shell electrons (i.e. impact ionization) provided that their kinetic energy is higher than the impact ionization threshold. Subsequently, another electron from higher levels fills the remaining hole and again X-ray photons are emitted (figure 2.5-b). This emission is known as “characteristic line” emission, which in contrast to the Bremsstrahlung emission has a discrete spectrum.

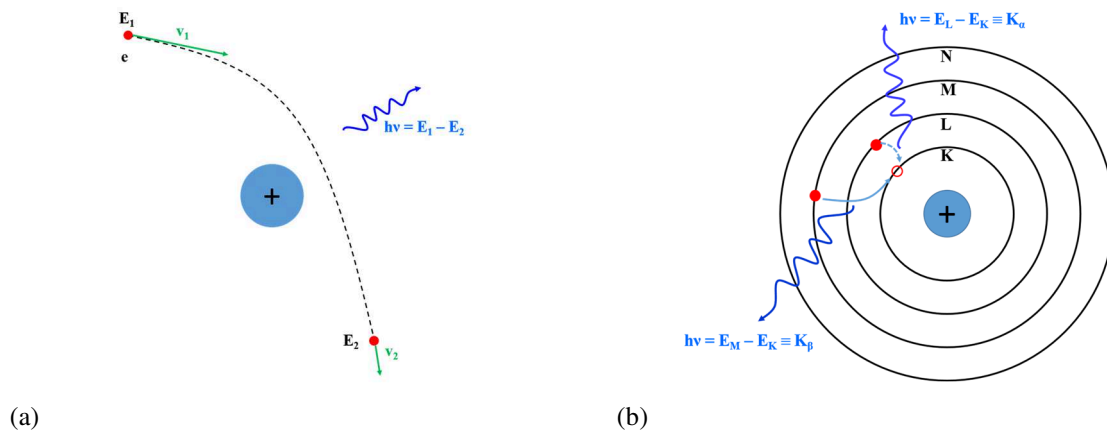


**Figure 2.5:** Two different types of X-ray emission in the cold solid target: the Bremsstrahlung (a) and characteristic line (b). The electronic transition from the L shell to the K shell leads to the  $K_\alpha$  lines radiation, which due to the spin-orbit coupling contains the  $K_{\alpha 1}$  and  $K_{\alpha 2}$  lines. The transition from the M shell to the K shell generates the  $K_\beta$  line emission.

In many of applications (e.g. diffraction), the characteristic line emission and, particularly, the  $K_\alpha$  emission is more desired. The  $K_\alpha$  emission occurs as long as the *hot* electrons with energy higher than the K-shell ionization energy exist in the solid target. Since these *hot* electrons are generated by the direct laser-plasma interaction, one can expect that the X-ray pulse duration is ultrashort and comparable to the laser pulse duration. This makes the  $K_\alpha$  radiation suitable for time-resolved X-ray experiments. Strictly speaking, the  $K_\alpha$  pulse duration is not essentially identical to the laser pulse duration because after the laser pulse is gone and the electron acceleration is terminated, the X-ray emission will continue until the energy of the last *hot* electron drops below the K-shell ionization energy. The time interval during which the X-rays are emitted after the laser pulse is called “afterglow” time duration. Thus, the  $K_\alpha$  pulse duration is the sum of the laser pulse duration and the afterglow time duration. Reich *et al.*

[137] used a PIC (Particle-In-Cell) simulation to estimate the  $K_{\alpha}$  pulse duration, which contains 90% of the emission, radiated from Ti, Cu, Ag and Ta bulk solid targets. They found that the  $K_{\alpha}$  pulse duration increases with increasing laser intensity for all the materials due to the increase in the afterglow time duration. They also demonstrated that except for the lightest element (i.e. Ti), it is not possible to generate efficient  $K_{\alpha}$  pulses with a 90%-pulse duration of 100 fs from the bulk targets. In the case of Ti, the estimated  $K_{\alpha}$  90%-pulse duration is between 200 and 400 fs for the laser intensities in a range of  $10^{16}$  -  $10^{17}$  W/cm<sup>2</sup>. Using thin foils as targets decreases the afterglow time duration and proper X-ray pulse durations can be achieved [137].

In general, interaction of ultrashort laser pulses with plasmas can be categorized in two collisional and collisionless absorption mechanisms. The former is also known as inverse Bremsstrahlung in which electrons that have gained energy from the laser, lose this energy in collisions with ions [138, 139]. Thus, the laser is damped by the plasma and, consequently, the plasma heats up. Collisional absorption is the effective absorption mechanism for  $I\lambda^2 < 10^{15}$  W $\mu$ m<sup>2</sup>/cm<sup>2</sup> and above that, alternative absorption mechanisms (i.e. collisionless mechanisms) would be the reason for the laser power loss in the plasma [135].

In fact, there are several different collisionless mechanisms, which can transfer part of the laser energy into the plasma, such as resonance absorption, vacuum heating, relativistic  $\mathbf{J} \times \mathbf{B}$  heating, anomalous skin effect and sheath inverse Bremsstrahlung [135, 138]. All the collisionless processes finally result in creation of the *hot* electrons with much higher temperature compared to the residual plasma electrons [135, 140]. The most relevant collisionless absorption mechanisms of ultrashort laser pulses with intensities  $10^{16} < I < 10^{17}$  W/cm<sup>2</sup> are resonance absorption and vacuum heating [138, 141, 142]. Since the laser intensity used in this work is in the same range, in the following, these two collisionless absorption mechanisms will be discussed shortly.

When a metal is irradiated by a femtosecond laser pulse, due to field ionization and ultrafast heat-wave propagation inside the target, a very dense plasma layer within an effective depth of several tens of nanometers is generated over the pulse duration [135]. This occurs if the laser intensity is high enough ( $I > 10^{12}$  W/cm<sup>2</sup>) [138]. In most laser systems with a peak intensity of  $10^{16}$  -  $10^{17}$  W/cm<sup>2</sup>, either the rising edge of the laser pulse or pedestals due to the amplified spontaneous emissions (ASE) can generate the plasma layer. The plasma layer also expands out with a typical velocity of a few times  $10^6$  -  $10^7$  cm/s [142]. One can model the time-dependent spatial profile of the plasma electron density  $N_e$  as [143]

$$\begin{aligned}
 N_e &= N_0 e^{-\frac{z}{L}} \\
 L(t) &= C_s t \\
 C_s &= \sqrt{\frac{ZkT_e}{M}}
 \end{aligned}
 \tag{2.30}$$

where  $N_0$  is the initial ionized electron density,  $L(t)$  is the plasma scale length,  $C_s$  is the expansion velocity of the plasma,  $Z$  is the ionization degree,  $k$  is the Boltzmann constant and  $M$  is the ion mass. The time interval between the plasma-formation threshold and the maximum intensity determines the plasma scale length seen by the pulse during the interaction. Hence, the contrast ratio of the laser pulse largely determines this time interval and in turn the plasma scale length.

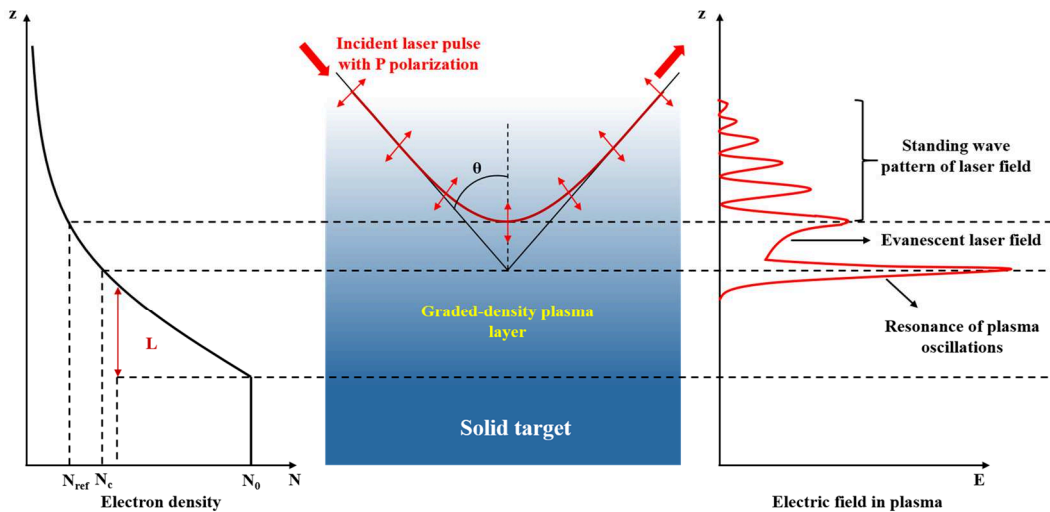


**Figure 2.6:** Schematic of the resonance absorption mechanism in a graded-density plasma.

As depicted in figure 2.6 [140], when the laser pulse is obliquely incident on the plasma layer with the electron density gradient parallel to the  $z$  direction (see equation (2.30)), it can resonantly transfer energy into the plasma and excite the plasma wave if it has P polarization. This P-polarized wave is reflected before the critical density is reached [144]. The electron density at the turning point is given by  $N_{\text{ref}} = N_c \cos^2\theta$ , which is less than the critical density  $N_c$  for all incident angles  $\theta > 0$  (figure 2.6). This means that electrons, forced by the laser field to oscillate, do not match the local plasma frequency and as a result no resonance occurs in that region. If the distance between the turning point and the

position of the critical density is small enough, the laser wave tunnels (evanescent laser field) into the critical density region and, thus, an electrostatic plasma wave can be resonantly excited by the laser field. This process is called *resonance absorption*. As the electrostatic plasma wave grows, non-linear wave-breaking [140, 145, 146] occurs and the plasma wave breaks. Therefore, a sufficient number of *hot* electrons are pushed into the target resulting in X-ray generation.

According to Gibbon *et al.* [135], resonance absorption desists to work in its usual form in very steep density gradients, i.e.  $L/\lambda \ll 1$ . For instance, in a very steep plasma when the plasma scale length is less than the electron quiver amplitude  $A$ , the laser field does not couple to the electrostatic plasma wave resonantly and, thus, the resonance breaks down. The electron quiver amplitude is defined as [138]

$$A = \frac{v_{\text{osc}}}{\omega} = \frac{\lambda}{2\pi} \sqrt{\frac{I\lambda_{\mu}^2}{1.3 \times 10^{18}}} \quad (2.31)$$

where  $v_{\text{osc}}$  is the quiver velocity of an electron in the laser field,  $\omega$  and  $\lambda$  are the incident laser frequency and wavelength,  $I$  is the pulse intensity and  $\lambda_{\mu}$  is the laser wavelength in micrometer. Nevertheless, one can see that electrons near the plasma-vacuum sharp interface will be directly exposed to the laser field. When a P-polarized laser pulse is obliquely incident on a very sharp-edge plasma, it will be reflected and close to the reflecting point a standing wave is generated. During the first half cycle of the laser electric field, electrons are dragged out from the plasma into the vacuum by the standing wave. As the field reverses its direction, these electrons will be turned around and accelerated back towards the plasma (figure 2.7 [147]).

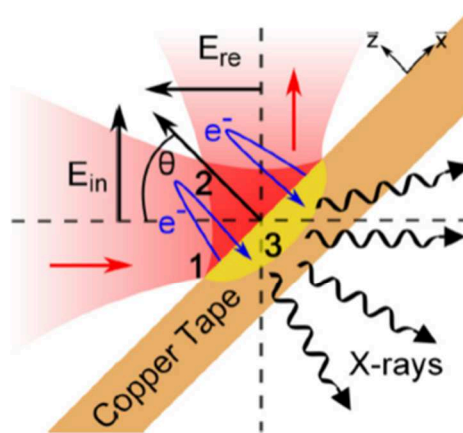


**Figure 2.7:** Schematic of electrons acceleration due to vacuum heating in a very steep plasma layer ( $L/\lambda \ll 1$ ). In a very steep plasma layer when the plasma scale length is less than the electron quiver amplitude  $A$  (equation (2.31)), the relevant collisionless absorption mechanism is vacuum heating.

Since the plasma is highly over-dense, the laser electric field can only penetrate into the skin depth (evanescent field), so the accelerated electrons are soon screened from the evanescent laser field. Hence, these *hot* electrons can travel almost unhindered into the target and lead to X-ray generation [135, 140]. This collisionless absorption mechanism is called *vacuum heating* that was first pointed out by F. Brunel [148] through an analytical model in which the plasma has a step function profile. However, the situation becomes more complicated for more realistic density profiles with finite gradients and one must use numerical methods. Gibbon *et al.* [149] performed a PIC simulation to investigate the laser plasma coupling mechanisms for ultrashort laser pulses incident on plasma layers with a scale length ranging from  $0.01\lambda$  to  $2\lambda$ . They found a highly complex transition between resonance absorption and vacuum heating depending on the irradiance ( $I\lambda^2$ ) and plasma scale length ( $L$ ). They showed that for  $L/\lambda < 0.1$ , vacuum heating dominates over resonance absorption.

W. Lu *et al.* [142] investigated the generation of ultrashort  $K_\alpha$  pulses through the laser-plasma interaction at laser intensities from  $10^{16}$  to  $10^{17}$  W/cm<sup>2</sup>. They found that for  $L/\lambda \geq 0.1$  the dominant absorption mechanism is resonance absorption. Their results also imply that resonance absorption results in more  $K_\alpha$  X-ray generation compared to vacuum heating. In addition, they demonstrated that the X-ray production can be optimized when coupling between the laser field and the plasma through resonance absorption is maximum. This optimum condition is described by [144, 150]

$$\left(\frac{2\pi L}{\lambda}\right)^{2/3} \sin^2\theta_{\max} \approx 0.6 \quad (2.32)$$

where  $L$  is the plasma scale length,  $\lambda$  is the laser wavelength and  $\theta_{\max}$  is the laser angle of incidence at which resonance absorption is optimized. Equation (2.32) indicates that the angle of incidence for the optimum coupling decreases with increasing plasma scale length. Furthermore, it implies that for a fixed angle of incidence, resonance absorption can be optimized if a proper plasma scale length is achieved. In laser systems with a high contrast ratio, employing an additional “pre-pulse” to produce the plasma before the arrival of the “main-pulse” allows to have a control on the scale length. In this case, the plasma scale length is related to the variable delay time between the pre- and main-pulse. Thereby, the optimum scale length corresponding to the maximum X-ray yield can be obtained [142, 151-155].

The plasma scale length is not the only parameter, which affects the X-ray production. The laser intensity also strongly influences the  $K_\alpha$  production efficiency. The average energy of the *hot* electrons is described by a power scaling law as a function of  $I\lambda^2$ , where  $I$  and  $\lambda$  are the laser intensity and wavelength, respectively [139, 156-158]. For optimum  $K_\alpha$  generation, it is required that the average energy of the *hot* electrons to be few times the K-shell ionization energy [137, 151, 159]. In addition, the so-called “emission factor”, defined as the probability that a  $K_\alpha$  photon escapes from the target before

being reabsorbed, depends on the average energy of the *hot* electrons as well [137]. These considerations make the laser intensity as a key factor for optimization of the  $K_{\alpha}$  emission. As will be shown in the next chapter, by varying the laser intensity as well as the plasma scale length the  $K_{\alpha}$  radiation flux is significantly increased.

## *Chapter 3*

### **Ultrashort laser-plasma based X-ray pulse source**

The theoretical background for this thesis was presented in the previous chapter, particularly the mechanism of ultrashort X-ray pulse generation. This chapter discusses an optical-pump - X-ray-probe setup based on a laser-plasma X-ray source working at Ti- $K_{\alpha 1}$  characteristic line. In order to generate an X-ray burst, a highly intense laser pulse has to be focused on a solid target (here Ti). Efficient X-ray generation requires operation in vacuum. Irradiating a target in air leads to a severe spatial and temporal distortion in the intensity distribution of the focused femtosecond pulse due to non-linear effects and plasma breakdown in the surrounding atmosphere. Consequently, the required on-target intensities cannot be reached and the X-ray flux will be suppressed tremendously. One conventional scheme is to place all experimental components (the X-ray source, X-ray optics, samples and X-ray detectors) in a big vacuum chamber [160]. A “modular” scheme, used in the current work, is the second possible design, where only the X-ray source is placed in a small vacuum chamber and the other experimental components are placed in air. This has many advantages, such as more space for experimental components and convenience in adjusting them. In addition, it provides the opportunity to study lattice dynamics of samples under particular conditions. For example, in the current setup, by implementation of a cryostat it is possible to investigate lattice dynamics at cryogenic temperatures.

This chapter is organized as follows: In section 3-1, a brief description of the used laser system and its relevant properties is given. Setup configuration, different schemes of X-ray detection and its characteristics are discussed in detail in sections 3-2 and 3-3, respectively. Section 3-4 presents the working principles of a toroidally bent crystal mirror used as the X-ray optic to partially collect the emitted X-rays and focusing them onto the sample. The emitted X-ray spectrum is described in section 3-5. Section 3-6 deals with the enhancement of X-ray production by using a suitable on-target laser intensity and pre-plasma as well. Static X-ray diffractions from samples as well as their normalization to the incident X-ray flux and the procedure to find the spatial-temporal overlap between the optical pump and the X-ray probe are discussed in sections 3-7, 3-8 and 3-9, respectively. Finally, a summary is drawn in section 3-10.

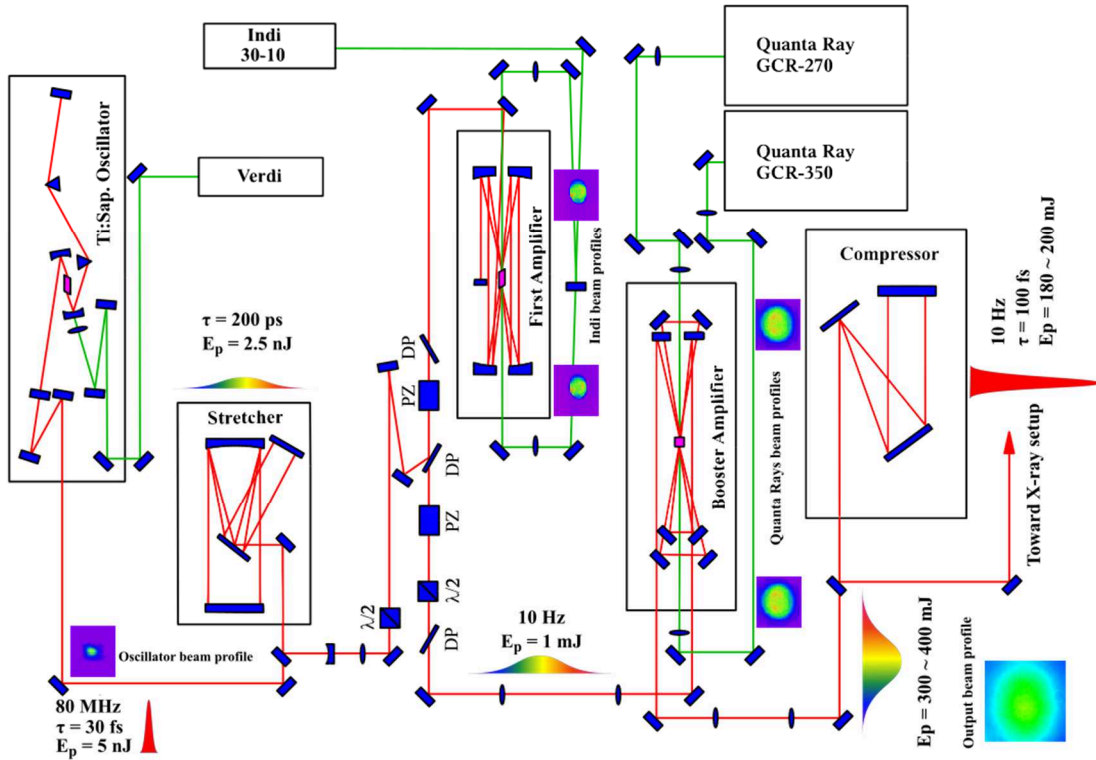


Figure 3.1: Schematic of the 10 Hz laser setup.

### 3-1 Femtosecond laser system

The laser system provides ultrashort pulses, which are an essential part of the experimental setup to generate X-ray bursts. The contrast ratio of the laser pulses as well as their intensity and duration are the key parameters of the X-ray generation (see chapter 2). Moreover, to excite and draw samples to a non-equilibrium state one has to use a very short stimulant, such that its duration is shorter than the time scales of investigated processes (e.g. lattice vibration period). Therefore, ultrashort laser pulses are suitable to generate such a non-equilibrium conditions.

The laser system used in this experiment is depicted in figure 3.1 [161]. It is a Titanium-Sapphire laser, which uses the chirp pulse amplification (CPA) technique [162]. It comprises an oscillator, a stretcher, a pre-amplifier, a booster amplifier and a compressor. By using the non-linear Kerr lensing (passive mode locking), phases of the longitudinal modes are locked to each other, which leads to an ultrashort pulse [163]. The oscillator delivers low energy (5 nJ/pulse) ultrashort pulses at 80 MHz repetition rate and a wavelength of 782 nm with a pulse duration of 30 fs (Full Width Half Maximum). To avoid damaging optical elements in the amplifier system and to have a minimum change in the pulse parameters due to non-linear processes in the amplification mechanism, it is necessary to decrease the pulse intensity by stretching it temporally. Thus, the output of the oscillator is directed to the stretcher before being amplified. The stretcher uses a dispersive line (combination of gratings and curved mirrors

or lenses) to impose a suitable phase modulation leading to an almost linear chirp and increase in the pulse duration. The output pulses from the stretcher have a duration of 200 ps and energy of 2.5 nJ/pulse.

As a first stage, an eight-pass pre-amplifier with a Titanium-Sapphire crystal is utilized. The crystal is pumped by a frequency doubled Q-switched Nd: YAG laser ( $\lambda = 532$  nm,  $E_p = 50-60$  mJ/pulse and a pulse duration of 6-9 ns) at 10 Hz repetition rate. A Pockels cell situated before the pre-amplifier reduces the repetition rates of the 80 MHz train of seed pulses to 10 Hz. The pre-amplified pulses with  $E_p = 0.5-0.7$  mJ/pulse are guided to the second amplifier, called here the booster amplifier. The booster is a four-pass amplifier with a Ti: Sapphire crystal maintained in a cryostat to refrain from thermal effects and damaging the crystal due to the intense pumping. Two frequency doubled Q-switched Nd: YAG lasers pump the crystal from both sides with average pulse energy up to 400 mJ/pulse on each side. After this amplification stage, the energy of the amplified pulses reaches up to 300 mJ/pulse. Even a broad pulse in this energy regime can already damage sensitive optical elements like a compressor grating. To overcome this problem, the laser beam is expanded to a radius of 25 mm (FWHM) transversely before heading to the compressor.

Eventually, by using the compressor containing two gratings and a mirror, the amplified pulses are recompressed. Recovering the initial pulse duration and shape (i.e. compensation of the phase modulation introduced by the stretcher) is not the only thing that the compressor has to deal with, but it also has to compensate for the dispersion introduced in the amplification stages as well. Therefore, the distance between the gratings has to be larger than the one in the stretcher. The time-structure of the output of the compressor was measured carefully using a third order autocorrelator and a second order FROG as well as the spectrum. As illustrated in figure 3.2-c, the amplified laser pulse has a contrast ratio of about  $10^7$  (relative intensity of the pulse maximum to 2 ps ahead) and the shortest achievable pulse duration is 41 fs (FWHM) (figure 3.2-b). The efficiency of the compressor is approximately 60 percent, which means that after the compressor the pulse energy can be up to 180 mJ/pulse. The linear dispersion effects (e.g. GVD) together with non-linear ones (self-phase modulation and/or self-focusing) modify the pulse and introduce a positive chirp to it when the beam passes through optical elements and/or is focused. Therefore, the compressor is adjusted to introduce an additional negative chirp to pre-compensate for the positive chirp, resulting in a final pulse duration at the X-ray source and the sample of about 100 fs (figure 3.2-e).

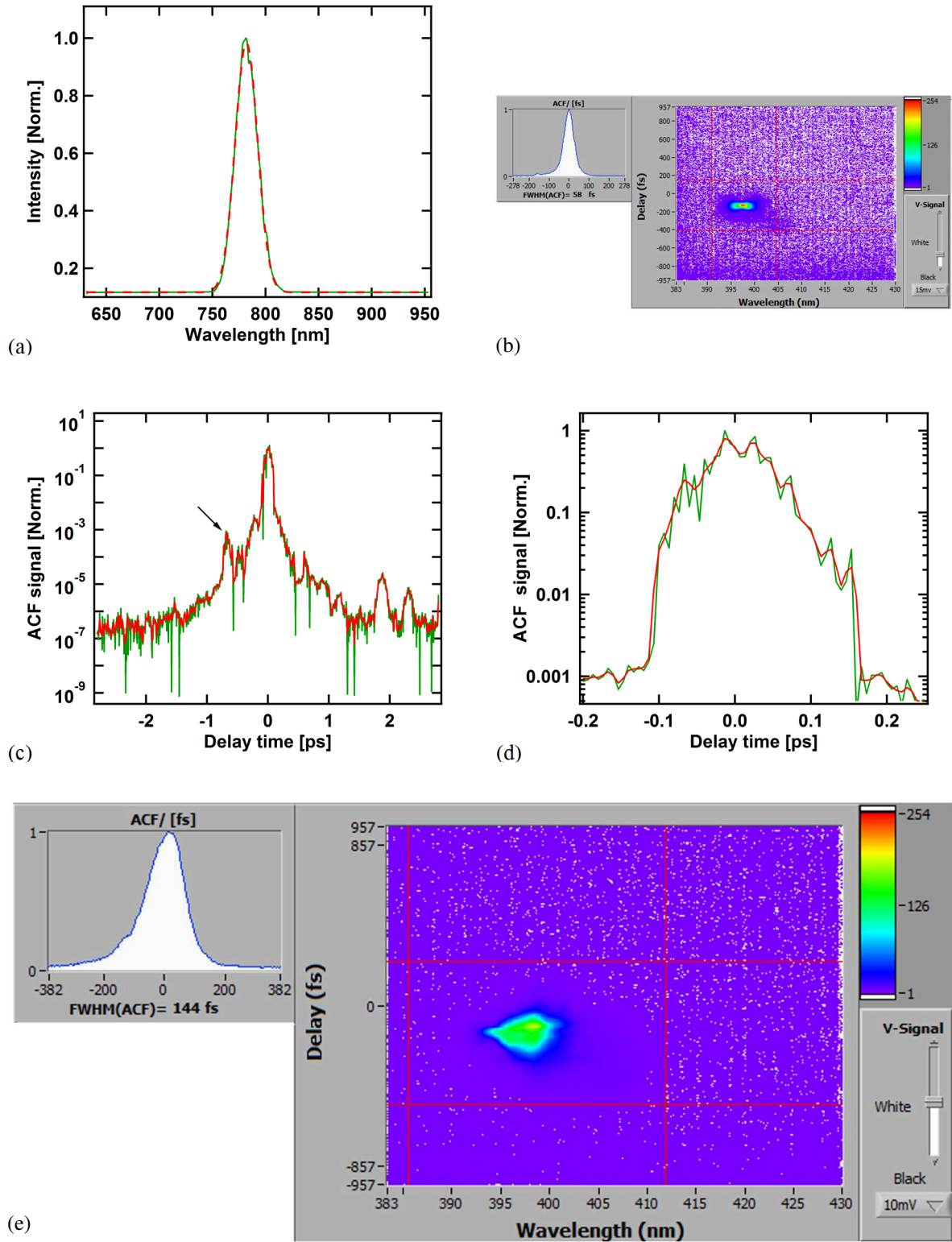


**Figure 3.2:** Temporal and spectral characteristics of the laser pulses after the compressor with a bandwidth of 25 nm (FWHM) (a) and minimum pulse duration of 41 fs (FWHM) (b). The 3<sup>rd</sup> order autocorrelation trace shows a contrast ratio of  $10^7$  (c) and (d). The red solid lines correspond to the smoothed ACF signal. The small satellite shown with an arrow in figure (c) is due to the reflection from a backside of a mirror in the autocorrelator. To compensate for the linear and nonlinear dispersion effects the compressor is adjusted to introduce an additional negative chirp resulting in a final pulse duration of 100 fs (e).

### 3-2 Setup configuration

The experimental pump-probe setup, shown schematically in figure 3.3, contains several different parts. Initially, the incoming laser beam is separated into a “main-pulse” beam to be used for X-ray generation and a weaker “pre-pulse” beam, which - after introducing a suitable delay (D1) - is used to generate a pre-plasma to enhance X-ray generation (see section 3-6). These two beams are recombined together again. Subsequently, the sample “pump” beam is split and an additional delay line (D2) allows introducing a variable delay on the sample between the pump pulse and the X-ray probe pulse generated by the main-pulse. For X-ray generation the recombined main- and pre-pulse beams are focused on a 250- $\mu\text{m}$  diameter Ti wire inside a small vacuum chamber. The wire is continuously moved to provide an un-irradiated surface for each pulse (pair). Part of the incoherently emitted X-rays (into the full solid angle) are collected and focused on the sample by a toroidally bent X-ray mirror (see section 3-4). In the next subsections, the details and characteristics of the different parts of the setup will be presented.

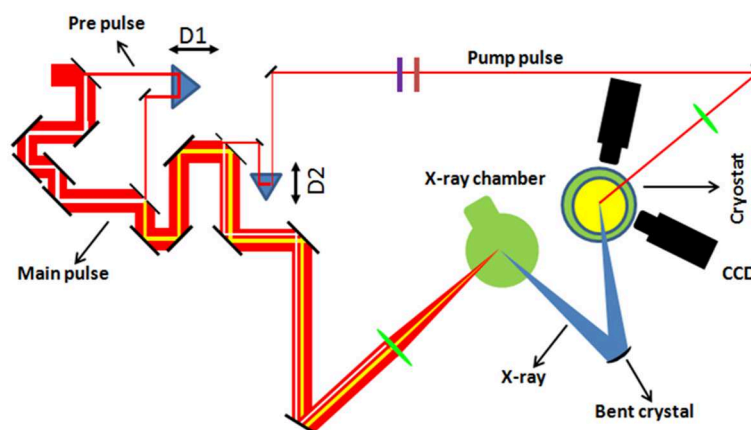
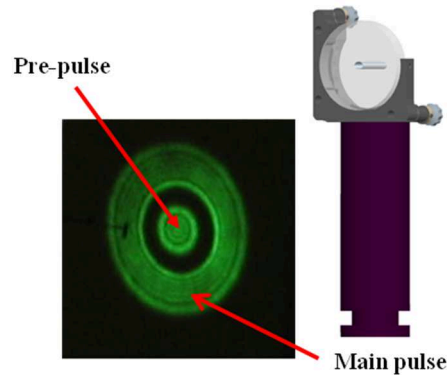


**Figure 3.3:** Schematic drawing of the optical pump X-ray probe setup

#### 3-2-1 Optical part of the setup

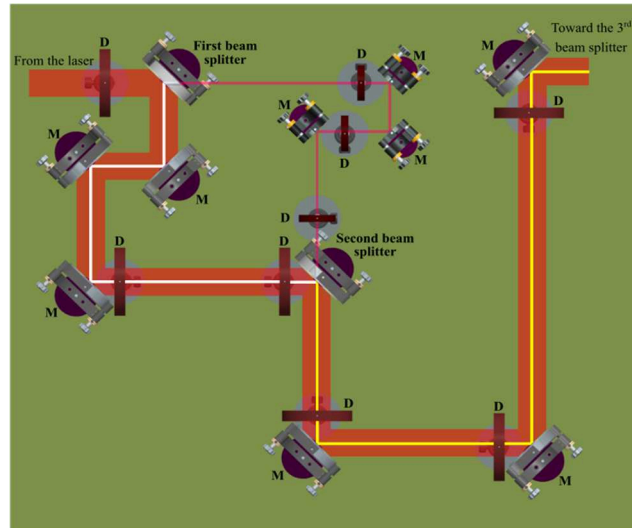
It is convenient to divide the discussion of the experimental setup into two parts, the optical part and the X-ray part. In this subsection, the former is discussed and subsection 3-2-2 deals with the X-ray part. As mentioned above, the incoming laser beam is split into three beams with different delays with respect to each other. Applying a beam splitter in which a BK7 or fused silica substrate has a partial reflective coating is the conventional method to split a laser beam as a reflected beam and a transmitted one. However, in this method the temporal structure of the laser pulse will be distorted (due to GVD and nonlinear effects) when the laser passes through the optical substrate. Thereby, a new beam splitter was designed and employed in the setup based on a mirror with a hole in the center. Figure 3.4 illustrates this so-called “holey-mirror” beam splitter. It is a three-inch dielectric mirror for 800 nm wavelength

and 45° angle of incidence. A 9 mm (diameter) hole in the center of the mirror is made in a way that the axis of the hole and the mirror surface normal intersects at a 45° angle.



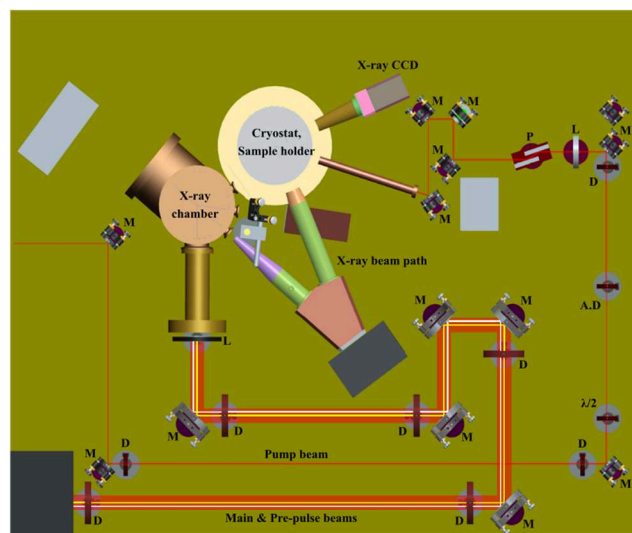
**Figure 3.4:** Designed beam splitter and its holder. The reflected (main-pulse) beam has a hole in the center. The transmitted beam (pre-pulse) is recombined with the main-pulse after being delayed by approx. 2 ps.

When the laser beam hits the beam splitter (figure 3.5), about 97 percent of its power is reflected (main-pulse). The transmitted beam, which is used for the pre-plasma generation (pre-pulse), is guided to a delay stage to introduce a suitable delay ( $\tau \sim 2$  ps) with respect to the main-pulse beam, i.e. the pre-pulse arrives 2 ps earlier than the main-pulse. It is subsequently recombined with the main-pulse by using a second holey-mirror beam splitter. After recombination, both of them are parallel and have the same optical path to the Ti wire inside the X-ray chamber. Although the temporal features of the pulses are intact, when the beam passes through the hole, the spatial intensity distribution of both the reflected and transmitted beams are modulated due to the diffraction caused by the hole. Another holey-mirror beam splitter, but with an off-center hole, is utilized to split the third beam from the main-pulse beam. This beam is directed to a variable delay line and is used for sample excitation (pump beam). The delay ranges from -45 ps to +300 ps (positive delay times mean that the laser pulse arrives earlier than the X-ray pulse).



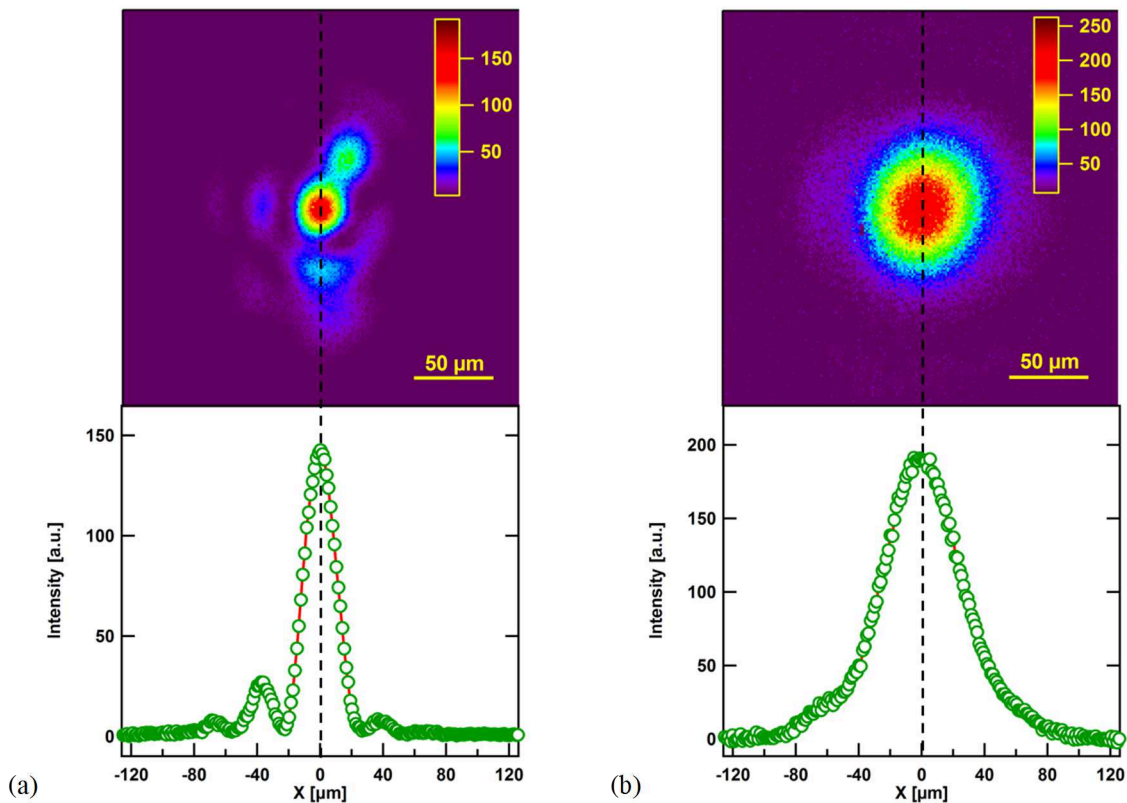
**Figure 3.5:** The part of the setup used to split the pre-pulse from the main-pulse. The pre-pulse undergoes a delay time of  $\sim 2$  ps (it reaches to the Ti wire earlier) to generate a pre-plasma before arriving the main-pulse.

After splitting the pump beam from the main- and pre-pulse beams, a plano-concave lens with a focal length of 30 cm focuses both of the beams on the Ti wire inside the X-ray vacuum chamber through a fused silica window with an antireflection coating at 800 nm on both sides (figure 3.6). The pump beam, after being delayed, is directed and focused by a lens with  $f = 95$  cm onto the sample. Due to the diffraction caused by the holes of the holey-mirror beam splitters, an adjustable diaphragm (A.D) is employed to shape the pump beam as a Gaussian beam. Also, its intensity (fluence) can be controlled by using a combination of a lambda half-wave retarder ( $\lambda/2$ ) and a dielectric Brewster polarizer (P).



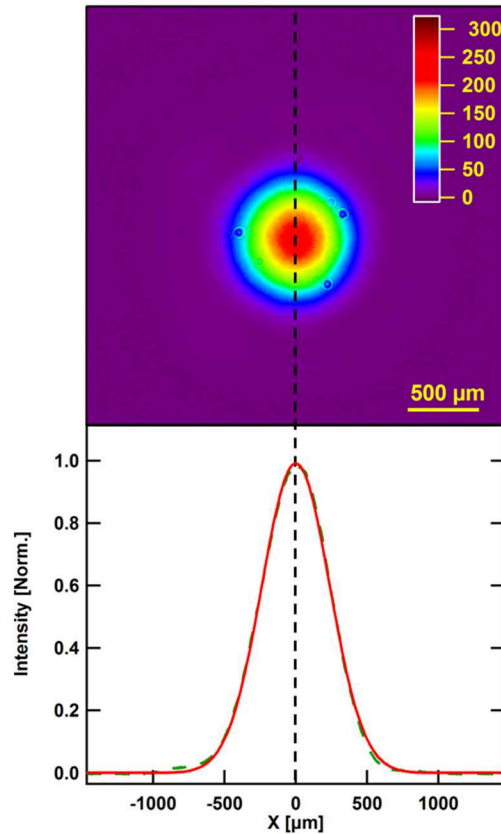
**Figure 3.6:** Schematic of the setup showing the three beams for the X-ray generation and the sample excitation. The main-pulse (red) and pre-pulse (yellow) (after being delayed) have the same optical path and they are focused on the Ti wire inside the X-ray chamber. The white line represents the lack of the pump beam within the main-pulse.

Figure 3.7 shows the measured intensity distributions of the main-pulse (figure 3.7-a) and pre-pulse (figure 3.7-b) beams at their focuses. The diameter of the main-pulse beam is approximately  $24\ \mu\text{m}$  (FWHM) and  $27\ \mu\text{m}$  (FWHM) in the horizontal and vertical directions, respectively. The side wings around the peak intensity are due to the diffraction caused by the holes in the holey-mirror beam splitters. The central peak in the main-pulse beam contains  $\sim 60$  percent of the total incident energy. The pre-pulse beam diameter is  $\sim 60\ \mu\text{m}$  (FWHM).



**Figure 3.7:** The intensity distributions of the main-pulse (a) and pre-pulse beams (b) at the focus. The main-pulse beam diameter in the horizontal direction is  $24\ \mu\text{m}$  (FWHM) and in the vertical one  $27\ \mu\text{m}$  (FWHM). The size of the pre-pulse beam is almost  $60 \times 60\ \mu\text{m}^2$  (FWHM). Since the main-pulse beam wave front is strongly distorted (due to the diffraction caused by beam splitters), there are some side wings around the central peak, which contains  $\sim 60$  percent of the total incident energy.

The intensity distribution of the pump beam was measured at the sample position for an ensemble of pulses to check the stability of the pump beam. As illustrated in figure 3.8, the average size of the pump beam is  $\sim 560 \times 560\ \mu\text{m}^2$  (FWHM). Deviation of the beam center and diameter from their mean values are less than 5 % and 2 % of the mean diameter, respectively.



**Figure 3.8:** The intensity distribution of the pump beam at the sample surface. The mean beam size is  $\sim 560 \times 560 \mu\text{m}^2$  (FWHM)

### 3-2-2 X-ray part of the setup

In addition to the reasons mentioned in the introduction of this chapter (nonlinear response of air and plasma breakdown at high optical intensities), the absorption of the emitted X-rays in air is large at atmospheric pressure. Therefore, to avoid these drawbacks the Ti wire is placed in a small vacuum chamber. In figure 3.9, the X-ray part of the setup is depicted. By focusing the laser on the Ti target, the X-rays are emitted into the full solid angle. A fraction of the emitted X-rays are collected and focused onto the sample held in the sample holder of a cryostat by a toroidally bent Ge crystal (see section 3-4). He-purged pipes, called “X-ray path chamber”, are used to minimize absorption losses of the X-rays (it will be discussed later). Finally, the diffracted X-ray pattern is detected using a Si based CCD in a coplanar symmetric geometry.

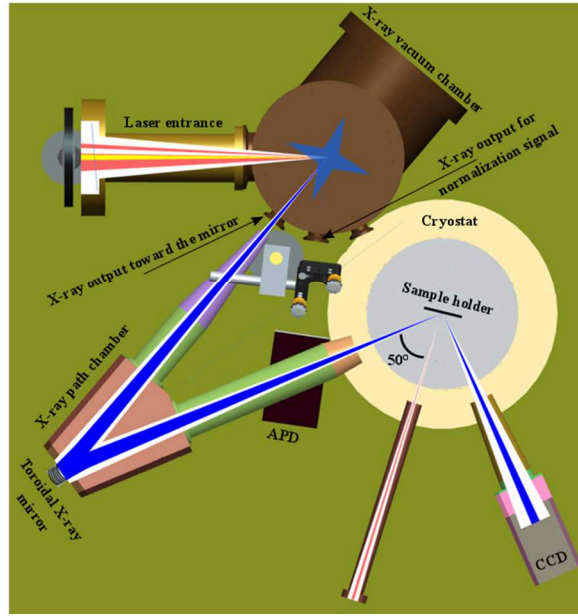


**Figure 3.9:** Schematic of the X-ray part of the setup. The laser beam is focused on the Ti wire inside the X-ray vacuum chamber. A fraction of the emitted X-rays are reflected and focused by the bent crystal mirror onto the sample. To reduce the X-ray absorption in air, the He-purged “X-ray path chamber” is used between the output of the X-ray vacuum chamber to the bent mirror and from there to the entrance of the cryostat. The angle between the incident X-ray and pump beam on the sample is  $\sim 50^\circ$ .

The angle between the X-ray and optical pump beams is  $\sim 50^\circ$ . As a consequence, the actual delay between the optical pump and X-ray probe varies across the sample surface. With  $\Delta w_x$  the X-ray beam diameter,  $\alpha$  the angle between the X-ray and optical pump beams and  $\theta_B$  the Bragg angle, the variation in delay time  $\Delta t$  is given by

$$\Delta t = \frac{\Delta w_x}{c} \left( \frac{\cos \theta_B}{\sin \theta_B} - \frac{\cos(\alpha + \theta_B)}{\sin \theta_B} \right) \quad (3.1)$$

As it is evident from equation (3.1), this geometrical “smearing”, which limits the achievable temporal resolution, does not only depend on the angle between the pump and probe, but also on the Bragg angle of the diffraction peak of interest. For example, for the (111)-reflection of Ge ( $\theta_B = 24.89^\circ$  at 4.51 keV  $\equiv$  Ti- $K_{\alpha 1}$ ) the effective time resolution is  $\sim 0.5$  ps. This is sufficient for the study of acoustic phenomena in the ps time-range. In the following, the details of the X-ray chamber, X-ray path chamber and cryostat are presented, respectively.

A compact cylindrical X-ray vacuum chamber made of Al with a diameter of 153 mm, height of 368 mm and thickness of 6 mm (figure 3.10-a) was designed and built [95].

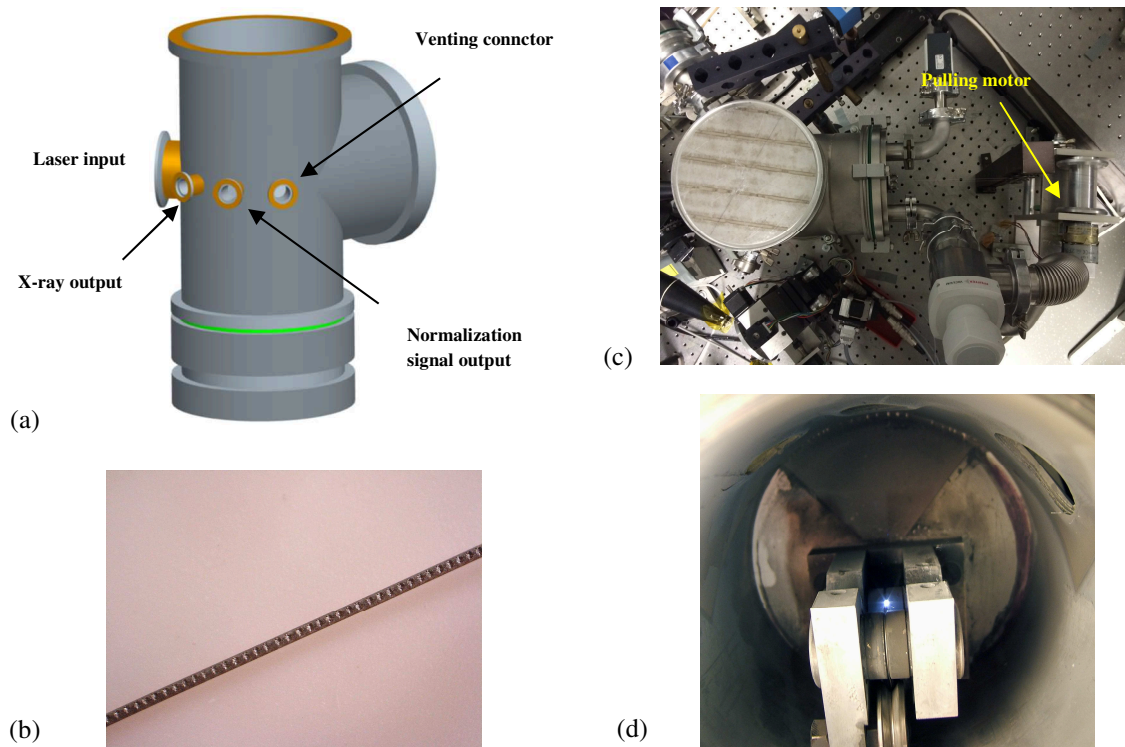


**Figure 3.10:** Schematic of the X-ray vacuum chamber (a). The wire moves with a proper speed to establish a fresh spot for every laser pulse (b). The pulling motor is placed out of the chamber and the wire goes in and out through tiny holes covered by Teflon gaskets (c). The image (d) shows the plasma plume caused by a laser pulse.

To minimize background radiation (both for radiation protection as well as to reduce noise/background), another cylinder made of Pb with 100 mm diameter, 150 mm height and thickness of 6 mm is used to confine the Ti wire. In addition, Al and Pb plates surround the whole table containing the X-ray part with a thickness of 6 mm and 2 mm, respectively. The chamber includes vacuum pump, pressure gauge and venting connectors as well as laser input and two X-ray outputs for the X-ray probe and normalization signal (figure 3.10-a). The wire moves with a proper speed to establish a fresh spot for every laser pulse (figure 3.10-b). The motor, which pulls the wire, cannot work in the vacuum. Therefore, it is placed outside of the chamber (figure 3.10-c) and the wire with a diameter of 250  $\mu\text{m}$  goes in and out through two tiny holes embedded in the chamber. Special gaskets made of Teflon surround the wire in its input and output to preserve the vacuum inside the chamber. To prevent deposition of the debris on the input and outputs windows of the chamber, the input one (fused silica window) is protected by 8  $\mu\text{m}$  Mylar foil and outputs of the interior lead-shield are covered by 8  $\mu\text{m}$

Kapton foil. These foils have to be replaced time to time to provide optimum X-ray flux on the sample. Moreover, Kapton foils of the same kind are glued to the X-ray outputs of the chamber (with a transmission of  $\sim 0.96$  at Ti- $K_{\alpha 1}$  characteristic line [164]). The dimension of the Kapton window is  $9 \times 5$  mm<sup>2</sup> to ensure that the pressure difference of almost  $10^3$  mbar (pressure inside the chamber is  $10^{-2}$  mbar) would not break the Kapton foil.

To minimize absorption losses of the X-rays in air over a distance of  $\sim 81$  cm, a He-purged chamber called “X-ray path chamber” (figure 3.9) is employed. This increases the overall transmission to  $\sim 0.84$ . The bent crystal mirror is placed outside of the X-ray path chamber, but due to the short distance ( $\sim 1$  mm) between the mirror and the output/input of the chamber, the absorption is negligible. Inputs and outputs of the X-ray path chamber are again covered by the thin Kapton foils.

The sample is held in the sample holder of a closed cycle cryostat (figure 3.11-b) working with the liquid Helium, which provides a functional temperature range from 330 K to 7 K. A vacuum turbo pump is used to establish the minimum required pressure  $10^{-5}$  mbar. The sample holder is on a 3-axis manipulator with a maximum moving range of  $\pm 3$ mm in X-Y plane as well as 0 to 50 mm in Z direction. The cryostat has two Kapton windows (with a thickness of  $240 \mu\text{m}$ ) for the input and output of the X-ray and a small optical window (fused Silica) for the optical pump. However, the experiments performed for this thesis (see chapter 4) were carried out at room temperature and only the sample holder stage of the cryostat was used.

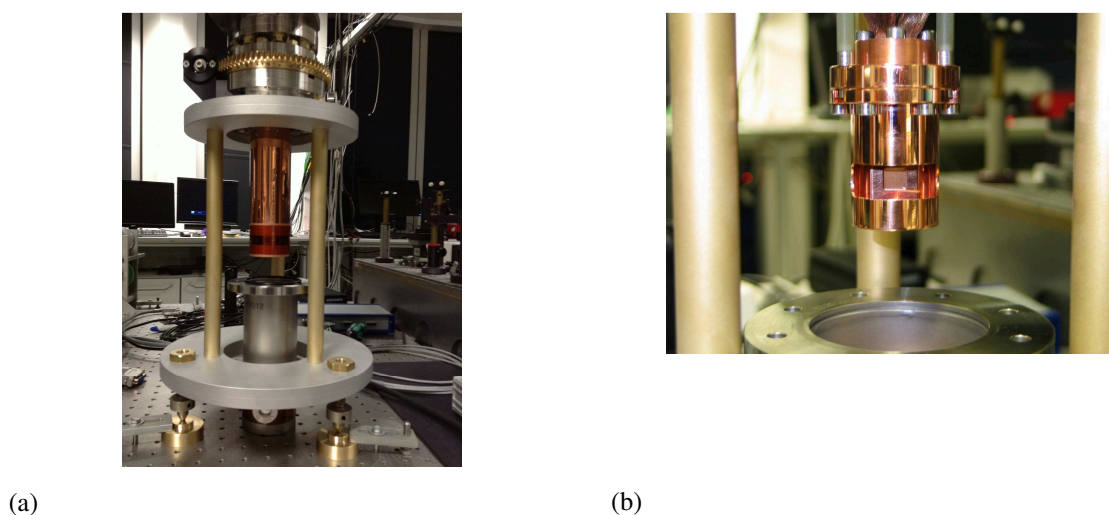


**Figure 3.11:** Photos of the cryostat (a) and its sample holder (b)

The following table summarizes the characteristics of the cryostat.

Maximum temperature	330 K
Minimum temperature	7 K
Required pressure	$>10^{-5}$ mbar
Time to reach at the minimum temperature	24 h
X-Y manipulator	$\pm 3$ mm
Z manipulator	0 to 50 mm
Temperature sensor	Diode type

**Table 3.1:** Characteristics of the closed cycle cryostat.

### 3-3 X-ray detection

Using cooled CCD detectors have provided the convenience in recording and displaying images digitally. Direct and indirect detection methods are two main approaches for detecting X-ray photons.

In the direct method, an X-ray photon is absorbed within the Si depletion region of the CCD as illustrated in figure 3.12 [165] and produces multiple electron-hole pairs due to the impact ionization. An internal electric field separates the electrons from the holes. While the holes undergo a rapid recombination, the electrons are trapped in the pixel until being read out.

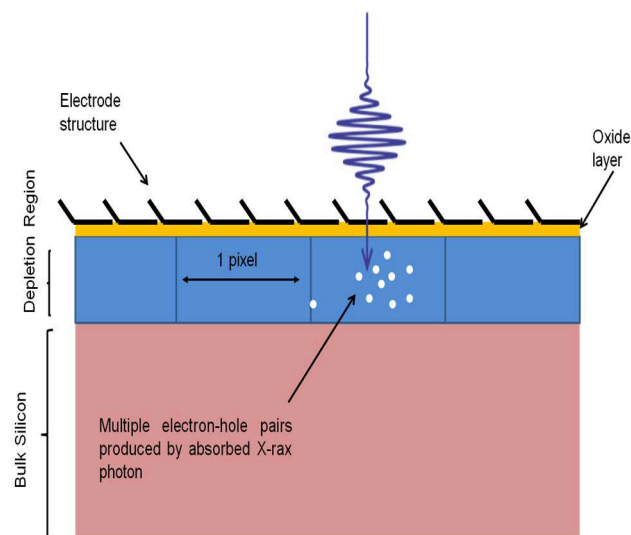


**Figure 3.12:** Schematic of the direct detection of X-ray photons. Photoelectrons generated outside the depletion region will not contribute to the signal.

In contrast to the case for the absorption of visible wavelengths in which only one photoelectron is produced per absorbed photon, one X-ray photon produces many photoelectrons [165]. The following equation describes the relation between the number of generated photoelectrons  $N_E$  and the photon energy  $E$  (eV)

$$N_E = \frac{E}{3.65} \quad (3.2)$$

Another important factor is the quantum efficiency (QE) defined as the probability of a photon being absorbed within the depletion region. The QE is a function of photon energy with some discontinuities, which are the result of intrinsic properties of Si, namely absorption edges. The use of a thicker depletion region increases the probability of a photon being stopped in this region and therefore improves the QE. The generated photoelectron flux density (with unit of  $1/s\text{-cm}^2$ ) is given by

$$N_F = QE N_E F \quad (3.3)$$

where  $F$  is the photon flux density ( $\text{photons/s}\text{-cm}^2$ ). An additional descriptor of the CCD is its gain  $g$  and by using it the number of counts,  $N_C$ , generated per photon can be defined as

$$N_C = g N_E \quad (3.4)$$

Besides all performance advantages of the direct method like improved signal to noise and linearity, one interesting point is its application to determine the energy distribution of the incident X-ray photons from the number of counts generated in the detector. At low flux levels of incoming photons, which no more than one photon is likely to be incident on any given pixel, a histogram of the detected signal provides information of the photon spectrum (see section 3-5). However, the direct detection method has also disadvantages, such as low QE for photon energy above 10 KeV, relatively small image area and radiation-damage issues in case of exposure to high X-ray doses.

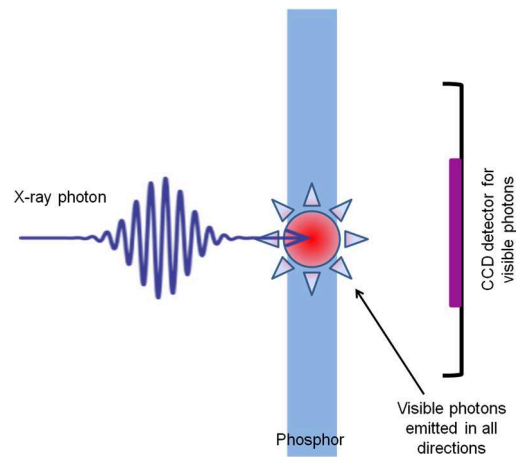


**Figure 3.13:** Illustration of the indirect X-ray detection

The second common method for detecting X-ray photons is indirect detection (figure 3.13). This method employs a scintillator (also called phosphor) to convert the X-ray photons into visible photons, which are then collected partially and guided to the CCD chip usually by a fiber optic. Comparing to the direct detection method, it does not give any information about the energy of the incident X-ray photons nor the absolute incident photon flux because of several conversion processes.

In this work, the direct detection scheme has been employed by using a thinned, back-illuminated Si-CCD (type: Roper Scientific PI-MTE: 1300B [166]), which gives a wider range of photon energy detection compared to the front illuminated one. This CCD provides a very good QE for photon energy in the range of a few KeV, e.g. 55% at  $E = 4.5 \text{ KeV} \equiv \text{Ti-K}_\alpha$  [166], which makes it a suitable candidate to detect the X-ray signals from the sample for the current experimental work. The incident radiation is not the only reason for electron generation in a CCD, but during the acquisition of an image, electrons can also be generated due to the dark current. The dark current describes the rate of generation of thermal electrons at a given CCD temperature, which can be reduced by cooling the device. More important, the dark current noise, which degrades the quality of captured images, can be reduced as well. In the current setup, the CCD is cooled down to  $-30^\circ \text{ C}$ . In order to prevent the condensation of contaminants (i.e. water) on the chip, the CCD has to be operated in vacuum. However, the used CCD (PI camera) has been designed to be operated completely in vacuum. Therefore, it is not equipped - as standard CCDs - with a sealed chip housing and it was necessary to construct a suitable housing (figure 3.14) for the modular setup. Using this housing, the CCD operates at a pressure of  $10^{-2} \text{ mbar}$ .

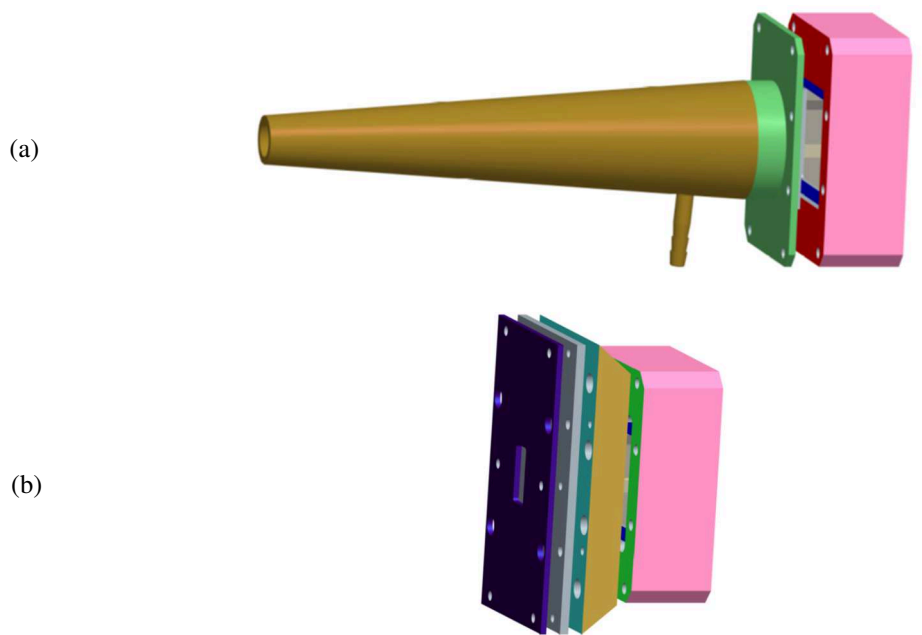


**Figure 3.14:** 3-D sketch of the designed CCD vacuum housings. The conical pipe provides a non-absorptive length between the output of the cryostat and the CCD chip (a). The cap used to measure mirror topography (b) (see section 3-4).

The conical pipe (with an entrance diameter of 12.6 mm, length of 172 mm and output diameter of 36 mm) shown in figure 3.14-a, minimizes absorption over the distance between the output of the cryostat and the CCD chip. A Kapton foil with a thickness of 8  $\mu\text{m}$  is glued to the entrance of the pipe. A Beryllium window (thickness of 150  $\mu\text{m}$ ) stacked between two fold of Kapton foil with a total transmission of 0.78 (at 4.5 KeV photon energy) is used to block optical stray light.

### 3-4 X-ray optics

It is important that in a setup light beams can be manipulated, directed and/or focused to give a suitable performance for an intended application. In ordinary optics, optical elements such as lenses and mirrors made of optical glasses, for example, carry out this task. Of course, in special cases, e.g. ultrashort pulses, one has to consider proper materials and coatings. Since the refractive index of optical materials differs considerably from unity in the visible range of the light spectrum, the direction of light crossing their interfaces with air shows significant changes. In the X-ray range, the refractive index is smaller, but very close to one, which requires different approaches to realize suitable optics [125]. Depending on the type of X-ray sources and the physical phenomena under investigation, refractive, reflective and diffractive optics can be used to modify and direct X-ray beams. For example, X-ray lenses (refractive optics) [167] as well as X-ray curved mirrors operating based on the total reflection (reflective optics) [168] are employed in accelerator based X-ray sources in which X-ray beams are well collimated and monochromatized. In contrast, bent crystals (diffractive optics), multilayer mirrors and

capillary optics are utilized in the laser-plasma based X-ray sources in which X-rays are emitted into the full solid angle. These kinds of optics collect a fraction of the emitted X-rays and focus it onto the sample. In addition, the optimum choice of one of the mentioned optics depends mainly on the desired phenomena under investigation. Bargheer *et al.* [169] and Nicoul *et al.* [95] have characterized and compared the operation of these three kinds of X-ray optics using a laser-plasma based X-ray source. They showed that the bent crystals provide extremely well monochromatic X-ray photons on the sample. Moreover, the transverse X-ray intensity distribution is angular-independent (description is provided later). These features of the bent crystals make them extremely suitable to be used for measuring the transient change of rocking curves that is the aim of this thesis. In the following subsection, the principle of operation and measured characteristics of a toroidally bent crystal made of Ge is presented.

### 3-4-1 Toroidally bent crystal mirror

The principle of operation of bent crystal mirrors is based on the Bragg reflection of X-rays from lattice planes of crystals. In these mirrors, the lattice planes are parallel to the geometrical surface of crystals and bent either spherically or toroidally [170]. The used bent crystal mirror in the current setup is a 90  $\mu\text{m}$  thick Ge crystal grown along the [100] direction which is bound to a toroidally bent glass substrate [171]. A toroidally bent crystal mirror provides a monochromatic point-to-point image in a “Rowland circle” geometry as depicted in figure 3.15-b provided that  $R_V/R_H = \sin^2\theta_B$  [170], where  $R_V$  and  $R_H$  are the vertical and horizontal radii of curvature, respectively and  $\theta_B$  is the Bragg angle.

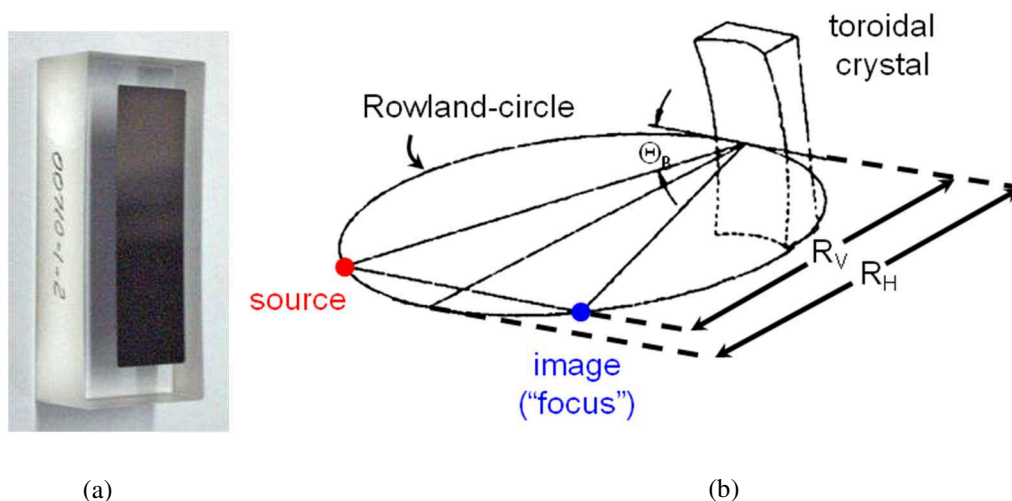


**Figure 3.15:** The toroidally bent crystal mirror made of Ge(100) (a). The Rowland circle geometry to give a 1:1 image (b).

Here the toroidally bent Ge crystal has radii of curvature corresponding to the Bragg (400)-reflection at Ti- $K_{\alpha 1}$ . Table 3.2 summarizes the technical data of the used toroidally bent mirror.

Characteristic line	Ti- $K_{\alpha 1}$
Photon Energy (eV)	4510.899
Size (mm <sup>2</sup> )	12.5×40
Orientation	(100)
Orientation error (")	< 10
Bragg reflection	(400)
Brag angle (°)	76.32
Convergence angle (°)	~ 1.4
R <sub>H</sub> (mm)	498.6
R <sub>V</sub> (mm)	473.7
R <sub>V</sub> /R <sub>H</sub>	0.9500
Sin <sup>2</sup> θ <sub>B</sub>	0.9447
Thickness (μm)	90
Acceptance solid angle (sr)	1.63×10 <sup>-4</sup> π
Distance from the source (mm)	487.5

**Table 3.2:** Technical data for the used toroidally bent Ge crystal mirror properly designed for the  $K_{\alpha 1}$  characteristic line of Ti.

The total efficiency of the mirror is an important quantity and defined as its integrated reflectivity multiplied by the acceptance solid angle of the mirror divided by  $4\pi$ . Also, the integrated reflectivity itself is given by the ratio of the energy bandwidth of the Bragg reflection over the bandwidth of the used characteristic line [170]. The energy bandwidth of the Ge (400)-reflection of a flat crystal is 0.26 eV. Since the radii of curvature of the toroidally bent mirror are relatively large (see table 3.2), this value can be considered as an approximation for the energy bandwidth of the toroidally bent Ge crystal [94]. In addition, the energy bandwidth of Ti- $K_{\alpha 1}$  is ~ 3.1 eV (see section 3-5). Using these values one can estimate the total efficiency of the mirror as  $3.4 \times 10^{-6}$ .

The X-ray mirror needs to be properly placed at the Rowland circle to ensure a homogeneous reflectivity across the mirror surface. Therefore, the intensity distribution of the reflected/diffracted  $K_{\alpha 1}$  radiation was monitored by placing the X-ray CCD close to the mirror. Figure 3.16 depicts the reflection image and its vertical and horizontal average cross-sections at the corresponding Ti- $K_{\alpha 1}$  Bragg angle (76.32 °).

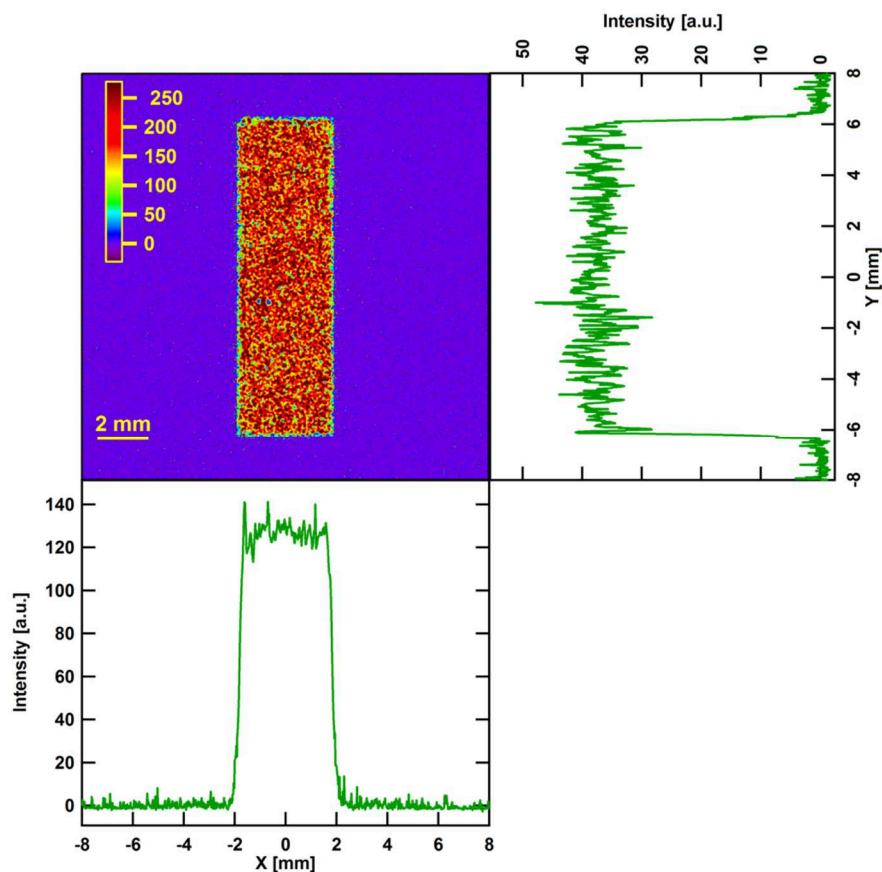


**Figure 3.16:** Topography of the Ti- $K_{\alpha 1}$  mirror. Horizontal and vertical average cross-sections show almost a uniform behavior (fluctuations are due to the single photon effect because of 20 s exposure time). This homogeneity implies the independency of the intensity upon the angular position.

Despite the fluctuations coming from the short exposure time, the average cross-sections are flat, evidencing homogeneous reflectivity across the mirror surface. As a consequence, in the X-ray focus on the sample the incident intensity will be constant as a function of angle.

The exact determination of the focus position is crucial in optical-pump - X-ray-probe experiments performed by convergent X-ray beams. It has been shown by Shymanovich *et al.* [172] that the sample needs to be properly positioned in the focus of the mirror, otherwise the so-called “acoustic artifact” causes the angular distribution of the X-rays diffracted off the laser-excited sample (rocking curve) to be severely altered/distorted.

In principle, the X-ray CCD can be used to find the focus and measure the focal spot size, however, this technique has some limits. First, there is a risk of damaging the CCD’s chip close to the focus, where the X-ray fluence is relatively large. Second, the accuracy of replacing the CCD with the sample after finding the focus is limited. Therefore, the knife-edge method was employed to localize the focal point and measure the focal spot size of the X-ray beam.

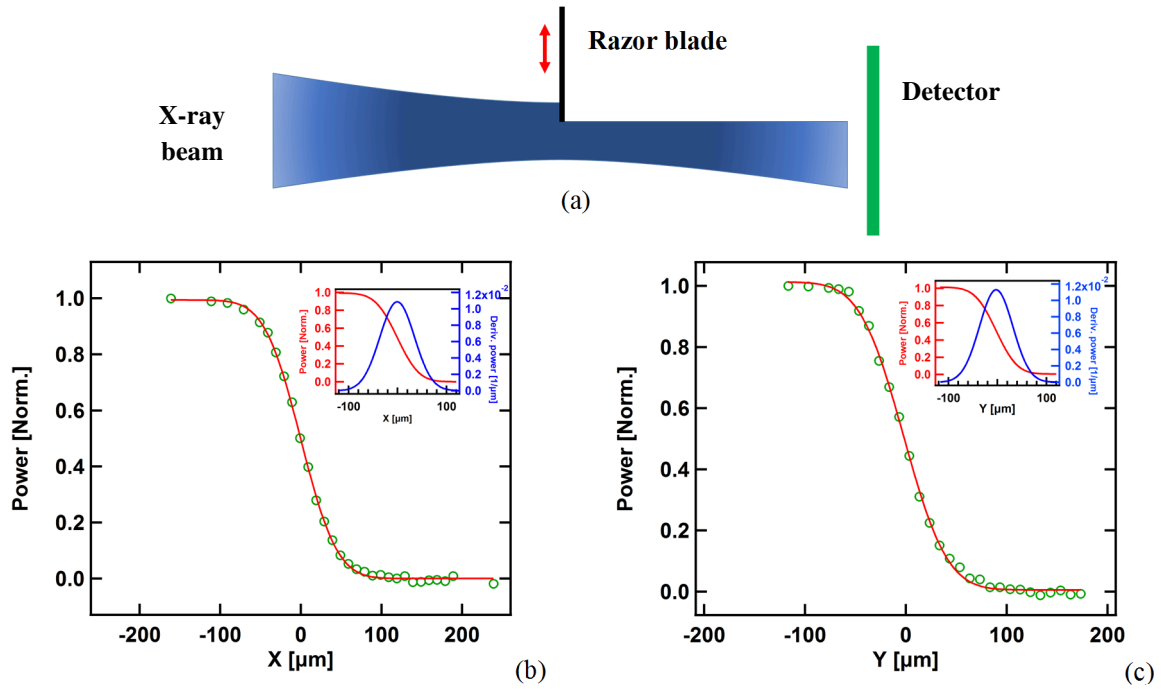


**Figure 3.17:** Schematic of the Knife-edge method (a). Measured transmitted power (green circles) and error function fit (red solid line) in the horizontal direction. The inset shows derivative of the fit function corresponding to the horizontal cross-section of the X-ray beam intensity distribution, which is a Gaussian function (b). Similarly, measured transmitted power in the vertical direction (c).

In this method, a razor blade with a thickness of  $100\ \mu\text{m}$  is placed close to the estimated position of the focus and the X-ray CCD (placed far away from the blade) detects the transmitted signal while the blade is translated through the beam using a calibrated translation stage in both vertical and horizontal directions (figure 3.17-a). Measurement were made for several different points along the X-ray propagation axis and the minimum spot size was found. Figures 3.17-b and 3.17-c depict the normalized transmitted power versus lateral position of the blade in the horizontal and vertical directions, respectively. An error function given by equation (3.5) was fitted to the measured data

$$P(x) = \frac{P_0}{2} \left( 1 - \operatorname{erf} \left( \frac{\sqrt{2}(x - x_0)}{w} \right) \right) \quad (3.5)$$

where  $P_0$  is the total transmitted power and  $w$  corresponds to the  $1/e^2$  radius of a Gaussian beam (figure 3.17 insets). The extracted focus diameter from the above equation is  $83 \pm 1.5\ \mu\text{m}$  (FWHM) and  $80 \pm 2\ \mu\text{m}$  (FWHM) for the horizontal and vertical directions, respectively. This size corresponds to a convolution between imaging properties of the bent mirror and the X-ray source size [173].

### 3-5 X-ray spectrum

As mentioned in chapter 2, the emitted X-ray spectrum consists of broadband bremsstrahlung radiation and sharp characteristic lines. To measure the spectrum, the X-ray CCD was placed directly in front of the output of the X-ray chamber. The X-ray flux was reduced by using an Al filter with a proper thickness in front of the CCD to ensure that no more than one photon is likely to be incident on a given CCD pixel for a single X-ray pulse. Under these conditions, every pixel delivers a given value (in count) corresponding to the incident photon energy and the histogram of the CCD image provides the spectrum of the incident X-ray pulse (see section 3.3). In order to find the maximum ratio between the X-ray characteristic lines and the continuum one, the spectrum was measured for different positions of the focusing lens that focuses the laser on the wire. As an example, figure 3.18 shows the spectrum (histogram of the CCD image) at the best position of the lens.

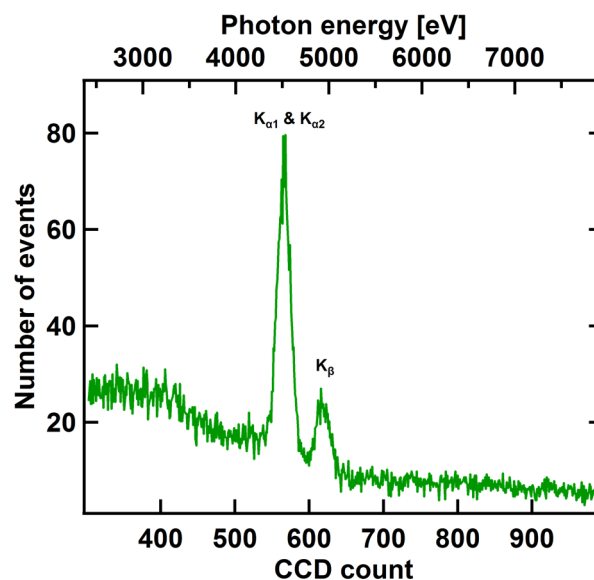


**Figure 3.18:** X-ray spectrum measured by the X-ray CCD operating in single-photon mode. At low flux levels of incoming photons, which no more than one photon is likely to be incident on a pixel of the CCD, the histogram of the CCD image reveals the spectrum of the photons. This spectrum corresponds to the emitted X-rays from the Ti target.

Besides the continuum spectrum, the  $K_{\alpha}$  and  $K_{\beta}$  lines are well pronounced. Because of the low energy resolution (10 eV), this method is not able to distinguish the  $K_{\alpha 1}$  and  $K_{\alpha 2}$  lines (with energy difference of 5.98 eV) from each other. Another point regarding this method is that depending on the incident photon energy there is a considerable chance that a single photon does not generate charge in only a single CCD pixel, but the generated charge is shared over several pixels (“many-pixel-events”) [174]. Therefore, a considerable fraction of the apparent continuum is detected/counted as several

photons of apparently lower energy, which actually belongs to the  $K_{\alpha}$  radiation. To overcome the mentioned limits the following technique was used to measure the emitted X-ray spectrum.

The toroidally bent mirror provides higher spectral resolution. Only the radiation in the energy interval corresponding to the width of its rocking curve is diffracted by the mirror. As mentioned before, due to the relatively large radii of curvature of the toroidally bent mirror, the energy bandwidth of the Ge (400)-reflection of a flat crystal ( $\Delta E = 0.26$  eV) is a proper approximation for the energy bandwidth of the toroidally bent Ge crystal (see section 3-4). According to the Bragg's law, the spectrum of the emitted  $K_{\alpha}$  radiation can be measured by scanning the glancing angle (i.e. rotating the mirror in the direction of Rowland circle normal). The spectrum was measured with the help of this method and the result is illustrated in figure 3.19 (green circles). Due to the higher spectral resolution, the  $K_{\alpha 1}$  and  $K_{\alpha 2}$  lines are completely resolved. The linewidths of the  $K_{\alpha 1}$  line was found as  $\sim 3.1$  eV by fitting the so-called double Pearson VII function, which is given by [175]

$$\begin{aligned} y(x) &= Af(x - x_0) + Bf(x - x_0 - \delta) \\ f(x - x_0) &= [1 + K^2(x - x_0)^2/M]^{-M} \end{aligned} \quad (3.6)$$

where  $K$  governs the line width and  $M$  the rate of decay of the tails. Constants  $A$  and  $B$  determine the amplitudes of  $K_{\alpha 2}$  and  $K_{\alpha 1}$  lines, respectively. The measured  $K_{\alpha 1}$  linewidth is broader than the expected value (1.45 eV) reported in literature [176].

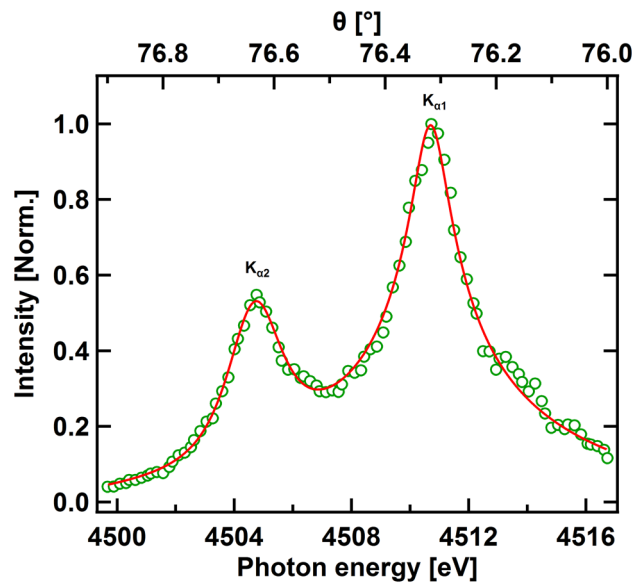


**Figure 3.19:** Spectrum of the Ti- $K_{\alpha}$  radiation measured by the toroidally bent mirror. The green circles represent the measured data and solid red line is a double Pearson VII fit. The  $K_{\alpha 1}$  line width is  $\sim 3.1$  eV.

According to Sengebusch *et al.* [177], the emitted radiation from the ionized atoms in higher ionization stages is the main reason for such a broadening. They calculated emission energy of various ionization stages and found a blue shift with increasing ionic charge, which is caused by a stronger Coulomb interaction within the ion (emitter) when electrons are removed. Such a shift results in a broadened linewidth.

### 3-6 X-ray yield optimization

Another important characteristic of the X-ray source is the number of  $K_{\alpha 1}$  photons per pulse incident on the sample after reflection from the bent crystal mirror (“X-ray yield”), which depends on the laser intensity on the target. As discussed in chapter 2, obtaining an efficient  $K_{\alpha}$  X-ray emission requires a productive ionization of the K-shell electrons of the target (e.g. Ti) via impact ionization by *hot* electrons with proper kinetic energy. The intensity of the laser plays an important role to control and optimize the kinetic energy of the *hot* electrons and corresponding to it the X-ray yield. Changing the relative position of the lens with respect to the target position, changes the laser intensity on the surface of the target. Figure 3.20 shows the measured X-ray yield (with no pre-pulse) versus the relative lens position when the toroidally bent mirror was adjusted to reflect only  $K_{\alpha 1}$  radiation. In this measurement, the X-ray yield was measured by scanning of the lens position in the direction of the laser propagation to find the optimum X-ray yield (zero position in the figure).

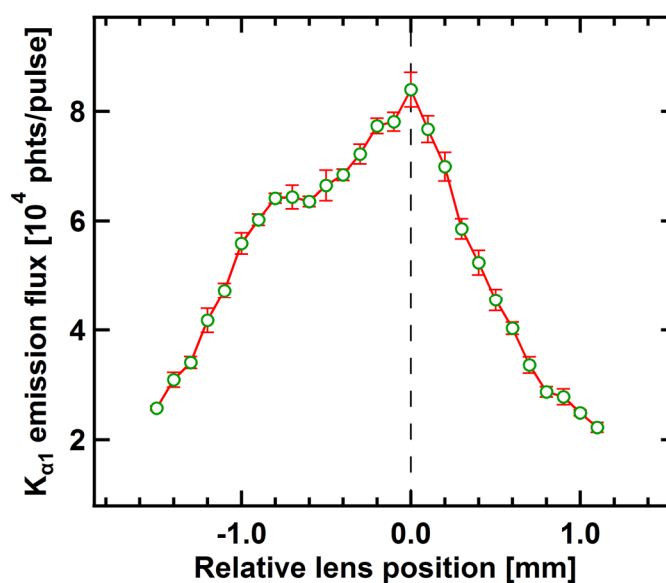


**Figure 3.20:** Ti- $K_{\alpha 1}$  emission flux versus the lens position (green circles). The red solid line between points are only to guide the eye. The zero position corresponds to the maximum of the X-ray yield.

The optimum laser intensity corresponding to the maximum  $K_{\alpha}$  yield for Ti is a few times  $10^{16}$  W/cm<sup>2</sup> [173]. Taking into account the intensity of the laser at its best focus  $\sim 6.6 \times 10^{16}$  W/cm<sup>2</sup>, by approaching the focus to the wire (target), the intensity gets closer to the optimum value and the X-ray yield increases. It reaches up to a value of  $(6.4 \pm 0.2) \times 10^4$  photons/pulse (first maximum in figure 3.20 at the position of -0.7 mm). Further approaching causes higher intensity of the laser, but a decrease in the X-ray yield. The X-ray yield increases again by passing the best focus position from the target surface. The optimum/maximum value is  $(8.4 \pm 0.3) \times 10^4$  photons/pulse. As discussed in chapter 2, there are two reasons to explain this intensity dependence. First, the dependence of the K-shell ionization cross-section on the energy of the *hot* electrons [159]. The average energy of the *hot* electrons depends upon the laser intensity. Second, intensities higher than the optimum one generate *hot* electrons with higher energy, which penetrate deeply into the target beyond the  $K_{\alpha 1}$  absorption length. Thus, most of the generated photons are reabsorbed on their way to the target surface [137, 173]. Reich *et al.* found a symmetric profile of X-ray yield around the best focus [173], but in the measured yield here, there is an asymmetry. Lu *et al.* [142] have also reported such an asymmetry. This asymmetry may be due to the deviation of the laser beam profile from the perfect Gaussian profile (i.e. the wave front has been distorted strongly by reflection from two holey-mirror beam splitters and there are two holes in the beam.). Thus, the intensity of the laser with respect to the focus is not symmetric.

So far, the optimization of the X-ray yield with respect to the incident laser intensity on the wire (target) has been discussed, while the plasma scale length  $L$  was constant. In this case,  $L$  is determined by the time interval between the plasma formation threshold and the maximum intensity of the laser on the target. The coupling efficiency of the laser pulse to the plasma and consequently to the X-ray yield depends strongly on  $L$  (see chapter 2). Lu *et al.* [142] made a systematic investigation about the effect of the plasma scale length and laser angle of incidence on the  $K_{\alpha}$  radiation flux on flat Cu and Ti targets. They used a pre-pulse to generate a pre-plasma before the arrival of a main-pulse, which produced the X-rays. By varying the delay between the pre- and main-pulse, the plasma scale length could be controlled. Their results indicate that at negative delay times (the main-pulse arrives earlier), the  $K_{\alpha}$  yield decreases with decrease in the laser angle of incidence on the target and reaches its minimum value when approaching normal incidence. On the other hand, for all angles of incidence the  $K_{\alpha}$  yield starts improving at positive delay times (extended scale length). However, the optimum delay time corresponding to the maximum observed yield is angle-dependent and decreases with increase in the angle of incidence. Moreover, the yield improvement also depends on the angle of incidence so that it is more for smaller angles compared to larger angles. They also found that the optimized  $K_{\alpha}$  yield (maximum yield) is independent on the angle of incidence and it is achievable by choosing a proper pre-pulse timing.

Based on the above discussion, the  $K_{\alpha 1}$  radiation flux was investigated by using a pre-pulse to generate a pre-plasma. As discussed in subsection 3-2-1, a few percent of the laser beam passes through the first holey-mirror beam splitter. This beam after undergoing a variable delay is recombined with the main-pulse beam and is eventually focused on the target (with an intensity at best focus  $\sim 7.8 \times 10^{14}$  W/cm<sup>2</sup>) to produce the pre-plasma. It was checked that the pre-pulse alone does not produce any hard X-rays. The measured  $K_{\alpha 1}$  flux versus delay time is depicted in figure 3.21. Positive delay times mean that the pre-pulse arrives earlier than the main-pulse, so the scale length is larger for longer delay times.

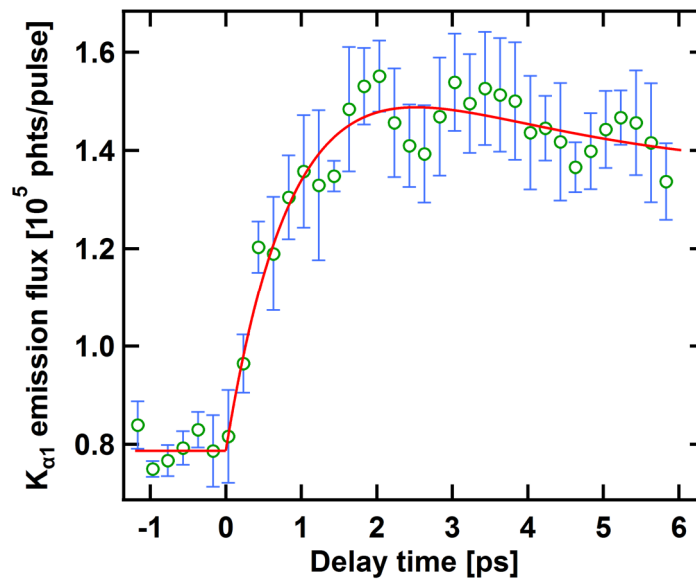


**Figure 3.21:**  $K_{\alpha 1}$  emission flux vs. the delay time between the pre-pulse and main-pulse (green circles). The red solid line is only to guide the eye.

As expected, the X-ray yield starts improving when L is extended in contrast to the case that there is no pre-pulse (negative delay times). The yield is improved with a factor of  $\sim 2$  at a delay time of approximately 2 ps. Afterwards, it drops again with further increase in delay time.

The measured X-ray yield in figure 3.21 was obtained when the lens was adjusted to its optimum position to deliver the highest yield in the case of no pre-pulse existence. It turned out that the X-ray yield with pre-pulse could be further improved by modifying the relative lens position. Figure 3.22 illustrates the X-ray yield improvement by changing the lens position when the delay between pre- and main-pulse is  $\sim 2$  ps.

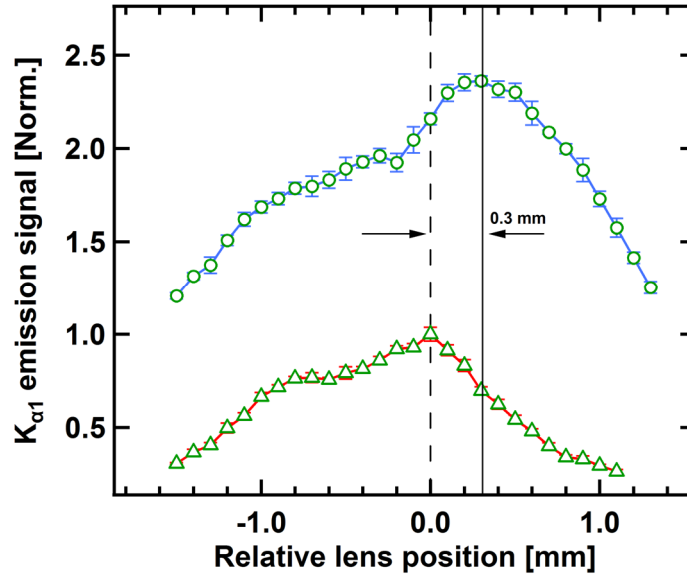


**Figure 3.22:** The X-ray yield vs. the lens position. Results are normalized to the maximum yield in the case of no pre-pulse existence (triangles). The maximum of the signal with pre-pulse (circles) is achieved when the focus is 0.3 mm further behind the target position. The zero position again corresponds to the maximum of the X-ray yield when no pre-pulse exists.

Similar to the no pre-pulse case, the X-ray yield with pre-pulse exhibits an asymmetric profile upon changing the lens position. However, the maximum value is observed when the lens is an additional 0.3 mm away from the position corresponding to the maximum yield without pre-pulse. Recalling that the maximum X-ray yield with no pre-pulse is obtained when the focus is behind the target surface, in the case of existence of the pre-pulse the focus has to be placed 0.3 mm further behind the target surface. The ratio between the two maximum values is 2.36, which means that under the optimum conditions the incident  $K_{\alpha 1}$  flux on the sample is  $\sim 2 \times 10^5$  photons/pulse.

### 3-7 Static X-ray diffraction

In order to measure a rocking curve, it is necessary to provide a continuous variation of the X-ray incident wave vector. In general, there are two methods to achieve this, namely the Laue and Bragg diffraction geometries. In the Laue-geometry, the X-ray wavelength is varied, while keeping the angle of incidence constant. For the Bragg-geometry used in this work, the angle of incidence is varied, while keeping the wavelength constant. Conventionally, to scan the glancing angle of the X-ray beam on the sample surface, the sample and the detector are rotated in the so-called  $\theta$ - $2\theta$  geometry. Since here a convergent X-ray beam is used and thus all angles of incidence are present, the complete rocking curve can be measured without rotating the sample and the detector. As an example, figure 3.23 shows the measured rocking curves of the Ge(111) thin film and Si(111) substrate at the same time (see section 4-2 for the sample characteristics).

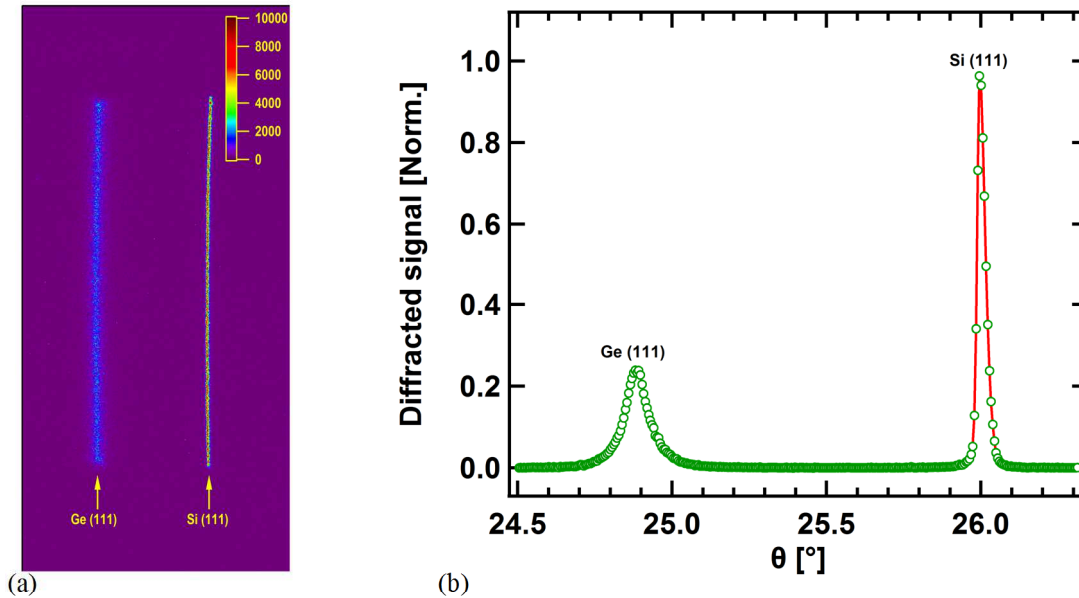


**Figure 3.23:** Diffraction pattern obtained from the Ge(111)/Si(111) heterostructure (a). The normalized rocking curves with peaks at  $\theta = 24.88^\circ$  and  $\theta = 25.99^\circ$  corresponding to the Bragg angles of the Ge (111)-reflection and Si (111)-reflection, respectively (b).

As stated in table 3.2 with the toroidally bent Ge crystal mirror, the convergence angle of the incident X-ray beam is around  $1.4^\circ$ . This is large enough to cover both the reflection of the Si substrate as well as the Ge overlayer without rotating the sample. By integrating along the direction normal to the dispersion direction (horizontal direction in figure 3.23-a) the rocking curves can be obtained (figure 3.23-b). Since the Bragg angles of both the reflections can be obtained from the known lattice constants of Si and Ge, this allows to calibrate the angular scale of the measured rocking curves. It has to be mentioned that for measuring the transient rocking curves, the glancing angle of incidence is chosen in a way that only one of the patterns is detectable. This ensures that the whole transient rocking curve remains inside the convergence angle. From figure 3.23-a, it is obvious that the diffraction patterns do not represent straight lines, but they are curved. The reason for this effect is explained by figure 3.24. For every individual point on the sample, one can define two cones. The first one is called Kossel cone (blue cone in figure 3.24). The axis of the Kossel cone is perpendicular to the atomic planes involved in the diffraction and its apex angle is defined as  $\pi/2 - \theta_B$ . The X-ray convergent beam determines the second cone (the green cone in figure 3.24).

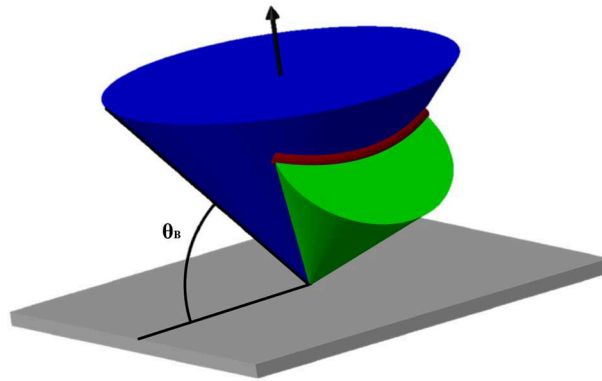


**Figure 3.24:** Schematic of the incident X-ray cone and the Kossel cone.

According to the Bragg's law, rays that are only on the surface of the Kossel cone can be diffracted. Therefore, the diffracted pattern is the intersection of two cones (red line), which is a curved line. To maintain the angular resolution of the experiment, it is necessary to numerically compensate for this curvature of the diffraction pattern before integrating in the vertical direction. Therefore, a "Matlab" routine was utilized to correct the bending. The raw diffraction pattern is divided into 24 segments and by fitting a Gaussian function on each segment, their center is determined. Afterwards, a parabola is fitted on the calculated centers and by using this parabola, the image is corrected (figure 3.25).

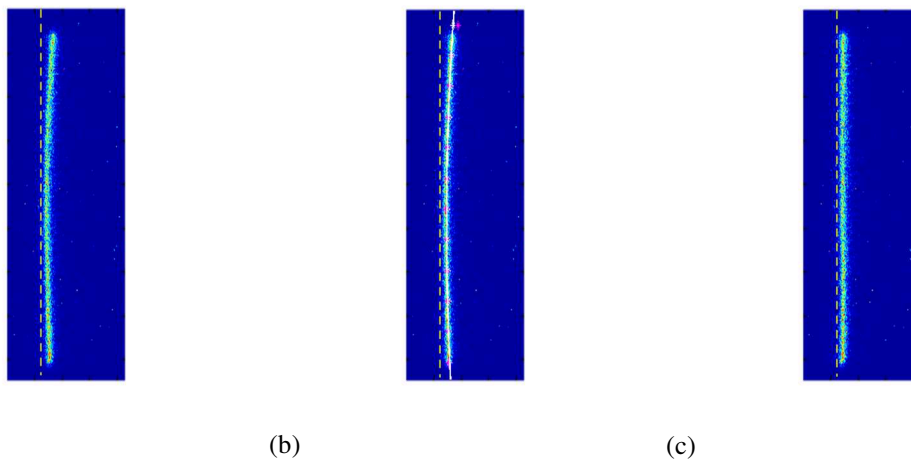


**Figure 3.25:** The process of bending correction. The bent pattern (a) is divided into 24 segments and by fitting a Gaussian profile on each segment cross section the center of them is determined. A parabola is fitted on the calculated centers (b) and is used to correct the bending (c). The yellow dashed line is to guide the eye.

According to the dynamical X-ray diffraction theory presented in chapter 2, the calculated rocking curves for the Ge thin film crystal with 180 nm thickness and the Si substrate (thickness of 0.5 mm) for the (111)-reflection were calculated. Figure 3.26 compares the calculated and measured normalized rocking curves for both of the materials. It is obvious that the measured rocking curves (green circles in figure 3.26-a and green solid line in figure 3.26-b) are wider than the calculated ones (blue solid lines) even after unbending. There are two main sources of broadening in a measured rocking curve. The first one comes from the X-ray source and the second one originates from the sample. The latter refers to the quality of the sample while the former one is due to the intensity distribution of the X-ray spot on the sample and the energy bandwidth reflected by the bent mirror. Since the sample is placed at the image point of the bent crystal mirror, every point within the X-ray spot on the sample contains all incidence angles. Hence, one can assume that each point reflects a rocking curve. These rocking curves overlap with different weights and deliver a broadened rocking curve. This occurs for every wavelength within the bandwidth of the bent mirror, resulting in a broader rocking curve. Real crystals are often composed of small ideal crystal grains, known as mosaic blocks. The mosaic blocks have slightly different orientations. Thereby, every block diffracts a rocking curve with respect to its orientation. The final rocking curve is an accumulation of every individual rocking curve, which leads to an additional broadening. It has to be emphasized that in the case of Si, with its almost perfect structure, the contribution from mosaicity is negligible. Therefore, its broadening reflects source-related effects (e.g. source size, energy bandwidth), but in the case of the Ge thin film both of the broadening processes are play role. Mathematically, these broadenings are equivalent to a convolution of the ideal rocking curves (calculated) with corresponding broadening functions.

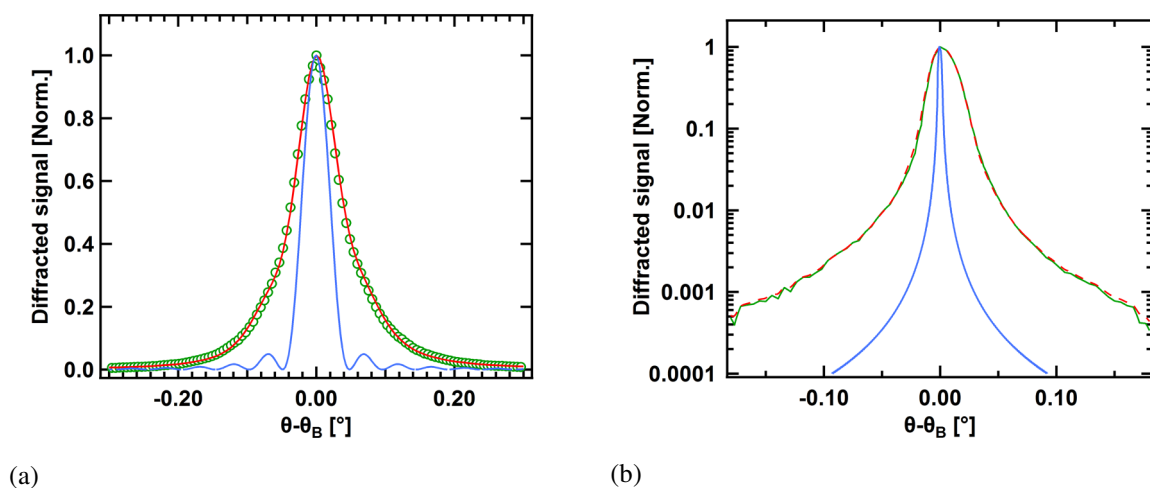


**Figure 3.26:** The measured (green circles), calculated (blue solid line) and convoluted (red solid line) rocking curves of 180 nm Ge(111) (a). The logarithmic plot of the measured (green solid line), calculated (solid blue line) and convoluted (red dashed line) rocking curves of 0.5 mm Si(111).

The measured rocking curves exhibit a slight asymmetry. Therefore, a double asymmetric Pearson VII function (equation (3.7)) was used to estimate the broadening function [175]. For Ge its width parameters have been varied such that the convolution with the calculated rocking curve fits the measured data. Since for Si the ideal/calculated rocking curve is very narrow, the measured rocking curve multiplied by a Lorentzian function (to reduce its width) was employed. The red solid and dashed lines in figure 3.26 show the convoluted rocking curves.

$$f(\theta) = \begin{cases} \left[ \frac{1}{1 + \frac{K_l^2}{\alpha} (\theta - \theta_B)^2} \right]^\alpha + A_l \left[ \frac{1}{1 + \frac{K_l^2}{\alpha} (\theta - \theta_B + \delta\theta_l)^2} \right]^\alpha, & \theta \leq \theta_B \\ \left[ \frac{1}{1 + \frac{K_r^2}{\beta} (\theta - \theta_B)^2} \right]^\beta + A_r \left[ \frac{1}{1 + \frac{K_r^2}{\alpha} (\theta - \theta_B - \delta\theta_r)^2} \right]^\beta, & \theta > \theta_B \end{cases} \quad (3.7)$$

As mentioned in the previous sections, the improved X-ray yield and its small dimension on the sample as well as its narrow bandwidth result in high quality rocking curves with a dynamic range of almost  $10^4$ . This gives the opportunity to study even subtle transient changes of the rocking curves in a pump-probe experiment.

### 3-8 Normalization of measured signals

Since the X-ray photon flux diffracted off the samples is low (particularly in thin film samples), relatively long integration times are required to obtain a sufficient signal-to-noise ratio in a typical time-resolved X-ray diffraction experiment performed by laser-plasma based X-ray sources. Therefore, it takes several hours to complete an experiment and during this long time, the intensity of the incident X-rays on the sample changes.

This change of the X-ray incident intensity is explained in terms of long-term drifts (happens within minutes up to hours) and short-term fluctuations (occurs within seconds down to pulse-to-pulse fluctuations). The latter ones are mainly due to the driving laser intensity and pointing instabilities as well as the mechanical position instability of the moving target. Recalling that the emitted X-ray yield from the source depends strongly on the incident intensity of the laser on the target and the angle of incidence (see section 3-6), these instabilities lead to a fluctuation in the emitted X-ray yield. The long-term drifts can also happen due to the drifts of the laser intensity and pointing (particularly the angular drift) on the target, contamination of the X-ray chamber by target material debris, and the spatial shift

of the target [178]. On the other hand, the reflection efficiency of the X-ray optics are sensitive to the position of the source so the laser pointing and target position fluctuations/drifts result in an additional variation in the X-ray incident intensity [95]. Thus, to exclude the effect of temporal variations of the X-ray incident intensity from the measured signal it is necessary to employ a normalization procedure.

Depending on the sample under investigation and features of setups, different normalization schemes such as the so-called “un-pumped normalization”, “substrate normalization” and “direct normalization” methods have been introduced [179]. In some experiments [180] a divergent emitted X-ray beam (without any X-ray optics) is used in which the detected X-ray diffraction pattern contains excited and non-excited regions. The non-excited part is used as the normalization signal (un-pumped normalization). In experiments where samples are grown on suitable substrates, the X-ray diffraction patterns of the samples and substrates can be detected at the same time and the substrate signal is used for the normalization (substrate normalization)[178, 179]. However, these two methods are not always applicable. The latter case is sample-dependent and in the former case, since no X-ray optic is used, the X-ray fluence on the sample is low and it is not well monochromatic. The direct normalization scheme does not have the mentioned disadvantages. In this method, the X-ray flux of the source is monitored directly either using an additional detector [178, 181, 182] or the same detector used to detect the measured signal [179].

In the current setup, a direct normalization scheme has been realized in which a GaAs crystal is properly placed at the second output opening of the X-ray chamber (see figures 3.9 and 3.10) to observe the (111)-reflection by a large area (10 mm diameter) X-ray sensitive avalanche photodiode (APD) [183]. The APD combines the advantages of a photomultiplier (gain) and conventional Si photodiodes (high quantum efficiency). Moreover, it allows single-pulse readout at the system repetition rate of 10 Hz using a gated charge-integrating analog to digital converter (ADC) [184]. The APD/ADC signal is used to normalize measured rocking curves of the sample under investigation.

A simultaneous measurement of the APD/ADC signal and the diffracted signal from the non-excited sample detected by the X-ray CCD, while the laser energy is being reduced, can provide the calibration of the normalization signal. As an example, figure 3.27 illustrates the average diffracted X-ray photon flux over 560 pulses versus the APD/ADC signal (green circles) while the laser energy was being reduced. This measurement was performed for the (111)-reflection of both the Ge (180 nm) overlayer and Si (0.5 mm) substrate. Both graphs exhibit a very good linearity (red solid lines represent the linear fit on the data) between the diffracted signal from the sample recorded by the X-ray CCD and the APD/ADC signal.

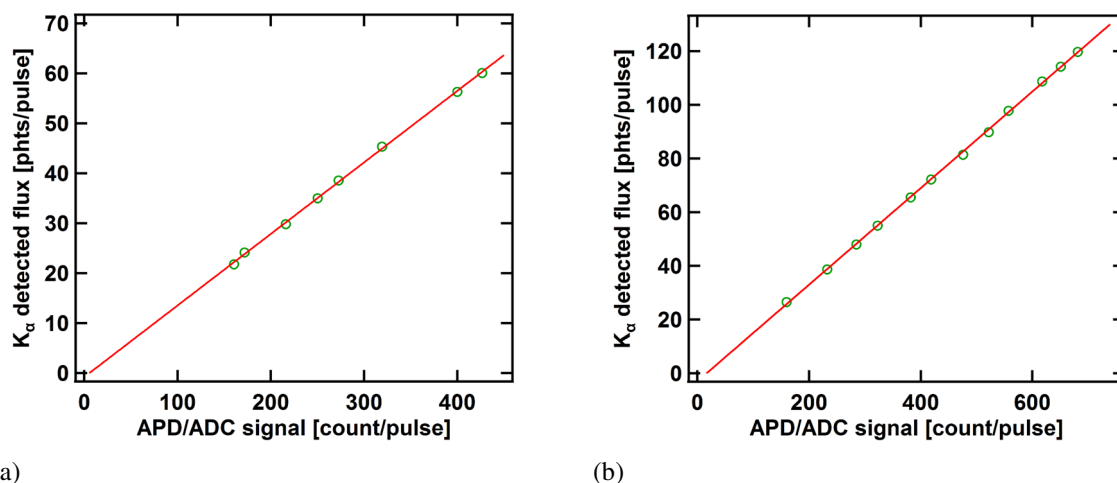


**Figure 3.27:** Detected  $K_{\alpha 1}$  diffracted photon flux from Ge (a) and Si (b) vs. APD/ADC signal (green circles) and a linear fit on the data (red solid lines). This measurement was performed for (111)-reflection of Ge and Si.

The stability of this normalization method was checked by measuring the APD/ADC signal (averaged over 560 pulses) and the integrated reflectivity of non-excited Ge and Si (separately) over a typical measurement time ( $\sim 5$  hours). The standard deviation of the normalized integrated reflectivities are 2% and 0.8% for Ge and Si, respectively.

### 3-9 Spatial and temporal overlap between the pump and probe

A very important aspect of any pump-probe experiment is establishing the spatial and temporal overlap between pump and probe. This is a challenging task when either the probe or the probe is “invisible” like here. Due to the significant improvement of the X-ray yield in the current setup, a simple method is applied to adjust the spatial overlap. A piece of Al foil covered by phosphor (type: Sylvania 2611 Lo + 60 Ax 28) is used to detect the incident X-ray position and then the pump beam is spatially overlapped. A typical X-ray spot detected on the phosphor screen is shown in figure 3.28-a. The focused X-rays are not the only radiation that the mirror reflects. It also reflects the visible radiation from the plasma as well as a part of laser radiation scattered from the wire. Due to the very small mismatch in the orientations between the geometrical surface of the toroidally bent mirror and the lattice planes, the reflected X-rays and visible light do not spatially overlap.

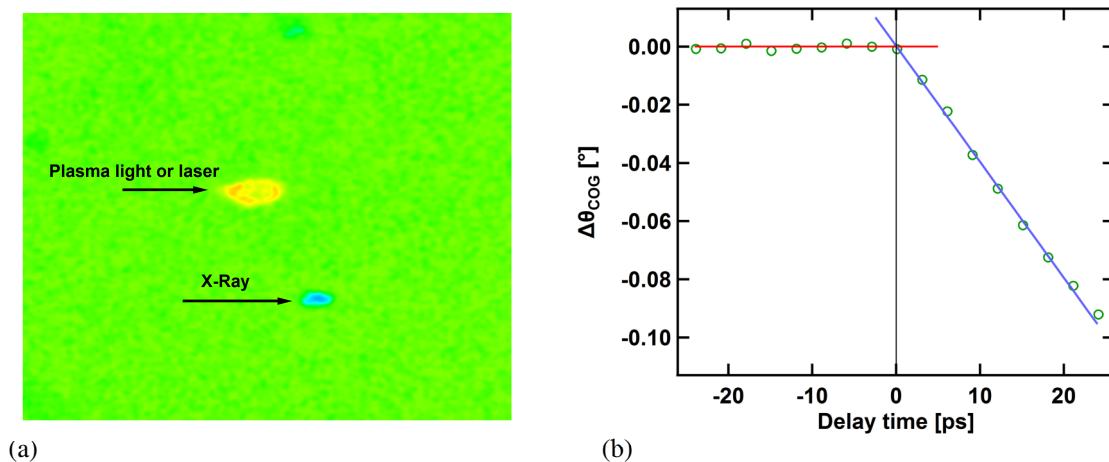


**Figure 3.28:** Image of the phosphor screen taken by a normal CCD with an exposure time of 20 s (a). Transient angular shift of the center of gravity of the measured Ge(111) rocking curves (green circles) with two linear fits to the data in negative delay times (red solid line) and positive delay times (blue solid line). The intersection of these two lines determines time zero (b).

In order to find time zero and adjusting the optical pump delay line (with an appropriate time window covering negative and positive delay times), one can use the transient shift in the angular center of gravity of the diffracted rocking curves when the sample (e.g. Ge(111)) is pumped (see chapter 4 for more details). Therefore, the phosphor screen is replaced by the sample and the delay line is varied until a detectable shift in the center of gravity can be obtained. Then the spatial overlap between the pump and X-ray beams is further optimized by slightly moving the pump beam over the sample surface to find the maximum shift corresponding to the optimum spatial overlap. Afterwards, for every delay between the optical pump and X-ray probe, the X-ray diffraction pattern is captured by the X-ray CCD over 560 pulses and its center of gravity is calculated. The transient angular shift in the center of gravity of the measured Ge(111) rocking curves (figure 3.28-b) is used to find time zero. The intersection of the two lines fitted to a few data points at negative (red line) and positive (blue line) delay times determines time zero. The accuracy in the determination of time zero using this method is  $\pm 0.3$  ps. Since the electronic part of the photo-induced stress, which has a considerable effect in the lattice deformation of Ge (see chapter 4), is established simultaneously with the optical excitation, one can say that the determined time zero according to this method represents almost real time zero.

### **3-10 Summary and outlook**

This chapter discussed the details of a new setup for time-resolved X-ray diffraction experiments based on a modular scheme. Due to the modularity of the setup, adjustments and operation of the different equipment are more precise and convenient. Employing a pre-plasma leads to an improvement in the X-ray photon flux on the sample, which is of the order of  $10^6$  photons/s, almost an order of magnitude increase with respect to all previous setups used at the University of Duisburg-Essen. The improved X-ray yield, its small dimension on the sample and its narrow energy bandwidth result in high quality rocking curves. This gives the opportunity to study even subtle transient changes of the rocking curves in a pump-probe experiment (see next chapter). According to the setup configuration, it will be possible to study the lattice dynamics of samples at cryogenic temperatures by employing a cryostat. Furthermore, the practical time resolution of the pump-probe experiments can be improved by using the so-called laser pulse-front tilt technique [185]

## Chapter 4

### Picosecond acoustic response of a Ge-Si heterostructure

The transient acoustic response following the absorption of ultrashort laser pulses in different materials has been extensively studied for more than two decades with time-resolved optical reflectivity [117, 186, 187], electron diffraction [114, 115] and X-ray diffraction methods [26, 28, 39, 51]. Thomsen *et al.* [117] developed a 1-D phenomenological model based on the thermo-elastic and electronic (i.e. deformation potential) photo-induced stress terms. This model can qualitatively describe general characteristics of excited coherent acoustic phonons (CAP) by an ultrashort laser pulse. However, the experimental data presented in literature have been treated in different ways concerning the portion of each stress term. For instance, in some measurements on metals (Ni, Cr [188], Al [4], Cu [189], Ag [3] and Au [3, 190]) only the thermo-elastic stress has been taken into account. On the other hand, there are other reports that explain the CAP generation by assuming both thermo-elastic and electronic stress sources (Al [191], and Au [39]).

These discrepancies are not only limited to metals. The CAP generation in GaAs has been investigated by Rose-Petruck *et al.* [51], Cavalleri *et al.* [32] and Lee *et al.* [192]. The results were explained only by employing the thermo-elastic stress. On the other hand, Wright *et al.* [187] and Babilotte *et al.* [193] could describe their measured data (in GaAs) only by taking into account the electronic stress caused by the deformation potential (DP). In contrast, Young *et al.* [194] applied both the thermo-elastic and electronic DP stress sources to analyze the strain pulses.

InSb is another semiconductor for which the acoustic response has been studied experimentally in some detail. Like GaAs, experimental data have been interpreted in different ways. Some of the data were explained only by the thermo-elastic stress [25], while others by using both the thermo-elastic and electronic stress sources [28, 31, 195].

DeCamp *et al.* [36] detected transient strain waves in an ultrafast laser-excited Ge bulk crystal and analyzed their data using the electronic and thermo-elastic stress sources. In comparison, Chigarev *et al.* [196] studied coherent sub-nanosecond acoustic pulses generated in a Ge bulk crystal and justified the experimental data only using the electronic deformation potential stress source. Cavalleri *et al.* [27, 32] expounded the acoustic wave generation in a Ge thick film (400 nm) by using only the thermo-elastic stress. Shymanovitch *et al.* [160] investigated ultrafast atomic motion of a Ge thin film (150 nm) excited

by ultrafast laser pulses using time-resolved X-ray diffraction. They used both the thermo-elastic and electronic stress sources as a time-dependent photo-induced stress to describe the experimental data.

In this chapter, the picosecond acoustic response of a Ge(111)-Si(111) heterostructure due to the optical excitation of the Ge film is discussed. The new improved X-ray source gave the opportunity to provide not only information about the lattice dynamics in the Ge film, but also in the Si substrate. A time-dependent photo-induced stress, including both the thermo-elastic and electronic sources, was employed to model the temporal behavior of the Ge and Si lattices. The experiments revealed that the recombination dynamics of the excited electron-hole plasma does not only contribute to the electronic stress, but also affects the thermo-elastic stress due to the secondary lattice heating (delayed Auger-heating [197]). In addition, some other ambiguities with respect to the fluence dependence of the acoustic response [160] were resolved.

In section 4-1, a brief description and some numerical estimations of the carrier excitation and relaxation processes in the Ge film and consequently the photo-induced stress are given. In section 4-2, the experimental time-resolved optical-pump - X-ray-probe conditions are presented. Section 4-3, discusses the measured transient rocking curves of the Ge film and the Si substrate. These experimental results are compared with simulations of the acoustic response based on the time-dependent photo-induced stress model from section 4-4 and finally section 4-5 draws a summary.

## **4-1 Relevant mechanisms for photo-induced stress generation in Ge**

An ultrashort laser pulse excites the electronic subsystem of Ge and due to the electron-phonon coupling within a time scale of approximately 1 ps [160], the energy is transferred to the lattice. This and the electronic excitation itself lead to a rapid build-up of stress and the subsequent excitation of coherent acoustic phonons. The carrier dynamics play an important role in the photo-induced lattice deformation. In subsection 4-1-1, the physical mechanisms of the electronic excitation, relaxation and some numerical estimations for the time scales of these events will be presented. Subsequently, subsection 4-1-2 deals with the photo-induced stress in Ge.

### **4-1-1 Carrier excitation and relaxation mechanisms in Ge**

Germanium belongs to the IV<sup>th</sup> group of the periodic table and crystalizes in the diamond lattice structure like Carbon and Silicon. It is a semiconductor with an indirect band gap  $E_g = 0.66$  eV at room temperature [198], which is the energy difference between the minimum of the conduction band at the L-point in the Brillouin zone and the top of the valence band at the  $\Gamma$ -point. Its calculated energy band and crystal structures are depicted in figure 4.1 [199].

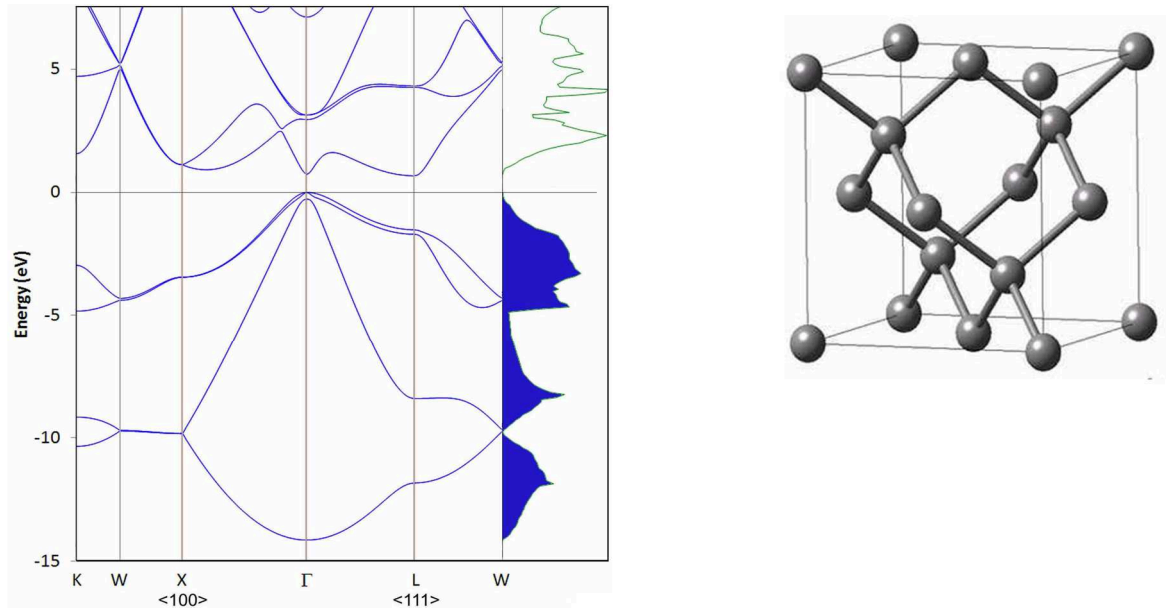


**Figure 4.1:** Energy band structure and density of states of Ge (left). The Ge diamond lattice structure (right)

An absorbed photon (in the visible and NIR spectral range) promotes an electron from the valence band to the conduction band provided that the conservation of energy and momentum are fulfilled. The momentum of photons is very small in comparison with the typical crystal momentum of electrons and holes, therefore the optical absorption can be assumed as a vertical line transition in the E-k diagram. The minimum energy band gap at the  $\Gamma$ -point for Ge is  $E_{\Gamma 1} = 0.8$  eV [198], so with photon energy of  $h\nu = 1.55 - 1.58$  eV the electrons are dominantly excited in the  $\Gamma$ -valley, while the holes are generated close to the  $\Gamma$ -point. For the mentioned photon energy and excitation fluences in the range of few tens of  $\text{mJ}/\text{cm}^2$ , non-linear absorption is negligible, since the effective linear absorption coefficient for two-photon absorption mechanism is approximately three order of magnitude less than the one for linear absorption [200]. Since the energy of phonons is much smaller compared to the energy of photons, the amount of energy transferred to the lattice during absorption is negligible compared to the total amount of absorbed energy. Therefore, ultrashort optical excitation of Ge creates highly non-equilibrium states of the electronic subsystem. A complex sequence of scattering and relaxation processes occur to bring back the irradiated Ge thin film to a new equilibrium as schematically illustrated in figure 4.2. One can summarize them as follows: Carrier-carrier scattering, carrier-phonon scattering and carrier recombination (the blue arrow).

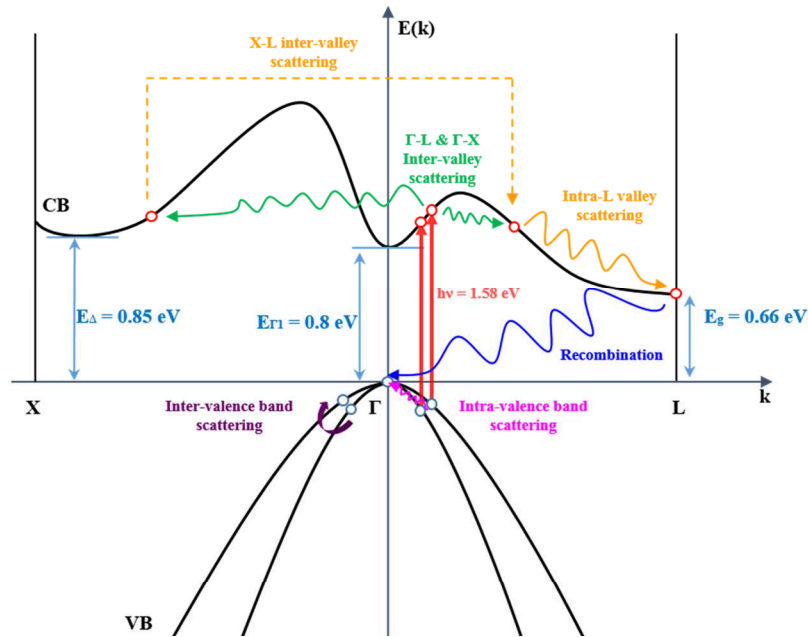


**Figure 4.2:** Schematic view of the carrier excitation and relaxation processes in Ge. The red arrows represent the linear inter-band optical excitation, the green and dashed orange arrows depict the electron inter-valley scattering, the orange and pink arrows show the intra-valley and intra-valence band scattering for electrons and holes, respectively, the purple arrow indicates the inter-valence band scattering of holes and the blue arrow depicts the inter-band relaxation processes (recombination).

Collisions between the carriers do not change their density. However, they ensure that the distribution of the electrons and holes will be quasi-Fermi like with a common temperature. Carrier-phonon scattering in Ge includes phonon-assisted inter- and intra-valley scattering of electrons and intra- and inter-valence band scattering of holes [201, 202]. These scattering processes do not change the carrier density, but result in energy transfer from the carriers to the lattice, i.e. carrier cooling and lattice heating. The electron inter-valley scattering process also provides a quasi-Fermi level between the electrons in the different conduction band valleys, which is essentially different from the quasi-Fermi level of the holes. In general, carrier recombination can be radiative and non-radiative. The radiative recombination process itself may be direct or indirect. If an electron in the  $\Gamma$ -valley of the conduction band recombines with a hole in the valence band by means of emission of a photon, it will be direct radiative recombination. An electron also in the L- or X-valley can recombine with a hole in the valence band by means of simultaneous emission of a photon and emission or absorption of a phonon. This event is called indirect radiative recombination. Non-radiative recombination includes surface recombination, defect recombination and Auger recombination [203]. Carrier recombination together with carrier diffusion change the local density of the carriers. These processes will be discussed later in more detail.

The time scale for carrier-carrier and electron inter-valley scattering is approximately  $\sim 100$  fs at low excitation levels (carrier density  $< 10^{19}$  cm $^{-3}$ ) [202], which means that within a few hundred femtoseconds the carriers have a quasi-Fermi like distribution with a common temperature ( $T_e = T_h$ ) and different quasi-Fermi levels for the electrons and holes. However, it is usually assumed that at higher excitation levels - resulting in a carrier density of  $\sim 10^{20}$  -  $10^{21}$  cm $^{-3}$  - these processes get faster [204]. It should be emphasized that within this time scale the amount of transferred energy from the carriers to the lattice is negligible. This can be realized by the fact that carrier-phonon collisions are almost elastic and, thus, the energy relaxation time scale is much larger than the momentum relaxation one. Carrier cooling (lattice heating) takes place on a time scale of a picosecond. Shymanovich *et al.* [160] measured the lattice heating process in a 150 nm thick Ge thin film by means of time-resolved X-ray diffraction (TRXD) for several different Bragg reflections and excitation fluences. They showed that the TRXD could be used for a direct measurement of lattice heating during the carrier-lattice energy transfer. According to the Debye-Waller effect [134], the integrated Bragg diffraction signal represents the random motion of the lattice. They obtained an electron-lattice relaxation time of 1.1 ps for Ge.

The recombination processes, which change the carrier density, occur on different time scales. The radiative recombination events happen on time scales larger than a nanosecond [203, 205]. The non-radiative recombination processes due to defects and surface recombination take place within time scales of  $\mu$ s [205, 206]. Since the experiments here were performed within the time range  $< 300$  ps, these recombination processes are not important. The remaining mechanisms, which change the local density of the carriers, are carrier diffusion and Auger recombination. In the following, these two mechanisms will be discussed in detail.

In compliance with the Lambert-Beer's law, one can determine the excited carrier density right after the optical excitation (equation (4.1)). Since the laser pulse duration ( $\sim 100$  fs) is shorter than most of the relevant relaxation time scales, it is reasonable to assume the excitation as an instantaneous process.

$$\delta n(z, 0) = \frac{(1 - R)F}{E_{ph}\mu} \left( e^{-\frac{z}{\mu}} \right) \quad (4.1)$$

here  $\delta n$  is the excited carrier density,  $R$  is the reflectivity,  $F$  is the incident peak excitation fluence,  $E_{ph}$  is the photon energy and  $\mu$  is the absorption depth. For the given experimental conditions:  $R = 0.44$ ,  $\mu = 200$  nm [27],  $E_{ph} = 1.58$  eV and  $F = 11.7$  mJ/cm $^2$ , the excited carrier density over a distance equal to the absorption depth varies from  $1.3 \times 10^{21}$  to  $4.8 \times 10^{20}$  cm $^{-3}$ . At such a high carrier density, ambipolar diffusion is significantly fast due to the large density-dependent diffusion coefficient [207]. Figure 4.3 shows the time evolution of the carrier density in a 180 nm thick Ge thin film under the above mentioned

excitation conditions obtained by a numerical solution of the diffusion equation. To simplify the calculation an average diffusion coefficient of  $D_{e,h} \sim 250 \text{ cm}^2/\text{s}$  was assumed [207].

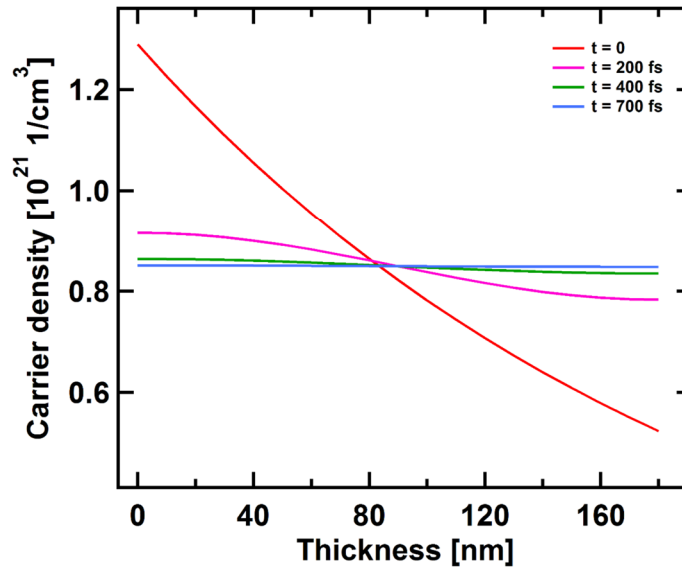


**Figure 4.3:** Carrier density in a 180 nm thick Ge thin film at different times after excitation by a 100 fs pulse with a fluence of  $11.7 \text{ mJ}/\text{cm}^2$ . The employed diffusion coefficient is  $250 \text{ cm}^2/\text{s}$ . The carrier density after few hundred femtoseconds is homogenous over the film thickness.

Due to the large diffusion coefficient, after a few hundred femtoseconds, the excited carriers are almost homogeneously distributed over the film thickness ( $d_{\text{Ge}}$ ) and can be expressed by the average carrier density given by equation (4.2).

$$\delta n(0) = \frac{(1 - R)F}{E_{\text{ph}}d} \left( 1 - e^{-\frac{d_{\text{Ge}}}{\mu}} \right) \quad (4.2)$$

The estimated value for  $\delta n(0)$  given by this equation for the mentioned experimental conditions is around  $8.5 \times 10^{20} \text{ cm}^{-3}$ .

Non-radiative Auger recombination is the main recombination mechanism at high carrier densities in Ge. The basis of the Auger effect is the Coulomb interaction between the carriers, by which the excess energy due to the electron-hole recombination is transferred to an electron in the conduction band (e-e-h process) or to a hole in the valence band (e-h-h process) [208]. Figure 4.4 shows the Auger recombination mechanism in a non-reduced zone representation in the [111] direction for Ge. One electron in the bottom or near the bottom of the L-valley in the conduction band can recombine with one hole near the top of the valence band (blue arrow in figure 4.4). According to the energy and momentum

conservation, another electron in the same valley can be promoted to a new level in the  $\Gamma$ -valley (green arrow in figure 4.4). This process is called “direct e-e-h Auger” recombination. In the case of an e-h-h process, by recombination of the L-valley electron with the  $\Gamma$ -valley hole another hole makes a transition (pink arrow in figure 4.4).

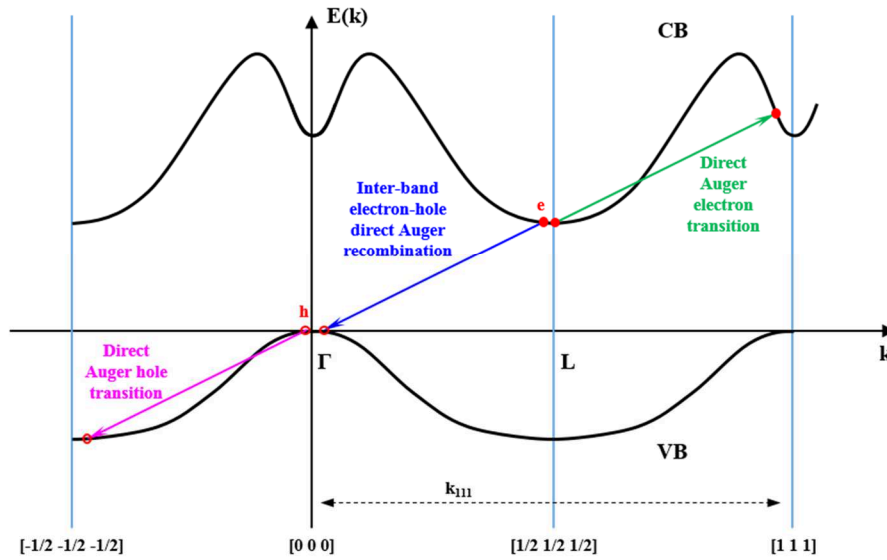


**Figure 4.4:** Direct Auger processes in an indirect band gap Ge. In the e-e-h process the electron in the L-valley recombines with the hole in the valence band (blue) and a second electron is excited to a new level in the  $\Gamma$ -valley (green). In the e-h-h event the excess energy of electron and hole recombination is delivered to a second hole (pink).

In addition to the direct Auger recombination process mentioned above, Auger recombination can happen indirectly. This process is a phonon-assisted process to sustain the momentum conservation [209]. Recently, Dominici *et al.* [210] calculated the rate of the various Auger processes for different carrier densities in Ge. Their results showed that the direct e-e-h and e-h-h processes are much stronger compared to the indirect ones. Assuming intrinsic Ge ( $n_e = n_h = n$ ), the Auger relaxation rate is given by the following equation

$$\left(\frac{\partial n}{\partial t}\right)_{\text{Auger}} = -Cn^3 \quad (4.3)$$

where  $n$  is the carrier density and  $C$  is the Auger constant.

At a sufficiently high carrier density ( $\sim 10^{21}\text{cm}^{-3}$ ), screening of the Coulomb interaction between carriers leads to a modification of the Auger rate equation [208, 211, 212]

$$\left(\frac{\partial n}{\partial t}\right)_{\text{Auger}} = -C'(n)n^3$$

$$C'(n) = \frac{C}{\left[1 + \frac{n}{n_{\text{c-non-deg}}}\right]^2} \quad \text{non-degenerate} \quad (4.4)$$

or

$$C'(n) = \frac{C}{\left[1 + \sqrt{\frac{n}{n_{\text{c-deg}}}}\right]^2} \quad \text{degenerate}$$

where  $C$  is the Auger constant,  $n_{\text{c-non-deg}}$ ,  $n_{\text{c-deg}}$  are the critical carrier densities for the non-degenerate and degenerate electron-hole plasma, respectively, at which the screening would be important. In literature, to the best knowledge of the author, there is a significant discrepancy with respect to the values of the Auger constant and critical densities [198, 205, 213-216]. However, to give a rough estimate of the time dependence of the carrier density, equation (4.4) has been solved numerically by using the Auger constant  $C = 1.1 \times 10^{-31} \text{ cm}^6/\text{s}$  [217]. The results are shown in figure 4.5 for both the degenerate and non-degenerate cases.

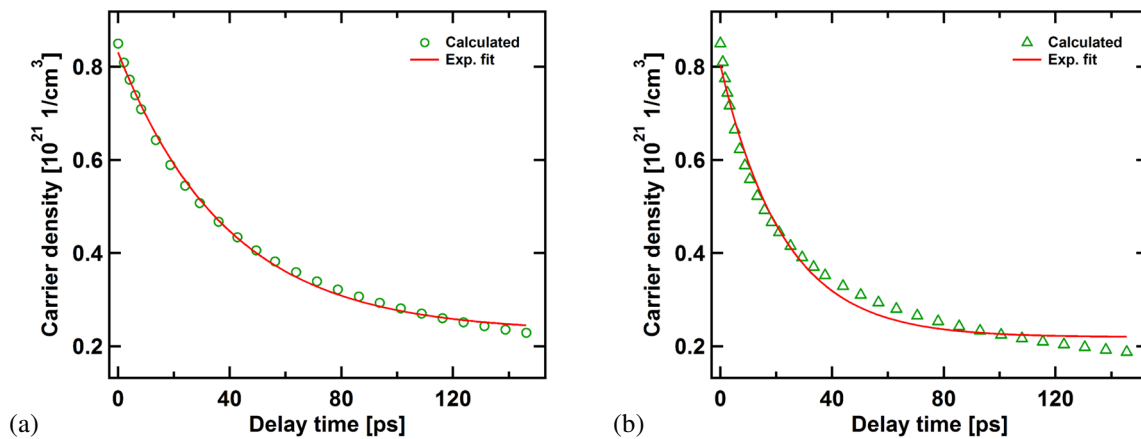


**Figure 4.5:** Temporal variation of the carrier density due to Auger recombination in the non-degenerate (a) and degenerate (b) cases. The solid red lines represent the exponential fits to the calculated (green circles and triangles) data.

In the above calculations, it has been considered that before recombination becomes important the carriers have been relaxed to the edges of the conduction and valance bands. Furthermore, due to fast carrier diffusion, the initial carrier density was assumed homogenously distributed over the film thickness with a value of  $8.5 \times 10^{20} \text{ cm}^{-3}$  corresponding to a fluence of  $11.7 \text{ mJ/cm}^2$  (see equation (4.2)). The critical carrier densities were roughly estimated as  $1.1 \times 10^{21} \text{ cm}^{-3}$  and  $4 \times 10^{22} \text{ cm}^{-3}$  for the non-degenerate and degenerate cases, respectively [208, 211, 212]. As is clear from equation (4.4), the Auger decay time depends on the momentary concentration of the excited carriers. However, to have an estimate of the average decay time for Auger recombination an exponential function with some time constant is fitted to the calculated data points (red solid lines in figure 4.5). The time constants of the exponential fits are almost 39 ps and 23 ps for the non-degenerate and degenerate cases, respectively. It is complicated to determine whether the system is non-degenerate or degenerate. This is because it depends on the carrier temperature, density and the quasi-Fermi levels of electrons and holes, which are all time-dependent quantities. Nevertheless, one can say that since the carrier temperature is high in the very beginning, the system is initially non-degenerate and after the energy transfer from the carriers to the lattice it may be degenerate. Finally, due to the change of the excited carrier density and the consequent change of the quasi-Fermi levels, it should be again non-degenerate. It has to be noted that the calculations just give a rough estimate of the temporal behavior of the excited carriers and the range of their average decay time, which is in the range of several tens of picoseconds.

Another important aspect of Auger recombination is a secondary lattice heating known as delayed Auger heating [197]. The second excited electron to the higher energy level in the conduction band relaxes again to the lower levels due to the electron-phonon interaction and consequently the lattice is heated up. This holds for the holes as well. Since the time scale for the carrier-phonon relaxation (1.1 ps) is much shorter than the average Auger decay time, one can assume that the lattice is heated up with a time constant equal to the average Auger decay time.

## 4-1-2 Photo-induced stress in Ge

In chapter 2, the microscopic mechanisms of the photo-induced stress in solids were presented. The situation is treated a bit differently for semiconductors compared to metals, although the origin of the photo-induced stress is identical. Since Ge is a centrosymmetric crystal, the photo-induced stress consists only of the thermo-elastic stress and the stress corresponding to the electronic system due to the deformation potential mechanism [90]. In this case, the photo-induced stress given in equations (2.15) and (2.16) still holds as a general formulation [117]

$$\begin{aligned}
 \sigma &= \sigma_{\text{TE}} + \sigma_{\text{DP}} \\
 \sigma_{\text{TE}} &= \sum_{\mathbf{k}} \delta n_{\text{p}}(\mathbf{k}) \frac{\partial \hbar \omega_{\mathbf{k}}}{\partial \eta} \\
 \sigma_{\text{DP}} &= \sum_{\mathbf{k}} \delta n_{\text{e}}(\mathbf{k}) \frac{\partial E_{\mathbf{k}}}{\partial \eta}
 \end{aligned} \tag{4.5}$$

where  $E_{\mathbf{k}}$  and  $\omega_{\mathbf{k}}$  are the energy of an electron and the frequency of a phonon mode at the wave vector  $\mathbf{k}$ , respectively.  $\delta n_{\text{e}}(\mathbf{k})$  and  $\delta n_{\text{p}}(\mathbf{k})$  are the change of the electronic and phononic occupation at the level  $\mathbf{k}$ , respectively.  $\eta$  represents the level of strain and  $\partial E_{\mathbf{k}}/\partial \eta$  is the deformation potential parameter.

While fast ambipolar carrier diffusion ensures that the spatial dependence of the excited carrier density and stress can be neglected, the photo-induced stress is time-dependent. The time scale for the carriers excitation and relaxation towards the band edges and the lattice heating caused by the laser pulse is too short ( $\sim 1.1$  ps) to allow for any significant deformation of the Ge film. Thus, the generated stress following femtosecond excitation can be assumed quasi-isochoric (step function like). By passing time, Auger recombination plays an important role in both the electronic (DP) and thermo-elastic (TE) stress sources, i.e. changing the carrier density and heating up the lattice on a time scale comparable to the so-called ‘‘acoustic response time scale’’ ( $d_{\text{Ge}}/V_{\text{s-Ge}}$ , where  $d_{\text{Ge}}$  is the Ge film thickness and  $V_{\text{s-Ge}}$  is the Ge sound velocity along the sample normal) [90]. Cooling the Ge film caused by heat conduction to surrounding atmosphere and into the Si substrate is not important within the time range studied in the experiments here ( $< 300$  ps). The cooling time constant is around 2.5 ns [160].

Under certain conditions, equation (4.5) can be simplified. For example, in the limiting case that the excited carriers relax to the band edges or close to the band edges,  $\sigma_{\text{DP}}$  is related to the band gap energy  $E_{\text{g}}$ . On the other hand, for each absorbed photon of energy  $E$ , phonons of total energy  $(E - E_{\text{g}})$  and for each excited carrier due to the Auger recombination process, phonons of total energy  $E_{\text{g}}$  are generated. Assuming that the carriers and phonons can be described by means of thermal distributions, equation (4.5) can be written as [90, 117]

$$\begin{aligned}
 \sigma_{\text{TE-laser}} &= -\frac{3B\beta}{C}(E - E_{\text{g}})\delta n_0 \\
 \sigma_{\text{TE-Auger}} &= -\frac{3B\beta}{C}E_{\text{g}}(\delta n_0 - \delta n(t)) \\
 \sigma_{\text{DP}} &= -B\frac{dE_{\text{g}}}{dP}\delta n(t)
 \end{aligned} \tag{4.6}$$

$$\sigma = -\frac{3B\beta}{C}E\delta n_0 - \left(B\frac{dE_g}{dP} - \frac{3B\beta}{C}E_g\right)\delta n(t) \quad (4.7)$$

where  $B$  is the bulk modulus,  $\beta$  the linear thermal expansion coefficient,  $C$  the specific heat,  $P$  the pressure and  $\delta n_0$  is the initial excited carrier density given by equation (4.2).  $\delta n(t)$  is the momentary concentration of carriers and  $B(dE_g/dP)$  provides the so-called “*electron-hole-phonon deformation potential parameter*” [90].

Equation (4.7) suggests that the total photo-induced stress includes a constant part and a time-dependent part, the latter being governed by the density of the excited carriers at a given time. For the experimental conditions mentioned in the previous subsection, the initial ratio between the time-dependent and time-independent parts is

$$r = \frac{\left(\frac{dE_g}{dP} - \frac{3\beta E_g}{C}\right)}{\frac{3\beta E}{C}} = 2.75 \quad (4.8)$$

where  $dE_g/dP = 5.1 \times 10^{-3}$  eV/kbar [218],  $\beta = 6.5 \times 10^{-6}$  K<sup>-1</sup> [219],  $E = 1.58$  eV,  $E_g = 0.62$  eV [198],  $C = 1.9 \times 10^6$  Jm<sup>-3</sup>K<sup>-1</sup> [220] and  $B = 68 \times 10^9$  Pa [198]. This means that the time-dependent part has a significant effect in the lattice deformation of the Ge film. Moreover, the linear thermal expansion coefficient is usually positive. This means that the constant part represents a negative stress (positive pressure). However, the deformation potential parameters ( $\partial E_k/\partial \eta$ ), depending on the material and the electronic energy levels, can be positive or negative. In the limiting case mentioned above,  $B(dE_g/dP)$  is positive and equation (4.8) shows that their ratio is also positive. Therefore, one expects a negative total photo-induced stress and as a result an expansion in Ge.

To derive equations (4.6) - (4.8) it was assumed that not only the population of the electronic, but also of the phononic subsystem follow a thermal distribution, i.e. Fermi-Dirac and Bose-Einstein, respectively. While thermalization of the electronic subsystem is fast compared to the acoustic response time scale at the excitation levels considered in the experiments here, it has been recently reported that the phononic subsystem may exhibit a transient non-thermal distribution for a few tens to several hundreds of picoseconds before the thermal state is restored by phonon-phonon and electron-phonon scattering [221-223]. In principle, this means that to obtain the thermo-elastic stress, knowledge of the time- and momentum-dependent phonon distribution (see equation (4.5)) is necessary. However, since

these data are not available for the experiments performed in this thesis, a thermal phonon distribution has been assumed as an approximation.

## 4-2 Pump-probe experimental conditions

In the experiment described here, the acoustic response of a Ge-Si heterostructure has been studied. The Ge film with (111) surface orientation and a nominal thickness of  $170 \pm 17$  nm was grown on a large Si(111) wafer with a thickness of 0.5 mm. It will be shown later that from the experimental data a film thickness of  $\sim 180$  nm was estimated (see section 4.4). In order to obtain highly perfect crystal layers (rms surface roughness 0.3 nm, density of threading dislocations  $< 10^8$  1/cm<sup>3</sup> [76]) a third species (Sb) has been used as surfactant during the thin film growing procedure. This surfactant-mediated heteroepitaxy provides low defect, fully relaxed epitaxial Ge films of arbitrary thicknesses on Si substrates [224].

Figure 4.6-a schematically illustrates the geometry of the optical-pump - X-ray-probe measurement. The surface of the Ge film was placed accurately in the focus of the convergent X-ray beam with the orientation given by the Bragg angle (either for Ge or for Si). The coplanar symmetric geometry was used for X-ray diffraction. In the coplanar geometry, the incident and diffracted X-ray wave vectors, the geometrical surface normal and the reciprocal lattice vector lie in a same plane (figure 4.6-b). If the geometrical surface normal and the reciprocal lattice vector are parallel, it will be called symmetric X-ray diffraction.

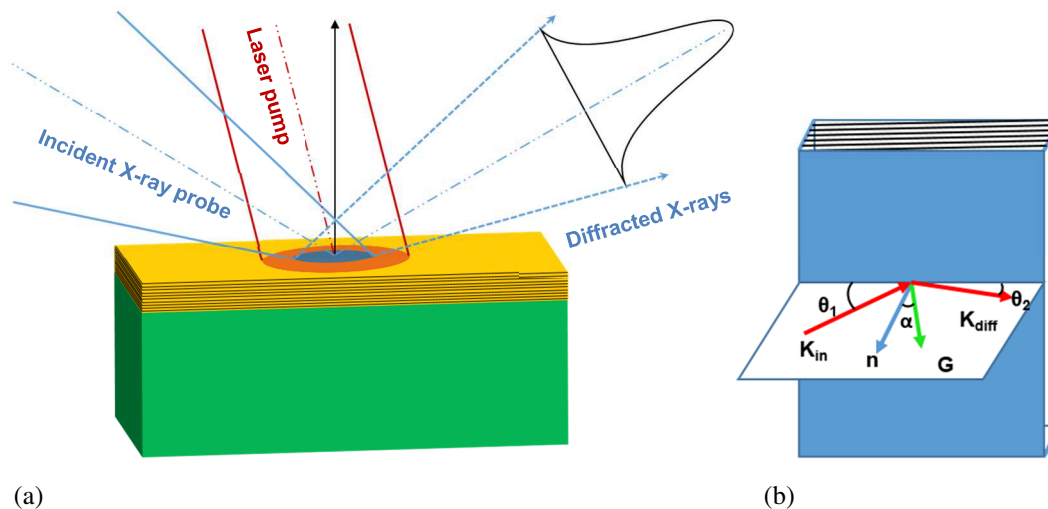


**Figure 4.6:** Schematic of the optical-pump - X-ray-probe measurement (a). The coplanar X-ray diffraction geometry (b) in which the incident X-ray wave vector  $\mathbf{K}_{in}$  and the diffracted one  $\mathbf{K}_{diff}$ , the geometrical surface normal  $\mathbf{n}$  and the reciprocal lattice vector  $\mathbf{G}$  corresponding to a particular atomic plane family are in a same plane. If the geometrical surface normal and the reciprocal lattice are parallel, the diffraction will be called symmetric.

Table 4.1 summarizes the experimental conditions used in the experiment.

Parameters	Optical pump	X-ray
Pulse duration	< 100 fs	
Photon energy	1.58 eV	4511 eV
Spot size on the sample	582×560 $\mu\text{m}^2$	196×80 $\mu\text{m}^2$
Repetition rate	10 Hz	10 Hz
Glancing angle	~ 75°	~ 24.89° & 25.99°
Polarization	S polarization	Unpolarized
Reflectivity	0.44	
Absorption depth	200 nm	
Incident fluence	~11.7; 15.6; 23.4 $\text{mJ}/\text{cm}^2$	~ $4 \times 10^8$ photon/pulse- $\text{cm}^2$
Sample	Germanium	Silicon
Thickness	180 nm	0.5 mm
Orientation	(111)	(111)
Bragg angle	24.89°	25.99 °
Surface roughness	0.3 nm (rms)	
Threading density	< $10^8 \text{ cm}^{-3}$	

**Table 4.1:** Experimental parameters of the pump-probe experiment

### 4-3 Detection of strain waves propagating in the Ge-Si heterostructure

This section deals with time-resolved X-ray diffraction measurements on the transient acoustic response of a Ge(111)-Si(111) heterostructure after femtosecond optical excitation. The photoexcitation occurs mainly in the Ge thin film ( $\alpha_{\text{abs}} = 5 \times 10^4 \text{ cm}^{-1}$ ). Silicon is a semiconductor with indirect band gap energy of 1.12 eV and direct band gap energies of 3.4 and 4.2 eV [198]. While the direct optical excitation ( $E = 1.58 \text{ eV}$ ) is forbidden, it can happen indirectly (phonon assisted) with an absorption coefficient of  $\alpha_{\text{abs}} = 1.1 \times 10^3 \text{ cm}^{-1}$  [225]. According to the above experimental conditions and Ref. [124], the absolute value of the photo-induced pressure inside Si near the interface is two order of magnitudes less than the one in Ge (see subsection 4-4). Therefore, it is reasonable to assume that the initial photo-induced pressure occurs only in the Ge thin film. The experiments were mainly motivated by earlier results from Shymanovich *et al.* [160] on a similar Ge-Si heterostructure, but with a thinner Ge film (~ 150 nm). They measured only transient rocking curves of the Ge film. Their measurements indicated a periodic expansion and recompression of the Ge film after the excitation. They also reported that at low excitation levels the time intervals for the expansion and recompression are identical, however, at higher

excitation levels the time interval for the recompression is almost twice the time interval for the expansion. Making full use of the much improved performance of the new modular setup (in particular higher X-ray flux and better signal-to-noise), the experiments discussed here go significantly beyond the previous work by measuring the response for different excitation levels not only in the Ge thin film, but also in the Si substrate. Thus, this study provides a more complete picture of the acoustic dynamics in this heterostructure.

### 4-3-1 Detection of strain waves propagating in the Ge thin film

Transient measurements of the Ge(111) rocking curves were made for incident laser fluences of  $\sim 11.7$ ,  $15.6$  and  $23.4$  mJ/cm<sup>2</sup>. Results are presented in figure 4.7 in 2-D false color plots. They show the normalized measured rocking curves at different delay times. A vertical cross section at a given time gives the rocking curve.

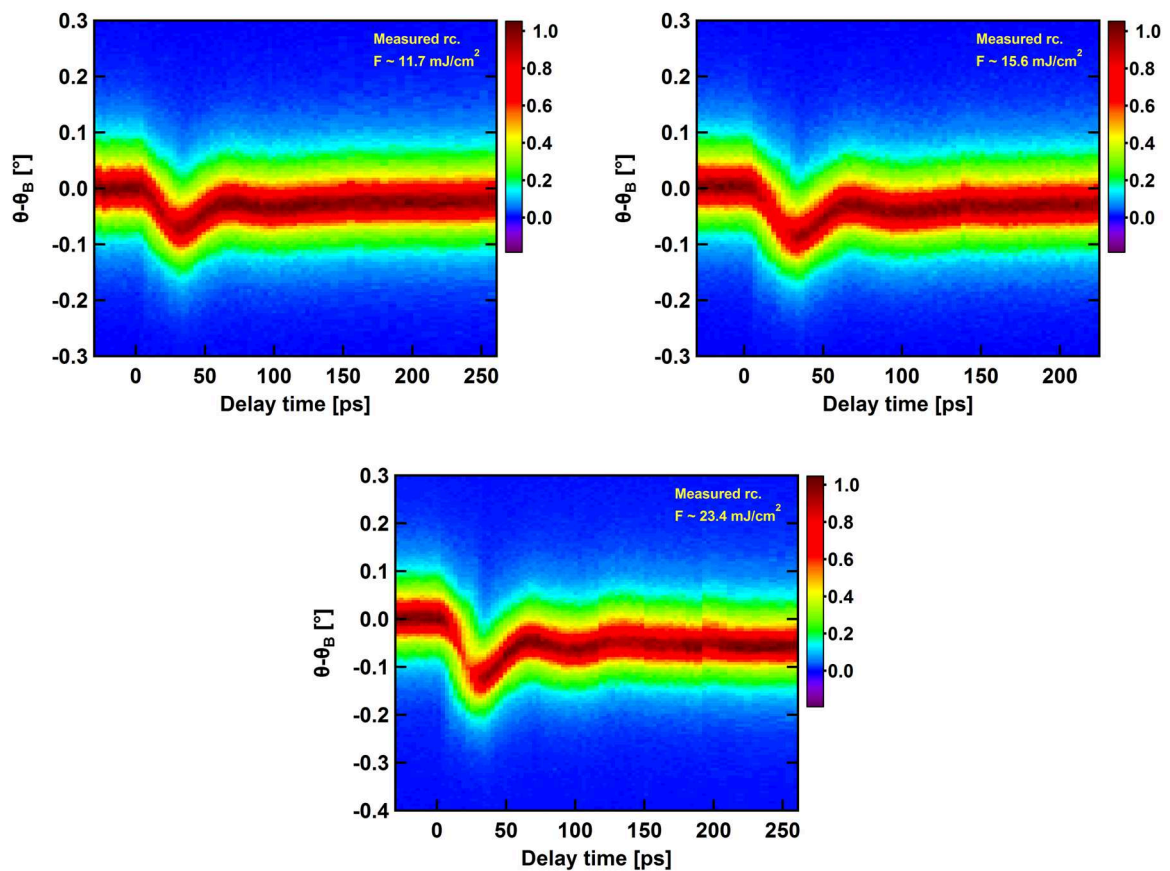


**Figure 4.7:** Measured time- and angle-resolved rocking curves of an optically excited Ge(111) thin film for different incident laser fluences.

An initial shift of the rocking curves to smaller angles is observed consistent with the fact that a negative stress results in a positive strain (as discussed in subsection 4-1-2). This means that the Ge film initially expands. The expansion is followed by a partial recompression, which leads to a shift of the rocking curves back towards larger angles. This expansion/recompression process occurs periodically for two cycles and, after that, the oscillation is terminated at long delay times. In addition, the rocking curves do not simply shift, but they become deformed. This deformation of the rocking curves over time implies that the lattice is inhomogeneously deformed (strained), particularly, within the time interval corresponding to the initial expansion.

In order to visualize the oscillatory behavior quantitatively, the shift of the angular center of gravity (COG) of the rocking curves was extracted from the measured data for each incident fluence. They are shown in figure 4.8. The shift of the COG is a measure of the average strain ( $\eta$ ) inside the excited thin film. By using the Bragg's diffraction law the following equation can be found

$$\begin{aligned}\Delta\theta_{\text{COG}} &= -\eta \times \tan \theta_B \\ \eta &= \frac{-\Delta\theta_{\text{COG}}}{0.46}\end{aligned}\tag{4.9}$$

In accordance with equation (4.9) and figure 4.8, the average strain attains its maximum values around  $(2.5 \pm 1) \times 10^{-3}$ ,  $(3.1 \pm 1) \times 10^{-3}$  and  $(4.3 \pm 1) \times 10^{-3}$  for incident pump fluences of  $\sim 11.7$ ,  $15.6$  and  $23.4$  mJ/cm<sup>2</sup>, respectively at a delay time of  $33 \pm 0.3$  ps. After this time, the average strain becomes smaller (i.e. recompression takes place) and reaches its minimum at a delay time of twice the expansion time. A secondary expansion and recompression cycle with smaller amplitudes follows the first one with the same periodicity. After a time  $\sim 200$  ps the level of strain is almost constant. While the strain level increases with increasing fluence, “no change in the periodicity of the oscillation is observed”. The red and pink solid lines (figure 4.8) mark the initial expansion and recompression times, respectively, and confirm that the time intervals for expansion and recompression are identical and fluence-independent. This clearly contradicts the results reported by Shymanovich *et al.* [160] at high excitation levels. Their results show that for a high excitation fluence corresponding to a COG shift of  $-0.12^\circ$ , the time for recompression is almost twice the time for initial expansion. However, at lower excitation levels corresponding to a COG shift of  $-0.06^\circ$  the expansion and recompression time constants are identical. No explanation for this unexpected behavior has been given by Shymanovich *et al.* Based on the findings of this study, it has, therefore, to be considered as an experimental error/artifact.

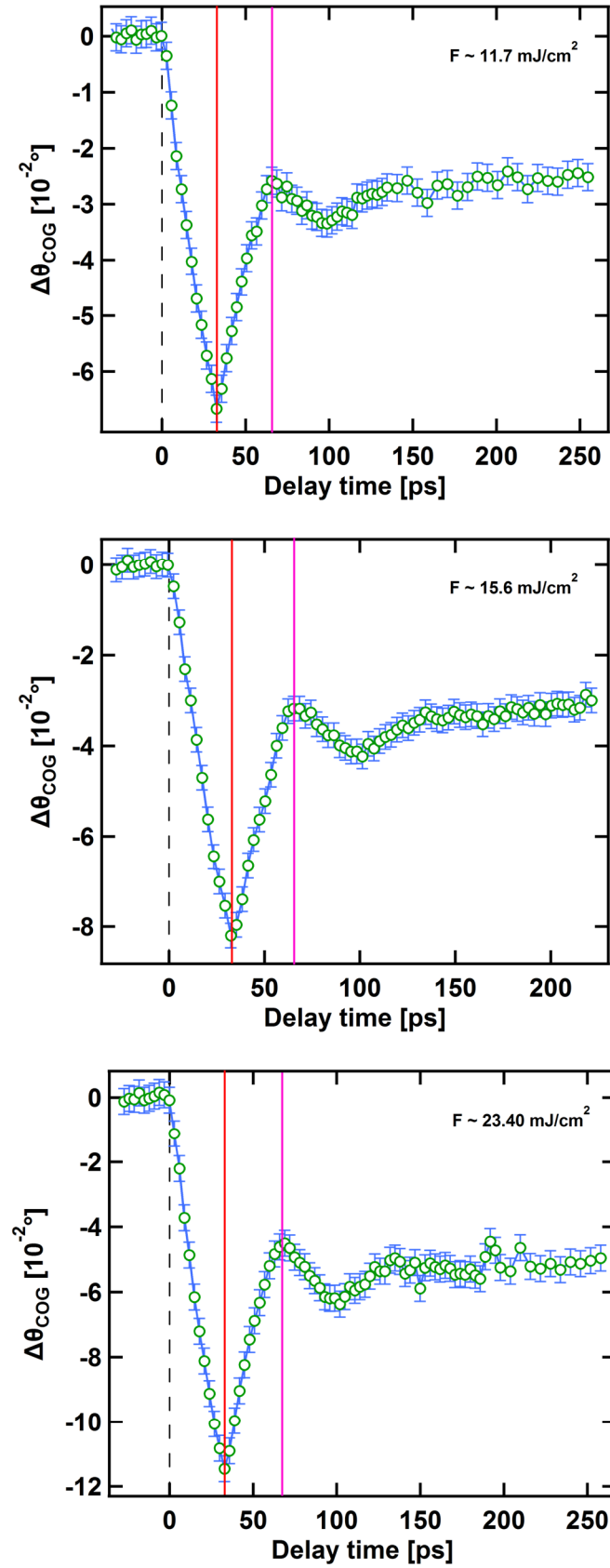


**Figure 4.8:** Transient shift of the center of gravity of the measured Ge(111) rocking curves for pump fluences of 11.7, 15.6 and 23.4  $\text{mJ/cm}^2$ , respectively. The red and pink solid lines refer to the maximum expansion and recompression times, respectively.

### 4-3-2 Detection of strain waves propagating in the Si substrate

In the previous subsection, the experimental data on the transient changes of the rocking curves of the Ge thin film upon laser excitation were presented. In general, one expects that some strain wave propagates into the substrate due to the strain generation in the Ge film and its transmission into the Si substrate. To monitor the response of the substrate, its rocking curves at several, selected, delay times were measured for the same mentioned experimental conditions. Figures 4.9 - 4.11 depict the experimental results on a logarithmic scale for a few number of selected delay times for excitation fluences of  $\sim 11.7$ ,  $15.6$  and  $23.4$   $\text{mJ}/\text{cm}^2$ , respectively (more rocking curves are provided in appendix B).

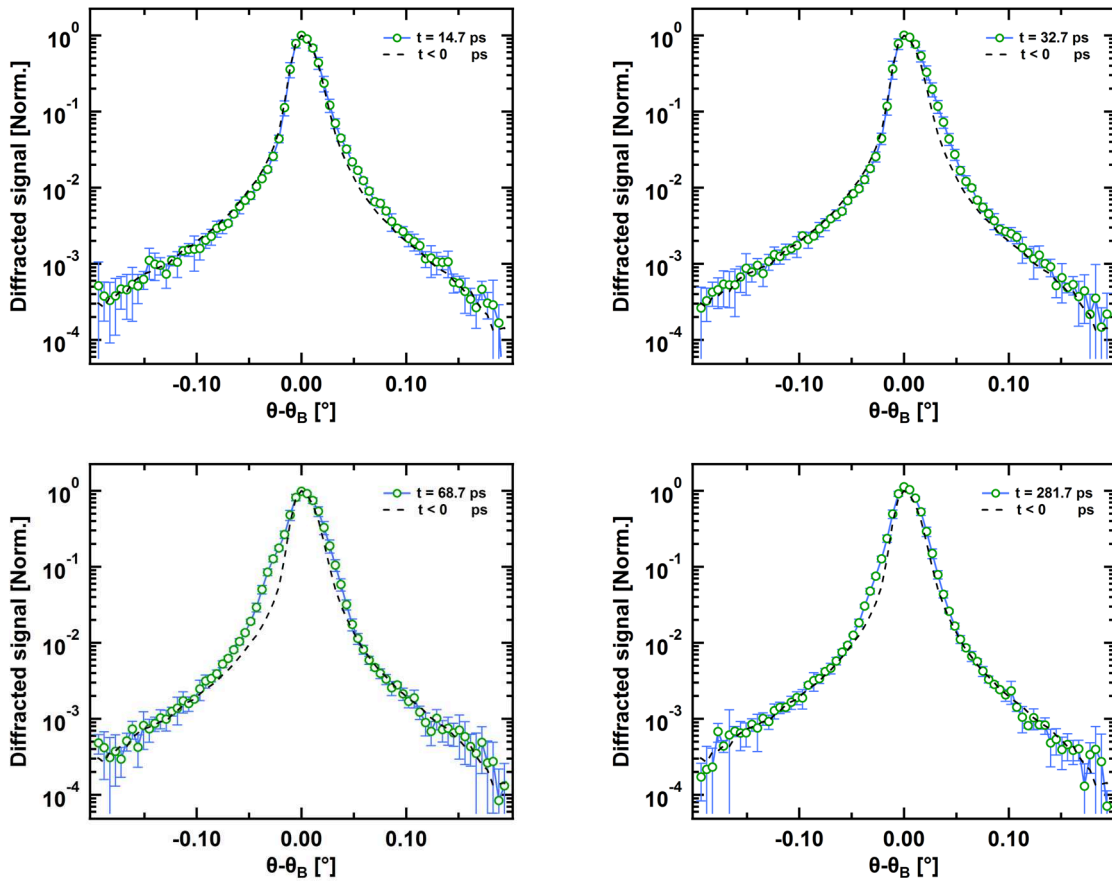


**Figure 4.9:** Measured transient rocking curves (logarithmic scale) of the Si substrate for an excitation fluence of  $11.7$   $\text{mJ}/\text{cm}^2$ . The black dashed lines show the rocking curves at a negative delay time (the X-ray probe arrives earlier).

In contrast to the time evolution of the Ge thin film rocking curve, the transient rocking curves of the bulk substrate are dominated by the largely unstrained part of the sample within the extinction depth. The strained parts produce only relatively weak satellites/wings. In this sense, in the time interval  $\Delta t \leq$

$33 \pm 0.3$  ps, only a weak satellite at higher angles ( $\theta > \theta_B$ ) is observed. This means within the time that the Ge film expands the Si substrate is partially compressed (i.e. negatively strained). After this time, an additional satellite at smaller angles ( $\theta < \theta_B$ ) can be recognized. The secondary satellite at smaller angles indicates that a positive strain starts to propagate into the Si substrate.

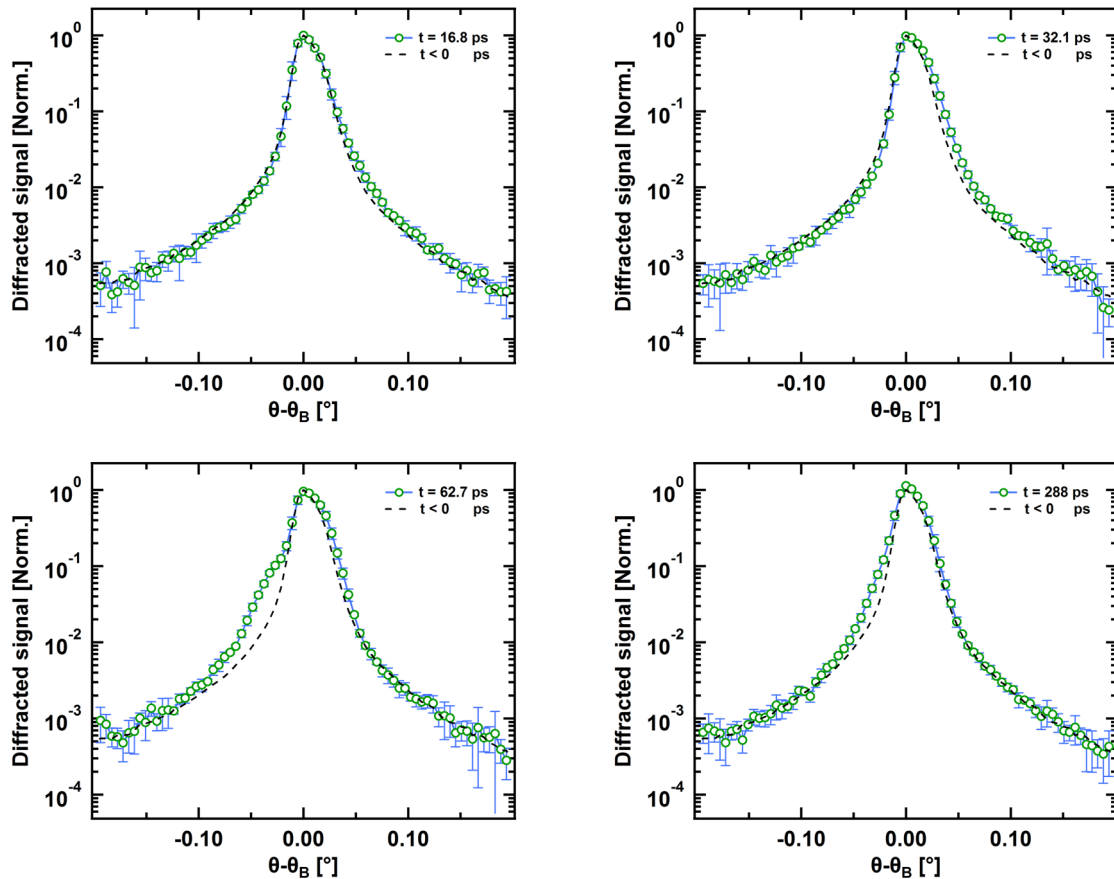


**Figure 4.10:** Measured transient rocking curves (logarithmic scale) of the Si substrate for an excitation fluence of  $15.6 \text{ mJ/cm}^2$ . The black dashed lines show the rocking curves at a negative delay time (the X-ray probe arrives earlier).

At long delay times, the transmitted strain waves will exceed the extinction depth (probing area) of the X-ray and, therefore, the measured rocking curves tend to the un-pumped rocking curve. A common important point that draws the attention is the asymmetry of the satellites at smaller and the higher angles.

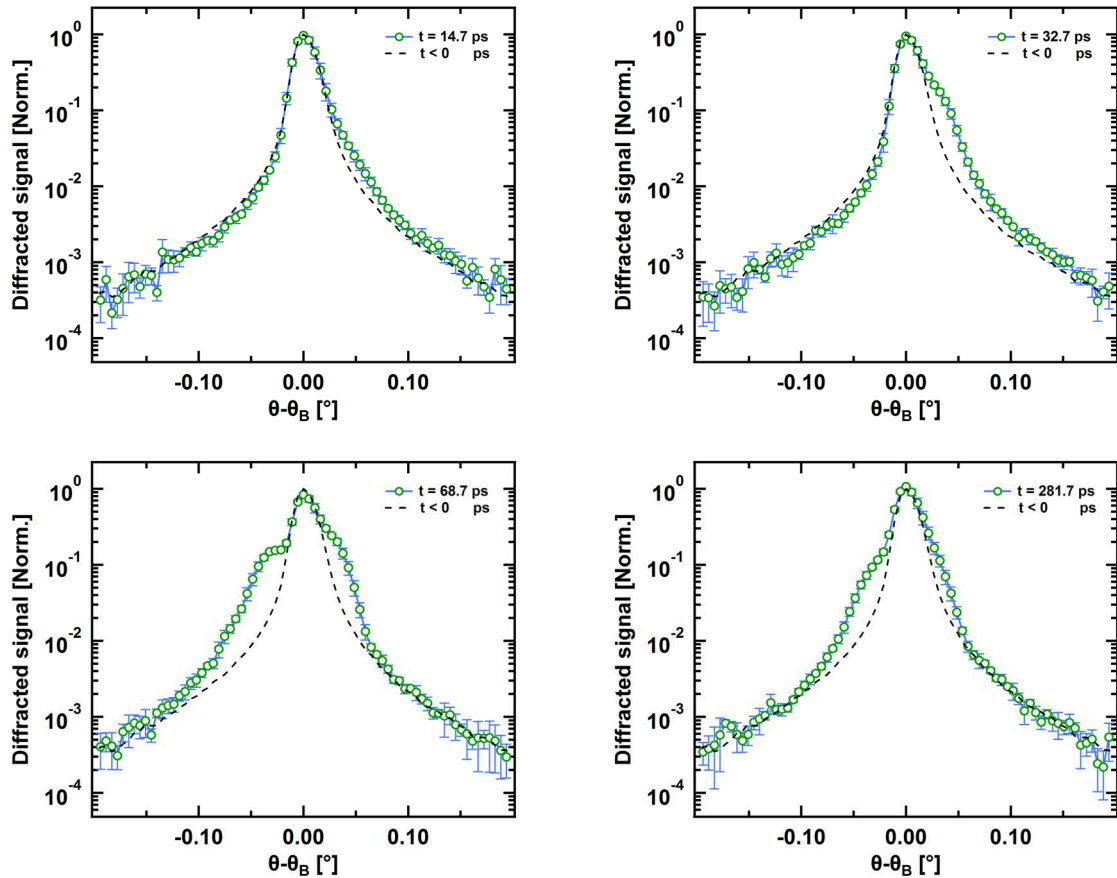


**Figure 4.11:** Measured transient rocking curves (logarithmic scale) of the Si substrate for an excitation fluence of  $23.4 \text{ mJ/cm}^2$ . The black dashed lines show the rocking curves at a negative delay time (the X-ray probe arrives earlier).

#### 4-4 Modeling of the acoustic response of the Ge-Si heterostructure

In order to obtain a better understanding of the observed transient changes of the rocking curves, a model was employed to describe the measured data. Shymanovich *et al.* [160] developed a model only for a single layer of a thin film based on a semi-analytical solution of the 1-D acoustic wave equation and a numerical calculation of X-ray diffraction according to the dynamical X-ray diffraction theory. Here, a similar model was implemented, which enables one to calculate the acoustic response not only in the excited film, but also in the substrate. This provides a description (including the rocking curves) for the complete heterostructure (film + substrate). Moreover, the accuracy and the speed of the calculations were significantly improved. The “Matlab” routine package utilized for the modeling is presented in detail in appendix C. The input of the routine is the quasi-isochoric photo-induced pressure (here in the Ge film). Inspired by equation (4.7) the pressure (negative of the stress) at  $t \geq 0$  comprises a constant term and a time-dependent term in the following form (see figure 4.12)

$$P(t) = \begin{cases} 0 & t < 0 \\ P_c \cdot \left(1 + r \cdot e^{-\frac{t}{\tau}}\right) & t \geq 0 \end{cases} \quad (4.10)$$

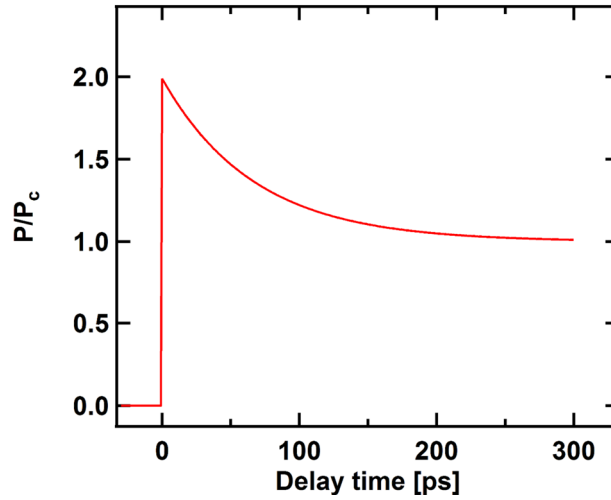


**Figure 4.12:** Typical temporal dependence of the photo-induced pressure in the Ge film used in the modeling with  $r = 0.93$  and  $\tau = 61$  ps.

where  $P_c$  is the amplitude of the constant pressure,  $r$  is the ratio between the constant and time-dependent terms at  $t = 0$  and  $\tau$  is the decay time constant. A single exponential function was assumed for the time-dependent part of the pressure ( $t \geq 0$ ). As discussed before (figure 4.5), this represents only an approximate description of the time dependent part of the pressure, but allows a one-parameter and thus straightforward quantification of its time dependence. As will become clear below, it allows a good description of the observed response of both the Ge film as well as the Si substrate. Since the excitation area was much bigger than the film thickness and due to the high quality of the Ge-Si heterostructure, a 1-D sound wave propagation along the surface normal is justified.

The wave equation solution strongly depends on the form of the photo-induced pressure. For example, under the assumption of a constant, time-independent pressure at  $t \geq 0$  (i.e.  $r = 0$  or  $\tau = \infty$ ) the strain waves have a simple rectangular shape, as illustrated in figure 4.13. In the Ge film, two positive strain waves (i.e. expansion) commence from the film boundaries and propagate with the sound velocity in the [111] direction ( $V_{s-Ge} = 5470$  m/s [see appendix A]) into the film. At time  $T = d_{Ge}/V_{s-Ge} \sim 33$  ps, these two initial waves have traveled the complete film thickness and the level of strain is maximum due to the superposition of the waves. The waves travel back and forth due to the reflection at the film boundaries.

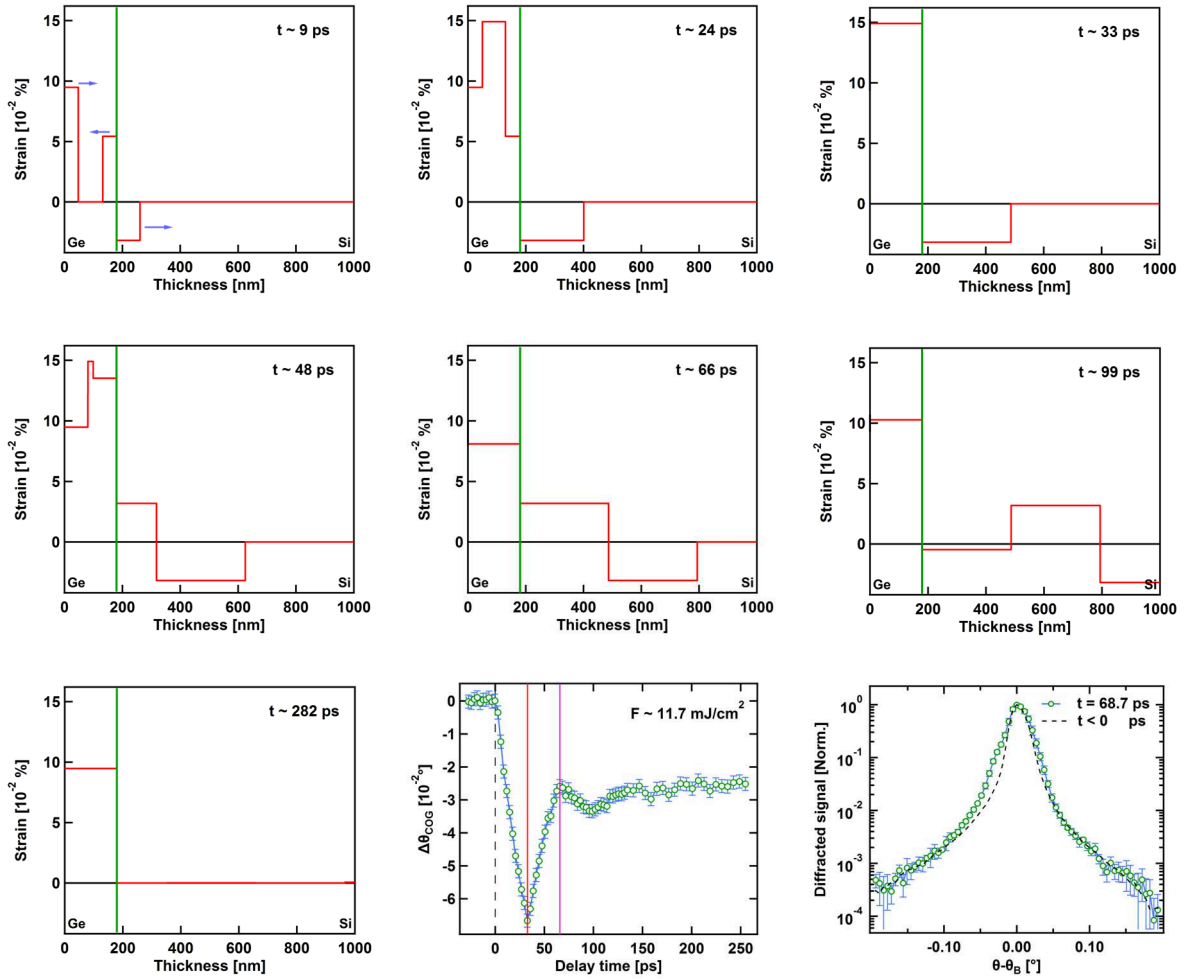


**Figure 4.13:** Transient strain wave profiles in the Ge-Si heterostructure at several selected delay times after the optical excitation. The photo-induced pressure is a step like function of time (constant pressure model). The constant pressure amplitude used in this calculation is  $P_c = 150$  MPa ( $F \sim 11.7$  mJ/cm<sup>2</sup>). The transient shift of the COG of the Ge rocking curves and the rocking curve of Si are also presented.

Since the reflection coefficients are negative ( $-1$  at the free surface and  $-0.15$  at the Ge-Si interface see equation (2.9)), the waves change sign at each reflection. In addition, because of partial transmission into the substrate the amplitude of the waves propagating back and forth in the Ge film decreases upon every reflection at the Ge-Si interface. This leads to a damped oscillatory behavior in the average strain with a period of  $2T$  and eventually at long times the level of strain will be time-independent (final thermal expansion).

On the other hand, the initial expansion in the Ge film at the Ge-Si interface results in a compression in the substrate. As depicted in figure 4.13, in the time interval  $0 < t < T$ , a negative rectangular strain wave travels into the substrate bulk with the sound velocity of Si ( $V_{s-Si} = 9322$  m/s [226]). Additionally, the transmitted part of the positive strain wave that was launched at the free surface of the Ge film causes a positive strain wave at time  $t = T$  close to the interface. This wave travels again into the bulk. The bouncing of the strain waves in the film leads to a train of bi-polar strain pulses with a decreasing

amplitude. The negative (compressive) part of these pulses results from the initial wave launched from the Ge-Si interface, whereas the positive (expansive) part stems from the originated wave at the free surface of the film. It should be noted that in this case (i.e. constant pressure) the absolute amplitudes of the compressive and expansive parts are identical.

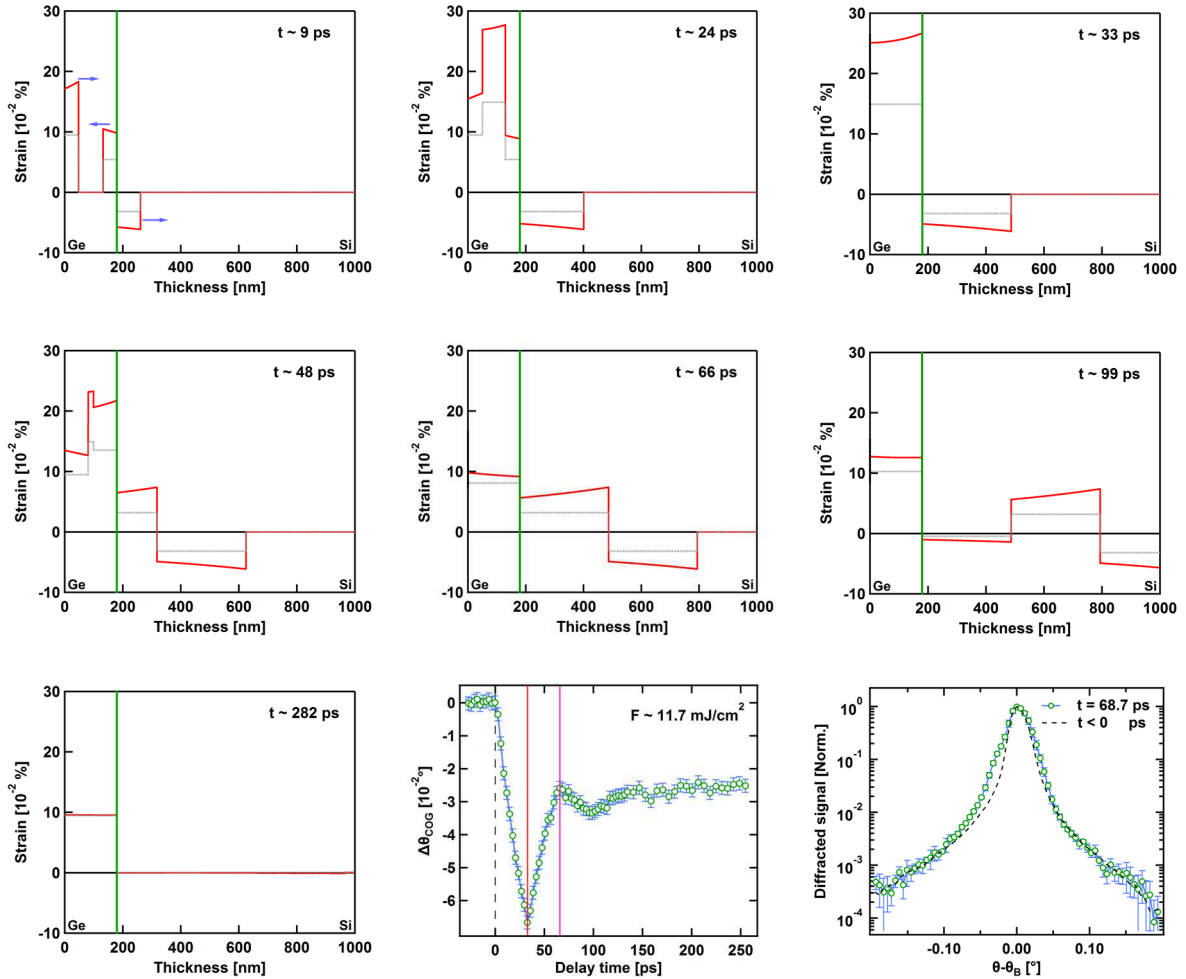


**Figure 4.14:** The calculated strain profiles at several selected delay times after the excitation based on the time-dependent photo-induced pressure in the Ge-Si heterostructure. The used parameters are  $P_c = 150$  MPa,  $r = 0.93$  and  $\tau = 61$  ps ( $F \sim 11.7$  mJ/cm<sup>2</sup>). The gray line shows the same results of figure 4.13. The transient shift of the COG of the Ge rocking curves and the rocking curve of Si are also presented

In contrast to the constant pressure case discussed above, the strain waves have different shapes when the photo-induced pressure becomes time-dependent (equation (4.10)). The oscillatory behavior and damping due to transmission, however, remain the same, i.e. two waves are launched from the film boundaries and reflected (transmitted) with the same coefficients with respect to the constant pressure case. Figure 4.14 represents the strain waves in the Ge-Si heterostructure when the pressure has an exponential time dependence. It is clear that the strain waves have no longer a rectangular shape. A characteristic scale length determines their spatial profile at a given time  $t$ . This scale length is

determined by the sound velocity and pressure decay time. Thus, it is different in the film and in the substrate.

$$\begin{aligned} l_{\text{Ge}} &= V_{\text{s-Ge}} \times \tau \\ l_{\text{Si}} &= V_{\text{s-Si}} \times \tau \end{aligned} \quad (4.11)$$

The most important effect of the time-dependent pressure is that the positive and negative strain pairs in the substrate do not have equal absolute amplitudes anymore. Also, the superposition of the waves in the film at times  $t = T, 2T, 3T$  does not lead to a fully homogenous strain distribution.

#### 4-4-1 Failure of the constant photo-induced pressure model

The calculated strain profiles based on the constant photo-induced pressure describe the general features of the measured transient rocking curves. To obtain a quantitative comparison between the model and the experimental data, a numerical calculation of X-ray diffraction has been performed. The transient COG shift of the Ge rocking curves was employed as a reference to determine the only free parameter, i.e. constant pressure amplitude. The Tagaki-Taupin (TT) equation [13] for the dynamical X-ray diffraction was solved at different delay times with the given strain profiles (see chapter 2). Strictly speaking, the TT equation is valid only for a statically deformed crystal. In the case of acoustic waves, however, using such a quasi-static approximation is justified. The acoustic response time scale  $T = d_{\text{Ge}}/V_{\text{s-Ge}}$  is in the range of several tens of picoseconds. This time scale is much longer than the X-ray pulse duration ( $< 0.3$  ps) and the X-ray diffraction characteristic time  $\tau_x$ , given for the film and the substrate as

$$\begin{aligned} \tau_{\text{x-Ge}} &= \frac{d_{\text{Ge}}}{c \sin\theta_{\text{B-Ge}}} = 1.4 \times 10^{-3} \text{ ps} \\ \tau_{\text{x-Si}} &= \frac{l_{\text{ext}}}{c \sin\theta_{\text{B-Si}}} \cong 18 \times 10^{-3} \text{ ps} \end{aligned} \quad (4.12)$$

where  $d_{\text{Ge}}$  is the Ge film thickness and  $l_{\text{ext}} \sim 2.4 \mu\text{m}$  is the X-ray extinction depth of Si. Thus, the deformation can be considered time-independent within the time scale of the diffraction process and the X-ray pulse duration.

Assuming the constant pressure amplitude as a free parameter in the modeling, several different calculations were run to find the best approximation to the COG shift of the measured Ge film rocking curves. The results show that the constant pressure model can properly describe the experimental results

at long delay times (as illustrated in figure 4.15) as well as the period of the oscillatory behavior at early delay times. The best values for the pressure were found  $150 \pm 10$ ,  $190 \pm 10$  and  $300 \pm 10$  MPa for incident fluences of  $\sim 11.7$  mJ/cm<sup>2</sup>,  $15.6$  mJ/cm<sup>2</sup> and  $23.4$  mJ/cm<sup>2</sup> respectively. These values are in good agreement with the estimated constant pressure amplitudes given by the constant term of equation (4.7) within the accuracy of the experiments. The estimated values are 151, 201 and 303 MPa. Thus, the constant pressure model is able to describe the COG shift of the rocking curves at long delay times ( $t \geq 200$  ps), which corresponds mainly to the final thermal expansion in the film including the thermal expansion caused by the laser pulse and delayed Auger heating.

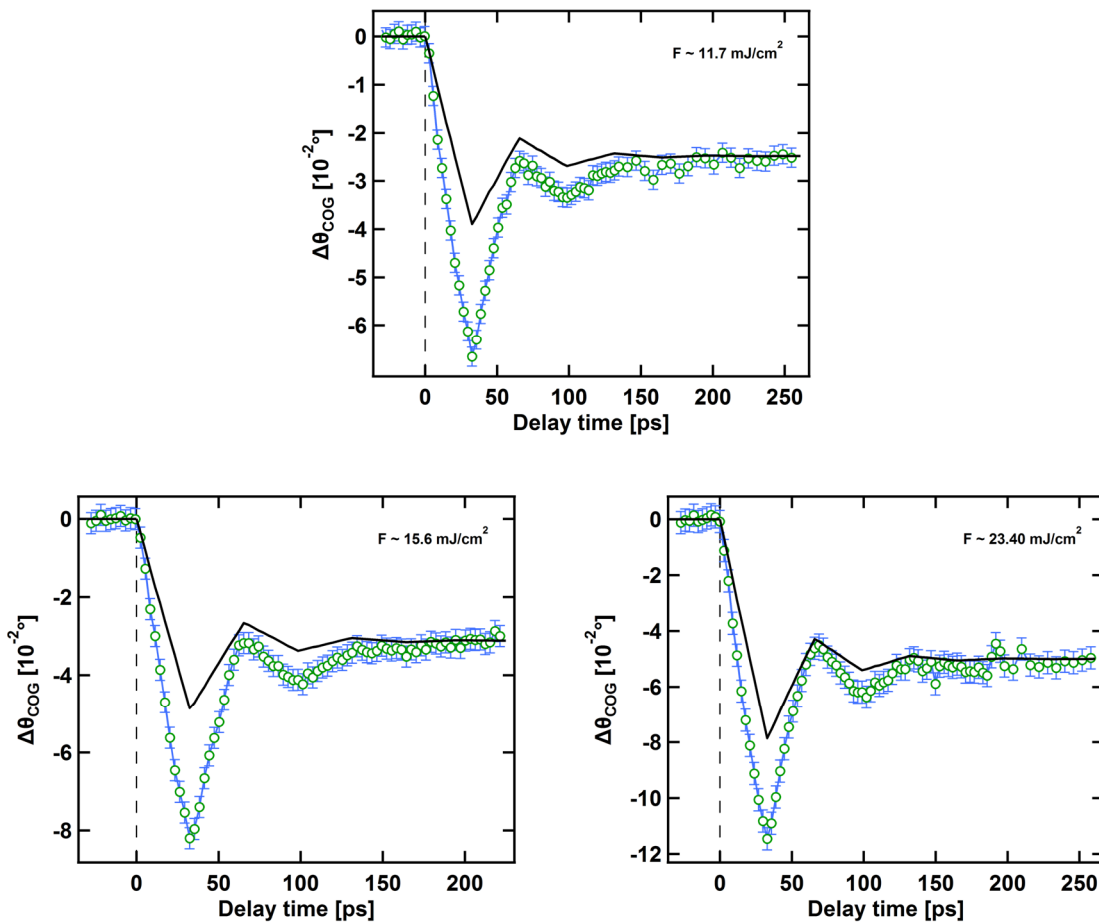


**Figure 4.15:** Comparison between the measured transient center of gravity shift (green circles) and the calculated one (black solid lines) based on the constant driving pressure for different incident pump fluences.

In general, the sound velocity is temperature- and pressure-dependent. For Ge, it increases with pressure and decreases with increase in temperature. However, for the experimental conditions here its change is small. Moreover, since the pressure changes periodically around zero and the temperature always rises over time, one expects that on average only the temperature variation affects the sound velocity. In order to simplify the modeling, an average sound velocity of  $V_{\text{s-Ge}} = 5470$  m/s was assumed. This is slightly less than its value of 5510 m/s at room temperature [198] and corresponds to the final

average temperature rise for the given experimental conditions [see appendix A]. Using this value for the sound velocity and the observed time interval of the expansion/recompression, the thickness of the Ge film was estimated as  $\sim 180$  nm. This is within the accuracy of the nominal thickness of the Ge film. These values for the sound velocity and the film thickness can reproduce the periodicity of the measured transient COG shifts.

Nonetheless, there is a clear quantitative disagreement between the calculated COGs and the measured ones at delay times  $t < 200$  ps, specifically at the extreme points. As an obvious evidence, the amount of the absolute shift at  $t = T$  (the maximum expansion) is much higher than the calculated one. To have a systematic study, the rocking curves at two reference points  $t = 33 \pm 0.3$  ps and  $287 \pm 0.3$  ps were measured explicitly as a function of the incident laser fluence. The asymptotic absolute shift ( $t = 287 \pm 0.3$  ps) increases linearly with laser fluence, while the amount of the maximum absolute shift is not linear, as indicated in figure 4.16-a. The ratio between the maximum and asymptotic absolute shifts decreases with increasing fluence (figure 4.16-b) roughly from  $3.6 \pm 0.3$  at  $F \sim 1.3$  mJ/cm<sup>2</sup> to  $2.3 \pm 0.2$  at  $F \sim 23.4$  mJ/cm<sup>2</sup>. In contrast, the constant pressure model results in a much smaller and fluence-independent ratio between the maximum and asymptotic shifts of about 1.6, in clear disagreement with the experimental data.

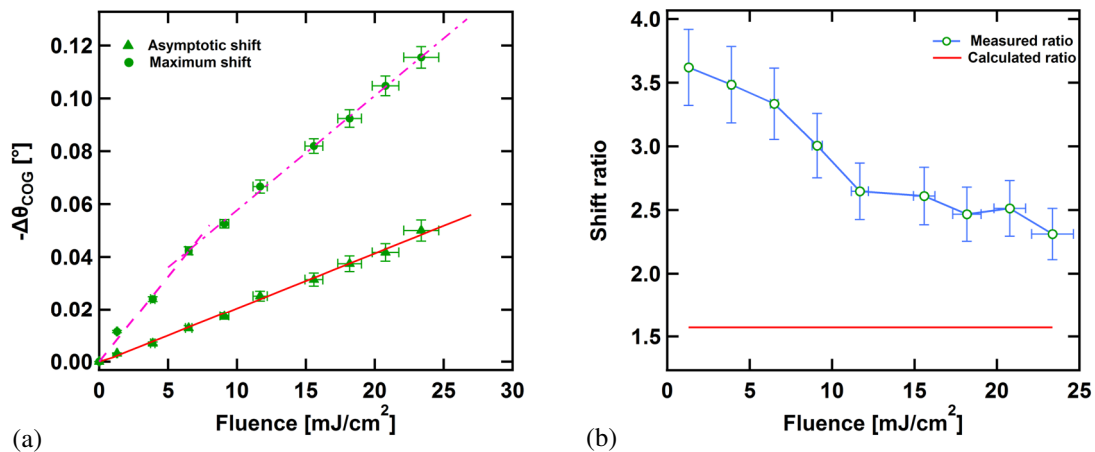


**Figure 4.16:** The measured shift of the COG at delay times  $t = 33 \pm 0.3$  ps (green circles) and  $t = 287 \pm 0.3$  ps (green triangles). The red solid line represents a linear fit to the asymptotic shift and the pink dashed lines show the non-linearity of the maximum shift (a). The measured maximum-to-asymptotic ratio (green circles) and the calculated ratio (red solid line) based on the constant photo-induced pressure (b).

As a conclusion, the disagreements mentioned above give clear evidence that the simple constant photo-induced pressure cannot describe the transient behavior of the measured rocking curves completely. In compliance with the considerations regarding the time dependence of the pressure, it will

be shown in the following subsection that a time-dependent driving pressure results in a more complete description.

#### 4-4-2 Time-dependent photo-induced pressure model

In the calculations based on the time-dependent photo-induced pressure model, the parameters  $r$  and  $\tau$  (see equation (4.10)) were considered as free parameters.  $P_c$  was adopted from the constant pressure model in order to describe the quasi-asymptotic behavior at late times. To identify these free parameters the measured COG shift of the Ge film was used as a reference. First, a value for the ratio between the time-dependent and time-independent parts of  $r = 2.75$ , as given by equation (4.8), was used. This left the decay time constant as the only free parameter. It was chosen to yield the observed ratio of the maximum-to-asymptotic COG shift for each laser fluence. As an example, figure 4.17 compares the measured (green circles) and calculated COG shifts (red solid lines) of the film for a laser fluence of  $\sim 11.7 \text{ mJ/cm}^2$ .

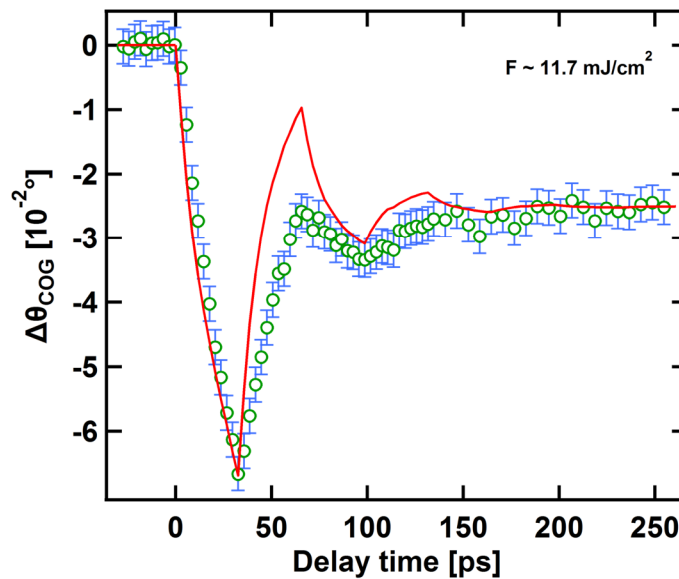


**Figure 4.17:** Comparison between the measured transient COG shift (green circles) of the Ge rocking curves and calculated one (red solid line) for a laser fluence of  $\sim 11.7 \text{ mJ/cm}^2$ . The used constant coefficient of the photo-induced pressure are  $P_c = 150 \pm 10 \text{ MPa}$ ,  $r = 2.75$  and  $\tau = 8.5 \pm 1.1 \text{ ps}$ .

To match the observed maximum-to-asymptotic shift ratio of  $2.6 \pm 0.2$  at the given laser fluence, a decay time of  $8.5 \pm 1.1 \text{ ps}$  had to be used. However, from the comparison between the measured and calculated COG shifts, it becomes evident that this rather short decay time (see figure 4.17) is not able to satisfactorily describe the overall time dependence. The constant pressure model implies that the time-dependent term of the pressure must be positive, thereby, using smaller values of  $r$  seems reasonable. On the other hand, decreasing  $r$  results in a longer decay time constant. Considering  $\tau \gg T$  is also not a proper choice because in this case the time-dependent term will significantly influence the temporal

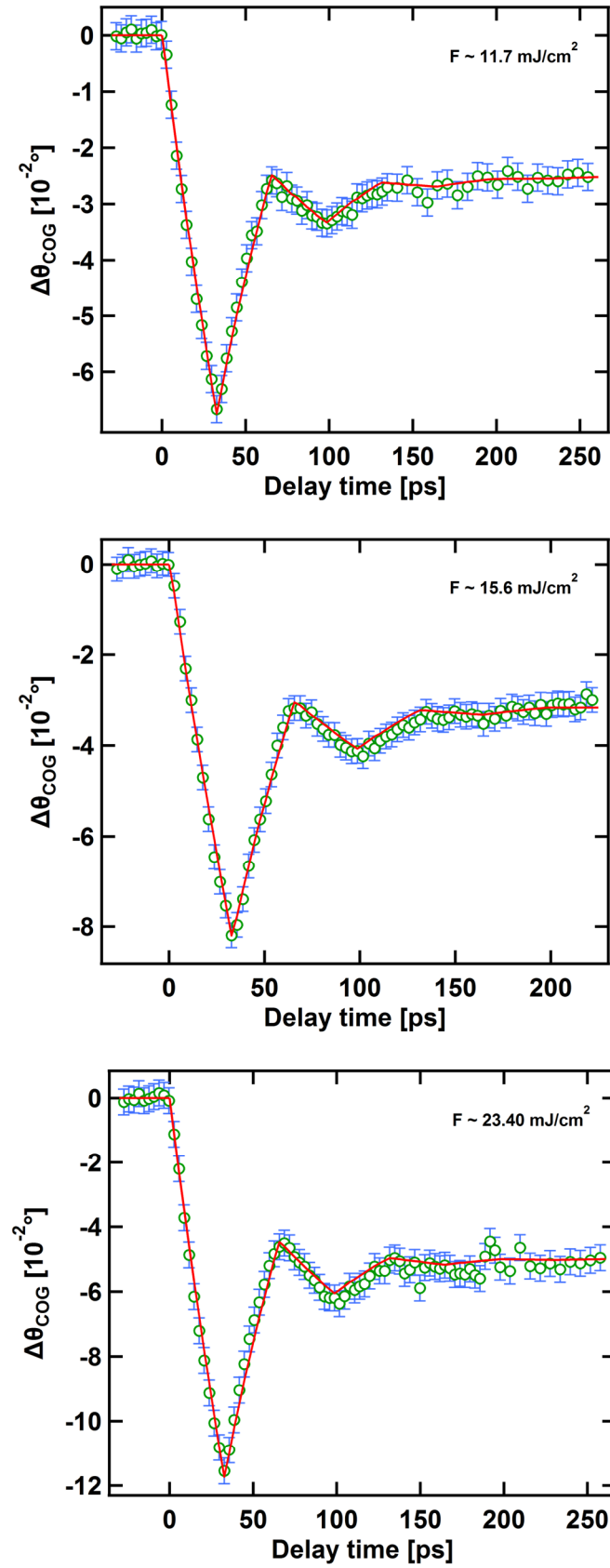
behavior of the COG shift even at delay times  $t > 200$  ps. This is in disagreement to the experimental data and the results of the constant pressure model at long delay times. As discussed by Shymanovich *et al.* [160], the only option would be that the decay time is of the order of the acoustic response time scale  $T$ . Several different calculations were run for each laser fluence to find that pair of  $r$  and  $\tau$  that provides the best approximation to the measured COG shift. The results are illustrated in figure 4.18, where the red solid lines are the calculated COG shift and the green circles again represent the measured data. The used parameters in the modeling are summarized in table 4.2

Fluence	$P_c$	$r$	$\tau$
11.7 mJ/cm <sup>2</sup>	(150 ± 10) MPa	0.93 ± 0.09	61 ± 6 ps
15.6 mJ/cm <sup>2</sup>	(190 ± 10) MPa	0.89 ± 0.09	58 ± 6.5 ps
23.4 mJ/cm <sup>2</sup>	(300 ± 10) MPa	0.68 ± 0.07	48 ± 8 ps

**Table 4.2:** The best parameters of the time-dependent photo-induced pressure used in the calculation to get the best approximation to the experimental COG shift of the rocking curves of the Ge film. These parameters correspond to the results shown in figure 4.18.

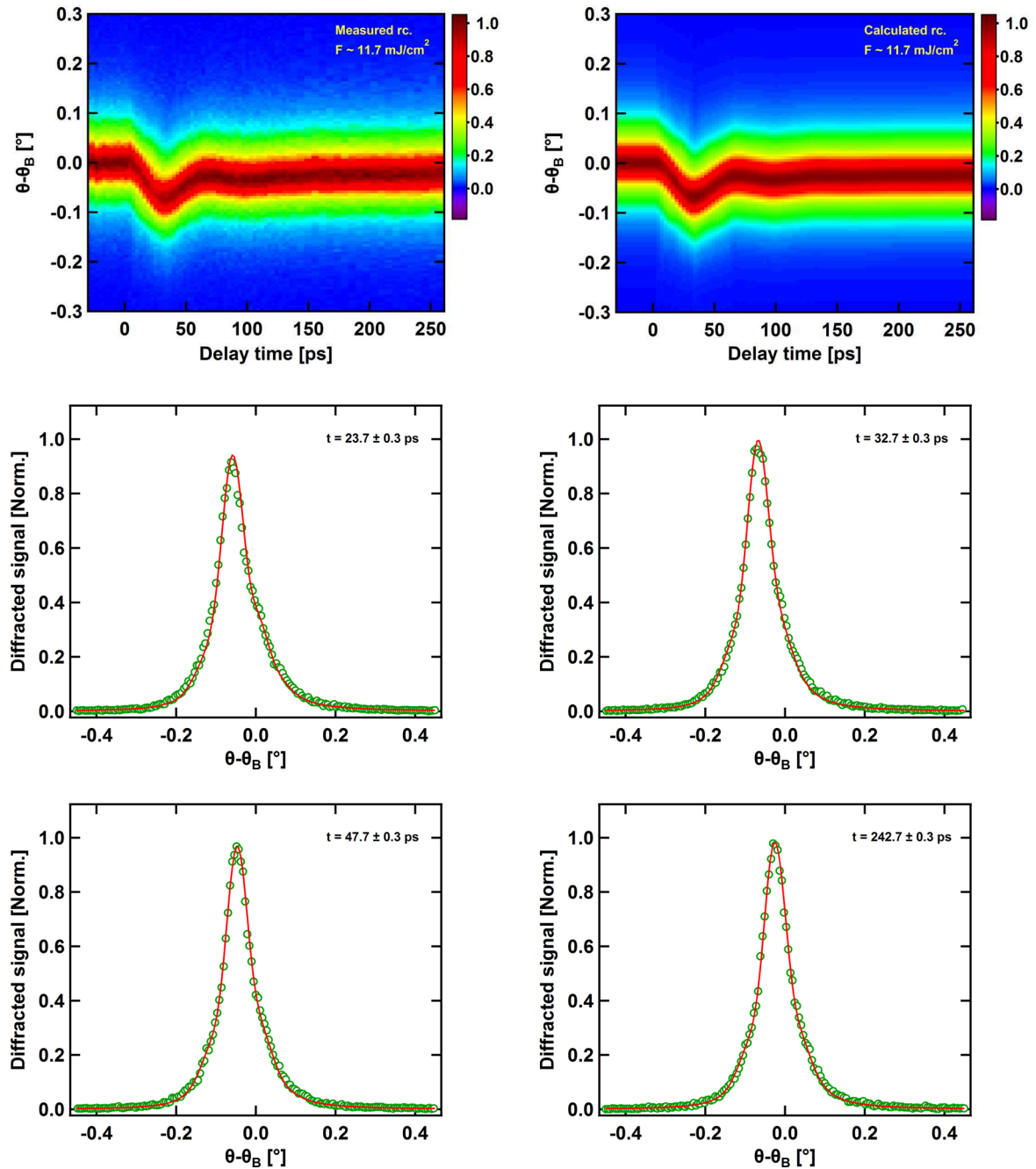
The overall agreement between the calculations and the experimental data is very good. This means that by using the time-dependent photo-induced pressure model, the temporal behavior of the measured COG shift, such as its maximum-to asymptotic shift ratio and the periodicity, is well reproduced.

What is also remarkable is that the obtained pressure decay times are comparable to the average decay times of Auger recombination (see subsection 4-1-1) estimated roughly by the numerical solution of the Auger rate equation. The obtained pressure decay time decreases with increasing excitation fluence and thus carrier density. This is what one expects from the Auger rate equation that the Auger decay time is density-dependent. In addition, the observed decrease of  $r$  with fluence implies that for very low fluences the electronic contribution in the photo-induced stress prevails. The estimated value of  $r = 2.75$  was obtained in the limiting case that the photo-excited carriers occupied the states close to the edges of the conduction and valance bands. However, in the case that the photo-excited carrier concentration is in the order of  $10^{21}$  cm<sup>-3</sup>, one expects that the carriers to be distributed over the different energy levels with different momenta. Therefore, according to equation (4.5), the corresponding deformation potential parameters for each occupied energy level and momentum likewise the distribution of the carries are required to calculate the electronic contribution of the photo-induced pressure. Obtaining this information is difficult (if not possible) for the given experimental conditions. Nevertheless, substituting the found values of  $r$  in equation (4.8), the effective (average) fluence-dependent *electron-hole-phonon deformation potential parameters* can be obtained as  $\sim 1.46$ ,  $1.41$  and  $0.41$  eV for given fluences of 11.7, 15.6 and 23.4 mJ/cm<sup>2</sup>, respectively.



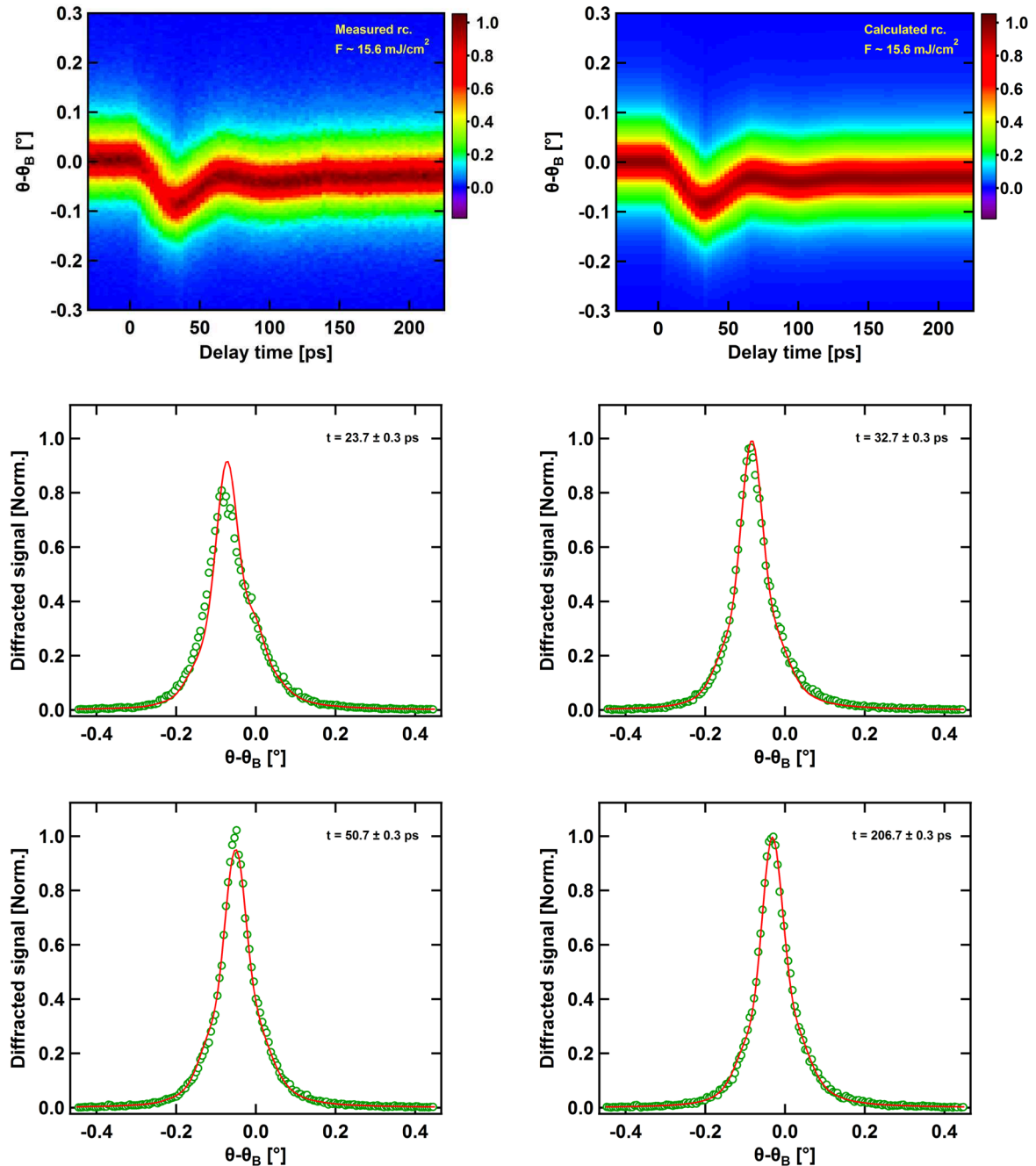
**Figure 4.18:** Transient shift of the center of gravity of the measured Ge(111) rocking curves (green circles) and the calculated COG shift (red solid lines) based on the time-dependent photo-induced pressure model. The used parameters for each laser fluence are shown in table 4.2.

The COG shift of the rocking curves represents a measure of the average strain in the sample. Therefore, to get more information about the detailed strain profiles it is necessary to explicitly compare the measured and calculated rocking curves. Since the X-ray diffraction calculation has been done for an ideally perfect crystal, all calculated rocking curves of Ge as well as Si were convoluted according to the procedures described in section 3-7 to account for any broadening effects, i.e. mosaicity of the Ge film and finite angular resolution of the setup.



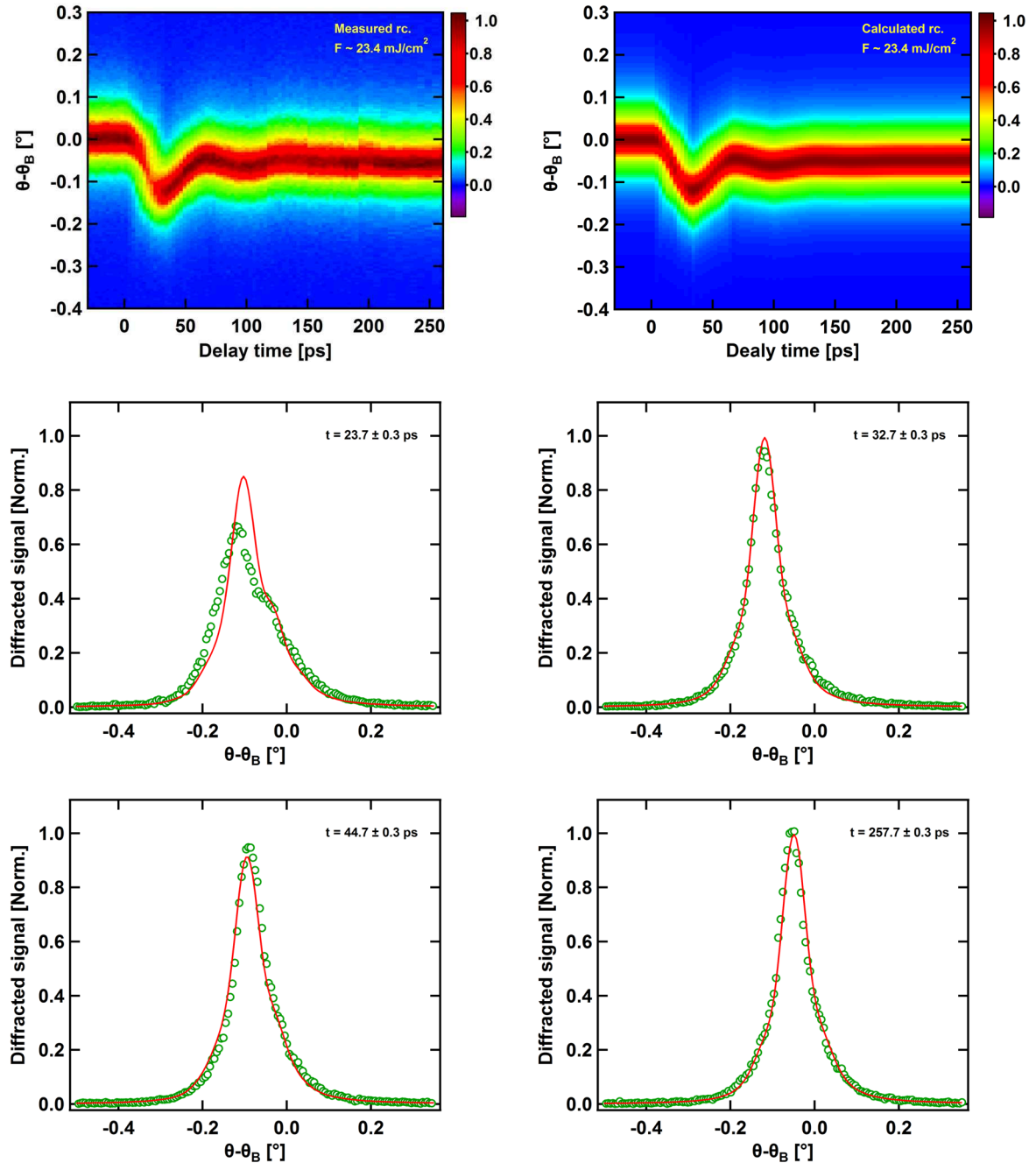
**Figure 4.19:** Comparison between the measured (top left) and calculated (top right) rocking curves of the Ge film in a 2-D false color plot. The measured (green circles) and calculated (red solid lines) rocking curves are presented for a number of selected delay times after excitation with a fluence of  $F \sim 11.7 \text{ mJ/cm}^2$ . More rocking curves are presented in appendix B.

Figure 4.19 illustrates the transient normalized calculated (top right) and measured (top left) rocking curves of the Ge film in a 2-D false color plot as well as the measured and calculated rocking curves for a number of selected delay times after optical excitation with a fluence of  $F \sim 11.7 \text{ mJ/cm}^2$ . The calculated rocking curves reproduce the measured ones very well.



**Figure 4.20:** Comparison between the measured (top left) and calculated (top right) rocking curves of the Ge film in a 2-D false color plot. The measured (green circles) and calculated (red solid lines) rocking curves are presented for a number of selected delay times after excitation with a fluence of  $F \sim 15.6 \text{ mJ/cm}^2$ . More rocking curves are presented in appendix B.

The same procedure was employed for the two other excitation fluences. The results are presented in figures 4.20 and 4.21 for  $F \sim 15.6$  and  $F \sim 23.4$  mJ/cm<sup>2</sup>, respectively. There is again good qualitative agreement between the measured and calculated rocking curves. Nevertheless, with increasing fluence, the measured rocking curves are broader than the calculated ones for early times  $t < T$ .



**Figure 4.21:** Comparison between the measured (top left) and calculated (top right) rocking curves of the Ge film in a 2-D false color plot. The measured (green circles) and calculated (red solid lines) rocking curves are presented for a number of selected delay times after excitation with a fluence of  $F \sim 23.4$  mJ/cm<sup>2</sup>. More rocking curves are presented in appendix B.

In order to calculate the transient rocking curves of the Si substrate, the strain was computed according to the parameters given by table 4.2 and the Tagaki-Taupin equation was solved for each X-ray polarization (i.e. S and P polarizations) separately. Rocking curves, in general, are different for different polarizations but in the case of X-ray diffraction in thin films, the deviation is negligible with a very good approximation. Since the X-ray source is un-polarized, the results at each delay time were taken as an average of the rocking curves of the different polarizations. They were eventually convoluted according the procedure described in section 3-7. The results are depicted in figure 4.22 for a number of selected delay times for an excitation fluence of  $F \sim 11.7 \text{ mJ/cm}^2$  [more rocking curves are provided in appendix B].

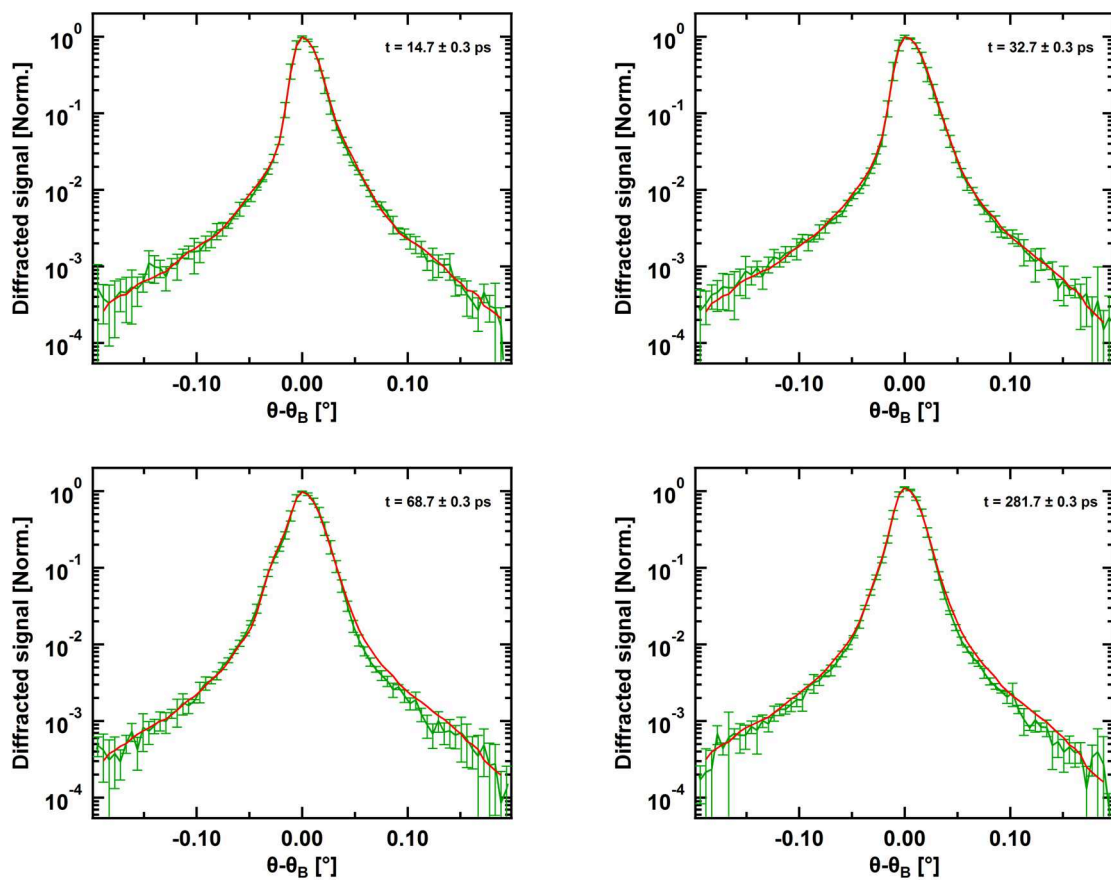


**Figure 4.22:** Comparison between the measured rocking curves (logarithmic scale) of the Si(111) substrate (green solid lines) and the calculated rocking curves (red solid lines) for a number of selected delay times after excitation with a fluence of  $F \sim 11.7 \text{ mJ/cm}^2$ .

The overall agreement between the measured and calculated rocking curves is again very good. The model describes in particular the pronounced asymmetry around the main peak in the rocking curves mainly caused by the different average amplitudes of the positive and the negative strain parts (see figure 4.14). Attention should be paid that even in the case of the constant pressure model in which the absolute

amplitudes of the positive and negative strain parts are identical; the calculated rocking curves still exhibit a slight asymmetry.

The calculated rocking curves of the Si substrate for the higher excitation fluences reproduce the experimental data qualitatively well. However, there is again a quantitative deviation between the measure and calculated data (see figures 4.23 and 4.24). More rocking curves are provided in appendix B.

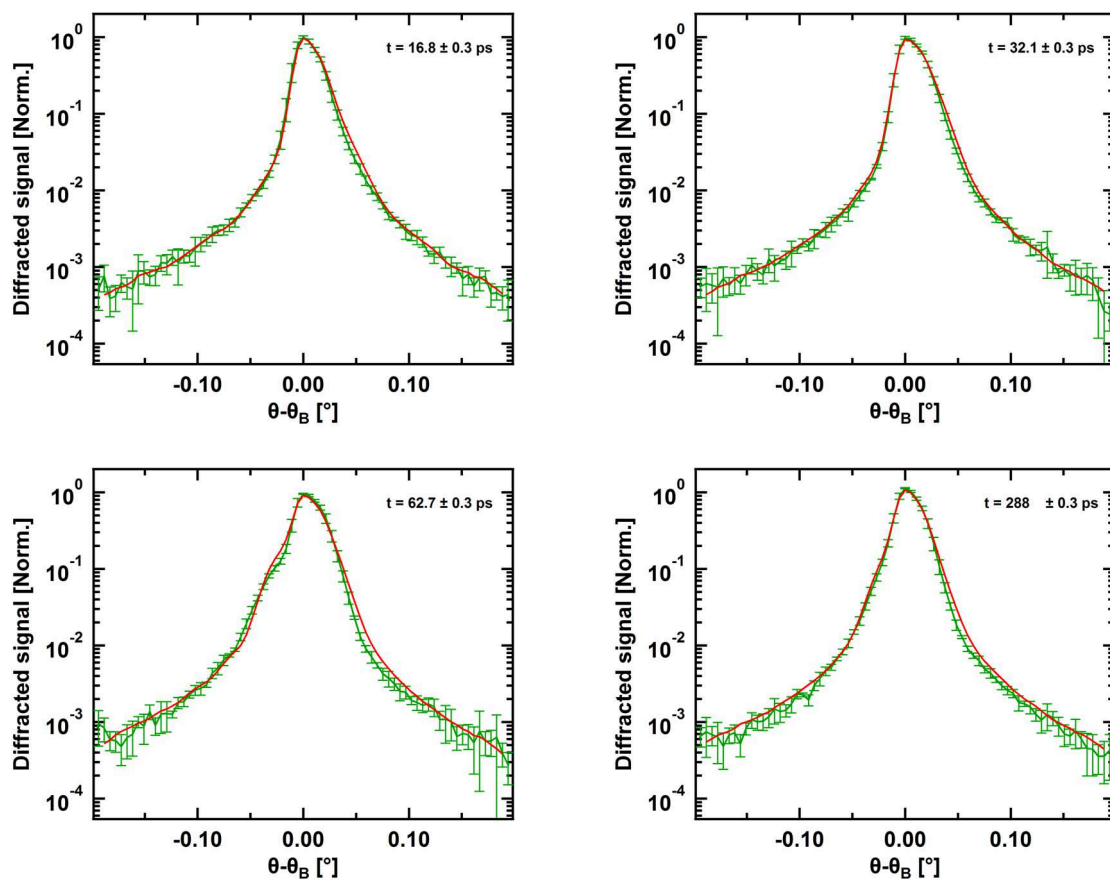


**Figure 4.23:** Comparison between the measured rocking curves (logarithmic scale) of the Si(111) substrate (green solid lines) and the calculated rocking curves (red solid lines) for a number of selected delay times after excitation with a fluence of  $F \sim 15.6$  mJ/cm<sup>2</sup>.

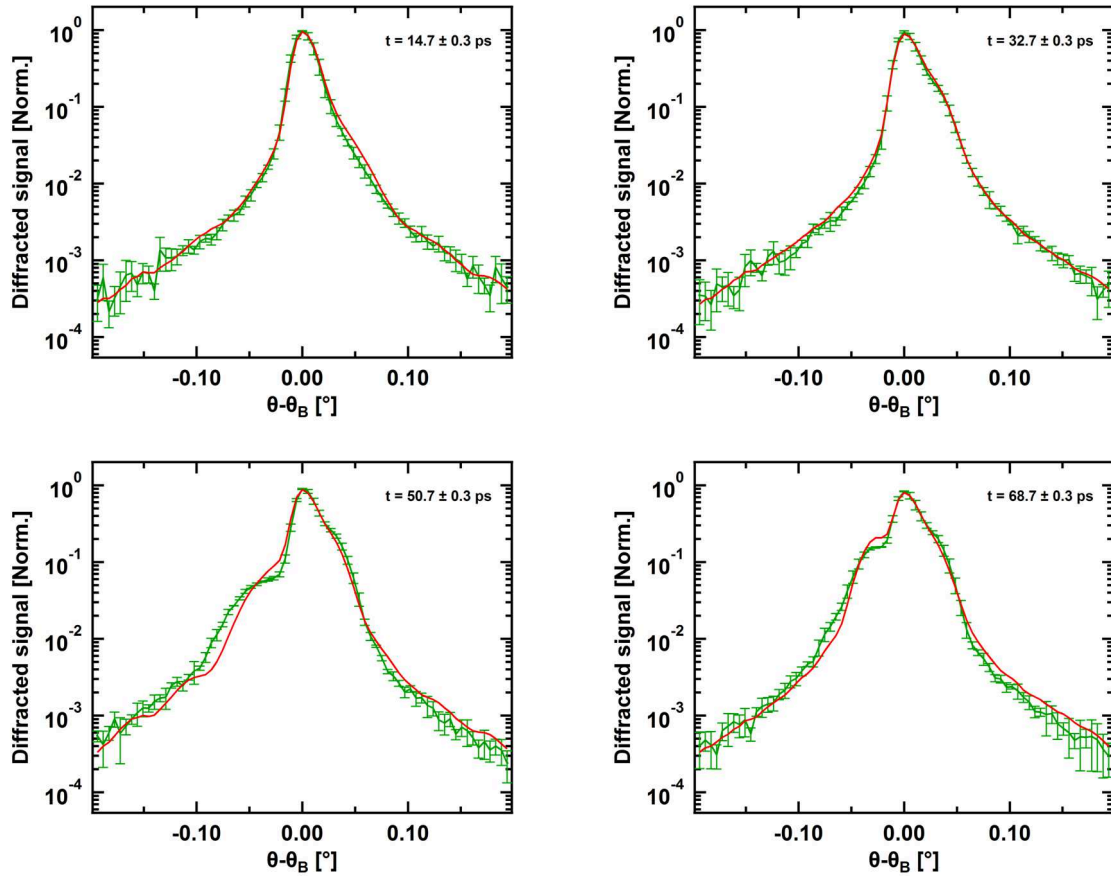


**Figure 4.24:** Comparison between the measured rocking curves (logarithmic scale) of the Si(111) substrate (green solid lines) and the calculated rocking curves (red solid lines) for a number of selected delay times after excitation with a fluence of  $F \sim 23.4 \text{ mJ/cm}^2$ .

As mentioned above, with increasing fluence the calculated rocking curves for both the Ge thin film as well as the Si substrate deviate from the experimental data. This is particularly pronounced at the highest fluence of  $23.4 \text{ mJ/cm}^2$ . In the following, some mechanisms that might explain these effects will be discussed.

- Since for each delay time the data have been accumulated over 560 pulses, pump energy fluctuations lead to an apparent broadening of the measured rocking curves. As a first approximation, pulse-to-pulse energy variation results in a proportional shift of the rocking curve, which varies from pulse to pulse. Therefore, it is expected that the final measured rocking curves become broader. This broadening can be estimated from a convolution of the calculated rocking curve with an angular shift distribution function corresponding to the pump energy distribution. The pump energy had 5% (standard deviation) fluctuation. To estimate this broadening, the calculated rocking curve at  $t = 23.7 \pm 0.3 \text{ ps}$  shown in figure 4.21 was chosen. A Gaussian function with a width of  $0.02^\circ$  (FWHM) was considered for the angular shift distribution and the calculated rocking curve was convoluted by this function. The calculated rocking curve after the convolution becomes approximately 0.2 % broader. Therefore, the

pulse-to-pulse energy fluctuation cannot be the main reason for the observed broadening shown in figure 4.21. Furthermore, the pump energy fluctuations should result in a symmetric deviation of the satellites at lower and higher angles in the measured Si rocking curves from the calculated ones. However, the rocking curves at delay times  $t = 50.7 \pm 0.3$  ps and  $t = 68.7 \pm 0.3$  ps in figure 4.24, for instance, indicate that the satellite at the high angle side of the main peak is less shifted compared the satellite in the calculated rocking curve. At the same time, the satellite at the low angle side is shifted more than the calculated one. This also confirms that the pump energy fluctuations are not the main reason for the observed deviation between the measured and calculated rocking curves for higher excitation fluences.

- Similarly, the finite pump-probe beam size ratio (3:1) as well as fluctuations of the spatial overlap between the pump and probe beams lead to an additional broadening. This broadening is of similar magnitude as the broadening due to pulse-to-pulse energy fluctuations discussed above. Moreover, it also should lead to a symmetric deviation of satellites in the measured rocking curves of the Si substrate from the calculated ones. This again contradicts the observed asymmetric deviation of the measured rocking curves with respect to the calculated rocking curves of Si (see figure 4.24). Thus, these effects cannot be mainly responsible for the observed deviations as well.

- More inhomogeneity in the strain profile can be another reason for such an observed deviation between the calculated and measured rocking curves. In the used model, it is assumed that the driving pressure is spatially homogeneous, but time-dependent. As mentioned before, the temporal dependence results in initially inhomogeneous strain waves launched from the boundaries (see figure 4.14). In the Ge film, partial superposition of these waves gives more inhomogeneity in the strain profile at a given time. An additional inhomogeneity in the strain can be produced due to an additional temporal or spatial inhomogeneity in the driving pressure. Recently, Höfer *et al.* [181] have measured the acoustic response of a bulk InSb under strong excitation by ultrafast time-resolved X-ray diffraction. They showed that the usual linear inter-band excitation mechanism is not enough to describe the measured transient rocking curves at early times after the excitation. They developed a new modified excitation mechanism based on the transient change of reflectivity and absorption due to the electron-hole pairs during the excitation and calculated the time- and depth-dependent absorption as well as the time-dependent reflectivity. This calculation indicates that the average reflectivity increases by a factor of  $\sim 1.4$  and the average absorption depth decreases by a factor of 20 compared to the linear excitation mechanism for lower fluences. Assuming such a phenomenon for the current work, it is expected that the driving pressure contain an additional transient spatial inhomogeneity. This is due to the strongly density-dependent and consequently space- and time-dependent ambipolar diffusion [207] and Auger recombination parameters. Therefore, the strain waves would have more inhomogeneity. Furthermore, it is also expected that the strain wave launched from the free surface of the film would have a larger (average) amplitude than the strain wave given by the model, while the (average) amplitude of the strain wave launched from the Ge-Si interface is weaker with respect to the calculated one. Subsequently, the positive and negative strain parts of the bi-polar strain pulses in the Si substrate would also have larger

and smaller (average) amplitudes compared to positive and negative parts given by the model, respectively. This qualitative description might describe the deviation between the calculated and measured rocking curves in both the Ge film and Si substrate. For example, if the positive parts of the bi-polar strain pulses in Si are larger, it will cause that the satellite at the lower angle side of the main peak to be more shifted and if the negative parts are smaller, the satellite at the higher angle side will be less shifted (see figure 4.24). These effects will be more pronounced at times  $t < T$  before the complete superposition of the strain waves together with the small reflectivity at the Ge-Si interface smear out this inhomogeneity. This is in agreement with the finding that deviations between the experimental data and the model with spatially homogeneous driving pressure are only observed for early delay times  $t < T$ , while later they agree again very nicely.

- It should also be emphasized that the Debye-Waller effect cannot be the reason for such a behavior. Firstly, because it does not change the shape of rocking curves. Secondly, the temperature increase, as derived from the final expansion of the film, is only  $\sim 220$  K for the highest fluence of  $F \sim 23.4$  mJ/cm<sup>2</sup>. This results in an almost negligible reduction of the integrated reflectivity of the (111)-reflection of Ge of only 1 % [160] (below the accuracy of the measurement).

## 4-5 Summary and discussion

In summary, using the optical-pump - X-ray-probe technique the picosecond acoustic response of a laser excited Ge-Si heterostructure was investigated. The results are comparable with the reported results by Shymanovitch *et al.* [160] in Ge for a low excitation fluence. However, no fluence dependence in the periodicity of the transient COG shift was detected even in the high excitation regime.

A time-dependent photo-induced pressure model including both the thermo-elastic and electronic (deformation potential) contributions was applied to interpret the experimental data. It was found that the decay time constant of the driving pressure was in the order of the acoustic response time scale of the Ge film. According to the best fits to the experimental data, the decay time constants were extracted as  $61 \pm 6$ ,  $58 \pm 6.5$  and  $48 \pm 8$  ps for laser fluences of  $\sim 11.7$ ,  $15.6$  and  $23.4$  mJ/cm<sup>2</sup>, respectively. These values are comparable to the expected Auger recombination times in Ge, which is the source of the time dependence of the driving pressure. As discussed in subsection 4-1-2, this includes the electronic pressure contribution as well as a “slow” contribution to the thermo-elastic pressure resulting from delayed Auger heating. The estimated constant thermal pressure including the direct laser and delayed Auger lattice heating was in very good agreement with the experimental data.

Moreover, it was shown that the ratio between the amplitude of the time-dependent and constant parts of the driving pressure decreases with increasing laser fluence. The obtained ratios ( $0.93 \pm 0.09$ ,  $0.89 \pm 0.09$  and  $0.68 \pm 0.07$ ) are much smaller than the predicted values from a simple theoretical

estimation based on the thermal expansion and the pressure dependence of the band gap (see equation (4.8)). This is most probably because for the experimental conditions here with high carrier densities, the excited carriers do not occupy states close to the band edges, but are distributed over wider parts of the Brillouin zone. The acoustic response investigations in an InSb bulk crystal and a Ge thin film made by Lindenberg *et al.* [28] and Shymanovitch *et al.* [160], respectively, also revealed such a difference. Using these ratio values, effective (average) fluence-dependent *electron-hole-phonon deformation potential parameters* as 1.46, 1.41 and 0.41 eV were obtained, which are also much smaller than an *electron-hole-phonon deformation potential parameter* of  $B(dE_g/dP) = 3.47$  eV at the band edges [218].

The variation of the pressure decay time constant and the ratio between the time-dependent and constant terms can shed light on the apparent discrepancies in the role of the electronic and thermo-elastic contributions of the photo-induced pressure. For example, the results here showed that with decreasing excitation fluence the electronic pressure would prevail over the thermo-elastic one. This can explain why in experiments at low excitation levels (mostly using time-resolved optical techniques) only the electronic pressure has been taken into account. In contrast, when the excitation level is high both the thermo-elastic and electronic contributions are considered. Assuming only the thermo-elastic pressure would be reasonable when the acoustic response time scale is much longer than the pressure decay time constant. For example, Cavalleri *et al.* [27] described the acoustic response of a thick Ge film (400 nm) only taking into account the thermo-elastic driving pressure.

The model developed here can reproduce the transient measured rocking curves of the Ge film and the Si substrate for the lowest excitation fluence very well. In particular, the asymmetric shape of the Si rocking curves is mainly explained by the difference between the amplitudes of the positive and negative strain parts in the substrate, which is a direct consequence of the time dependence of the driving pressure in the excited Ge thin film. However, there is a quantitative deviation between the calculated rocking curves and the measured ones in both Ge and Si for higher excitation fluences. In this regime, the model cannot provide a complete quantitative explanation, which is attributed to an additional transient spatial inhomogeneity of the driving stress and of the strain profiles at early delay times, although the qualitative agreement is good. Therefore, some care is required with respect to quantities (e.g. *effective electron-hole-phonon deformation potential parameter*) obtained by applying the spatially homogeneous but time-dependent model also for high excitation fluences.

## *Chapter 5*

### **Summary and outlook**

#### **5-1 Summary**

In this work, the picosecond acoustic response of a Ge-Si heterostructure following femtosecond optical excitation has been studied by means of time-resolved X-ray diffraction. Besides, it represents significant achievements on design and optimization of a new modular optical-pump - X-ray-probe setup.

Employing an appropriate technique with high enough spatial and temporal resolution is required to directly follow the ultrafast lattice deformations induced by ultrashort laser excitation. Here, this has been achieved by applying time-resolved diffraction of an ultrashort, convergent and highly monochromatic X-ray pulse derived from a laser-plasma based source. A new optical-pump - X-ray-probe setup based on a modular scheme has been designed, built and carefully characterized. In this modular scheme, only the X-ray source itself is placed in a small vacuum chamber and the rest of the setup is placed in air. This provides larger flexibility for modifying the setup for different purposes and allows for convenient and more precise adjustments of the individual components.

X-ray optics represent a key element to make efficient use of the spatially incoherent emission of the laser-plasma based source. Here, a toroidally bent Ge crystal mirror has been used, which allows 1:1 imaging of the X-ray source onto the sample. It provides extremely well monochromatic Ti- $K_{\alpha 1}$  focused X-ray beam with a dimension of  $\sim 83 \times 80 \mu\text{m}^2$  and a convergence angle of  $\sim 1.4^\circ$  in the imaging plane. With such a convergent and monochromatic beam, it is possible to record the complete rocking curve without rotating the sample (and the X-ray detector) with high angular resolution. The optical pump and the X-ray probe are perfectly synchronized because they are derived from the laser beam by a beam splitter. A two-pulse scheme with a weak pre-pulse for plasma generation followed after a few ps by an intense main-pulse for X-ray generation allows enhancing and stabilizing the  $K_{\alpha 1}$  yield. This allowed to increase the  $K_{\alpha 1}$  flux on the sample to about  $10^6$  photons/s, which is almost an order of magnitude higher compared to all previous setups used at the University of Duisburg-Essen. The improved X-ray flux, the small X-ray focus on the sample as well as the narrow energy bandwidth make the setup the perfect tool for measuring high quality rocking curves to follow even subtle transient changes in a pump-probe experiment.

This new optical-pump - X-ray probe setup was used to measure the angle- and time-resolved X-ray diffraction patterns (rocking curves) of a Ge(111)-Si(111) heterostructure following femtosecond optical excitation with different fluences. The motivation of this study was to explore the interplay of different photo-induced stress sources, e.g. the thermo-elastic and electronic stress sources (deformation potential) and to complete earlier investigations by Shymanovich *et al.* [160]. The excellent improvement in the X-ray flux enabled us to measure not only the transient rocking curves of the Ge overlayer, but also the transient rocking curves of the Si substrate with a very high dynamic range of  $\sim 10^4$ . The results are comparable with the reported results by Shymanovich *et al.* [160] in Ge for a low excitation fluence. However, no fluence dependence in the periodicity of the transient COG shift of Ge was detected even in the high excitation regime. The measured transient Si rocking curves reflect the temporal expansion and recompression behavior of the Ge film. These rocking curves exhibit a clear asymmetry with respect to the main peak.

To interpret the experimental data, the photo-induced pressure inside the Ge film due to the thermo-elasticity and deformation potential mechanisms was modeled by a time-dependent function with an initial isochoric rise followed by an exponential decay. The profile of strain waves inside the heterostructure and the transient X-ray rocking curves of both the Ge film and Si substrate were calculated numerically. The results indicate that the decay time of the driving pressure is of similar magnitude as the acoustic response time of the Ge film. They were obtained as  $61 \pm 6$ ,  $58 \pm 6.5$  and  $48 \pm 8$  ps for excitation fluences of  $\sim 11.7$ ,  $15.6$  and  $23.4$  mJ/cm<sup>2</sup>, respectively. These values are comparable to the expected Auger recombination times in Ge. Moreover, the theoretically estimated value for the constant term of the modeled pressure, which represents the thermal expansion of the lattice at long delay times, is in very good agreement with the experimental data. This reveals that delayed Auger lattice heating has an important effect on the coherent acoustic response of semiconductors. Another important information is the obtained ratios ( $0.93 \pm 0.09$ ,  $0.89 \pm 0.09$  and  $0.68 \pm 0.07$ ) between the amplitude of the time-dependent and constant parts of the driving pressure. These values are much smaller than the simple estimated value based on the thermal expansion coefficient and the pressure dependence of the band gap (see equation (4.8)). This reflects the fact that the excited carriers are distributed over wider parts of the Brillouin zone rather occupying states close to the band edges. As a result the effective (average) fluence-dependent *electron-hole-phonon deformation potential parameters*, here determined as 1.46, 1.41 and 0.41 eV for the three different fluences mentioned above, are significantly smaller than the value at the band edges ( $B(dE_g/dP) = 3.47$  eV) [218]. In addition, the fluence dependence of the pressure decay time constant and the ratio between the time-dependent and constant terms indicates that at very low excitation fluences the electronic pressure dominates the thermo-elastic one. In contrast, at high excitation fluences both the thermo-elastic and electronic pressure sources are involved. When the pressure decay time is much smaller than the acoustic response time scale, one can expect that the dominant process is the thermo-elasticity.

The developed model here successfully reproduces the experimental data at the lowest excitation fluence. In particular, the pronounced asymmetric shape of the Si rocking curves is caused by the difference in the amplitudes of the positive and negative strain parts in the substrate, which is a direct consequence of the time dependence of the driving pressure in the excited Ge thin film. While the overall agreement between the model calculations and experimental data is good also for higher fluences, systematic deviations in the detailed shape of the rocking curves of both the Ge film and Si substrate begin to develop with increasing fluence. This is attributed to an additional transient spatial inhomogeneity of the driving stress and of the strain profiles at early delay times. Therefore, some care is required with respect to quantities (e.g. effective *electron-hole-phonon deformation potential*) obtained by applying the spatially homogeneous but time-dependent model at high excitation fluences.

## 5-2 Outlook

The work presented in this thesis has proved that the ultrashort laser-plasma based X-ray pulse sources are appropriate to study the lattice dynamics of solids in which high X-ray photon flux is not necessary. These sources can be set up much easier on a laboratory scale with a lower cost compared to synchrotrons or XFELs and virtually no access limitations. Therefore, it is vital to continuously improve and optimize them. Recently, it has been demonstrated that the X-ray flux can be significantly enhanced when the source is driven by intense mid-infrared sub-100-fs pulses [227] rather than near infrared pulses.

As mentioned in the previous section, the developed model based on a spatially homogenous but time-dependent photo-induced pressure can explain the acoustic response of the Ge-Si heterostructure very well for low excitation fluences. At high excitation levels, however, a more rigorous model is required. According to Höfer *et al.* [181], for high excitation fluences a modified carrier excitation mechanism including free carrier effects is required to explain the acoustic response of InSb. Similar complicated numerical calculations can be performed in the case of the Ge-Si heterostructure to verify the validity of the suggestions made in this thesis.

Due to fundamental aspects and potential applications of semiconductor-semiconductor and metal-semiconductor heterostructures, it is desirable to investigate the acoustic response of different kinds of such heterostructures. Recently, Brinks *et al.* [228] have started to investigate the lattice acoustic dynamics of several different metal-GaAs heterostructures using the presented optical-pump - X-ray-probe setup.

The performed experiments here exhibit the capability of the setup to explore the ultrafast lattice dynamics. This suggests studying other sources of the lattice acoustic motion such as the inverse piezoelectric mechanism [90] and the electrostriction [121]. In addition, if the time resolution of the

setup is improved, it will be possible to study coherent optical phonons. Since the X-ray flux has been enhanced, it is expected to get more accurate results in this field as well.

The investigation presented in this thesis, emphasized the importance of electron-lattice coupling and its significant influence on the lattice dynamics as well as the electronic dynamics. Therefore, it is of fundamental interest to extend such experiments to other kinds of samples (e.g. complex materials) in which the electron-phonon coupling mechanism is significantly important and many issues are still unknown. For instance, electron-phonon coupling in high critical temperature superconductors plays an important role in both the electronic and lattice dynamics. While there are many investigations on the electronic dynamics [229-235], only few investigations have been made to directly monitor the lattice dynamics in such materials [60, 236]. Since the current setup supports the conditions for experiments at cryogenic temperatures, it will be possible to study the lattice dynamics of such samples.

## Appendixes

### A. Sample material properties

#### A-1 Ge

Germanium is a semiconductor belonged to the IV<sup>th</sup> group of the periodic table of elements and has the diamond lattice structure. In the following, its physical properties, which have been used in this thesis, are presented.

Properties	symbols	Values
Atomic mass [237]	$m_a$ (u)	72.61
Density [238]	$P$ (g/cm <sup>3</sup> )	5.3244
Lattice constant [238]	$a$ (Å)	5.6578
Absorption depth @ $\lambda = 800$ nm [27]	$\mu$ (nm)	200
Optical reflectivity @ S pol, $\theta = 16.3^\circ$ [239]	$R$	0.44
E-h-p deformation potential parameter at the band edges[218]	$dE_g/dP$ (eV/kbar)	$5.1 \times 10^{-3}$

**Table A-1-1:** General properties of Ge.

Properties	Symbols	T = 410 K	T = 440 K	T = 520 K
Sound velocity in the [111] direction [198]	$V_s$ (m/s)	5485	5476	5448
Bulk modulus [198]	$B$ (GPa)	68.2	68	67.3
Indirect band gap energy [198]	$E_g$ (eV)	0.62	0.60	0.57
Specific heat [220]	$C$ (J cm <sup>-3</sup> K <sup>-1</sup> )	1.9	1.92	1.98
Linear thermal expansion coefficient [219]	$\beta$ (10 <sup>-6</sup> K <sup>-1</sup> )	6.5	6.6	6.9

**Table A-1-2:** The used thermal, elastic and electronic properties of Ge. The temperature values have been estimated by applying the acoustic model to the experimental data.

In general, the parameters given by table A-1-2 are temperature- and pressure-dependent. Since after the excitation the pressure varies periodically around zero (i.e. the Ge film gets periodically expanded and recompressed) and the temperature only increases, we assume that on average only the temperature change influences these properties. The temperature dependence of them are depicted in figure A-1. The values in table A-1-2 were extracted from the data shown in figure A-1 at the final temperature in the Ge film, i.e. the estimated temperature values at long delay times. The temperature value itself was estimated by applying the acoustic model (see chapter 4) to the experimental data. These values (shown in table A-1-2) are corresponding to the pump incident fluences of  $\sim 11.7$ ,  $15.6$  and  $23.4$   $\text{mJ}/\text{cm}^2$ , respectively. To simplify the numerical calculations, an average sound velocity of  $V_s = 5470$   $\text{m/s}$  was assumed for all the fluences. This value is slightly less than its value of  $V_s = 5510$   $\text{m/s}$  at room temperature and pressure [198].

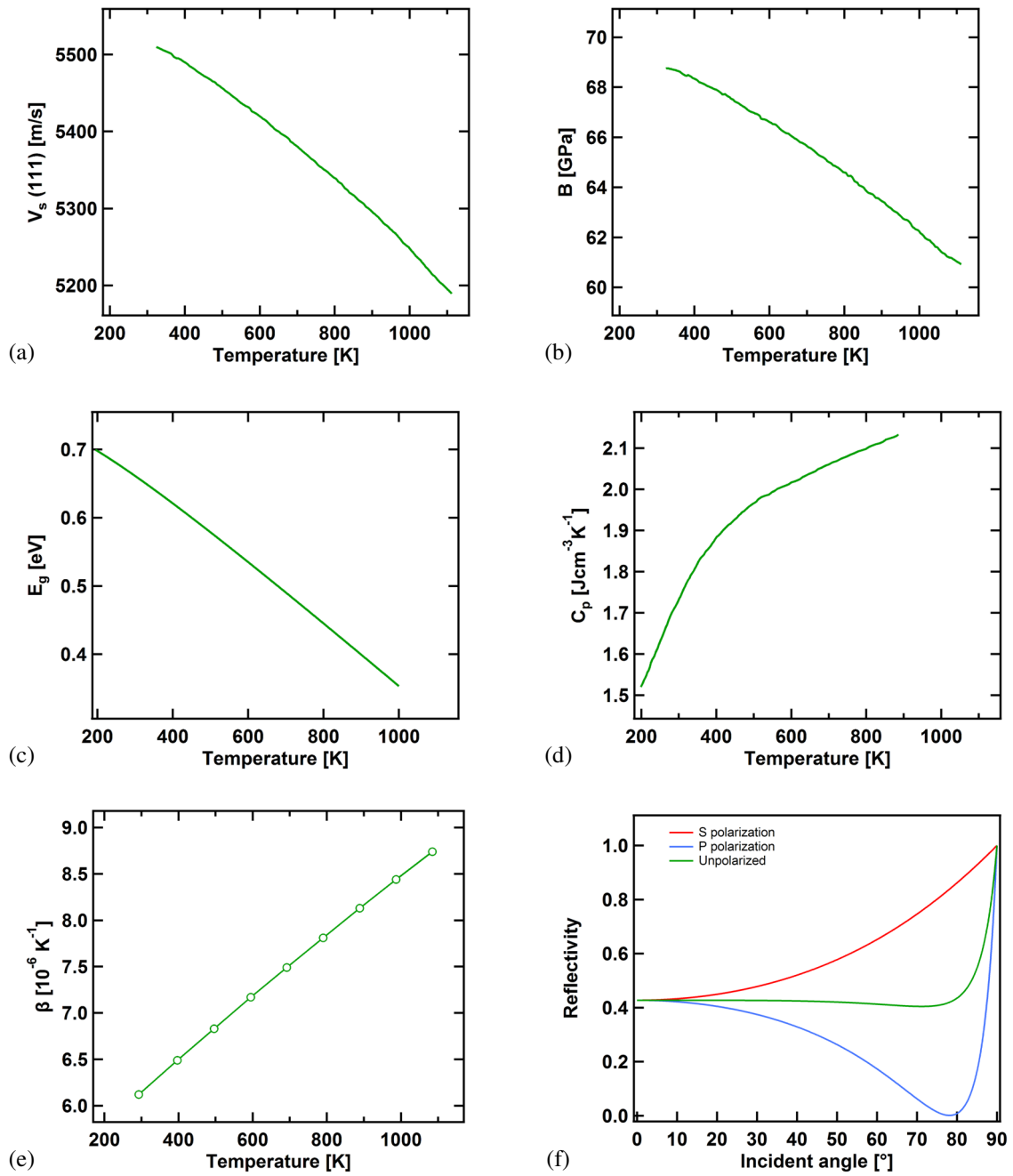


**Figure A-1:** Temperature dependence of the Ge thermal, elastic and electronic properties including: the sound velocity (a), bulk modulus (b), indirect energy band gap (c), specific heat (d), linear thermal expansion coefficient (e). The graph (f) presents the optical reflectivity of Ge at 800 nm.

## A-2 Si

Silicon is also a semiconductor belonged to the IV<sup>th</sup> group of the periodic table of elements and has the diamond lattice structure. In the following, its physical properties, which are related to this thesis, are presented.

Properties	symbols	Values
Density [238]	$\rho$ (g/cm <sup>3</sup> )	2.3293
Sound velocity in (111) direction [226]	$V_s$ (m/s)	9322
Indirect band gap energy [198]	$E_g$ (eV)	1.12

**Table A-2-1:** Physical properties of Si related to this work here.

## B. Measured and calculated rocking curves of Ge and Si

In this section more measured and calculated transient rocking curves of 180 nm Ge(111) and 0.5 mm Si(111) are provided. Figures B-1, B-2 and B-3 illustrate the measured (green circles) and calculated rocking curves of Ge(111) for a number of selected delay times after excitation with optical pump fluences of ~ 11.7, 15.6 and 23.4 mJ/cm<sup>2</sup>, respectively. In addition, figures B-4, B-5 and B-6 present the measured (green solid lines) and calculated (red solid lines) rocking curves (logarithmic scale) of Si(111) for a number of selected delay times after excitation with fluences of ~ 11.7, 15.6 and 23.4 mJ/cm<sup>2</sup>, respectively. The Si rocking curves at negative delay times are represented by gray dashed lines.

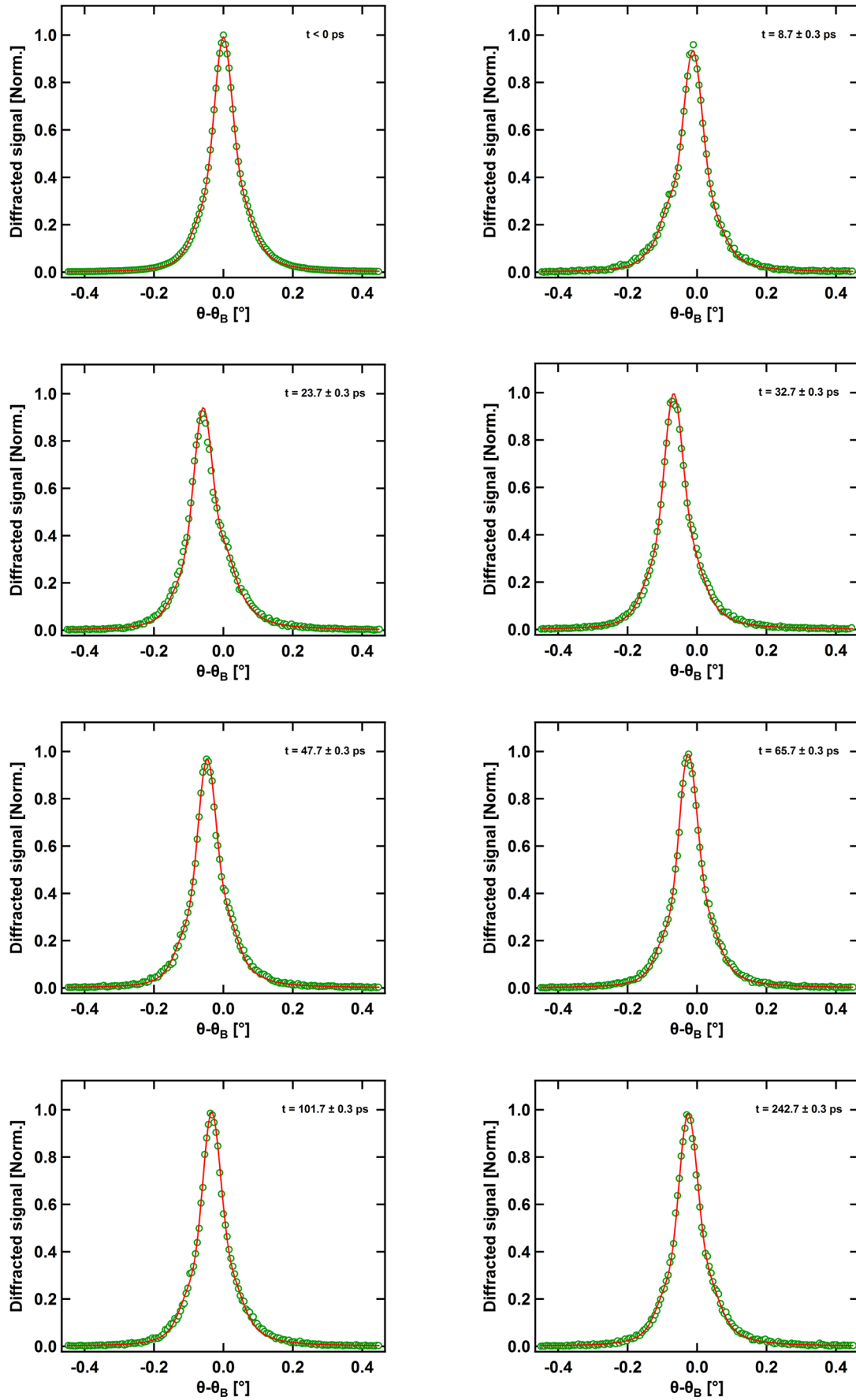


**Figure B-1:** Measured (green circles) and calculated (red solid lines) rocking curves of Ge(111) for a number of selected delay times after excitation with a fluence of  $F \sim 11.7 \text{ mJ/cm}^2$ .

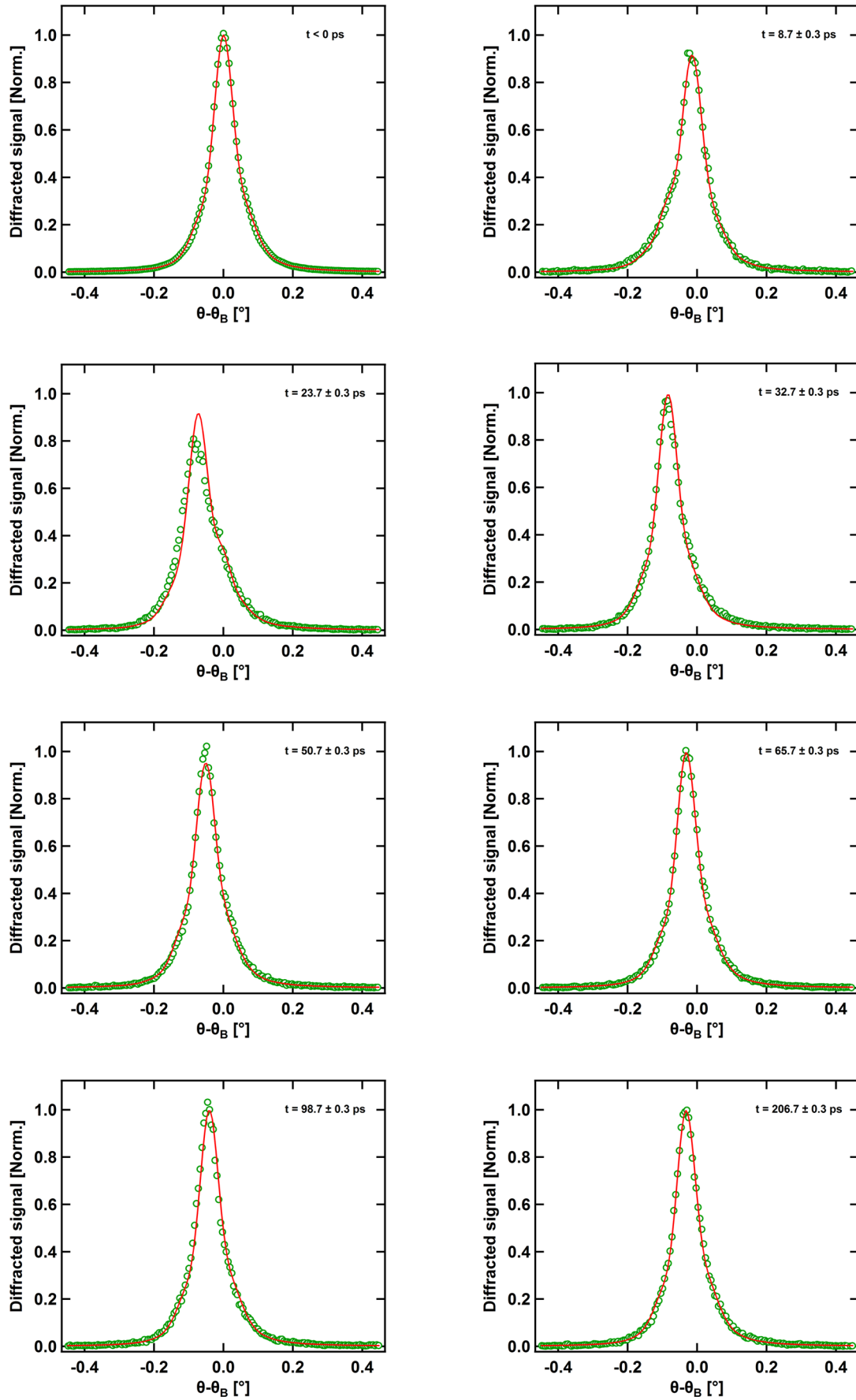


**Figure B-2:** Measured (green circles) and calculated (red solid lines) rocking curves of Ge(111) for a number of selected delay times after excitation with a fluence of  $F \sim 15.6 \text{ mJ/cm}^2$ .

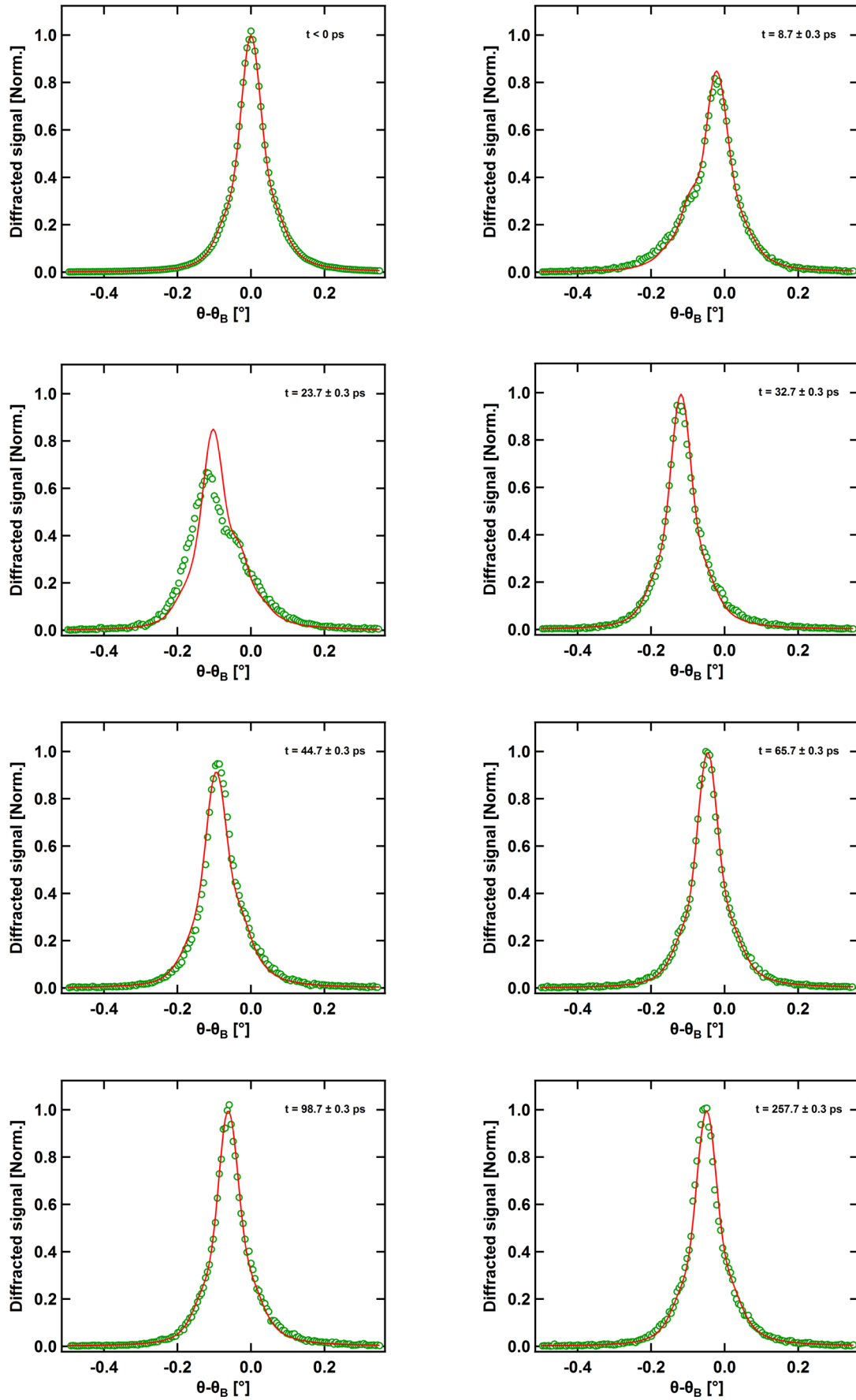


**Figure B-3:** Measured (green circles) and calculated (red solid lines) rocking curves of Ge(111) for a number of selected delay times after excitation with a fluence of  $F \sim 23.4 \text{ mJ/cm}^2$ .

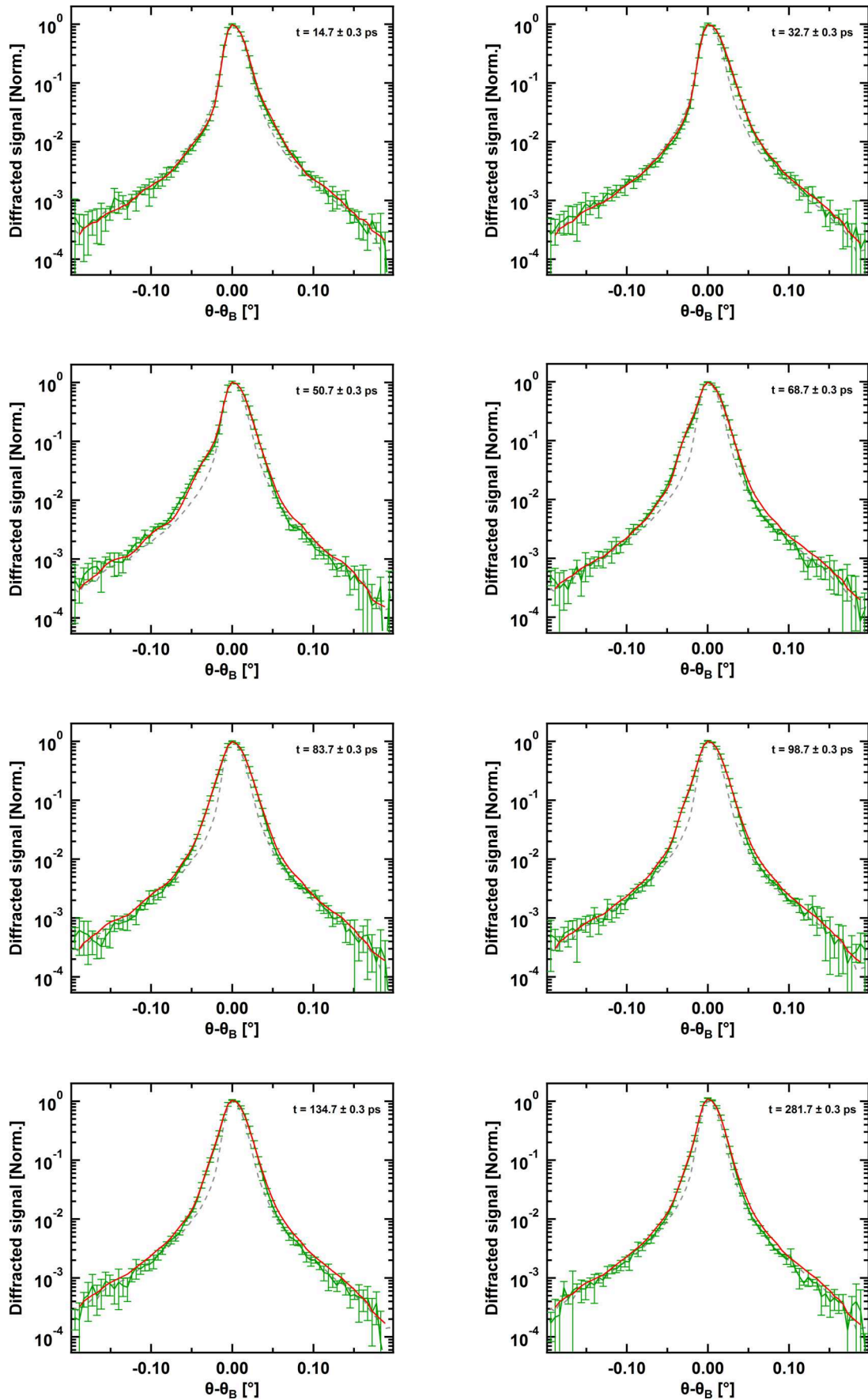


**Figure: B-4:** Measured (green solid lines) and calculated (red solid lines) rocking curves (logarithmic scale) of Si(111) for a number of selected delay times after excitation with a fluence of  $F \sim 11.7$  mJ/cm<sup>2</sup>. Dashed lines illustrate the rocking curve at negative delay times.

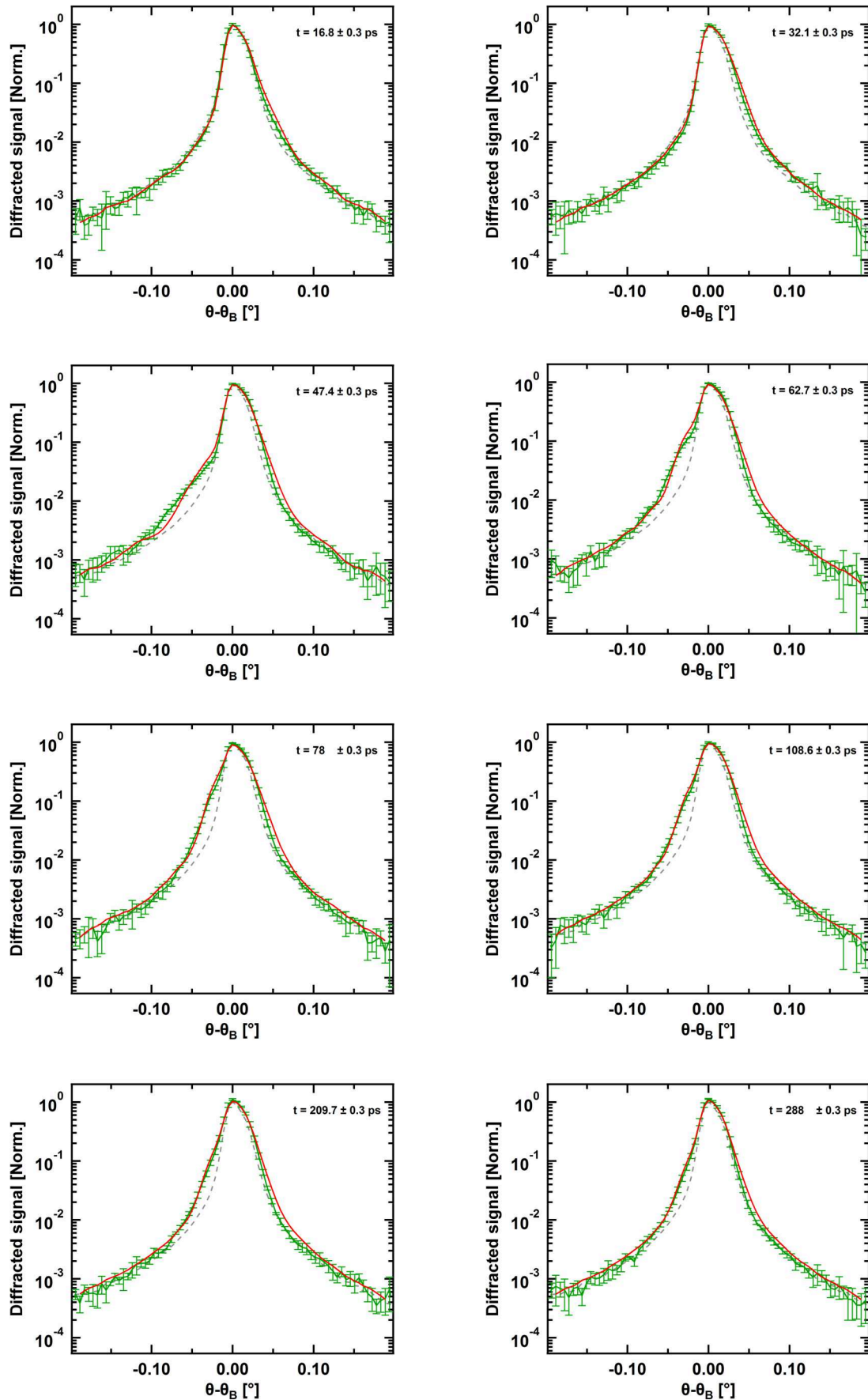


**Figure: B-5:** Measured (green solid lines) and calculated (red solid lines) rocking curves (logarithmic scale) of Si(111) for a number of selected delay times after excitation with a fluence of  $F \sim 15.6 \text{ mJ/cm}^2$ . Dashed lines illustrate the rocking curve at negative delay times.

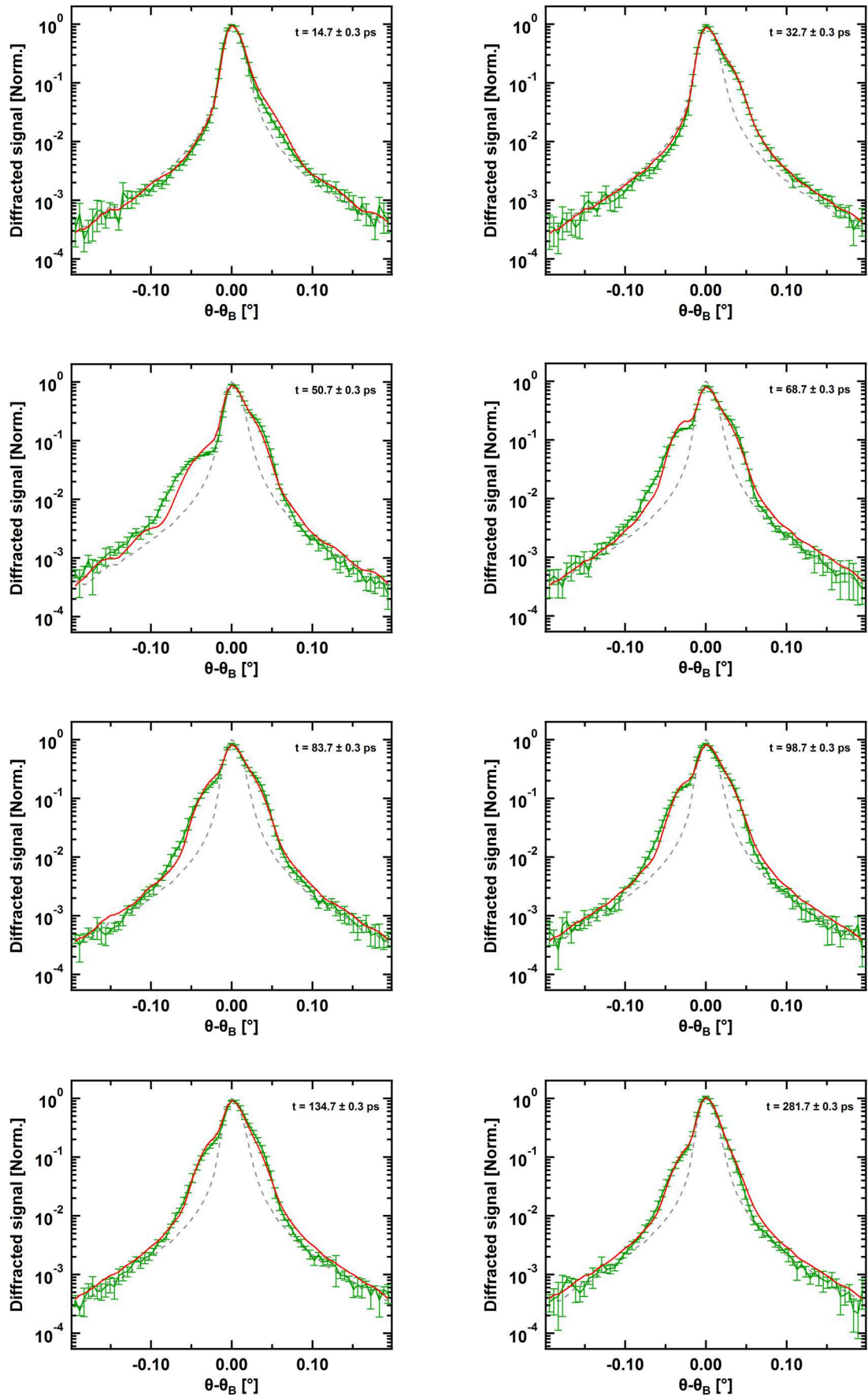


**Figure: B-6:** Measured (green solid lines) and calculated (red solid lines) rocking curves (logarithmic scale) of Si(111) for a number of selected delay times after excitation with a fluence of  $F \sim 23.4$  mJ/cm<sup>2</sup>. Dashed lines illustrate the rocking curve at negative delay times.

## C. “Matlab” codes

In this section, the “Matlab” codes used in the modeling of photo-induced strains and numerical dynamical X-ray diffraction are presented. Also at the end, the code which was used to calculate the phot-excited carries diffusion according to the Crank-Nicolson method will be demonstrated.

### Main program for calculation the transient rocking curves of Ge (111) after excitation:

```
% *****
% This code calculates the transient Rocking curves of a thin film (e.g.
% Ge) after excitation by a fs laser pulse. It contains several
% sub-function
% #####
% Mohammadmahdi Afshari
% 12-04-2017
% University of Duisburg-Essen
% #####
% *****

clc;
close all;
clear all;
```

In this part we define all parameters needed for Ge (111) strain profile

```
%*****
% the used formula for the photo-induced pressure is
%  $P = P_{thl}[1 + R_{el\_th} * \exp(-t/\tau_1) + TT*R_{el\_th}*\exp(-t/\tau_2) + R_{el\_th}*y_{na}]$ 
%*****

Ge_D = 180/1000000000;      % Thickness of Ge(111) (m)
Ge_Velocity = 5450;        % sound velocity of Ge(111) (m/s)
Ge_impedance = 29017980;   % Ge acoustic impedance [density(kg/m3)* Velocity(m/s)]
Ge_R_el_th = 0.72;        % the ratio between the amplitude of first exponential in electronic pressure to
thermal pressure
Ge_tau_1 = 40/1000000000000; % first decay time for auger process (s)
Ge_TT = 0;                 % ratio between the second exponential term of electronic pressure to thermal
pressure
Ge_tau_2 = 257.15/1000000000000; % second auger decay time (s)
Ge_y_na = 0;               % ratio between constant term in electronic pressure to the thermal one
Ge_P_thL = 307000000;      % the time_independent (thermal) pressure at long delay times (Pascal).
```

## Appendixes

in this part we define all parameters needed for Si(111) strain profile

```
Si_D = 500/1000000;      % Thickness of Si (m)
Si_Velocity = 9322;      % sound velocity of Si(111) (m/s)
Si_impedance = 21713734.6; % Si acoustic impedance [density(kg/m3)* Velocity(m/s)]
```

Here we define all parameters for Ge (111) needed for XRD

```
F0_Re = 255.15750120;    % Structural factors in forward direction (source XOP) real part
F0_Im = 20.18899760;    % Structural factors in forward direction (source XOP) imaginary part
Fpsi_Re = 154.97068254; % Structural factor for (111) reflection (source XOP) real part
Fpsi_Im = 14.27577711; % Structural factor for (111) reflection (source XOP) imaginary part
DWF = 1;                % Debye_waller factor
Pol_flag = 0;           % This flag determines the polarization of the X-Ray [0 means s pol]
Theta_B = 24.8811501;  % Bragg angle for Ge(111) (°)
lambda = 2.748486/10000000000; % The X-Ray wave length (m)
a = 5.6578/10000000000; % Unit cell constant
R_elctron = 2.817940325/100000000000000; % Electron radius (m)
% The following 2 lines prepare new parameters needed for XRD for Ge(111) and kills the above parameters
Ge=XRD_inputsV8_m_s(F0_Re, F0_Im, Fpsi_Re, Fpsi_Im, DWF, Pol_flag, Theta_B, lambda, a, R_elctron);
clearvars F0_Re F0_Im Fpsi_Re Fpsi_Im DWF Pol_flag Theta_B lambda a R_elctron;
```

In this part we simulate the TDXR for the Ge(111) 180 nm

```
Theta_max = 0.6;        % in case of lager earea you should change it to the larger amounts. (°)
Theta_min = -0.8;       % in case of lager earea you should change it to the larger amounts. (°)
N = 280;                % Number of points in the range Theta_min to Theta_max
thetaDelta = (Theta_max-Theta_min)/N;
step = 3;
UMin = 0;               % the time span that the RC will be calculated [UMin ,UMax]
UMax = 279;             % the time span that the RC will be calculated [UMin ,UMax]
R0 = zeros(1,N+1);     % allocating the arrays that the results of calculation will be saved
R = zeros(N+1,((UMax-UMin)/step)+1); % allocating the arrays that the results of calculation will be saved
RR0 = zeros(1,N+1);    % allocating the arrays that the results of calculation at time zero will be saved
RR = zeros(N+1,1);     % allocating the arrays that the results of calculation at time zero will be saved
%Tofset = (2.3721)/1000000000000; % the offset of time in (s) for 60 microjule
%Tofset = (2.671)/1000000000000; % the offset of time in (s) for 45 microjule
Tofset = (2.862)/1000000000000; % the offset of time in (s) for 90m]
```

Here we calculate the rocking curves

Calculation of the rocking curve at time zero

```
T = 0;
tic
for j = 1:N+1
    theta=Theta_min+(j-1)*thetaDelta;
```

```

gamma_zero = -sin((theta+Ge.theta_B)*pi/180);
gamma_H = gamma_zero + 2*sin(Ge.theta_B*pi/180);
myfact = sqrt(abs(gamma_zero.*gamma_H));
Amax = Ge_D./(Ge.A_T.*myfact); % thickness to the reduced coordinate

[A,X]=ode45('d_DynXDiffEquFilmV8_m_s',[Amax,0], [0;0], [], theta, Ge.k, Ge.g_c, Ge.y_a, Ge.y_c, Ge.theta_B,T, Ge_D,
Ge.A_T, Ge_Velocity, Ge_impedance, Si_impedance, Ge_R_el_th, Ge_tau_1,Ge_TT, Ge_tau_2, Ge_yna ,Ge_P_thL);
RR0(j) = (X(length(A),1).^2 + X(length(A),2).^2); %calculation of the X-ray reflectivity
end;
RR(:,1)=RR0;
ExecTime = toc

% calculation of rocking curves at delay times T > 0
for tt =UMin:step:UMax
    T = (tt/1000000000000)+Tofset; % determination of time delays that the rocking curves are calculated
    tic
    %begining of the loop which calculates the rocking curve for the given time delay
    for j = 1:N+1
        theta=Theta_min+(j-1)*thetaDelta;
        gamma_zero = -sin((theta+Ge.theta_B)*pi/180);
        gamma_H = gamma_zero + 2*sin(Ge.theta_B*pi/180);
        myfact = sqrt(abs(gamma_zero.*gamma_H));
        Amax = Ge_D./(Ge.A_T.*myfact);% thickness to the reduced coordinate
        [A,X]=ode45('d_DynXDiffEquFilmV8_m_s',[Amax,0], [0;0], [], theta, Ge.k, Ge.g_c, Ge.y_a, Ge.y_c, Ge.theta_B,T, Ge_D,
Ge.A_T, Ge_Velocity, Ge_impedance, Si_impedance, Ge_R_el_th, Ge_tau_1,Ge_TT, Ge_tau_2, Ge_yna, Ge_P_thL);
        R0(j) = (X(length(A),1).^2 + X(length(A),2).^2); %calculation of the X-ray reflectivity
    end;
    R(:,(tt-UMin)/step+1)=R0;
    ExecTime = toc
end;

```

In this part we present and save Ge results

```

%initialization of the arrays which will be needed to show and save the data
CenterGrav = zeros(((UMax-UMin)/step)+1 , 1);
CenterGrav_corr = zeros(((UMax-UMin)/step)+1 , 1);
Int_Intensity = zeros(((UMax-UMin)/step)+1 , 1);
M0 = 0;
M1 = 0;
for j=1:N+1
    M1 = M1 + RR(j,1)*(Theta_min +(Theta_max - Theta_min)*(j-1)/(N));
    M0 = M0 + RR(j,1);
end;
CenterGrav_T0 = M1/M0;
Int_Intensity_T0 = M0;

```

```

for tt =UMin:step:UMax
    M0 = 0;
    M1 = 0;
    for j=1:N+1
        M1 = M1 + R(j,((tt-UMin)/step)+1)*(Theta_min +(Theta_max - Theta_min)*(j-1)/(N));
        M0 = M0 + R(j,((tt-UMin)/step)+1);
    end;
    CenterGrav(((tt-UMin)/step)+1,1) = M1/M0;
    Int_Intensity(((tt-UMin)/step)+1,1) = M0;
end;
for tt =UMin:step:UMax
    CenterGrav_corr(((tt-UMin)/step)+1,1) = CenterGrav_T0 - CenterGrav(((tt-UMin)/step)+1,1);
end;
Times = ((UMin:step:UMax))+ (Tofset*1000000000000);
%the center of gravity is plotted here
plot(Times,CenterGrav_corr,'-o');
xlabel('time [ps]');
ylabel('angular shift [°]');
axis([0 300 -0.002 0.14])
%here some horizontal lines are drawn at the plot
line([Ge_D/Ge_Velocity*1000000000000 Ge_D/Ge_Velocity*1000000000000],[0 0.2],'color',[.8 .8 .8])
line([2*Ge_D/Ge_Velocity*1000000000000 2*Ge_D/Ge_Velocity*1000000000000],[0 0.2],'color',[.8 .8 .8])
line([3*Ge_D/Ge_Velocity*1000000000000 3*Ge_D/Ge_Velocity*1000000000000],[0 0.2],'color',[.8 .8 .8])
line([4*Ge_D/Ge_Velocity*1000000000000 4*Ge_D/Ge_Velocity*1000000000000],[0 0.2],'color',[.8 .8 .8])
line([5*Ge_D/Ge_Velocity*1000000000000 5*Ge_D/Ge_Velocity*1000000000000],[0 0.2],'color',[.8 .8 .8])
line([6*Ge_D/Ge_Velocity*1000000000000 6*Ge_D/Ge_Velocity*1000000000000],[0 0.2],'color',[.8 .8 .8])
%here we prepare arrays with the data we want to save
My_size = size(Times);
%here we prepare the array of centre of gravity shift and save it
m_save_array=zeros([My_size(2)+1 2]);
m_save_array(1,1) = 0;
m_save_array(1,2) = 0;
m_save_array(2:end,1) = Times(:);
m_save_array(2:end,2) = CenterGrav_corr(:);
filename = 'C:\calculated_data\Ge\90m\1_exp\khata\mycenter_grav_Ge_90m\publish.txt';
save(filename,'m_save_array','-ASCII','-tabs');
clearvars CenterGrav_T0 CenterGrav CenterGrav_corr m_save_array;
%here we prepare the array of Int_intensity and save it
m_save_array_Int = zeros([My_size(2)+1 2]);
m_save_array_Int(1,1) = 0;
m_save_array_Int(1,2) = Int_Intensity_T0;
m_save_array_Int(2:end,1) = Times(:);
m_save_array_Int(2:end,2) = Int_Intensity(:);
filename = 'C:\calculated_data\Ge\90m\1_exp\khata\my_Int_Ge_90m\publish.txt';
save(filename,'m_save_array_Int','-ASCII','-tabs');

```

```

clearvars Int_Intensity_T0 Int_Intensity m_save_array_Int;
%here we prepare an array of RC and save it
m_save_RC = zeros(N+1,((UMax-UMin)/step)+3);
Angles = Theta_min:(Theta_max-Theta_min)/(N):Theta_max;
m_save_RC(:,1) = Angles';
m_save_RC(:,2) = RR;
m_save_RC(:,3:end) = R;
filename = 'C:\calculated_data\Ge\90mJ\1_exp\khata\RC_Ge_90mJ_publish.txt';
save(filename,'m_save_RC','-ASCII','-tabs');
clearvars RR R R0 RR0;
%here we prepare a table of parameters and save it
par = [Ge_D; Ge_Velocity; Ge_impedance; Ge_R_el_th; Ge_tau_1; Ge_TT; Ge_tau_2;Ge_yna ;Ge_P_thL;Theta_max;
Theta_min;N+1;UMin;UMax;step;thetaDelta];
Parlist ={'Thickness';'Sound velocity';'Acoustic Impedance';'Electronic/Thermal pressure1';...
'Auger decay rate1 ','Electronic/Electronic Density ratio';'Auger decay rate2 ','constant electronic density
ratio';'Initial Lattice thermal pressure';'Max delta theta';'Min delta theta';...
'No. point in RC';'Initial Time';'Final Time';'time step';'delta_theta'};
my_table = table(par,'RowNames',Parlist);
filename = 'C:\calculated_data\Ge\90mJ\1_exp\khata\Par_Ge_90mJ_publish.txt';
writetable(my_table,filename,'Delimiter','\t','WriteRowNames',true);
%clearvars -except Ge Ge_D Ge_P_th Ge_R_el_th Ge_Velocity Ge_impedance Ge_tau Si Si_D Si_Velocity Si_impedance;
display ('Ge calculation is done');
display ('done!!!!');

```

### Main program for calculation the transient rocking curves of Si (111) after excitation:

```

close all;
clear all;
clc;

```

In this part we define all parameters needed for Ge (111) strain profile

```

Ge_D = 180/1000000000;           % Thickness of Ge (m)
Ge_Velocity = 5510;             % sound velocity of Ge(111) (m/s)
Ge_impedance = 29337444;        % Ge acoustic impedance [density(kg/m3)* Velocity(m/s)]
Ge_R_el_th = 0;                 % the ratio between the amplitude of first exponential in electronic
pressur to thermal pressur
Ge_tau_1 = 58/1000000000000;     % first decay time for auger process (s)
Ge_TT = 0;                       % ratio between the second exponential term of electronic peressur to
thermal pressur
Ge_tau_2 = 257.15/1000000000000; % second auger decay time (s)

```

## Appendixes

---

```
Ge_yna = 0; % ratio between constant term in electronic pressur to the thermal one
Ge_P_thL = 292500000; % the optical induced thermal pressur at long delays
```

In this part we define all parameters needed for Si (111) strain profile

```
Si_D = 50/1000000; % Thickness of Si (m)
Si_Velocity = 9322; % sound velocity of Si(111) (m/s)
Si_impedance = 21713734.6; % Si acoustic impedance [density(kg/m3)* Velocity(m/s)]
```

Here we define all parameters for Si (111) needed for XRD

```
F0_Re = 115.46549984000001; % Structural factors in forward direction (source XOP) real part
F0_Im = 7.6741371200000001; % Structural factors in forward direction (source XOP) imaginary part
Fpsi_Re = 62.994932369856933; % Structural factor for (111) reflection (source XOP) real part
Fpsi_Im = 5.4264343973073990; % Structural factor for (111) reflection (source XOP) imaginary part
DWF = 1; % Debye_waller factor
Pol_flag = 1; % This flag determines the polarization of the X-Ray [0 means s pol]
Theta_B = 25.995262500865682; % Bragg angle for Si(111) (°)
lambda = 2.748486/10000000000; % The X-Ray wave length (m)
a = 5.4309/10000000000; % Unit cell constant
R_elctron = 2.817940325/1000000000000000; % Electron radius (m)
% The following 2 lines prepare new parameters needed for XRD for Si(111)
% and kills the above parameters
Si=XRD_inputsV8_m_s(F0_Re, F0_Im, Fpsi_Re, Fpsi_Im, DWF, Pol_flag, Theta_B, lambda, a, R_elctron);
clearvars F0_Re F0_Im Fpsi_Re Fpsi_Im DWF Pol_flag Theta_B lambda a R_elctron;
```

In this part we simulate the TDXRD for the Ge (111) 170 nm

```
Theta_max = 0.05; % in case of lager earea you should change it to the larger amounts. (°)
Theta_min = -0.05; % in case of lager earea you should change it to the larger amounts. (°)
N = 200; % Number of points in the range Theta_min to Theta_max
thetaDelta = (Theta_max-Theta_min)/N;
Times = [65.34]; % this vector determines the delay times at which the rocking curve
should be calculated
nt = size(Times,2);
R0 = zeros(1,N+1); % allocating the arrays that the results of calculation will be saved
R = zeros(N+1,nt); % allocating the arrays that the results of calculation will be saved
RR0 = zeros(1,N+1); % allocating the arrays that the results of calculation at time zero will be
saved
RR = zeros(N+1,1); % allocating the arrays that the results of calculation at time zero will be
saved
```

Here we calculate the Rocking curves  
Calculation of rocking curve at time zero

```

T = 0;
tic
for j = 1:N+1
    theta=Theta_min+(j-1)*thetaDelta;
    gamma_zero = -sin((theta+Si.theta_B)*pi/180);
    gamma_H = gamma_zero + 2*sin(Si.theta_B*pi/180);
    myfact = sqrt(abs(gamma_zero.*gamma_H));
    Amax = Si_D./(Si.A_T.*myfact);           % thickness to the reduced coordinate
    [A,X]=ode45('d_DynXDiffEquSubsV8_m_s',[Amax,0], [0;0], [], theta, Si.k, Si.g_c, Si.y_a, Si.y_c, Si.theta_B,T, Ge_D,
    Si.A_T, Ge_Velocity, Si_Velocity, Ge_impedance, Si_impedance, Ge_R_el_th, Ge_tau_1,Ge_TT, Ge_tau_2, Ge_yna ,Ge_P_thL);
    RR0(j) =(X(length(A),1).^2 + X(length(A),2).^2);   %calculation of the X-ray reflectivity
end;
RR(:,1)=RR0;
ExecTime = toc
% calculation of rocking curve at time T>0
for ntt = 1:nt
    T = Times(ntt)/1000000000000;           % determination of time delays that the rocking curves are calculated
    tic
    %begining of the loop which calculates the rocking curve for the given time delay
    for j = 1:N+1
        theta=Theta_min+(j-1)*thetaDelta;
        gamma_zero = -sin((theta+Si.theta_B)*pi/180);
        gamma_H = gamma_zero + 2*sin(Si.theta_B*pi/180);
        myfact = sqrt(abs(gamma_zero.*gamma_H));
        Amax = Si_D./(Si.A_T.*myfact);           % thickness to the reduced coordinate
        [A,X]=ode45('d_DynXDiffEquSubsV8_m_s',[Amax,0], [0;0], [], theta, Si.k, Si.g_c, Si.y_a, Si.y_c, Si.theta_B,T, Ge_D,
        Si.A_T, Ge_Velocity, Si_Velocity, Ge_impedance, Si_impedance, Ge_R_el_th, Ge_tau_1,Ge_TT, Ge_tau_2, Ge_yna ,Ge_P_thL);
        R0(j) =(X(length(A),1).^2 + X(length(A),2).^2);   %calculation of the X-ray reflectivity
    end;
    R(:,ntt)=R0;
    ExecTime = toc
    %end of the main time loop
end;

```

In this part we present and save Ge results

Here the temporal dependence of Si rocking curve profile in a false color representation will be shown as results

```

Int_Intensity = zeros(nt, 1);
Int_Intensity_T0 = 0;
for j=1:N+1
    Int_Intensity_T0 = Int_Intensity_T0 + RR(j,1);
end;
for ntt=1:nt

```

```

M0 = 0;
for j=1:N+1
    M0 = M0 + R(j,ntt);
end;
Int_Intensity(ntt,1) = M0;
end;
imagesc(Times,[Theta_min Theta_max],R)
colorbar
xlabel('time [ps.]');
ylabel('angular shift [deg.]');
%here we prepare arrays with the data we want to save
My_size = size(Times);
%here we prepare the array of Int_intensity and save it
m_save_array_Int = zeros([My_size(2)+1 2]);
m_save_array_Int(1,1) = 0;
m_save_array_Int(1,2) = Int_Intensity_T0;
m_save_array_Int(2:end,1) = Times(:);
m_save_array_Int(2:end,2) = Int_Intensity(:);
filename = 'C:\Users\Ultra125\Desktop\test_symetry\my_Int_Si_1_ppol_28_02_2018_publish.txt';
save(filename,'m_save_array_Int','-ASCII','-tabs');
clearvars Int_Intensity_T0 Int_Intensity m_save_array_Int;
%here we prepare an array of RC and save it
m_save_RC = zeros(N+1,nt+2);
Angles = Theta_min:(Theta_max-Theta_min)/(N):Theta_max;
m_save_RC(:,1) = Angles';
m_save_RC(:,2) = RR;
m_save_RC(:,3:end) = R;
filename = 'C:\Users\Ultra125\Desktop\test_symetry\RC_Si_1_ppol_28_02_2018_publish.txt';
save(filename,'m_save_RC','-ASCII','-tabs');
clearvars RR R m_save_RC R0 RR0;
%here we prepare a table of parameters and save it
par = [Si_D; Si_Velocity; Si_impedance; Ge_impedance; Ge_R_el_th; Ge_tau_1; Ge_TT; Ge_tau_2; Ge_yna; Ge_P_thL;
Theta_max; Theta_min; N+1; nt; thetaDelta; Si.pol];
Parlist ={'Si-Thickness';'Si-Sound velocity';'Si-Acoustic Impedance';'Ge-Acoustic Impedance';'Electronic/Thermal
pressure';...
'Auger decay rate-1 ';'Electronic/Electronic Density ratio';'Auger decay rate-2 ';'constant electronic density
ratio';'Initial thermal pressure';'Max delta theta';'Min delta theta';...
'No. point in RC';'Number of delay time points';'delta_theta';'polarization flag (0 means s pol)'};
my_table = table(par,'RowNames',Parlist);
filename = 'C:\Users\Ultra125\Desktop\test_symetry\Par_Si_1_ppol_28_02_2018_publish.txt';
writetable(my_table,filename,'Delimiter','\t','WriteRowNames',true);
display('DONE');

```

In the following the sub-functions, which are used in the main codes, are presented.

**The sub-function, which calculates the strain profile in a half-space bulk sample:**

```
function S = d_strainT1_m_s(A, Time, Velocity1, Velocity2, impedance, R_el_th, tau_1, TT, tau_2, yna, P_thL)
% *****
% this function calculates the strain profile for a half space bulk sample
% #####
% INPUTS
% #####
% A : the spatial coordinate ('x')
% Time : the delay time in the experiment
% Velocity1 : the sound velocity in the direction of strain propagation
% Velocity2 : the sound velocity in the direction of strain propagation in the second material " this one is used just
in case of 2 layered materials"
% impedance : the acoustic impedance of the material( density * velocity)
% R_el_th : the ratio between the amplitude of first exponential in electronic pressur to thermal pressur
% tau_1 : first decay time for auger process
% TT : ratio between the second exponential term of electronic peressur to thermal pressur
% tau_2: second auger decay time
% yna : ratio between constant term in electronic pressur to the thermal one
% P_th : the optical induced thermal pressur at long delays
% #####
% OUTPUT
% #####
% S : propagating strain in the material
% #####
% Mohammadmahdi Afshari
% 12-04-2017
% University of Duisburg-Essen
% *****

if Velocity1 == Velocity2
    if A >= (Time*Velocity1)
        S = 0;
    else
        S = (1/(impedance*Velocity1)) * P_thL * (1+ R_el_th*yna +R_el_th * exp(-(Time-(A/Velocity1))/tau_1)+
TT*R_el_th * exp(-(Time-(A/Velocity1))/tau_2));
    end
else
    if A >= (Time*Velocity2)
        S = 0;
    else

```

```
S = (1/(impedance*Velocity1)) * P_thL * (1+ R_el_th*yna+ R_el_th * exp(-(Time-(A/Velocity2))/tau_1)+
TT*R_el_th * exp(-(Time-(A/Velocity2))/tau_2));
end
end
```

**The sub-function, which calculates the strain profile in a thin film:**

```
function SF = d_strainThinfilm_m_s(A, Time, Thickness_Film, Velocity_Film, impedance_Film, impedance_Subs,
R_el_th, tau_1, TT, tau_2, yna, P_thL)
% *****
% this function calculates the strain profile in the thin film
% #####
% INPUTS
% #####
% A : the coordinate of thin film starting from the free surface
% Time : Delay Time
% Thickness_Film : thickness of the thin film
% Velocity_Film : sound velocity in the thin film in direction of strain propagation
% impedance_Film : Acoustic impedance of the thin film
% impedance_Subs : Acoustic impedance of the substrate
% R_el_th : the ratio between the amplitude of first exponential in electronic pressur to thermal pressur
% tau_1 : first decay time for auger process
% TT : ratio between the second exponential term of electronic peressur to thermal pressur
% tau_2: second auger decay time
% yna : ratio between constant term in electronic pressur to the thermal one
% P_th : the optical induced thermal pressur at long delays
% #####
% OUTPUT
% #####
% SF : propagating strain in the thin film
% #####
% Mohammadmahdi Afshari
% 12-04-2017
% University of Duisburg-Essen
% *****

%here we define local variables equal to the input parameters
T = Time;
D = Thickness_Film;
V1 = Velocity_Film;
V2 = Velocity_Film;
% Reflection coefficient at the Germanium-Silicon interface.
```

```

R = (impedance_Subs - impedance_Film)/(impedance_Subs + impedance_Film);
% Relative amplitude of strain between Ge_Si and Ge_Vacuum
relative_amp_Film = impedance_Film/(impedance_Film+impedance_Subs);
%The following line describes the wave originated from the Germanium-vacuum interface
SF1 = d_strainT1_m_s(A, T, V1, V2, impedance_Film, R_el_th, tau_1, TT, tau_2, yna, P_thL) + R*d_strainT1_m_s(-A, T-
(2*D)/V1, V1, V2, impedance_Film, R_el_th, tau_1,TT, tau_2, yna, P_thL)...
-R*d_strainT1_m_s(A, T-(2*D)/V1, V1, V2, impedance_Film, R_el_th, tau_1,TT, tau_2, yna, P_thL) -
R*R*d_strainT1_m_s(-A, T-(4*D)/V1, V1, V2, impedance_Film, R_el_th, tau_1,TT, tau_2, yna, P_thL)...
+R*R*d_strainT1_m_s(A, T-(4*D)/V1, V1, V2, impedance_Film, R_el_th, tau_1,TT, tau_2, yna, P_thL)
+R*R*R*d_strainT1_m_s(-A, T-(6*D)/V1, V1, V2, impedance_Film, R_el_th, tau_1,TT, tau_2, yna, P_thL)...
-R*R*R*d_strainT1_m_s(A, T-(6*D)/V1, V1, V2, impedance_Film, R_el_th, tau_1,TT, tau_2, yna, P_thL) -
R*R*R*R*d_strainT1_m_s(-A, T-(8*D)/V1, V1, V2, impedance_Film, R_el_th, tau_1,TT, tau_2, yna, P_thL)...
+R*R*R*R*d_strainT1_m_s(A, T-(8*D)/V1, V1, V2, impedance_Film, R_el_th, tau_1,TT, tau_2, yna,
P_thL)+R*R*R*R*R*d_strainT1_m_s(-A, T-(10*D)/V1, V1, V2, impedance_Film, R_el_th, tau_1,TT, tau_2, yna, P_thL);
%The following line describes the wave originated from the Germanium-silicon interface
SF2 = d_strainT1_m_s(-A, T-(D)/V1, V1, V2, impedance_Film, R_el_th, tau_1,TT, tau_2, yna, P_thL) - d_strainT1_m_s(A,
T-(D)/V1, V1, V2, impedance_Film, R_el_th, tau_1,TT, tau_2, yna, P_thL)...
-R*d_strainT1_m_s(-A, T-(3*D)/V1, V1, V2, impedance_Film, R_el_th, tau_1,TT, tau_2, yna, P_thL)
+R*d_strainT1_m_s(A, T-(3*D)/V1, V1, V2, impedance_Film, R_el_th, tau_1,TT, tau_2, yna, P_thL)...
+R*R*d_strainT1_m_s(-A, T-(5*D)/V1, V1, V2, impedance_Film, R_el_th, tau_1,TT, tau_2, yna, P_thL) -
R*R*d_strainT1_m_s(A, T-(5*D)/V1, V1, V2, impedance_Film, R_el_th, tau_1,TT, tau_2, yna, P_thL)...
-R*R*R*d_strainT1_m_s(-A, T-(7*D)/V1, V1, V2, impedance_Film, R_el_th, tau_1,TT, tau_2, yna, P_thL)
+R*R*R*d_strainT1_m_s(A, T-(7*D)/V1, V1, V2, impedance_Film, R_el_th, tau_1,TT, tau_2, yna, P_thL)...
+R*R*R*R*d_strainT1_m_s(-A, T-(9*D)/V1, V1, V2, impedance_Film, R_el_th, tau_1,TT, tau_2, yna, P_thL)-
R*R*R*R*d_strainT1_m_s(A, T-(9*D)/V1, V1, V2, impedance_Film, R_el_th, tau_1,TT, tau_2, yna, P_thL);
%the result is a sum of the two waves
SF = SF1 + relative_amp_Film * SF2;

```

**The sub-function, which calculates the strain profile in a substrate (bulk):**

```

function SB = d_strain_subs_m_s(A_S, Time, Thickness_Film, Velocity_Film, Velocity_Subs , impedance_Film,
impedance_Subs, R_el_th, tau_1, TT, tau_2 , yna, P_thL)
% *****
% this function calculates the strain profile of the substrate
% #####
% INPUTS
% #####
% A_S : the coordinate of substrate starting from the interface
% Time : Delay Time
% Thickness_Film : thickness of the thin film
% Velocity_Film : sound velocity in the thin film in direction of strain propagation
% Velocity_Subs : sound velocity in the sunstrate in direction of strain propagation

```

```

% impedance_Film : Acoustic impedance of the thin film
% impedance_Subs : Acoustic impedance of the substrate
% R_el_th : the ratio between the amplitude of first exponential in electronic pressur to thermal pressur
% tau_1 : first decay time for auger process
% TT : ratio between the second exponential term of electronic peressur to thermal pressur
% tau_2: second auger decay time
% yna : ratio between constant term in electronic pressur to the thermal one
% P_th : the optical induced thermal pressur at long delays
#####
% OUTPUT
#####
% SB : propagating strain in the substrate
#####
% Mohammadmahdi Afshari
% 12-04-2017
% University of Duisburg-Essen
% *****

%here we define local variables equal to the input parameters
T = Time;
D_F = Thickness_Film;
V_F = Velocity_Film;
V_S = Velocity_Subs;
% Reflection coefficient at the Germanium-Silicon interface.
R = (impedance_Subs - impedance_Film)/(impedance_Subs + impedance_Film);
%Transmission coefficient at the Germanium-Silicon interface.
L = (V_F/V_S)*((2*impedance_Film)/(impedance_Subs + impedance_Film));
% Relative amplitude of strain between Ge_Si and Ge_Vacuum for substrate
relative_amp_Sub = -impedance_Subs/(impedance_Film+impedance_Subs);
%a constant which is used in strain profile inside the substrate originated from Ge_Si interface
meh = (L*impedance_Film)/(impedance_Film+impedance_Subs);
%The following line define the strain profile originated from vacumm and Ge transmitted into the Si
SB1 = L*d_strainT1_m_s(A_S, T-(1*D_F/V_F), V_F, V_S, impedance_Film, R_el_th, tau_1, TT, tau_2 , yna, P_thL)-
L*R*d_strainT1_m_s(A_S, T-(3*D_F/V_F), V_F, V_S, impedance_Film, R_el_th, tau_1, TT, tau_2 , yna, P_thL)...
+ L*R*R*d_strainT1_m_s(A_S, T-(5*D_F/V_F), V_F, V_S, impedance_Film, R_el_th, tau_1, TT, tau_2 , yna, P_thL)-
L*R*R*R*d_strainT1_m_s(A_S, T-(7*D_F/V_F), V_F, V_S, impedance_Film, R_el_th, tau_1, TT, tau_2 , yna, P_thL)...
+ L*R*R*R*R*d_strainT1_m_s(A_S, T-(9*D_F/V_F), V_F, V_S, impedance_Film, R_el_th, tau_1, TT, tau_2 , yna, P_thL);
%The following line define the strain profile originated from Si and Ge, transmitted into the Si
SB2 = -d_strainT1_m_s(A_S, T-(2*D_F/V_F), V_F, V_S, impedance_Film, R_el_th, tau_1, TT, tau_2 , yna, P_thL) +
R*d_strainT1_m_s(A_S, T-(4*D_F/V_F), V_F, V_S, impedance_Film, R_el_th, tau_1, TT, tau_2 , yna, P_thL)...
-R*R*d_strainT1_m_s(A_S, T-(6*D_F/V_F), V_F, V_S, impedance_Film, R_el_th, tau_1, TT, tau_2 , yna, P_thL)
+R*R*R*d_strainT1_m_s(A_S, T-(8*D_F/V_F), V_F, V_S, impedance_Film, R_el_th, tau_1, TT, tau_2 , yna, P_thL)...
-R*R*R*R*d_strainT1_m_s(A_S, T-(10*D_F/V_F), V_F, V_S, impedance_Film, R_el_th, tau_1, TT, tau_2 , yna, P_thL);
SB2 = meh*SB2 + relative_amp_Sub*d_strainT1_m_s(A_S, T, V_S, V_S, impedance_Subs, R_el_th, tau_1, TT, tau_2 , yna,
P_thL);

```

```
%the result is a sum of the two waves
SB = SB1 + SB2;
```

**The sub-function, which provides the diff. equation for the dynamical X-ray diffraction in a thin film:**

```
function dX_Film = d_DynXDiffEquFilmV8_m_s(A, X_F, flag, theta, k, g_c, y_a, y_c, theta_B, Time, Thickness_Film, A_T,
Velocity_Film, impedance_Film, impedance_Subs, R_el_th, tau_1, TT, tau_2, yna, P_thL)
% *****
% this function provides the equation used in differential equation for Dynamic X-Ray diffraction for the thin film
% #####
% INPUTS
% #####
% R_A : the reduced spatial coordinate of thin film starting from the free surface
% X_F : the complex scattering amplitude for the thin film
% y : the reduced angular coordinate
% g : the parameter used in the x-ray dynamic equation, Larson paper
% k : the parameter used in the x-ray dynamic equation, Larson paper
% Angle_to_y : the coefficient used in the definition of y. (y = Angle_to_y * delta theta)
% Time : Delay Time
% Thickness_Film : thickness of the thin film
% Thickness_to_Acomplex : the coefficient used in the definition of R_A ( R_A = Thickness_to_Acomplex * z) here z is
the spatial coordinate.
% Velocity_Film : sound velocity in the thin film in direction of strain propagation
% impedance_Film : Acoustic impedance of the thin film
% impedance_Subs : Acoustic impedance of the substrate
% R_el_th : the ratio between the amplitude of first exponential in electronic pressure to thermal pressure
% tau_1 : first decay time for Auger process
% TT : ratio between the second exponential term of electronic pressure to thermal pressure
% tau_2 : second Auger decay time
% yna : ratio between constant term in electronic pressure to the thermal one
% P_th : the optical induced thermal pressure at long delays
% #####
% OUTPUT
% #####
% dX_Film : the function provides the equation used in differential equation for Dynamic X-Ray diffraction for the thin
film
% #####
% Mohammadmahdi Afshari
% 12-04-2017
% University of Duisburg-Essen
% *****
```

```

% first of all we need to calculate gamma_zero and gamma_H
gamma_zero = -sin((theta+theta_B)*pi/180);
%gamma_H = (gamma_zero + 2*sin(theta_B*pi/180))./(sqrt(1+ 4*sin(theta_B*pi/180)*sin(theta_B*pi/180) +
4*gamma_zero*sin(theta_B*pi/180)));
gamma_H=(gamma_zero + 2*sin(theta_B*pi/180));
% first of all we need to calculate the strain profile in the thin film
ttt = A_T.*A*sqrt(abs(gamma_zero.*gamma_H));
%ttt = A_T.*A.*sin(theta_B*pi/180);
SF = d_strainThinfilm_m_s(ttt, Time, Thickness_Film, Velocity_Film, impedance_Film, impedance_Sub, R_el_th,
tau_1,TT, tau_2, yna, P_thL);
%plot(ttt,SF);
% here we define constant b (which is theta dependent)
b = gamma_zero./(gamma_zero + 2*sin(theta_B*pi/180));
% here we define g
g = g_c*((b-1)./sqrt(abs(b)));
% here we define alphaH
alphaH = 4*sin(theta_B*pi/180)*( sin(theta_B*pi/180)+ gamma_zero - gamma_H.*SF );
%alphaH = 4*sin(theta_B*pi/180)*( sin(theta_B*pi/180)+ gamma_zero -
2*sin(2*theta_B*pi/180)*tan(theta_B*pi/180).*SF);
%alphaH = -2*sin(2*theta_B*pi/180)*(theta*pi/180); % for version 9
% here we define y
y = y_a * (b.*alphaH)./sqrt(abs(b)) + y_c*((b-1)./sqrt(abs(b)));
%here the differential equation to be calculated is determined
dX_Film = [k*(X_F(1).^2 - X_F(2).^2 + 1) + 2*X_F(2).*( X_F(1) - y)-2*g*X_F(1) ; -(X_F(1).^2 - X_F(2).^2 + 1) +
2*X_F(1).*(X_F(2)*k + y) - 2*g*X_F(2)];

```

**The sub-function, which provides the diff. equation for the dynamical X-ray diffraction in a substrate:**

```

function dX_Sub = d_DynXDiffEquSubsV8_m_s(R_A_S, X_S, flag, theta_S, k_S, g_c_S, y_a_S, y_c_S, theta_B_S, Time,
Thickness_Film, A_T_S,Velocity_Film, Velocity_Sub, impedance_Film, impedance_Sub, R_el_th, tau_1, TT, tau_2 , yna,
P_thL)
% *****
% this function provides the equation used in diffrential equation for Dynamic X-Ray diffraction for the thin film
% #####
% INPUTS
% #####
% R_A : the reduced spatial coordinate of thin film starting from the free surface
% X_F : the complex scattering amplitude for the thin film
% y : the reduced angular coordinate
% g : the parameter used in the x-rax dynamic equation, Larson paper

```

```

% k : the parameter used in the x-rax dynamic equation, Larson paper
% Angle_to_y : the coefficient used in the deffinition of y. (y = Angle_to_y * delta theta)
% Time : Delay Time
% Thickness_Film : thickness of the thin film
% Thickness_to_Acomplex : the coeffincient used in the deffinition of R_A ( R_A = Thickness_to_Acomplex * z) here z is
the spatial coordinate.
% Velocity_Film : sound velocity in the thin film in direction of strain propagation
% impedance_Film : Acoustic impedance of the thin film
% impedance_Subs : Acoustic impedance of the substrate
% R_el_th : the ratio between the amplitude of first exponential in electronic pressur to thermal pressur
% tau_1 : first decay time for auger process
% TT : ratio between the second exponential term of electronic peressur to thermal pressur
% tau_2: second auger decay time
% yna : ratio between constant term in electronic pressur to the thermal one
% P_th : the optical induced thermal pressur at long delays
#####
% OUTPUT
#####
% dX_Film : the function provides the equation used in diffrentioal equation for Dynamic X-Ray diffraction for the thin
film
#####
% Mohammadmahdi Afshari
% 12-04-2017
% University of Duisburg-Essen
% *****

% first of all we need to calculate gamma_zero and gamma_H
gamma_zero = -sin((theta_S+theta_B_S)*pi/180);
%gamma_H = (gamma_zero + 2*sin(theta_B_S*pi/180))./(sqrt(1+ 4*sin(theta_B_S*pi/180)*sin(theta_B_S*pi/180)
+ 4*gamma_zero*sin(theta_B_S*pi/180)));
gamma_H=(gamma_zero + 2*sin(theta_B_S*pi/180));
% first of all we need to calculate the strain profile in the thin film
ttt = A_T_S.*R_A_S*sqrt(abs(gamma_zero.*gamma_H));
SB = d_strain_subs_m_s(ttt, Time, Thickness_Film, Velocity_Film, Velocity_Subs , impedance_Film, impedance_Subs,
R_el_th, tau_1, TT, tau_2 , yna, P_thL);
% here we define constant b (which is theta dependent)
b = gamma_zero./(gamma_zero + 2*sin(theta_B_S*pi/180));
% here we define g
g = g_c_S*((b-1)./sqrt(abs(b)));
% here we define alphaH
alphaH = 4*sin(theta_B_S*pi/180)*( sin(theta_B_S*pi/180)+ gamma_zero - gamma_H.*SB ); % ***** in originale
barnameh ast*****
%alphaH = -2*sin(2*theta_B_S*pi/180)*((theta_S*pi/180)+ (tan(theta_B_S*pi/180)*gamma_H.^2 +
abs(gamma_H).*sqrt(1-gamma_H.^2))*SB); % check assymetry strain homogenous
%alphaH = -2*sin(2*theta_B_S*pi/180)*((theta_S*pi/180)+ tan(theta_B_S*pi/180)*SB); % for version 9

```

```

% here we define y
y = y_a_S * (b.*alphaH)./sqrt(abs(b)) + y_c_S*((b-1)./sqrt(abs(b)));
%here the differential equation to be calculated is determined
dX Subs = [k_S*(X_S(1).^2 - X_S(2).^2 + 1) + 2*X_S(2).*( X_S(1) - y)-2*g*X_S(1) ; -(X_S(1).^2 - X_S(2).^2 + 1) +
2*X_S(1).*(X_S(2)*k_S + y) - 2*g*X_S(2)];

```

**The sub-function, which provides a structure, which contains parameters used in the diff. equation for X-ray diffraction (two last above sub-functions):**

```

function Sample = XRD_inputsV8_m_s(varargin)
% *****
% this function provides a structure which contains parameter used in XRD
% simulation
% #####
% INPUTS
% #####
% varargin{1} = F0_Re Structural factors in forward direction (source XOP) real part
% varargin{2} = F0_Im Structural factors in forward direction (source XOP) im part
% varargin{3} = Fpsi_Re Structural factors in an desired direction (source XOP) real part
% varargin{4} = Fpsi_Im Structural factors in an desired direction (source XOP) im part
% varargin{5} = DWF % Debye_waller factor in an desired direction
% varargin{6} = flag chooses the polarization [0 means s pol and 1 means p pol
% varargin{7} = Bragg angle (°)
% varargin{8} = lambda the wave length of the x-ray (m)
% varargin{9} = a unit cell constant (m)
% varargin{10} = R_elctron electron radius (m)
%#####
% OUTPUT
% #####
% Sample.KPol : polarization factor
% Sample.Vc : unit cell volum
% Sample.Thickness_to_Acomplex : the coefficient used to define reduced spatial coordinate
% Sample.g : a parameter in larson paper
% Sample.k : a parameter in larson paper
% Sample.Angle_to_y : the coefficient used to define reduced angular coordinate
% #####
% Mohammadmahdi Afshari
% 12-04-2017
% University of Duisburg-Essen
% *****
switch nargin
case 10

```

```

if varargin{6} == 0
    Sample.KPol = 1; % s pol
else
    Sample.KPol = cos(2*varargin{7}*pi/180); % P polarization
end

Sample.Vc = varargin{9}*varargin{9}*varargin{9};
Sample.A_T = Sample.Vc./(Sample.KPol * varargin{10} * varargin{5} * varargin{3}*varargin{8});
Sample.g_c = 0.5*(varargin{2}/(Sample.KPol*varargin{5}*varargin{3}));
Sample.k = varargin{4}/varargin{3};
Sample.y_a = (pi*Sample.A_T)/(2*varargin{8}); % this is for symmetric case not for asymmetric diffraction
Sample.y_c = 0.5*(varargin{1}/(Sample.KPol*varargin{5}*varargin{3}));
Sample.theta_B = varargin{7};
Sample.pol = varargin{6};
otherwise
    error(' Invalid number of input arguments. It has to contain 10 inputs')
end

```

The following code was used to solve the diffusion equation of photo-excited carriers in Ge after excitation.

```

% This is a code which calculates density of electrons deffiusuin equation
% after excitation with a fs pulse. It uses crank-niconson method with
% neumann boundary conditions
% #####
% Mohammadmahdi Afshari
% 12-04-2017
% University of Duisburg-Essen
% *****
clc;
close all;
clear all;

```

Here we define the parameters used in the simulation

```

filename = 'electrondiff_publish.gif';
L = 180/1000000000; % film thicknes (m)
dx = 10/1000000000; % delta x (m)
N = ceil(L/dx)+1; % number od nodes in x direction

T = 2/1000000000000; % intersted Time interval (s)
dt= 1/100000000000000; % delta t (s)

```

```

M = ceil(T/dt)+1; % number of time steps

% here we define the diffusion coefficient
D = 0.025; % m2/s ref.PRB26 N,4 1982 Jeff F.Young
r = (D*dt)/(dx*dx); % parameter of the method

R = 0.44180; % sample reflectivity for s polarisation at 800 nm at angle
16.3 °
F = 11.69; % Incident fluence (mJ/cm2)
Eph= 1.58 * 1.60218e-16; % photon energy 800 nm (mj)
kesi = 200/1000000000; % absorption depth at 800 nm(m)
U0 = ((1-R)*F)/(Eph*kesi*100); % density at x = 0 (1/cm3)
U_mean = (1-R)*(1-exp(-L/kesi))*(F/(Eph*L*100));
% here we prepare matrixes used in the code
u = zeros(N,M);
uu = zeros(N,1);

```

Here we prepare the matrix M and initial conditions and x and time axis

```

% Initial value of U (density 1/cm3)
for i = 1:N
    x(i) = (i-1)*dx;
    u(i,1)= U0*exp(-x(i)/kesi);
end

% here we prepare the time axis
for k = 1:M
    tt(k) = (k-1)*dt;
end

% here we creat matrix MM
aa(1:N-3) = -1*r;
bb(1:N-2) = 2*(1+r);
cc(1:N-3) = -1*r;

MM = diag(bb,0) + diag(aa,1) + diag(cc,-1);
MM(1,1) = 2+(2*r/3);
MM(1,2) = -1*2*r/3;
MM(N-2,N-2) = 2+(2*r/3);
MM(N-2,N-3) = -1*2*r/3;

```

Here we implement Crank-Nicolson method

```

for k = 1: M-1
    uu = u(:,k);
    u(2:N-1,k+1) = MM\(((2-2*r)*uu(2:N-1)+ r*uu(1:N-2)+ r*uu(3:N));
    u(1,k+1) = (4/3)*u(2,k+1) - (1/3)*u(3,k+1);
    u(N,k+1) = (4/3)*u(N-1,k+1) - (1/3)*u(N-2,k+1);
end
min(u(:))
max(u(:))
display('Calculation is done!');
display('start plotting the results');
for k = 1:25:M
    figure (1); clf;
    plot(x,u(:,k),'LineWidth',2);
    ax =gca;
    set(ax,'LineWidth',1.5,'FontSize',0.1,'FontWeight','bold');
    xlim([0 L]);
    ylim([min(u(:)) max(u(:))]);
    %ylim([min(u(:)) 1.8e21]);
    title(['Delay Time= ' num2str(tt(k)*1000000000000000) ' fs;']);
    xlabel('Thickness [m]','FontSize',12,'FontWeight','bold');
    ylabel('Density [1/cm3] ','FontSize',12,'FontWeight','bold');
    %legend('Ge','Si')
    %pause(0.5);

    set(gcf,'color','w'); % set figure background to white
    drawnow
    frame = getframe(gcf);
    im = frame2im(frame);
    [imind,cm] = rgb2ind(im,256);
    % Write to the GIF File
    if k == 1
        imwrite(imind,cm,filename,'gif', 'Loopcount',inf);
    else
        imwrite(imind,cm,filename,'gif','WriteMode','append');
    end
end
end
display('DONE');

```

## Bibliography

1. U. Bovensiepen and P.S. Kirchmann, "*Elementary relaxation processes investigated by femtosecond photoelectron spectroscopy of two-dimensional materials*", **Laser & Photonics Reviews**. 6: p. 589, (2012).
2. K. Sokolowski-Tinten, M.H. Von Hoegen, D. Von Der Linde, A. Cavalleri, C.W. Siders, F.L.H. Brown, C. Toth, J.A. Squier, C.P.J. Barty, K.R. Wilson, and M.E.D.L.T. Kammler. *Time-resolved x-ray diffraction study of ultrafast acoustic phonon dynamics in Ge/Si-heterostructures*. in *Ultrafast Phenomena*. 2000. Charleston, South Carolina: Optical Society of America.
3. O.B. Wright, "*Ultrafast nonequilibrium stress generation in gold and silver*", **Phys. Rev. B**. 49: p. 9985, (1994).
4. G. Tas and H.J. Maris, "*Electron diffusion in metals studied by picosecond ultrasonics*", **Phys. Rev. B**. 49: p. 15046, (1994).
5. C. Suárez, W.E. Bron, and T. Juhasz, "*Dynamics and Transport of Electronic Carriers in Thin Gold Films*", **Phys. Rev. Lett.** 75: p. 4536, (1995).
6. M. Bonn, D.N. Denzler, S. Funk, M. Wolf, S.S. Wellershoff, and J. Hohlfeld, "*Ultrafast electron dynamics at metal surfaces: Competition between electron-phonon coupling and hot-electron transport*", **Phys. Rev. B**. 61: p. 1101, (2000).
7. A. Devos and C. Lerouge, "*Evidence of Laser-Wavelength Effect in Picosecond Ultrasonics: Possible Connection With Interband Transitions*", **Phys. Rev. Lett.** 86: p. 2669, (2001).
8. O. Matsuda, T. Tachizaki, T. Fukui, J.J. Baumberg, and O.B. Wright, "*Acoustic phonon generation and detection in GaAs / Al<sub>0.3</sub> Ga<sub>0.7</sub> As quantum wells with picosecond laser pulses*", **Phys. Rev. B**. 71: p. 115330, (2005).
9. N. Chigarev, C. Rossignol, and B. Audoin, "*Surface displacement measured by beam distortion detection technique: Application to picosecond ultrasonics*", **Rev. Sci. Instrum.** 77: p. 114901, (2006).
10. W.C. Röntgen, "*On a new kind of Ray*", **Nature**. 53: p. 274, (1896).
11. C. Davisson and L.H. Germer, "*The Scattering of Electrons by a Single Crystal of Nickel*", **Nature**. 119: p. 558, (1927).
12. G.P. Thomson and A. Reid, "*Diffraction of Cathode Rays by a Thin Film*", **Nature**. 119: p. 890, (1927).

13. B. Klar and F. Rustichelli, "*Dynamical neutron diffraction by ideally curved crystals*", **II Nuovo Cimento B (1971-1996)**. 13: p. 249, (1973).
14. R. Pynn, "*Neutron Scattering—A Non-destructive Microscope for Seeing Inside Matter*", **Book**. Neutron Applications in Earth, Energy and Environmental Sciences, ed. L. Liang, R. Rinaldi, and H. Schober. Springer, Boston, MA.(2009)
15. D. Kühlke, U. Herpers, and D. Von Der Linde, "*Soft x-ray emission from subpicosecond laser-produced plasmas*", **App. Phys. Lett.** 50: p. 1785, (1987).
16. M.M. Murnane, H.C. Kapteyn, M.D. Rosen, and R.W. Falcone, "*Ultrafast X-ray Pulses from Laser-Produced Plasmas*", **Science**. 251: p. 531, (1991).
17. U. Hinze, A. Egbert, B. Chichkov, and K. Eidmann, "*Generation of picosecond hard-x-ray pulses in a femtosecond-laser-driven x-ray diode*", **Opt. Lett.** 29: p. 2079, (2004).
18. R.W. Schoenlein, S. Chattopadhyay, H.H.W. Chong, T.E. Glover, P.A. Heimann, C.V. Shank, A.A. Zholents, and M.S. Zolotarev, "*Generation of Femtosecond Pulses of Synchrotron Radiation*", **Science**. 287: p. 2237, (2000).
19. S. Khan, K. Holldack, T. Kachel, R. Mitzner, and T. Quast, "*Femtosecond Undulator Radiation from Sliced Electron Bunches*", **Phys. Rev. Lett.** 97: p. 074801, (2006).
20. J.C. Williamson, M. Dantus, S.B. Kim, and A.H. Zewail, "*Ultrafast diffraction and molecular structure*", **Chemical Physics Letters**. 196: p. 529, (1992).
21. J.C. Williamson, J. Cao, H. Ihee, H. Frey, and A.H. Zewail, "*Clocking transient chemical changes by ultrafast electron diffraction*", **Nature**. 386: p. 159, (1997).
22. C.-Y. Ruan, V.A. Lobastov, R. Srinivasan, B.M. Goodson, H. Ihee, and A.H. Zewail, "*Ultrafast diffraction and structural dynamics: The nature of complex molecules far from equilibrium*", **Proceedings of the National Academy of Sciences**. 98: p. 7117, (2001).
23. B.J. Siwick, J.R. Dwyer, R.E. Jordan, and R.J.D. Miller, "*Ultrafast electron optics: Propagation dynamics of femtosecond electron packets*", **Journal of Applied Physics**. 92: p. 1643, (2002).
24. B.J. Siwick, J.R. Dwyer, R.E. Jordan, and R.J.D. Miller, "*An Atomic-Level View of Melting Using Femtosecond Electron Diffraction*", **Science**. 302: p. 1382, (2003).
25. A.H. Chin, R.W. Schoenlein, T.E. Glover, P. Balling, W.P. Leemans, and C.V. Shank, "*Ultrafast Structural Dynamics in InSb Probed by Time-Resolved X-Ray Diffraction*", **Phys. Rev. Lett.** 83: p. 336, (1999).
26. C.W. Siders, A. Cavalleri, K. Sokolowski-Tinten, C. Toth, T. Cuo, M. Kammler, M. Horn Von Högen, K.R. Wilson, D. Von Der Linde, and C.P.J. Barty, "*Detection of Nonthermal melting by ultrafast X-ray diffraction*", **Science**. 286: p. 1340, (1999).
27. A. Cavalleri, C.W. Siders, F.L.H. Brown, D.M. Leitner, C. Tóth, J.A. Squier, C.P.J. Barty, K.R. Wilson, K. Sokolowski-Tinten, M. Horn Von Hoegen, D. Von Der Linde, and M.

- Kammler, "Anharmonic Lattice Dynamics in Germanium Measured with Ultrafast X-Ray Diffraction", **Phys. Rev. Lett.** 85: p. 586, (2000).
28. A.M. Lindenberg, I. Kang, S.L. Johnson, T. Missalla, P.A. Heimann, Z. Chang, J. Larsson, P.H. Bucksbaum, H.C. Kapteyn, H.A. Padmore, R.W. Lee, J.S. Wark, and R.W. Falcone, "Time-Resolved X-Ray Diffraction from Coherent Phonons during a Laser-Induced Phase Transition", **Phys. Rev. Lett.** 84: p. 111, (2000).
29. M.F. Decamp, D.A. Reis, P.H. Bucksbaum, B. Adams, J.M. Caraher, R. Clarke, C.W.S. Conover, E.M. Dufresne, R. Merlin, V. Stoica, and J.K. Wahlstrand, "Coherent control of pulsed X-ray beams", **Nature.** 413: p. 825, (2001).
30. D.V.D. Linde, K. Sokolowski-Tinten, C. Blome, C. Dietrich, A. Tarasevitch, A. Cavalleri, and J.A. Squier, "'Ultrafast' Extended to X-Rays: Femtosecond Time-Resolved X-Ray Diffraction", **Zeitschrift für Physikalische Chemie.** 215: p. 1527, (2001).
31. D.A. Reis, M.F. Decamp, P.H. Bucksbaum, R. Clarke, E. Dufresne, M. Hertlein, R. Merlin, R. Falcone, H. Kapteyn, M.M. Murnane, J. Larsson, T. Missalla, and J.S. Wark, "Probing Impulsive Strain Propagation with X-Ray Pulses", **Phys. Rev. Lett.** 86: p. 3072, (2001).
32. A. Cavalleri, C.W. Siders, C. Rose-Petruck, R. Jimenez, C. Tóth, J.A. Squier, C.P.J. Barty, K.R. Wilson, K. Sokolowski-Tinten, M. Horn Von Hoegen, and D. Von Der Linde, "Ultrafast x-ray measurement of laser heating in semiconductors: Parameters determining the melting threshold", **Phys. Rev. B.** 63: p. 193306, (2001).
33. O. Synnergren, M. Harbst, T. Missalla, J. Larssona, G. Katona, R. Neutze, and R. Wouts, "Projecting picosecond lattice dynamics through x-ray topography", **App. Phys. Lett.** 80: p. 3727, (2002).
34. A.M. Lindenberg, I. Kang, S.L. Johnson, R.W. Falcone, P.A. Heimann, Z. Chang, R.W. Lee, and J.S. Wark, "Coherent control of phonons probed by time-resolved x-ray diffraction", **Opt. Lett.** 27: p. 869, (2002).
35. J. Larsson, A. Allen, P.H. Bucksbaum, R.W. Falcone, A. Lindenberg, G. Naylor, T. Missalla, D.A. Reis, K. Scheidt, A. Sjögren, P. Sondhauss, M. Wulff, and J.S. Wark, "Picosecond X-ray diffraction studies of laser-excited acoustic phonons in InSb", **Appl. Phys. A.** 75: p. 467, (2002).
36. M.F. Decamp, D.A. Reis, A. Cavalieri, P.H. Bucksbaum, R. Clarke, R. Merlin, E.M. Dufresne, D.A. Arms, A.M. Lindenberg, A.G. Macphee, Z. Chang, B. Lings, J.S. Wark, and S. Fahy, "Transient Strain Driven by a Dense Electron-Hole Plasma", **Phys. Rev. Lett.** 91: p. 165502, (2003).
37. M. Bargheer, N. Zhavoronkov, Y. Gritsai, J.C. Woo, D.S. Kim, M. Woerner, and T. Elsaesser, "Coherent Atomic Motions in a Nanostructure Studied by Femtosecond X-ray Diffraction", **Science.** 306: p. 1771, (2004).

38. H.J. Lee, J. Workman, J.S. Wark, R.D. Averitt, A.J. Taylor, J. Roberts, Q. McCulloch, D.E. Hof, N. Hur, S.W. Cheong, and D.J. Funk, "*Optically induced lattice dynamics probed with ultrafast x-ray diffraction*", **Phys. Rev. B.** 77: p. 132301, (2008).
39. M. Nicoul, U. Shymanovich, A. Tarasevitch, D. Von Der Linde, and K. Sokolowski-Tinten, "*Picosecond acoustic response of a laser-heated gold-film studied with time-resolved x-ray diffraction*", **App. Phys. Lett.** 98: p. 191902, (2011).
40. Y. Gao and M.F. Decamp, "*Generation of acoustic pulses from a photo-acoustic transducer measured by time-resolved x-ray diffraction*", **App. Phys. Lett.** 100: p. 191903, (2012).
41. D. Schick, A. Bojahr, M. Herzog, P. Gaal, I. Vrejoiu, and M. Bargheer, "*Following Strain-Induced Mosaicity Changes of Ferroelectric Thin Films by Ultrafast Reciprocal Space Mapping*", **Phys. Rev. Lett.** 110: p. 095502, (2013).
42. R. Shayduk, M. Herzog, A. Bojahr, D. Schick, P. Gaal, W. Leitenberger, H. Navirian, M. Sander, J. Goldshteyn, I. Vrejoiu, and M. Bargheer, "*Direct time-domain sampling of subterahertz coherent acoustic phonon spectra in SrTiO<sub>3</sub> using ultrafast x-ray diffraction*", **Phys. Rev. B.** 87: p. 184301, (2013).
43. D. Schick, M. Herzog, A. Bojahr, W. Leitenberger, A. Hertwig, R. Shayduk, and M. Bargheer, "*Ultrafast lattice response of photoexcited thin films studied by X-ray diffraction*", **Struct. Dyn.** 1: p. 064501, (2014).
44. D. Schick, M. Herzog, H. Wen, P. Chen, C. Adamo, P. Gaal, D.G. Schlom, P.G. Evans, Y. Li, and M. Bargheer, "*Localized Excited Charge Carriers Generate Ultrafast Inhomogeneous Strain in the Multiferroic BiFeO<sub>3</sub>*", **Phys. Rev. Lett.** 112: p. 097602, (2014).
45. A.I.H. Persson, H. Enquist, A. Jurgilaitis, B.P. Andreasson, and J. Larsson, "*Real-time observation of coherent acoustic phonons generated by an acoustically mismatched optoacoustic transducer using x-ray diffraction*", **Journal of Applied Physics.** 118: p. 185308, (2015).
46. A.I.H. Persson, A. Jarnac, X. Wang, H. Enquist, A. Jurgilaitis, and J. Larsson, "*Studies of electron diffusion in photo-excited Ni using time-resolved X-ray diffraction*", **App. Phys. Lett.** 109: p. 203115, (2016).
47. A. Koc, M. Reinhardt, A.V. Reppert, M. Rössle, W. Leitenberger, M. Gleich, M. Weinelt, F. Zamponi, and M. Bargheer, "*Grueneisen-approach for the experimental determination of transient spin and phonon energies from ultrafast x-ray diffraction data: gadolinium*", **Journal of Physics: Condensed Matter.** 29: p. 264001, (2017).
48. A. Koc, M. Reinhardt, A. Von Reppert, M. Rössle, W. Leitenberger, K. Dumesnil, P. Gaal, F. Zamponi, and M. Bargheer, "*Ultrafast x-ray diffraction thermometry measures the influence of spin excitations on the heat transport through nanolayers*", **Phys. Rev. B.** 96: p. 014306, (2017).

49. S. Lee, G.J. Williams, M.I. Campana, D.A. Walko, and E.C. Landahl, "*Picosecond x-ray strain rosette reveals direct laser excitation of coherent transverse acoustic phonons*", **Scientific Reports**. 6: p. 19140, (2016).
50. R. Li, O.A. Ashour, J. Chen, H.E. Elsayed-Ali, and P.M. Rentzepis, "*Femtosecond laser induced structural dynamics and melting of Cu (111) single crystal. An ultrafast time-resolved x-ray diffraction study*", **Journal of Applied Physics**. 121: p. 055102, (2017).
51. C. Rose-Petruck, R. Jimenez, T. Guo, A. Cavalleri, C.W. Siders, F. Rksi, J.A. Squier, B.C. Walker, K.R. Wilson, and C.P.J. Barty, "*Picosecond–milliångström lattice dynamics measured by ultrafast X-ray diffraction*", **Nature**. 398: p. 310, (1999).
52. K. Sokolowski-Tinten, C. Blome, J. Blums, A. Cavalleri, C. Dietrich, A. Tarasevitch, I. Uschmann, E. Förster, M. Kammler, M. Horn-Von-Hoegen, and D. Von Der Linde, "*Femtosecond X-ray measurement of coherent lattice vibrations near the Lindemann stability limit*", **Nature**. 422: p. 287, (2003).
53. M. Bargheer, N. Zhavoronkov, J.C. Woo, D.S. Kim, M. Woerner, and T. Elsaesser, "*Excitation mechanisms of coherent phonons unravelled by femtosecond X-ray diffraction*", **physica status solidi (b)**. 243: p. 2389, (2006).
54. D.M. Fritz, D.A. Reis, B. Adams, R.A. Akre, J. Arthur, C. Blome, P.H. Bucksbaum, A.L. Cavalieri, S. Engemann, S. Fahy, R.W. Falcone, P.H. Fuoss, K.J. Gaffney, M.J. George, J. Hajdu, M.P. Hertlein, P.B. Hillyard, M. Horn-Von Hoegen, M. Kammler, J. Kaspar, R. Kienberger, P. Krejcik, S.H. Lee, A.M. Lindenberg, B. Mcfarland, D. Meyer, T. Montagne, É.D. Murray, A.J. Nelson, M. Nicoul, R. Pahl, J. Rudati, H. Schlarb, D.P. Siddons, K. Sokolowski-Tinten, T. Tschentscher, D. Von Der Linde, and J.B. Hastings, "*Ultrafast Bond Softening in Bismuth: Mapping a Solid's Interatomic Potential with X-rays*", **Science**. 315: p. 633, (2007).
55. C. Von Korff Schmising, M. Bargheer, M. Kiel, N. Zhavoronkov, M. Woerner, T. Elsaesser, I. Vrejoiu, D. Hesse, and M. Alexe, "*Accurate time delay determination for femtosecond X-ray diffraction experiments*", **Appl. Phys. B**. 88: p. 1, (2007).
56. S.L. Johnson, P. Beaud, C.J. Milne, F.S. Krasniqi, E.S. Zijlstra, M.E. Garcia, M. Kaiser, D. Grolimund, R. Abela, and G. Ingold, "*Nanoscale Depth-Resolved Coherent Femtosecond Motion in Laser-Excited Bismuth*", **Phys. Rev. Lett.** 100: p. 155501, (2008).
57. S.L. Johnson, P. Beaud, E. Vorobeva, C.J. Milne, É.D. Murray, S. Fahy, and G. Ingold, "*Non-equilibrium phonon dynamics studied by grazing-incidence femtosecond X-ray crystallography*", **Acta Cryst. A**. 66: p. 157, (2010).
58. B. Freyer, J. Stingl, F. Zamponi, M. Woerner, and T. Elsaesser, "*The rotating-crystal method in femtosecond X-ray diffraction*", **Opt. Express**. 19: p. 15506, (2011).
59. W. Lu, "*Ultrafast time-resolved X-ray diffraction using an optimized laser-plasma based X-ray source*", **Dissertation**, Universität Duisburg-Essen, (2013)

60. S. Gerber, K.W. Kim, Y. Zhang, D. Zhu, N. Plonka, M. Yi, G.L. Dakovski, D. Leuenberger, P.S. Kirchmann, R.G. Moore, M. Chollet, J.M. Glowina, Y. Feng, J.S. Lee, A. Mehta, A.F. Kemper, T. Wolf, Y.D. Chuang, Z. Hussain, C.C. Kao, B. Moritz, Z.X. Shen, T.P. Devereaux, and W.S. Lee, "*Direct characterization of photoinduced lattice dynamics in BaFe<sub>2</sub>As<sub>2</sub>*", **Nature Communications**. 6: p. 7377, (2015).
61. K.G. Nakamura, S. Ishii, S. Ishitsu, M. Shiokawa, H. Takahashi, K. Dharmalingam, J. Irisawa, Y. Hironaka, K. Ishioka, and M. Kitajima, "*Femtosecond time-resolved x-ray diffraction from optical coherent phonons in CdTe(111) crystal*", **App. Phys. Lett.** 93: p. 061905, (2008).
62. E. Collet, M.-H. Lemée-Cailleau, M. Buron-Le Cointe, H. Cailleau, M. Wulff, T. Luty, S.-Y. Koshihara, M. Meyer, L. Toupet, P. Rabiller, and S. Techert, "*Laser-Induced Ferroelectric Structural Order in an Organic Charge-Transfer Crystal*", **Science**. 300: p. 612, (2003).
63. A. Cavalleri, S. Wall, C. Simpson, E. Statz, D.W. Ward, K.A. Nelson, M. Rini, and R.W. Schoenlein, "*Tracking the motion of charges in a terahertz light field by femtosecond X-ray diffraction*", **Nature**. 442: p. 664, (2006).
64. S.K. Streiffer, J.A. Eastman, D.D. Fong, C. Thompson, A. Munkholm, M.V. Ramana Murty, O. Auciello, G.R. Bai, and G.B. Stephenson, "*Observation of Nanoscale 180° Stripe Domains in Ferroelectric PbTiO<sub>3</sub> Thin Films*", **Phys. Rev. Lett.** 89: p. 067601, (2002).
65. R.V. Wang, D.D. Fong, F. Jiang, M.J. Highland, P.H. Fuoss, C. Thompson, A.M. Kolpak, J.A. Eastman, S.K. Streiffer, A.M. Rappe, and G.B. Stephenson, "*Reversible Chemical Switching of a Ferroelectric Film*", **Phys. Rev. Lett.** 102: p. 047601, (2009).
66. M. Woerner, C. V. Korff Schmising, M. Bargheer, N. Zhavoronkov, I. Vrejoiu, D. Hesse, M. Alexe, and T. Elsaesser, "*Ultrafast structural dynamics of perovskite superlattices*", **Appl. Phys. A**. 96: p. 83, (2009).
67. D. Daranciang, M.J. Highland, H. Wen, S.M. Young, N.C. Brandt, H.Y. Hwang, M. Vattilana, M. Nicoul, F. Quirin, J. Goodfellow, T. Qi, I. Grinberg, D.M. Fritz, M. Cammarata, D. Zhu, H.T. Lemke, D.A. Walko, E.M. Dufresne, Y. Li, J. Larsson, D.A. Reis, K. Sokolowski-Tinten, K.A. Nelson, A.M. Rappe, P.H. Fuoss, G.B. Stephenson, and A.M. Lindenberg, "*Ultrafast Photovoltaic Response in Ferroelectric Nanolayers*", **Phys. Rev. Lett.** 108: p. 087601, (2012).
68. A. Kirilyuk, A.V. Kimel, and T. Rasing, "*Ultrafast optical manipulation of magnetic order*", **Reviews of Modern Physics**. 82: p. 2731, (2010).
69. F. Quirin, M. Vattilana, U. Shymanovich, A.-E. El-Kamhawy, A. Tarasevitch, J. Hohlfeld, D. Von Der Linde, and K. Sokolowski-Tinten, "*Structural dynamics in FeRh during a laser-induced metamagnetic phase transition*", **Phys. Rev. B**. 85: p. 020103, (2012).
70. L. Wei, H. Ping, C. Zhe, H. Chenchong, W. Yuxin, and Y. Biao, "*Magnetization studies of first-order magnetostructural phase transition in polycrystalline FeRh thin films*", **J. Phys. D: Appl. Phys.** 45: p. 435001, (2012).

71. M.A. De Vries, M. Loving, M. McLaren, R.M.D. Brydson, X. Liu, S. Langridge, L.H. Lewis, and C.H. Marrows, "Asymmetric "melting" and "freezing" kinetics of the magnetostructural phase transition in B2-ordered FeRh epilayers", **App. Phys. Lett.** 104: p. 232407, (2014).
72. C.J. Kinane, M. Loving, M.a.D. Vries, R. Fan, T.R. Charlton, J.S. Claydon, D.A. Arena, F. Maccherozzi, S.S. Dhesi, D. Heiman, C.H. Marrows, L.H. Lewis, and L. Sean, "Observation of a temperature dependent asymmetry in the domain structure of a Pd-doped FeRh epilayer", **New Journal of Physics.** 16: p. 113073, (2014).
73. V.I. Zverev, A.M. Saletsky, R.R. Gimaev, A.M. Tishin, T. Miyanaga, and J.B. Staunton, "Influence of structural defects on the magnetocaloric effect in the vicinity of the first order magnetic transition in  $Fe_{50.4}Rh_{49.6}$ ", **App. Phys. Lett.** 108: p. 192405, (2016).
74. L. Lounès, S. Carlo, D. Renaud, F. Franck, O. Martin, G. Stefan, H.B. Christian, P. Horia, V. Franck, and S. Maurizio, "Temperature and field dependent magnetization in a sub-  $\mu$  m patterned Co/FeRh film studied by resonant x-ray scattering", **J. Phys. D: Appl. Phys.** 49: p. 205003, (2016).
75. C. Rischel, A. Rouse, I. Uschmann, P.-A. Albouy, J.-P. Geindre, P. Audebert, J.-C. Gauthier, E. Fröster, J.-L. Martin, and A. Antonetti, "Femtosecond time-resolved X-ray diffraction from laser-heated organic films", **Nature.** 390: p. 490, (1997).
76. K. Sokolowski-Tinten, C. Blome, C. Dietrich, A. Tarasevitch, M. Horn Von Hoegen, D. Von Der Linde, A. Cavalleri, J. Squier, and M. Kammler, "Femtosecond X-Ray Measurement of Ultrafast Melting and Large Acoustic Transients", **Phys. Rev. Lett.** 87: p. 225701, (2001).
77. T. Feurer, A. Morak, I. Uschmann, C. Ziener, H. Schwoerer, C. Reich, P. Gibbon, E. Förster, R. Sauerbrey, K. Ortner, and C.R. Becker, "Femtosecond silicon  $K\alpha$  pulses from laser-produced plasmas", **Phys. Rev. E.** 65: p. 016412, (2001).
78. A. Rouse, C. Rischel, S. Fourmaux, I. Uschmann, S. Sebban, G. Grillon, P. Balcou, E. Förster, J.P. Geindre, P. Audebert, J.C. Gauthier, and D. Hulin, "Non-thermal melting in semiconductors measured at femtosecond resolution", **Nature.** 410: p. 65, (2001).
79. K.J. Gaffney, A.M. Lindenberg, J. Larsson, K. Sokolowski-Tinten, C. Blome, O. Synnergren, J. Sheppard, C. Caleman, A.G. Macphee, D. Weinstein, D.P. Lowney, T. Allison, T. Matthews, R.W. Falcone, A.L. Cavalieri, D.M. Fritz, S.H. Lee, P.H. Bucksbaum, D.A. Reis, J. Rudati, A.T. Macrander, P.H. Fuoss, C.C. Kao, D.P. Siddons, R. Pahl, K. Moffat, J. Als-Nielsen, S. Duesterer, R. Ischebeck, H. Schlarb, H. Schulte-Schrepping, J. Schneider, D. Von Der Linde, O. Hignette, F. Sette, H.N. Chapman, R.W. Lee, T.N. Hansen, J.S. Wark, M. Bergh, G. Huldt, D. Van Der Spoel, N. Timneanu, J. Hajdu, R.A. Akre, E. Bong, P. Krejcik, J. Arthur, S. Brennan, K. Luening, and J.B. Hastings, "Observation of Structural Anisotropy and the Onset of Liquidlike Motion During the Nonthermal Melting of InSb", **Phys. Rev. Lett.** 95: p. 125701, (2005).

80. A.M. Lindenberg, J. Larsson, K. Sokolowski-Tinten, K.J. Gaffney, C. Blome, O. Synnergren, J. Sheppard, C. Caleman, A.G. Macphee, D. Weinstein, D.P. Lowney, T.K. Allison, T. Matthews, R.W. Falcone, A.L. Cavalieri, D.M. Fritz, S.H. Lee, P.H. Bucksbaum, D.A. Reis, J. Rudati, P.H. Fuoss, C.C. Kao, D.P. Siddons, R. Pahl, J. Als-Nielsen, S. Duesterer, R. Ischebeck, H. Schlarb, H. Schulte-Schrepping, T. Tschentscher, J. Schneider, D. Von Der Linde, O. Hignette, F. Sette, H.N. Chapman, R.W. Lee, T.N. Hansen, S. Teichert, J.S. Wark, M. Bergh, G. Huldt, D. Van Der Spoel, N. Timneanu, J. Hajdu, R.A. Akre, E. Bong, P. Krejcik, J. Arthur, S. Brennan, K. Luening, and J.B. Hastings, "*Atomic-Scale Visualization of Inertial Dynamics*", **Science**. 308: p. 392, (2005).
81. P.B. Hillyard, K.J. Gaffney, A.M. Lindenberg, S. Engemann, R.A. Akre, J. Arthur, C. Blome, P.H. Bucksbaum, A.L. Cavalieri, A. Deb, R.W. Falcone, D.M. Fritz, P.H. Fuoss, J. Hajdu, P. Krejcik, J. Larsson, S.H. Lee, D.A. Meyer, A.J. Nelson, R. Pahl, D.A. Reis, J. Rudati, D.P. Siddons, K. Sokolowski-Tinten, D. Von Der Linde, and J.B. Hastings, "*Carrier-Density-Dependent Lattice Stability in InSb*", **Phys. Rev. Lett.** 98: p. 125501, (2007).
82. G. Sciaini, M. Harb, S.G. Kruglik, T. Payer, C.T. Hebeisen, F.-J.M.Z. Heringdorf, M. Yamaguchi, M.H.-V. Hoegen, R. Ernstorfer, and R.J.D. Miller, "*Electronic acceleration of atomic motions and disordering in bismuth*", **Nature**. 458: p. 56, (2009).
83. M. Trigo, J. Chen, V.H. Vishwanath, Y.M. Sheu, T. Graber, R. Henning, and D.A. Reis, "*Imaging nonequilibrium atomic vibrations with x-ray diffuse scattering*", **Phys. Rev. B**. 82: p. 235205, (2010).
84. M. Trigo, M. Fuchs, J. Chen, M.P. Jiang, M. Cammarata, S. Fahy, D.M. Fritz, K. Gaffney, S. Ghimire, A. Higginbotham, S.L. Johnson, M.E. Kozina, J. Larsson, H. Lemke, A.M. Lindenberg, G. Ndabashimiye, F. Quirin, K. Sokolowski-Tinten, C. Uher, G. Wang, J.S. Wark, D. Zhu, and D.A. Reis, "*Fourier-transform inelastic X-ray scattering from time- and momentum-dependent phonon-phonon correlations*", **Nature Physics**. 9: p. 790, (2013).
85. D. Zhu, A. Robert, T. Henighan, H.T. Lemke, M. Chollet, J.M. Glowia, D.A. Reis, and M. Trigo, "*Phonon spectroscopy with sub-meV resolution by femtosecond x-ray diffuse scattering*", **Phys. Rev. B**. 92: p. 054303, (2015).
86. M. Kozina, M. Trigo, M. Chollet, J.N. Clark, J.M. Glowia, A.C. Gossard, T. Henighan, M.P. Jiang, H. Lu, A. Majumdar, D. Zhu, and D.A. Reis, "*Heterodyne x-ray diffuse scattering from coherent phonons*", **Struct. Dyn.** 4: p. 054305, (2017).
87. T. Henighan, M. Trigo, M. Chollet, J.N. Clark, S. Fahy, J.M. Glowia, M.P. Jiang, M. Kozina, H. Liu, S. Song, D. Zhu, and D.A. Reis, "*Control of two-phonon correlations and the mechanism of high-wavevector phonon generation by ultrafast light pulses*", **Phys. Rev. B**. 94: p. 020302, (2016).
88. M. Bargheer, N. Zhavoronkov, M. Woerner, and T. Elsaesser, "*Recent Progress in Ultrafast X-ray Diffraction*", **ChemPhysChem**. 7: p. 783, (2006).

89. T. Pfeifer, C. Spielmann, and G. Gerber, "*Femtosecond x-ray science*", **Reports on Progress in Physics**. 69: p. 443, (2006).
90. P. Ruello and V.E. Gusev, "*Physical mechanisms of coherent acoustic phonons generation by ultrafast laser action*", **Ultrasonics**. 56: p. 21, (2015).
91. T. Popmintchev, M.-C. Chen, D. Popmintchev, P. Arpin, S. Brown, S. Ališauskas, G. Andriukaitis, T. Balčiūnas, O.D. Mücke, A. Pugzlys, A. Baltuška, B. Shim, S.E. Schrauth, A. Gaeta, C. Hernández-García, L. Plaja, A. Becker, A. Jaron-Becker, M.M. Murnane, and H.C. Kapteyn, "*Bright Coherent Ultrahigh Harmonics in the keV X-ray Regime from Mid-Infrared Femtosecond Lasers*", **Science**. 336: p. 1287, (2012).
92. T. Tajima and J.M. Dawson, "*Laser Electron Accelerator*", **Phys. Rev. Lett.** 43: p. 267, (1979).
93. A. Félicie and G.R.T. Alec, "*Applications of laser wakefield accelerator-based light sources*", **Plasma Physics and Controlled Fusion**. 58: p. 103001, (2016).
94. I. Uschmann, "*Beiträge zur Röntgendiagnose Laserinduzierter Plasma mit gebogenen Kristallen*", **Dissertation**, (1991)
95. M. Nicoul, "*Time-resolved X-ray diffraction with accelerator- and laser-plasma-based X-ray sources*", **Dissertation**, Universität Duisburg-Essen, (2011)
96. S. Lee, I.W. Choi, I.-B. Sohn, K. Lee, G.I. Shim, Y.U. Jeong, B.H. Han, W.J. Ryu, H.-N. Kim, and H. Cha, "*Femtosecond laser-driven intense Cu K  $\alpha$  X-ray source with a novel film target driver*", **Journal of the Korean Physical Society**. 67: p. 800, (2015).
97. A. Baguckis, A. Plukis, J. Reklaitis, V. Remeikis, L. Giniūnas, and M. Vengris, "*Generation of plasma X-ray sources via high repetition rate femtosecond laser pulses*", **Appl. Phys. B**. 123: p. 290, (2017).
98. N.A. Krall, "*Principles of Plasma Physics*", **Book**. McGraw-Hill.(1973)
99. C. Pellegrini and J. Stöhr, "*X-ray free-electron lasers—principles, properties and applications*", **Nuclear Instruments and Methods in Physics Research Section A: Accelerators, Spectrometers, Detectors and Associated Equipment**. 500: p. 33, (2003).
100. L. Nugent-Glandorf, M. Scheer, D.A. Samuels, A.M. Mulhisen, E.R. Grant, X. Yang, V.M. Bierbaum, and S.R. Leone, "*Ultrafast Time-Resolved Soft X-Ray Photoelectron Spectroscopy of Dissociating Br<sub>2</sub>*", **Phys. Rev. Lett.** 87: p. 193002, (2001).
101. C. Stamm, T. Kachel, N. Pontius, R. Mitzner, T. Quast, K. Holldack, S. Khan, C. Lupulescu, E.F. Aziz, M. Wietstruk, H.A. Dürr, and W. Eberhardt, "*Femtosecond modification of electron localization and transfer of angular momentum in nickel*", **Nature Materials**. 6: p. 740, (2007).
102. I. Radu, C. Stamm, N. Pontius, T. Kachel, P. Ramm, J.U. Thiele, H.A. Dürr, and C.H. Back, "*Laser-induced generation and quenching of magnetization on FeRh studied with time-resolved x-ray magnetic circular dichroism*", **Phys. Rev. B**. 81: p. 104415, (2010).

103. M. Wietstruk, A. Melnikov, C. Stamm, T. Kachel, N. Pontius, M. Sultan, C. Gahl, M. Weinelt, H.A. Dürr, and U. Bovensiepen, "*Hot-Electron-Driven Enhancement of Spin-Lattice Coupling in Gd and Tb 4f Ferromagnets Observed by Femtosecond X-Ray Magnetic Circular Dichroism*", **Phys. Rev. Lett.** 106: p. 127401, (2011).
104. I. Radu, K. Vahaplar, C. Stamm, T. Kachel, N. Pontius, H.A. Dürr, T.A. Ostler, J. Barker, R.F.L. Evans, R.W. Chantrell, A. Tsukamoto, A. Itoh, A. Kirilyuk, T. Rasing, and A.V. Kimel, "*Transient ferromagnetic-like state mediating ultrafast reversal of antiferromagnetically coupled spins*", **Nature**. 472: p. 205, (2011).
105. **Web Page**, "*LCLC*", <http://www-ssrl.slac.stanford.edu/lcls/index.html>
106. T. Ishikawa Et Al., "*A compact X-ray free-electron laser emitting in the sub-ångström region*", **Nature Photonics**. 6: p. 540, (2012).
107. **Web Page**, "*XFEL*", <http://www.xfel.eu/XFELpresse/en/hintergrund/was/index.html>
108. M.V. Fischetti and S.E. Laux, "*Band structure, deformation potentials, and carrier mobility in strained Si, Ge, and SiGe alloys*", **Journal of Applied Physics**. 80: p. 2234, (1996).
109. S.E. Thompson Et Al., "*A 90-nm logic technology featuring strained-silicon*", **IEEE Transactions on Electron Devices**. 51: p. 1790, (2004).
110. S.E. Thompson and S. Parthasarathy, "*Moore's law: the future of Si microelectronics*", **Materials Today**. 9: p. 20, (2006).
111. X. Wang, H. Li, R. Camacho-Aguilera, Y. Cai, L.C. Kimerling, J. Michel, and J. Liu, "*Infrared absorption of n-type tensile-strained Ge-on-Si*", **Opt. Lett.** 38: p. 652, (2013).
112. J. Liu, X. Sun, D. Pan, X. Wang, L.C. Kimerling, T.L. Koch, and J. Michel, "*Tensile-strained, n-type Ge as a gain medium for monolithic laser integration on Si*", **Opt. Express**. 15: p. 11272, (2007).
113. X. Sun, J. Liu, L.C. Kimerling, and J. Michel, "*Direct gap photoluminescence of n-type tensile-strained Ge-on-Si*", **App. Phys. Lett.** 95: p. 011911, (2009).
114. A. Bugayev, A. Esmail, M. Abdel-Fattah, and H.E. Elsayed-Ali, "*Coherent phonons in bismuth film observed by ultrafast electron diffraction*", **AIP Advances**. 1: p. 012117, (2011).
115. A. Feist, N. Rubiano Da Silva, W. Liang, C. Ropers, and S. Schäfer, "*Nanoscale diffractive probing of strain dynamics in ultrafast transmission electron microscopy*", **Struct. Dyn.** 5: p. 014302, (2018).
116. A. Bedford and D.S. Drumheller, "*Introduction to Elastic Wave Propagation*", **Book**. Second ed. John Wiley & Sons, Ltd.(1994)
117. C. Thomsen, H.T. Grahn, H.J. Maris, and J. Tauc, "*Surface generation and detection of phonons by picosecond light pulses*", **Phys. Rev. B**. 34: p. 4129, (1986).
118. N.W. Ashcroft and N.D. Mermin, "*Solid State Physics*", **Book**. Harcourt Inc.(1976)
119. P.Y. Yu and M. Cardona, "*Fundamentals of Semiconductors*", **Book**. 2nd ed. Springer.(1996)

120. S.M. Sze and K.K. Ng, "*Physics of Semiconductor Devices*", **Book**. 3rd ed. John Wiley & Sons, Ltd.(2006)
121. R.W. Boyd and D. Prato, "*Nonlinear Optics*", **Book**. 3rd ed. Elsevier Inc.(2008)
122. I. Norio, "*Charge Density Dependence of Photoinduced Stress in Semiconductors*", **Japanese Journal of Applied Physics**. 45: p. 1675, (2006).
123. W.B. Gauster and D.H. Habing, "*Electronic Volume Effect in Silicon*", **Phys. Rev. Lett.** 18: p. 1058, (1967).
124. O.B. Wright and V.E. Gusev, "*Acoustic generation in crystalline silicon with femtosecond optical pulses*", **App. Phys. Lett.** 66: p. 1190, (1995).
125. J. Als-Nielsen and D. Mcmorrow, "*Elements of Modern X-ray Physics*", **Book**. Second ed. John Wiley & Sons, Ltd.(2011)
126. W.H. Zachariasen, "*Theory of X-Ray Diffraction in crystals*", **Book**. Dover Publications Inc.(1945)
127. B.E. Warren, "*X-Ray Diffraction*", **Book**. Courier Corporation.(1990)
128. B. Deng and D. Marks, "*Theoretical structure factors for selected oxides and their effects in high-resolution electron-microscope (HREM) images*", **Acta Cryst. A**. 62: p. 208, (2006).
129. P.F. Fewster, "*X-Ray Scattering from Semiconductors and other Materials*", **Book**. World Scientific Publishing Co. Pte. Ltd.(2015)
130. S. Takagi, "*A Dynamical Theory of Diffraction for a Distorted Crystal*", **Journal of the Physical Society of Japan**. 26: p. 1239, (1969).
131. C.R. Wie, T.A. Tombrello, and T. Vreeland, "*Dynamical x-ray diffraction from nonuniform crystalline films: Application to x-ray rocking curve analysis*", **Journal of Applied Physics**. 59: p. 3743, (1986).
132. B.C. Larson and J.F. Barhorst, "*X-ray study of lattice strain in boron implanted laser annealed silicon*", **Journal of Applied Physics**. 51: p. 3181, (1980).
133. B.W. Batterman and H. Cole, "*Dynamical Diffraction of X Rays by Perfect Crystals*", **Reviews of Modern Physics**. 36: p. 681, (1964).
134. B.C. Larson, J.Z. Tischler, and D.M. Mills, "*Nanosecond resolution time-resolved x-ray study of silicon during pulsed-laser irradiation*", **Journal of Materials Research**. 1: p. 144, (1985).
135. P. Gibbon, "*Short Pulse Laser Interactions with Matter; An Introduction*", **Book**. Imperial College Press.(2005)
136. A. Rousse, P. Audebert, J.P. Geindre, F. Fallières, J.C. Gauthier, A. Mysyrowicz, G. Grillon, and A. Antonetti, "*Efficient  $K\alpha$  x-ray source from femtosecond laser-produced plasmas*", **Phys. Rev. E**. 50: p. 2200, (1994).
137. C. Reich, P. Gibbon, I. Uschmann, and E. Förster, "*Yield Optimization and Time Structure of Femtosecond Laser Plasma  $K\alpha$  Sources*", **Phys. Rev. Lett.** 84: p. 4846, (2000).

138. S.C. Wilks and W.L. Kruer, "*Absorption of ultrashort, ultra-intense laser light by solids and overdense plasmas*", **IEEE Journal of Quantum Electronics**. 33: p. 1954, (1997).
139. P. Gibbon and E. Förster, "*Short-pulse laser - plasma interactions*", **Plasma Physics and Controlled Fusion**. 38: p. 769, (1996).
140. O.J. Hans-Peter Schlenvoigt, Sebastian M. Pfothenhauer, and Malte C. Kaluza, "*Laser-based Particle Acceleration, Advances in Solid State Lasers Development and Applications*", (2010), <http://www.intechopen.com/books/advances-in-solid-state-lasers-development-and-applications/laser-based-particle-acceleration>
141. C. Ziener, I. Uschmann, G. Stobrawa, C. Reich, P. Gibbon, T. Feurer, A. Morak, S. Düsterer, H. Schwoerer, E. Förster, and R. Sauerbrey, "*Optimization of  $K\alpha$  bursts for photon energies between 1.7 and 7 keV produced by femtosecond-laser-produced plasmas of different scale length*", **Phys. Rev. E**. 65: p. 066411, (2002).
142. W. Lu, M. Nicoul, U. Shymanovich, A. Tarasevitch, P. Zhou, K. Sokolowski-Tinten, D. Von Der Linde, M. Mašek, P. Gibbon, and U. Teubner, "*Optimized  $K\alpha$  x-ray flashes from femtosecond-laser-irradiated foils*", **Phys. Rev. E**. 80: p. 026404, (2009).
143. A. Tarasevitch, A. Orisch, D. Von Der Linde, P. Balcou, G. Rey, J.P. Chambaret, U. Teubner, D. Klöpfel, and W. Theobald, "*Generation of high-order spatially coherent harmonics from solid targets by femtosecond laser pulses*", **Physical Review A**. 62: p. 023816, (2000).
144. W. Kruer, "*The Physics Of Laser Plasma Interactions*", **Book**. Frontiers in Physics. Avalon Publishing.(2003)
145. A. Schmitt and R.S.B. Ong, "*The effect of collisions on wave-breaking in a cold plasma*", **Applied physics**. 22: p. 333, (1980).
146. J.P. Freidberg, R.W. Mitchell, R.L. Morse, and L.I. Rudisinski, "*Resonant Absorption of Laser Light by Plasma Targets*", **Phys. Rev. Lett.** 28: p. 795, (1972).
147. J. Weisshaupt, V. Juvé, M. Holtz, M. Woerner, and T. Elsaesser, "*Theoretical analysis of hard x-ray generation by nonperturbative interaction of ultrashort light pulses with a metal*", **Struct. Dyn.** 2: p. 024102, (2015).
148. F. Brunel, "*Not-so-resonant, resonant absorption*", **Phys. Rev. Lett.** 59: p. 52, (1987).
149. P. Gibbon and A.R. Bell, "*Collisionless absorption in sharp-edged plasmas*", **Phys. Rev. Lett.** 68: p. 1535, (1992).
150. Z.Y. Ge, W. Yu, H.B. Zhuo, C.T. Zhou, Y.Y. Ma, X.H. Yang, T.P. Yu, D.B. Zou, S.X. Luan, Y. Yin, F.Q. Shao, and X.J. Peng, "*Resonant absorption and not-so-resonant absorption in short, intense laser irradiated plasma*", **Physics of Plasmas**. 20: p. 073301, (2013).
151. D.C. Eder, G. Pretzler, E. Fill, K. Eidmann, and A. Saemann, "*Spatial characteristics of  $K\alpha$  radiation from weakly relativistic laser plasmas*", **Appl. Phys. B**. 70: p. 211, (2000).

152. H. Nakano, T. Nishikawa, and N. Uesugi, "*Enhanced K-shell x-ray line emissions from aluminum plasma created by a pair of femtosecond laser pulses*", **App. Phys. Lett.** 79: p. 24, (2001).
153. T. Schlegel, S. Bastiani, L. Grémillet, J.P. Geindre, P. Audebert, J.C. Gauthier, E. Lefebvre, G. Bonnaud, and J. Delettrez, "*Comparison of measured and calculated x-ray and hot-electron production in short-pulse laser-solid interactions at moderate intensities*", **Phys. Rev. E.** 60: p. 2209, (1999).
154. U. Teubner, G. Kühnle, and F.P. Schäfer, "*Detailed study of the effect of a short prepulse on soft X-ray spectra generated by a high-intensity KrF\* laser pulse*", **Appl. Phys. B.** 54: p. 493, (1992).
155. W. Theobald, C. Wülker, J. Jasny, S. Szatmári, F.P. Schäfer, and J.S. Bakos, "*Interaction of subpicosecond KrF laser pulses with a preformed carbon plasma*", **Phys. Rev. E.** 49: p. R4799, (1994).
156. T. Feurer, A. Morak, I. Uschmann, C. Ziener, H. Schwoerer, E. Förster, and R. Sauerbrey, "*An incoherent sub-picosecond X-ray source for time-resolved X-ray-diffraction experiments*", **Appl. Phys. B.** 72: p. 15, (2001).
157. Z. Jiang, J.C. Kieffer, J.P. Matte, M. Chaker, O. Peyrusse, D. Gilles, G. Korn, A. Maksimchuk, S. Coe, and G. Mourou, "*X-ray spectroscopy of hot solid density plasmas produced by subpicosecond high contrast laser pulses at 1018–1019 W/cm<sup>2</sup>*", **Physics of Plasmas.** 2: p. 1702, (1995).
158. D.D. Meyerhofer, H. Chen, J.A. Delettrez, B. Soom, S. Uchida, and B. Yaakobi, "*Resonance absorption in high-intensity contrast, picosecond laser-plasma interactions\**", **Physics of Fluids B: Plasma Physics.** 5: p. 2584, (1993).
159. F. Ewald, H. Schwoerer, and R. Sauerbrey, "*K<sub>α</sub>-radiation from relativistic laser-produced plasmas*", **EPL (Europhysics Letters).** 60: p. 710, (2002).
160. U. Shymanovich, "*Direct observation of ultrafast atomic motion using time-resolved X-ray diffraction*", **Dissertation**, Universität Duisburg-Essen, (2007)
161. C. Dietrich, "*Erzeugung Harmonischer hoher Ordnung an steilen Plasma-Dichtegradienten*", **Dissertation**, Universität Duisburg-Essen, (2004)
162. J.C. Diels and W. Rudolph, "*Ultrashort Laser Pulse Phenomena*", **Book**. Academic Press, Inc.(1996)
163. D.E. Spence, P.N. Kean, and W. Sibbett, "*60-fsec pulse generation from a self-mode-locked Ti:sapphire laser*", **Opt. Lett.** 16: p. 42, (1991).
164. **Web Page**, "*X-Ray Interactions With Matter*", [http://henke.lbl.gov/optical\\_constants](http://henke.lbl.gov/optical_constants)
165. **Web Page**, "*Quantum Efficiency (QE) in High Energy CCD detectors*", [http://www.andor.com/learning-academy/quantum-efficiency-\(qe\)-in-high-energy-ccd-detectors-understand-qe-in-a-high-energy-ccd](http://www.andor.com/learning-academy/quantum-efficiency-(qe)-in-high-energy-ccd-detectors-understand-qe-in-a-high-energy-ccd)

166. **Web Page**, "*Princeton Instruments, PI-MTE:1300B*", [www.roperscientific.de](http://www.roperscientific.de)
167. L. Bruno, G.S. Christian, K. Marion, B. Boris, G. Til Florian, K. Olga, Z. Federico, S. Anatoly, and S. Irina, "*Refractive x-ray lenses*", **J. Phys. D: Appl. Phys.** 38: p. A218, (2005).
168. H. Yumoto, H. Mimura, T. Koyama, S. Matsuyama, K. Tono, T. Togashi, Y. Inubushi, T. Sato, T. Tanaka, T. Kimura, H. Yokoyama, J. Kim, Y. Sano, Y. Hachisu, M. Yabashi, H. Ohashi, H. Ohmori, T. Ishikawa, and K. Yamauchi, "*Focusing of X-ray free-electron laser pulses with reflective optics*", **Nature Photonics**. 7: p. 43, (2012).
169. M. Bargheer, N. Zhavoronkov, R. Bruch, H. Legall, H. Stiel, M. Woerner, and T. Elsaesser, "*Comparison of focusing optics for femtosecond X-ray diffraction*", **Appl. Phys. B**. 80: p. 715, (2005).
170. T. Missalla, I. Uschmann, E. Förster, G. Jenke, and D. Von Der Linde, "*Monochromatic focusing of subpicosecond x-ray pulses in the keV range*", **Rev. Sci. Instrum.** 70: p. 1288, (1999).
171. M. Nicoul, U. Shymanovich, S. Kähle, T. Caughey, D. Sampat, K. Sokolowski-Tinten, and D.V.D. Linde, "*Bent crystal x-ray mirrors for time-resolved experiments with femtosecond laser-produced x-ray pulses*", **J. Phys.: Conf. Ser.** 21: p. 207, (2005).
172. U. Shymanovich, M. Nicoul, J. Blums, K. Sokolowski-Tinten, A. Tarasevitch, T. Wietler, M. Horn Von Hoegen, and D. Von Der Linde, "*Diffraction of strongly convergent X-rays from picosecond acoustic transients*", **Appl. Phys. A**. 87: p. 7, (2007).
173. C. Reich, I. Uschmann, F. Ewald, S. Düsterer, A. Lübcke, H. Schwoerer, R. Sauerbrey, E. Förster, and P. Gibbon, "*Spatial characteristics of  $K\alpha$  x-ray emission from relativistic femtosecond laser plasmas*", **Phys. Rev. E**. 68: p. 056408, (2003).
174. F. Zamponi, T. Kämpfer, A. Morak, I. Uschmann, and E. Förster, "*Characterization of a deep depletion, back-illuminated charge-coupled device in the x-ray range*", **Rev. Sci. Instrum.** 76: p. 116101, (2005).
175. P.S. Prevey, "*THE USE OF PEARSON VII DISTRIBUTION FUNCTIONS IN X-RAY DIFFRACTION RESIDUAL STRESS MEASUREMENT*", **Advances in X-Ray Analysis**. 29: p. 103, (1986).
176. S.I. Salem and P.L. Lee, "*Experimental widths of K and L x-ray lines*", **Atomic Data and Nuclear Data Tables**. 18: p. 233, (1976).
177. A. Sengebusch, H. Reinholz, G. Röpke, U. Zastra, T. Kämpfer, I. Uschmann, E. Förster, E. Stambulchik, E. Kroupp, and Y. Maron, "*K-line emission profiles with focus on the self-consistent calculation of plasma polarization*", **J. Phys. A: Math. Theor.** 42: p. 214061, (2009).
178. D. Schick, A. Bojahr, M. Herzog, C.V.K. Schmising, R. Shayduk, W. Leitenberger, P. Gaal, and M. Bargheer, "*Normalization schemes for ultrafast x-ray diffraction using a table-top laser-driven plasma source*", **Rev. Sci. Instrum.** 83: p. 025104, (2012).

179. B.B. Zhang, S.S. Sun, D.R. Sun, and Y. Tao, "Note: A novel normalization scheme for laser-based plasma x-ray sources", **Rev. Sci. Instrum.** 85: p. 096110, (2014).
180. C.V. Korff Schmising, M. Bargheer, M. Kiel, N. Zhavoronkov, M. Woerner, T. Elsaesser, I. Vrejoiu, D. Hesse, and M. Alexe, "Strain propagation in nanolayered perovskites probed by ultrafast x-ray diffraction", **Phys. Rev. B.** 73: p. 212202, (2006).
181. S. Höfer, T. Kämpfer, E. Förster, T. Stöhlker, and I. Uschmann, "Communication: The formation of rarefaction waves in semiconductors after ultrashort excitation probed by grazing incidence ultrafast time-resolved x-ray diffraction", **Struct. Dyn.** 3: p. 051101, (2016).
182. M. Holtz, C. Hauf, J. Weisshaupt, A.-a.H. Salvador, M. Woerner, and T. Elsaesser, "Towards shot-noise limited diffraction experiments with table-top femtosecond hard x-ray sources", **Struct. Dyn.** 4: p. 054304, (2017).
183. **Web Page**, "Avalanche Photodiode technical datasheet", [http://www.advancedphotonix.com/ap\\_products/pdfs/SD394-70-74-591.pdf](http://www.advancedphotonix.com/ap_products/pdfs/SD394-70-74-591.pdf)
184. **Web Page**, "ADC technical datasheet", <http://www.caen.it/jsp/Template2/CaenProd.jsp?parent=9&idmod=409>
185. A.K. Sharma, R.K. Patidar, M. Raghuramaiah, P.A. Naik, and P.D. Gupta, "Measuring pulse-front tilt in ultrashort pulse laser beams without ambiguity of its sign using single-shot tilted pulse-front autocorrelator", **Opt. Express.** 14: p. 13131, (2006).
186. C. Thomsen, J. Strait, Z. Vardeny, H.J. Maris, J. Tauc, and J.J. Hauser, "Coherent Phonon Generation and Detection by Picosecond Light Pulses", **Phys. Rev. Lett.** 53: p. 989, (1984).
187. O.B. Wright, B. Perrin, O. Matsuda, and V.E. Gusev, "Ultrafast carrier diffusion in gallium arsenide probed with picosecond acoustic pulses", **Phys. Rev. B.** 64: p. 081202, (2001).
188. T. Saito, O. Matsuda, and O.B. Wright, "Picosecond acoustic phonon pulse generation in nickel and chromium", **Phys. Rev. B.** 67: p. 205421, (2003).
189. O.B. Wright and V.E. Gusev, "Ultrafast generation of acoustic waves in copper", **IEEE Transactions on Ultrasonics, Ferroelectrics, and Frequency Control.** 42: p. 331, (1995).
190. O.B. Wright and V.E. Gusev, "Ultrafast acoustic phonon generation in gold", **Physica B: Condensed Matter.** 219-220: p. 770, (1996).
191. H. Park, X. Wang, S. Nie, R. Clinite, and J. Cao, "Mechanism of coherent acoustic phonon generation under nonequilibrium conditions", **Phys. Rev. B.** 72: p. 100301, (2005).
192. S.H. Lee, A.L. Cavalieri, D.M. Fritz, M.C. Swan, R.S. Hegde, M. Reason, R.S. Goldman, and D.A. Reis, "Generation and Propagation of a Picosecond Acoustic Pulse at a Buried Interface: Time-Resolved X-Ray Diffraction Measurements", **Phys. Rev. Lett.** 95: p. 246104, (2005).

193. P. Babilotte, P. Ruello, D. Mounier, T. Pezeril, G. Vaudel, M. Edely, J.M. Breteau, V. Gusev, and K. Blary, "*Femtosecond laser generation and detection of high-frequency acoustic phonons in GaAs semiconductors*", **Phys. Rev. B.** 81: p. 245207, (2010).
194. E.S.K. Young, A.V. Akimov, R.P. Campion, A.J. Kent, and V. Gusev, "*Picosecond strain pulses generated by a supersonically expanding electron-hole plasma in GaAs*", **Phys. Rev. B.** 86: p. 155207, (2012).
195. A. Morak, T. Kämpfer, I. Uschmann, A. Lübcke, E. Förster, and R. Sauerbrey, "*Acoustic phonons in InSb probed by time-resolved X-ray diffraction*", **physica status solidi (b).** 243: p. 2728, (2006).
196. N.V. Chigarev, D.Y. Paraschuk, X.Y. Pan, and V.E. Gusev, "*Coherent phonon emission in the supersonic expansion of photoexcited electron-hole plasma in Ge*", **Phys. Rev. B.** 61: p. 15837, (2000).
197. M.C. Downer and C.V. Shank, "*Ultrafast heating of silicon on sapphire by femtosecond optical pulses*", **Phys. Rev. Lett.** 56: p. 761, (1986).
198. **Web Page**, "*Physical properties of semiconductors*",  
<http://www.ioffe.ru/SVA/NSM/Semicond/Ge>
199. **Web Page**, "*Energy band structure of germanium*",  
<http://www.materialsdesign.com/appnote/energy-band-structure-germanium>
200. H. Garcia and K.N. Avanaki, "*Direct and indirect two-photon absorption in Ge within the effective mass approximation*", **App. Phys. Lett.** 100: p. 131105, (2012).
201. H. Roskos, B. Rieck, A. Seilmeier, and W. Kaiser, "*Cooling of a carrier plasma in germanium investigated with subpicosecond infrared pulses*", **App. Phys. Lett.** 53: p. 2406, (1988).
202. X.Q. Zhou, H.M. Van Driel, and G. Mak, "*Femtosecond kinetics of photoexcited carriers in germanium*", **Phys. Rev. B.** 50: p. 5226, (1994).
203. A. Elci, M.O. Scully, A.L. Smirl, and J.C. Matter, "*Ultrafast transient response of solid-state plasmas. I. Germanium, theory, and experiment*", **Phys. Rev. B.** 16: p. 191, (1977).
204. K. Sokolowski-Tinten and D. Von Der Linde, "*Generation of dense electron-hole plasmas in silicon*", **Phys. Rev. B.** 61: p. 2643, (2000).
205. T.-T. Yeh, H. Shirai, C.-M. Tu, T. Fuji, T. Kobayashi, and C.-W. Luo, "*Ultrafast carrier dynamics in Ge by ultra-broadband mid-infrared probe spectroscopy*", **Scientific Reports.** 7: p. 40492, (2017).
206. F. Pezzoli, A. Giorgioni, K. Gallacher, F. Isa, P. Biagioni, R.W. Millar, E. Gatti, E. Grilli, E. Bonera, G. Isella, D.J. Paul, and L. Miglio, "*Disentangling nonradiative recombination processes in Ge micro-crystals on Si substrates*", **App. Phys. Lett.** 108: p. 262103, (2016).
207. J.F. Young and H.M. Van Driel, "*Ambipolar diffusion of high-density electrons and holes in Ge, Si, and GaAs: Many-body effects*", **Phys. Rev. B.** 26: p. 2147, (1982).

208. L. Huldt, "*Band-to-band auger recombination in indirect gap semiconductors*", **physica status solidi (a)**. 8: p. 173, (1971).
209. L. Huldt, "*Phonon-assisted Auger recombination in germanium*", **physica status solidi (a)**. 33: p. 607, (1976).
210. S. Dominici, H. Wen, F. Bertazzi, M. Goano, and E. Bellotti, "*Numerical evaluation of Auger recombination coefficients in relaxed and strained germanium*", **App. Phys. Lett.** 108: p. 211103, (2016).
211. A. Haug, "*Carrier density dependence of Auger recombination*", **Solid-State Electronics**. 21: p. 1281, (1978).
212. E.J. Yoffa, "*Dynamics of dense laser-induced plasmas*", **Phys. Rev. B**. 21: p. 2415, (1980).
213. Y. Arafat, F.M. Mohammedy, and M.M. Shahidul Hassan, "*Optical and Other Measurement Techniques of Carrier Lifetime in Semiconductors*", **International Journal of Optoelectronic Engineering**. 2: p. 5, (2012).
214. C. Sevik and C. Bulutay, "*Auger recombination and carrier multiplication in embedded silicon and germanium nanocrystals*", **Phys. Rev. B**. 77: p. 125414, (2008).
215. L. Carroll, P. Friedli, S. Neuenschwander, H. Sigg, S. Cecchi, F. Isa, D. Christina, G. Isella, Y. Fedoryshyn, and J. Faist, "*Direct-Gap Gain and Optical Absorption in Germanium Correlated to the Density of Photoexcited Carriers, Doping, and Strain*", **Phys. Rev. Lett.** 109: p. 057402, (2012).
216. N.G. Nilsson, "*Band-to-band Auger Recombination in Silicon and Germanium*", **Physica Scripta**. 8: p. 165, (1973).
217. D.H. Auston, C.V. Shank, and P. Lefur, "*Picosecond Optical Measurements of Band-to-Band Auger Recombination of High-Density Plasmas in Germanium*", **Phys. Rev. Lett.** 35: p. 1022, (1975).
218. E. Ghahramani and J.E. Sipe, "*Pressure dependence of the band gaps of semiconductors*", **Phys. Rev. B**. 40: p. 12516, (1989).
219. H.P. Singh, "*Determination of Thermal Expansion of Germanium, Rhodium, and Iridium by X-rays*", **Acta Cryst. A**. A24: p. 469, (1968).
220. D. Gerlich, B. Abeles, and R.E. Miller, "*High-Temperature Specific Heats of Ge, Si, and Ge-Si Alloys*", **Journal of Applied Physics**. 36: p. 76, (1965).
221. T. Chase, M. Trigo, A.H. Reid, R. Li, T. Vecchione, X. Shen, S. Weathersby, R. Coffee, N. Hartmann, D.A. Reis, X.J. Wang, and H.A. Dürr, "*Ultrafast electron diffraction from non-equilibrium phonons in femtosecond laser heated Au films*", **App. Phys. Lett.** 108: p. 041909, (2016).
222. I. Klett and B. Rethfeld, "*Relaxation of a nonequilibrium phonon distribution induced by femtosecond laser irradiation*", **arXiv:1710.02355 [cond-mat.mtrl-sci]**, (2017).

223. M.J. Stern, L.P. René De Cotret, M.R. Otto, R.P. Chatelain, J.-P. Boisvert, M. Sutton, and B.J. Siwick, "*Mapping momentum-dependent electron-phonon coupling and nonequilibrium phonon dynamics with ultrafast electron diffuse scattering*", **Phys. Rev. B.** 97: p. 165416, (2018).
224. M. Horn-Von Hoegen and M. Henzler, "*Lattice matching periodic interfacial dislocation network in surfactant-mediated growth of Ge on Si(111)*", **physica status solidi (a).** 146: p. 337, (1994).
225. **Web Page**, "*Optical Absorption Coefficient Calculator*", <https://cleanroom.byu.edu/OpticalCalc>
226. K.D. Liss, T. D'almeida, M. Kaiser, R. Hock, A. Magerl, and J.F. Eloy, "*Time-resolved x-ray diffraction study of laser-induced shock and acoustic waves in single crystalline silicon*", **Journal of Applied Physics.** 106: p. 044914, (2009).
227. J. Weisshaupt, V. Juvé, M. Holtz, S. Ku, M. Woerner, T. Elsaesser, S. Ališauskas, A. Pugžlys, and A. Baltuška, "*High-brightness table-top hard X-ray source driven by sub-100-femtosecond mid-infrared pulses*", **Nature Photonics.** 8: p. 927, (2014).
228. F. Brinks, **Dissertation**, Universität Duisburg-Essen, (to be submitted)
229. R. Cortés, L. Rettig, Y. Yoshida, H. Eisaki, M. Wolf, and U. Bovensiepen, "*Momentum-Resolved Ultrafast Electron Dynamics in Superconducting  $\text{Bi}_2\text{Sr}_2\text{CaCu}_2\text{O}_{8+\delta}$* ", **Phys. Rev. Lett.** 107: p. 097002, (2011).
230. L. Rettig, R. Cortés, S. Thirupathaiiah, P. Gegenwart, H.S. Jeevan, M. Wolf, J. Fink, and U. Bovensiepen, "*Ultrafast Momentum-Dependent Response of Electrons in Antiferromagnetic  $\text{EuFe}_2\text{As}_2$  Driven by Optical Excitation*", **Phys. Rev. Lett.** 108: p. 097002, (2012).
231. C.L. Smallwood, J.P. Hinton, C. Jozwiak, W. Zhang, J.D. Koralek, H. Eisaki, D.-H. Lee, J. Orenstein, and A. Lanzara, "*Tracking Cooper Pairs in a Cuprate Superconductor by Ultrafast Angle-Resolved Photoemission*", **Science.** 336: p. 1137, (2012).
232. I. Avigo, R. Cortés, L. Rettig, S. Thirupathaiiah, H.S. Jeevan, P. Gegenwart, T. Wolf, M. Ligges, M. Wolf, J. Fink, and U. Bovensiepen, "*Coherent excitations and electron-phonon coupling in  $\text{Ba}/\text{EuFe}_2\text{As}_2$  compounds investigated by femtosecond time- and angle-resolved photoemission spectroscopy*", **Journal of Physics: Condensed Matter.** 25: p. 094003, (2013).
233. L. Rettig, R. Cortés, H.S. Jeevan, P. Gegenwart, T. Wolf, J. Fink, and U. Bovensiepen, "*Electron-phonon coupling in 122 Fe pnictides analyzed by femtosecond time-resolved photoemission*", **New Journal of Physics.** 15: p. 083023, (2013).
234. I. Avigo, S. Thirupathaiiah, M. Ligges, T. Wolf, J. Fink, and U. Bovensiepen, "*Doping dependence and electron-boson coupling in the ultrafast relaxation of hot electron populations in  $\text{Ba}(\text{Fe}_{1-x}\text{Co}_x)_2\text{As}_2$* ", **New Journal of Physics.** 18: p. 093028, (2016).

235. S. Parham, H. Li, T.J. Nummy, J.A. Waugh, X.Q. Zhou, J. Griffith, J. Schneeloch, R.D. Zhong, G.D. Gu, and D.S. Dessau, "*Ultrafast Gap Dynamics and Electronic Interactions in a Photoexcited Cuprate Superconductor*", **Physical Review X**. 7: p. 041013, (2017).
236. T. Konstantinova, J.D. Rameau, A.H. Reid, O. Abdurazakov, L. Wu, R. Li, X. Shen, G. Gu, Y. Huang, L. Rettig, I. Avigo, M. Ligges, J.K. Freericks, A.F. Kemper, H.A. Dürr, U. Bovensiepen, P.D. Johnson, X. Wang, and Y. Zhu, "*Nonequilibrium electron and lattice dynamics of strongly correlated  $\text{Bi}_2\text{Sr}_2\text{CaCu}_2\text{O}_{8+\delta}$  single crystals*", **SCIENCE ADVANCES**. 4: p. 7427, (2018).
237. H.H. Landolt and Börnstein, "*Zahlenwerte und Funktionen aus Naturwissenschaft und Technik*", **Book**. Springer, Madelung.(1961)
238. **Web Page**, "*X-ray dynamical diffraction data on Web*", [www.sergey.gmca.aps.anl.gov](http://www.sergey.gmca.aps.anl.gov)
239. **Web Page**, "*Optical properties of materials*", <https://refractiveindex.info/>

## Acknowledgements

Such a work would not have been possible without the help and support of many people, to whom this section is dedicated and to whom I am happy to give credits.

Firstly, I would like to express my sincere gratitude to my supervisor Dr. Klaus Sokolowski-Tinten for the continuous support of my Ph.D. study and related research, for his patience, motivation, and immense knowledge. His guidance helped me in all the time of research and writing of this thesis.

Besides my supervisor, I would like to thank the leader of our research group Prof. Dr. Uwe Bovensiepen for his insightful comments and encouragement, which incited me to widen my research from various perspectives.

I would like to express my special appreciation and thanks to Dr. Ping Zhou for his valuable helps and supports. You always had interesting and useful scientific and technical advices from which I always profited and learnt.

I also would like to thank Dr. Alexander Tarasevitch for his support, in particular for the laser-system. I thank my fellow labmates: Dennis Menn and Philipp Krumei for the stimulating discussions, for the sleepless nights we were working together before deadlines, and for all the fun we have had over past years.

Special thanks to our group secretary Christina Boese, for her helps in dealing with all the various paperwork and administration issues.

To our technical staffs, I want to thank Michael Bieske for making all the mechanical components, and Roland Kohn for all the computer related issues.

I thank Dr. Isabella Avigo and Dr. Ishita Agarwal for their helpful suggestions and comments on this work.

I also want to thank all former and current members working in AG Bovensiepen: Dr. Matthieu Nicoul, Dr. Wei Lu, Florian Quirin, Michael Vattilana, Dr. Nicolas Bergéard, Dr. Carla Streubüher, Dr. Manuel Ligges, Dr. Mathias Sandhofer, Dr. Jens Wiezorek, Abdul Samad Seyed, Andre Seyen, Fabian Brinks, Jinghao Chen, Yasin Beyazit and Marius Milnikel for all our exchange.

## Acknowledgements

---

Words cannot express how grateful I am to my parents for all of the sacrifices that they have made on my behalf. Your prayer for me was what sustained me thus far.

Last but not the least; I would like to thank my wife for supporting me spiritually throughout writing this thesis and my life in general.

“منا جان ازت خیلی ممنونم. ازت ممنونم برای صبر و تحملت و برای دلگرمیهایی که به من می دادی. دوستت دارم عزیزم.”